

---

# **Resolving heterogeneities in single and multiphase bioreactor systems**

## **Predictive modelling tools towards successful scale-up**

---

### **Dissertation**

Von der Fakultät Energie-, Verfahrens- und Biotechnik der  
Universität Stuttgart zur Erlangung der Würde eines  
Doktor-Ingenieurs (Dr.-Ing.) genehmigte Abhandlung

Vorgelegt von:

**Maike Kuschel**

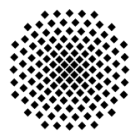
aus Mainz

Hauptberichter: Prof. Dr.-Ing. Ralf Takors

Mitberichter: Prof. Dr.-Ing. Michael Schlüter

Tag der mündlichen Prüfung: 20.11.2020

Institut für Bioverfahrenstechnik



**University of Stuttgart**  
Germany

2020



*Für Max*



## Acknowledgements

This work would have been hardly possible without the support of numerous people within my scientific and social environment. I want to use the following lines to thank everyone involved.

First and foremost I would like to express my gratitude to Prof. Dr.-Ing. Ralf Takors for giving me the opportunity to work in this interesting field and to be part of the IBVT team. His valuable feedback, support and encouragement helped me to prepare this thesis and I am very grateful for the freedom and trust he provided in my work. Furthermore, I want to thank Prof. Dr.-Ing. Michael Schlüter and Prof. Dr.-Ing. Eckart Laurien for their interest in this research and their participation in the examination committee as well as Prof. Dr. - Ing. Ulrich Nieken, Prof. Dr. Tovar and Prof. Dr.-Ing. Christian Bonten for their participation during the circulation procedure.

Secondly, I want to thank all my wonderful colleagues who became good friends to me. Many thanks go to my modelling partners and friends Flora Siebler and Julia Zieringer for their inspiring ideas and helpful discussions. Julia, thank you for the intense last year of joyful CFD office talks. Special thanks go to my project partner Adrian Eilingsfeld. During this sometimes bumpy road we always kept a good mood, took drawbacks with humour and managed to find a good solution. I am grateful to Dr. Alexey Lapin, who inspired me with his deep and profound knowledge about fluid mechanics. I would also like to thank the permanent staff at the IBVT for their support concerning daily tasks: Ms. Reu with her positive manner managed all administrative affairs and Andreas Freund, Alexander Dietrich and Salaheddine Laghrami always helped me when I needed special requirements for my experiments, especially Salah who supported me with his fermentation skills during my PhD. I thank Alexander Nieß for introducing me to the world of the IBVT.

I would not have enjoyed my time at the institute that much without the company of my office colleagues and friends Robert, Sebastian and also in my last year Martin. Thank you for the nerf gun fights and the bad jokes. I also want to thank Vikas for the refreshing breaks, distractions from daily work and the Indian food. Furthermore, I can call myself a proud member of the IBVT football team and thank all players for the wonderful summers on the pitch.

I am grateful to my students Tobias and Paul for their enthusiasm and great ideas. Special thanks go to Ruphay for his support in experimental work and the data created thereof. I want to thank my lunch partners Ashley, Paul and especially Rolf for his challenging arguments.

Finally, my biggest thanks go to my family who supported me all my life. My parents and grandparents were always there for me and trusted in my abilities, my sissy inspired me and showed me the way of a research career and I want to thank my partner and best friend Max - there are no words for the unlimited and unconditional support you gave me in every way. Thank you.



## **Declaration of Originality**

I declare that the submitted work has been completed by me and that I have not used any other than permitted reference sources or materials. All references and other sources used by me have been appropriately acknowledged in the work.

Hiermit erkläre ich, dass ich die vorliegende Arbeit selbstständig angefertigt habe. Es wurden von mir nur die in der Arbeit ausdrücklich benannten Quellen und Hilfsmittel benutzt. Übernommenes Gedankengut wurde von mir als solches kenntlich gemacht.

*Stuttgart, den 04.06.2020*

Ort, Datum

---

Maike Kuschel



# Contents

<b>Nomenclature</b>	<b>XI</b>
<b>List of Figures</b>	<b>XV</b>
<b>List of Tables</b>	<b>XVI</b>
<b>Abstract</b>	<b>XIX</b>
<b>Zusammenfassung</b>	<b>XXI</b>
<b>1 Introduction</b>	<b>1</b>
1.1 The biotechnological market and challenges of production . . . . .	1
1.2 Motivation of this thesis . . . . .	1
1.3 Objectives, strategies and thesis outline . . . . .	3
<b>2 Theory</b>	<b>5</b>
2.1 <i>Corynebacterium glutamicum</i> . . . . .	5
2.2 Scale up of fermentation processes . . . . .	5
2.3 Dimensionless numbers . . . . .	7
2.4 Computational fluid dynamics for biotechnology . . . . .	8
2.4.1 Fundamentals of flow simulation . . . . .	8
2.4.2 Modelling of turbulence in stirred tanks . . . . .	10
2.4.3 Modelling of agitation and mixing in stirred tanks . . . . .	15
2.4.4 Modelling of two phase flows in stirred tanks . . . . .	16
2.4.5 Modelling of population heterogeneity . . . . .	19
<b>3 Characterisation of bioprocesses with <i>C. glutamicum</i> as model organism</b>	<b>21</b>
3.1 Introduction . . . . .	21
3.2 Material and methods . . . . .	23
3.2.1 Materials . . . . .	23
3.2.2 Seed train . . . . .	25
3.2.3 Bioreactor cultivation . . . . .	26
3.2.4 Analytics . . . . .	27
3.3 Results and discussion . . . . .	34

3.3.1	Process kinetics . . . . .	34
3.3.2	Determination of broth viscosity . . . . .	36
3.3.3	Determination of broth surface tension . . . . .	38
3.4	Conclusion . . . . .	42
<b>4</b>	<b>Characterisation of a pilot scale bioreactor</b>	<b>43</b>
4.1	Introduction . . . . .	43
4.2	Experimental measurements . . . . .	44
4.2.1	Bioreactor setup . . . . .	44
4.2.2	Power consumption . . . . .	44
4.2.3	Mixing time . . . . .	45
4.2.4	Gas hold-up . . . . .	45
4.2.5	Measurement of $k_{La}$ . . . . .	45
4.3	Numerical simulations . . . . .	46
4.3.1	General setup . . . . .	46
4.3.2	Single phase simulations . . . . .	47
4.3.3	Multiphase simulations . . . . .	47
4.3.4	Validation parameters . . . . .	51
4.4	Results and discussion . . . . .	51
4.4.1	Experimental measurements . . . . .	52
4.4.2	Numerical simulations . . . . .	60
4.5	Conclusion . . . . .	74
<b>5</b>	<b>Simulated oxygen and glucose gradient</b>	<b>75</b>
5.1	Introduction . . . . .	75
5.2	Simulation setup . . . . .	76
5.2.1	Inclusion of the reaction . . . . .	76
5.2.2	Particle tracking . . . . .	78
5.2.3	Statistical evaluation . . . . .	78
5.3	Results and discussion . . . . .	79
5.3.1	Pseudo-stationary double gradient . . . . .	79
5.3.2	Statistical lifeline analysis . . . . .	81
5.3.3	Simplified design of scale-down devices . . . . .	84
5.4	Conclusion . . . . .	85
<b>6</b>	<b>Cell cycle model</b>	<b>87</b>
6.1	Introduction . . . . .	87
6.2	Model setup . . . . .	88
6.3	Results and discussion . . . . .	92
6.3.1	Cell cycle phases of <i>P. putida</i> . . . . .	92
6.3.2	Cell cycle phases of <i>C. glutamicum</i> . . . . .	94
6.4	Conclusion . . . . .	97

---

<b>7</b>	<b>Heterogeneity analysis in large scale</b>	<b>99</b>
7.1	Introduction . . . . .	99
7.2	Material and methods . . . . .	100
7.2.1	Case 1: Single phase with <i>P. putida</i> . . . . .	101
7.2.2	Case 2: Multiphase with <i>C. glutamicum</i> . . . . .	103
7.3	Results and discussion . . . . .	104
7.3.1	Case 1: <i>P. putida</i> . . . . .	104
7.3.2	Case 2: <i>C. glutamicum</i> . . . . .	109
7.4	Conclusion . . . . .	113
<b>8</b>	<b>Conclusion and outlook</b>	<b>115</b>
	<b>Bibliography</b>	<b>121</b>
	<b>Appendix A Tables</b>	<b>135</b>
A.1	List of instruments . . . . .	135
A.2	List of software . . . . .	136
A.3	List of chemicals . . . . .	136
	<b>Appendix B Authors contribution</b>	<b>137</b>
B.1	Manuscript I . . . . .	138
B.2	Manuscript II . . . . .	152



## Nomenclature

### Symbols

Sign	Unit	Description
$a_I$	$\text{m}^{-1}$	Interfacial surface area
$a_{\text{fit}}$	–	Fitted parameter
$a$	–	Normalised cell age
$B_c$	h	Time for cell cycle initiation of replication
$b_{\text{fit}}$	–	Fitted parameter
$C_c$	h	Time for cell cycle replication
$E(\kappa)$	$\text{m}^3 \text{s}^{-2}$	Turbulent kinetic energy spectrum
$c_{\text{O}_2,\text{L}}^*$	$\text{mol m}^{-3}$	Oxygen saturation concentration
$c_{\text{O}_2,\text{L}}$	$\text{mol m}^{-3}$	Oxygen concentration
$c_S$	$\text{kg m}^{-3}$	Substrate concentration
$c_X$	$\text{kg m}^{-3}$	Biomass concentration
$c_{\text{fit}}$	–	Fitted parameter
$c_t$	–	Tracer concentration
$C_{k_L}$	–	Constant of $k_L$ model
$C_D$	–	Drag coefficient
$D_c$	h	Time between cell cycle replication and cell division
$D$	$\text{m}^2 \text{s}^{-1}$	Diffusion coefficient
$D_I$	m	Impeller diameter
$d_0$	m	Nozzle diameter
$d$	m	Bubble diameter
$d_S$	m	Sauter diameter
$Eu$	–	Eötvös number
$F_i$	–	Number of replication forks
$Fl$	–	Flow number
$Fr$	–	Froude number
$F$	$\text{kg kg}^{-1} \text{h}^{-1}$	Feeding rate
$G$	–	Chromosome content per cell
$H_L$	m	Liquid height
$H^{cp}$	$\text{mol m}^{-3} \text{Pa}^{-1}$	Henry coefficient
$I$	A	Current
$K$	–	Fitted constant

## Symbols

---

Sign	Unit	Description
$L$	m	Length
$k_L a$	$\text{h}^{-1}$	Volumetric mass transfer coefficient
$k$	–	Turbulent kinetic energy
$K_S$	$\text{kg m}^{-3}$	Half saturation constant (substrate)
$K_{\text{O}_2}$	$\text{mol m}^{-3}$	Half saturation constant (oxygen)
$k_d$	–	DNA synthesis rate
$M$	N m	Rotational moment
$N_P$	–	Power number
$N$	$\text{s}^{-1}$	Agitation rate
$n$	–	Frequency
$P$	W	Power
$p_{\text{CO}_2}$	Pa	Partial pressure of carbon dioxide
$p$	Pa	Pressure
$Q_{\text{O}_2}$	$\text{mol m}^{-3} \text{h}^{-1}$	Volumetric oxygen uptake rate
$Q_g$	$\text{m}^3 \text{s}^{-1}$	Gassing rate
$m_{\text{ATP}}$	$\text{mmol g}^{-1} \text{h}^{-1}$	nongrowth-associated ATP maintenance
$q_{\text{CO}_2}$	$\text{mol kg}^{-1} \text{h}^{-1}$	Cell specific carbon dioxide production rate
$q_{\text{O}_2}$	$\text{mol kg}^{-1} \text{h}^{-1}$	Cell specific oxygen consumption rate
$q_S$	$\text{kg kg}^{-1} \text{h}^{-1}$	Cell specific substrate consumption rate
$RQ$	–	Respiratory quotient
$Re$	–	Reynolds number
$Sc$	–	Schmidt number
$T$	K	Temperature
$T_D$	m	Tank diameter
$t_{63}$	s	Probe response time
$U$	V	Voltage
$u, v, w$	$\text{m s}^{-1}$	Velocity components
$V_L$	$\text{m}^3$	Liquid volume
$\dot{V}_g$	$\text{Nm}^3/\text{h}$	Gas volume flow
$v_S$	$\text{m s}^{-1}$	Superficial gas velocity
$x, y, z$	m	Coordinates
$Y_{\text{XS}}$	$\text{kg kg}^{-1}$	Yield (biomass/substrate)
$Y_{\text{XO}_2}$	$\text{kg mol}^{-1}$	Yield (biomass/oxygen)
$Y_{\text{ATP}}$	$\text{g mmol}^{-1}$	Yield (biomass/ATP)
$y$	–	Molar gas fraction
$y_{\text{exp}}$	–	Experimental normal distribution
$y_{\text{sim}}$	–	Simulated normal distribution
$y_w^+$	–	Dimensionless wall distance
$y_w$	–	Actual wall distance

## Greek Symbols

Sign	Unit	Description
$\alpha$	–	Volume fraction
$\gamma$	–	Fitted constant
$\Delta C$	m	Impeller spacing
$\dot{\delta}$	$s^{-1}$	Strain rate
$\rho$	$kg\ m^{-3}$	Density
$\varepsilon_G$	–(%)	Gas holdup
$\varepsilon$	$m^2\ s^{-3}$	Turbulent dissipation rate
$\zeta$	–	Fitted constant
$\eta_\kappa$	$m^{-1}$	Kolgomorov length scale
$\eta$	Pa s	Dynamic viscosity
$\vartheta$	°C	Temperature
$\kappa$	$m^{-1}$	Wave number
$\lambda$	$W\ m^{-1}\ K^{-1}$	Thermal conductivity
$\lambda_{OD}$	–	OD/Biomass correlation factor
$\mu$	$h^{-1}$	Growth rate
$\nu$	$m^2\ s^{-1}$	Kinematic viscosity
$\Phi_g$	mol s	Molar gas flow
$\sigma$	$N\ m^{-1}$	Surface tension
$\tau_{95}$	s	Mixing time 95 %
$\tau_{dep}$	s	Time to substrate depletion
$\tau_d$	h	Doubling time
$\tau_s$	Pa	Shear stress
$\tau$	s	Dwelling time in the specific regime

## Indices

Sign	Description
CO <sub>2</sub>	Carbon Dioxide
eff	Effective
G	Gas
<i>i</i>	Control variable
in	In-flowing
L	Liquid
O <sub>2</sub>	Oxygen
out	Out-flowing
rad	Radial

## Acronyms

---

Sign	Description
sc	Scaled quantity
tip	Tip
t	Torque

## Constants

Sign	Value	Description
$g$	$9.81 \text{ m s}^{-2}$	Gravitational acceleration
$R$	$8.314 \text{ J mol}^{-1} \text{ K}^{-1}$	Gas constant

## Acronyms

**ATP** Adenosine triphosphate  
**BSD** bubble size distribution  
**CFD** computational fluid dynamics  
**CS** Computational Snapshot  
**DNS** Direct Numerical Simulation  
**DO** dissolved oxygen  
**DPM** Discrete Phase Model  
**IO** Inner-Outer  
**LDA** Laser Doppler Anemometry  
**LES** Large Eddy Simulation  
**MP** multiphase  
**MRF** Multiple Reference Frame  
**NSE** Navier-Stokes Equations  
**OD<sub>600</sub>** optical density at a wavelength of 600 nm  
**PBE** Population Balance Equations  
**PBM** Population Balance Model  
**PFR** plug flow reactor  
**RANS** Reynolds Average Navier-Stokes  
**RKE** realizable  $k - \varepsilon$   
**SD** scale-down  
**SKE** standard  $k - \varepsilon$   
**SM** Sliding Mesh  
**SP** single phase  
**STR** stirred tank reactor  
**UDF** user defined function  
**VOF** Volume of Fluid

## List of Figures

2.1	Fundamental flow equations . . . . .	10
2.2	Hierarchy of turbulence models and turbulent kinetic energy spectrum . . . . .	11
2.3	Multiphase models . . . . .	17
3.1	Seed train . . . . .	25
3.2	P&ID of the bioreactor in batch mode . . . . .	26
3.3	Principle of viscosity measurement with a rheometer. . . . .	30
3.4	Principle of the Du Noüy method. . . . .	31
3.5	Principle of bubble pressure method. . . . .	32
3.6	Time course of $c_X$ and $c_S$ . . . . .	35
3.7	Time course of $k_L a$ . . . . .	35
3.8	Elemental carbon balance of the exponential phase . . . . .	36
3.9	Fluorescence microscopy of viscosity samples . . . . .	37
3.10	Newtonian fluids . . . . .	37
3.11	Viscosity of the broth . . . . .	38
3.12	Viscosity of different biomass concentrations . . . . .	38
3.13	Surface tension of the broth . . . . .	39
3.14	Surface tension as function of biomass. . . . .	39
3.15	Surface tension of antifoam solutions (static method) . . . . .	40
3.16	Surface tension of antifoam solutions (dynamic method) . . . . .	40
3.17	Influence of antifoam on $k_L a$ values (lab scale) . . . . .	41
3.18	Influence of antifoam on $k_L a$ values (pilot scale) . . . . .	41
4.1	Pilot scale reactor geometry . . . . .	46
4.2	Power input as function of agitation rate . . . . .	52
4.3	Power number as function of Reynolds number . . . . .	53
4.4	Power ratio as function of flow number . . . . .	53
4.5	Gas hold up as function of $Fr$ . . . . .	55
4.6	Gas hold up as function of power consumption . . . . .	56
4.7	Mixing time as function of $Re$ . . . . .	57
4.8	Mixing time as function of the power consumption . . . . .	59
4.9	Volumetric mass transfer coefficient as function of power consumption . . . . .	59
4.10	Position of the lines for tracking flow variables . . . . .	61
4.11	Normalised radial velocity at various positions (SP) . . . . .	62

4.12	Merging flow field . . . . .	63
4.13	Tangentially averaged profiles of the normalised radial velocity (SP) . . . . .	63
4.14	Normalised turbulent dissipation rate at various positions (SP) . . . . .	64
4.15	Tangentially averaged profiles of the normalised turbulent dissipation rate (SP) . . . . .	64
4.16	Mixing time profile . . . . .	66
4.17	Drag dependent gas volume fraction . . . . .	67
4.18	Normalised radial velocity at various positions (MP) . . . . .	69
4.19	Tangentially averaged profiles of the normalised radial velocity (MP) . . . . .	70
4.20	Normalised turbulent dissipation rate at various positions (MP) . . . . .	70
4.21	Tangentially averaged profiles of the normalised turbulent dissipation rate (MP) . . . . .	71
4.22	Results of multiphase simulations of MPM3 . . . . .	71
4.23	Gas volume distribution of MPM4 . . . . .	73
5.1	Single substrate Monod kinetic . . . . .	78
5.2	Regime transition patterns . . . . .	79
5.3	Local distribution of simulated growth rates . . . . .	80
5.4	Spatial concentration profiles of glucose and oxygen . . . . .	80
5.5	Time course of glucose and oxygen profiles . . . . .	82
5.6	Frequency distribution of regime transition strategy . . . . .	83
5.7	Comparison of residence time prediction . . . . .	84
5.8	Examples of simplified scale down devices . . . . .	85
6.1	Cell cycle model overview . . . . .	89
6.2	Principle of the cell cycle model . . . . .	90
6.3	Cell cycle phases for <i>P. putida</i> . . . . .	93
6.4	Cell cycle phases for <i>C. glutamicum</i> . . . . .	96
7.1	Geometry of the 54 m <sup>3</sup> reactor . . . . .	101
7.2	Regime transition patterns for the 54 m <sup>3</sup> reactor . . . . .	103
7.3	Large scale single phase gradient and lifeline . . . . .	105
7.4	Frequency distribution of regime transition strategy for the 54 m <sup>3</sup> reactor . . . . .	106
7.5	Distribution of energy level and C-phase duration for the 54 m <sup>3</sup> reactor . . . . .	108
7.6	Comparison of pilot and large scale gas hold up and mass transfer coefficient . . . . .	110
7.7	Comparison of theoretical growth rates in pilot and large scale . . . . .	111
7.8	Oxygen and carbon dioxide local distribution in large scale . . . . .	112
8.1	Schematic overview of workpackages achieved in this study . . . . .	115

## List of Tables

3.1	Composition of 2×TY complex medium . . . . .	24
3.2	Composition of CGXII minimal medium . . . . .	24
4.1	Pilot scale geometry, operational conditions and media properties . . . . .	46
4.2	Setup for Single Phase Simulations . . . . .	47
4.3	Setup for Multiphase Simulations . . . . .	47
4.4	Determination of flooding regime. . . . .	54
4.5	Comparison with mixing time correlation . . . . .	58
4.6	Comparison of integral predicted energy dissipation with expected power input in single phase. . . . .	65
4.7	Mixing time in single phase . . . . .	66
4.8	Determination of the scaling factor in multiphase. . . . .	68
4.9	Comparison of different $k_L a$ models. . . . .	68
4.10	Simulated and experimental data in multiphase. . . . .	72
4.11	Simulated and experimental data of MPM4. . . . .	73
5.1	Regime transition statistics . . . . .	82
6.1	Results of cell cycle phases for <i>C. glutamicum</i> . . . . .	95
7.1	Setup of the 54 m <sup>3</sup> . . . . .	101
7.2	Measures of the different scales . . . . .	104
7.3	Regime transition statistics for the 54 m <sup>3</sup> reactor . . . . .	107
7.4	Results of the different scales in multiphase . . . . .	109
A.1	Instruments . . . . .	135
A.2	Software . . . . .	136
A.3	Chemicals . . . . .	136



## Abstract

In the past decades, biotechnological sales have increased steadily along with the range of products. Amino acids and organic acids as high-value feedstock are major contributors to the constantly growing market. Microbial production hosts such as *C. glutamicum* or *P. putida* yield stable production during process development in lab scale. However, as consequence of the process transfer into large scale, microorganisms may be prone to occurring inhomogeneities due to longer mixing times or hampered mass transfer, finally yielding deteriorated performance. Experimentally resolving environmental conditions in production scale bioreactors is rarely feasible due to difficulties in installing analytical instruments in the required resolution and low plant availability for optimisation topics. Consequently, in the past years computational fluid dynamics (CFD) has emerged as a tool to predict gradients in industrial scale fermenters. By tracking the bacteria on their way through the bioreactor, resulting flow fields can be used for the statistical evaluation of experienced concentration fluctuations. Although existing CFD studies already describe possible scenarios, the influence of multiple gradients at a time was neglected and focus was put solely on a single parameter such as glucose as main substrate. In fact, oxygen as growth determining substrate was omitted so far, due to the complexity of two-phase flow simulations. Moreover, if the gas phase was included, validation of gained multiphase simulation results was done sparsely.

This thesis provides supporting tools to characterise single and multiphase large scale conditions, which help to minimise the risk of suboptimal scale up. A framework is presented, depicting the necessary steps to investigate large scale conditions by CFD, consisting of the characterisation of the biological system and reactor setup, multiphase and gradient simulation as well as the subsequent analysis of large scale heterogeneities. Starting point was the determination of cell specific rates and yields by batch cultivations with *C. glutamicum*. Additionally, physical properties of the broth, such as viscosity, density and surface tension were identified to be similar to water. Accordingly, the experimental characterisation of a pilot scale bioreactor system was performed without adjusting to medium specific properties. By variation of agitation and gassing rates, ranges of volumetric power input, mixing time, volumetric mass transfer coefficient ( $k_L a$ ) and gas hold-up ( $\varepsilon_G$ ) were obtained and used for the validation of multiphase simulations. As a result, an operating point was chosen at 300 rpm and 0.25 vvm, yielding a specific power consumption of  $2.2 \text{ kW m}^{-3}$  and a  $k_L a$  value of  $125 \text{ h}^{-1}$  to mimic a late stage fed-batch scenario without flooding of the impellers but sufficient oxygen supply and realistic power input.

Subsequently, amongst several models for the description of two-phase flows, a suitable setup for the multiphase simulation of the pilot scale bioreactor was implemented. The introduction of a scaling factor for the turbulent dissipation rate, reduced the computational demand by enabling the

use of a coarser grid size ( $1.12 \cdot 10^5 \text{ \#}/\text{m}^3$ ), finally leading to only minor deviations of  $< 12 \%$  compared to the experimentally determined parameters.

Moreover, a 'snap-shot' of a late fed-batch scenario consisting of glucose and oxygen concentration profiles was depicted, using the said setup in combination with an Euler-Lagrange approach. The Roels kinetic served to model multi-substrate uptake, which is controlled by the local extra-cellular environment and therefore the reaction was coupled to the Eulerian phase. The bacterial phase was simulated as massless Lagrangian particles. The obtained concentration profiles were overlaid and classified into a low glucose ( $L_S$ ), a transient (T) and a low oxygen ( $L_{O_2}$ ) regime. So-called *lifelines*, records of bacterial cells encountering fluctuating environmental conditions were statistically evaluated, providing information on the frequency of regime transitions and average dwelling times in specific regimes. Since dwelling times in the transient regime were rather short ( $< 1 \text{ s}$ ) and the estimated volume was below  $5 \%$  of the total volume, the regime T can be neglected in the subsequent design of scale-down (SD) devices. Lacking detailed information on environmental conditions inside a bioreactor, traditionally, these SD devices are based on industrial mixing times. In contrast, more realistic transition patterns and dwelling times were extracted from the performed *lifelines* analysis. Consequently, a complex and a simplified design were proposed. Furthermore, the statistical analysis revealed mostly less than  $15 \%$  deviation in dwelling time distributions for the coarse grid size of  $1.12 \cdot 10^5 \text{ \#}/\text{m}^3$  compared to ten times finer meshes, thereby significantly decreasing the computational cost. In a case study, the multiphase approach was applied to a large scale setup showing fair agreement of overall simulated process parameters like  $k_L a$  and  $\varepsilon_G$  compared to predicted values by fitted correlations. As regime assignments were identical to the examined pilot scale, the transferability of the approach on larger scales was shown.

In a second case study with *P. putida* in a  $54 \text{ m}^3$  bioreactor, further information on the formation of large scale heterogeneities were retrieved. A single phase CFD simulation was coupled via *lifelines* analysis to a cell cycle model for *P. putida*, describing replication phase ( $C_c$ ) adjustments dependent on substrate availability. Short and long term responses were formulated, as well as subpopulations of different  $C_c$ -periods identified. Additionally, the cell cycle model was adapted for the use with *C. glutamicum* and fitted to display replication phase duration dependent on carbon dioxide stress and substrate availability. Hereby, the investigation of  $\text{CO}_2$  stress on *C. glutamicum* in large scale fermentations is enabled.

In conclusion, following the proposed framework, the proper prediction of physical and biological readouts in multiphase systems is possible. Proposed scale down devices and biological response models offer the potential for both wet-lab and *in silico* analysis to predict realistic industrial case scenarios. Accordingly, this work contributes to the *a priori* risk minimisation of suboptimal large scale performance while computational cost is reduced.

## Zusammenfassung

In den letzten Jahrzehnten hat sowohl der Umsatz als auch die Bandbreite an biotechnologischen Produkten stark zugenommen. Als Grundbausteine bio-basierter Chemikalien tragen hochwertige Rohstoffe wie Aminosäuren und organische Säuren entscheidend zum Wachstum des Biotech-Marktes bei. Typische mikrobielle Produzenten wie *C. glutamicum* oder *P. putida* zeigen dabei während der Prozessentwicklung im Labormaßstab ein stabiles Produktionsverhalten. Allerdings entstehen im Laufe des Prozesstransfers in den industriellen Maßstab aufgrund von längeren Mischzeiten und erschwertem Massentransfer häufig Inhomogenitäten, welche die Mikroorganismen in ihrem Metabolismus beeinflussen und letztendlich zur verschlechterten Prozessperformance führen können. Die experimentelle Untersuchung solcher Inhomogenitäten ist oftmals nur schwer umzusetzen. Zum Einen, da Produktionsanlagen in der Regel nicht für Optimierungsstudien zur Verfügung stehen, zum Anderen können analytischen Instrumente nicht in der erforderlichen Auflösung installiert werden. Ein vielversprechendes Tool, um Gradienten in industriellen Anlagen zu präzisieren bietet daher die numerische Strömungssimulation (CFD). Anhand der ermittelten Strömungsfelder können Bakterien auf ihrem Weg durch den Bioreaktor verfolgt werden und so die Auswirkungen der Konzentrationsänderungen statistisch ausgewertet werden. Obwohl derartige Studien bereits existieren, wurde der Einfluss mehrerer Gradienten bisher vernachlässigt und der Fokus unmittelbar auf ein Hauptsubstrat -meist Glukose- gesetzt. Aufgrund der Komplexität von Zweiphasenströmungen wurde Sauerstoff als wachstumslimitierendes Substrat für solche Studien bisher vernachlässigt. Hinzu kommt, dass Validierungsexperimente für Multiphasensimulationen nur sehr selten durchgeführt wurden.

Diese Arbeit stellt Werkzeuge vor, welche die Charakterisierung von großskaligen Ein- und Multiphasensystemen vereinfachen, um letztendlich das Risiko von suboptimalem Scale-up zu verringern. Notwendige Schritte zur Untersuchung industrieller Bioreaktoren mithilfe von CFD werden beschrieben, wie die Charakterisierung des verwendeten biologischen Systems und des Reaktorsetups, die Simulation von Multiphasensystemen und Gradienten sowie die folgende Analyse von großskaligen Heterogenitäten. Ausgangspunkt war die Bestimmung von zellspezifischer Raten und Ausbeuten mittels Batch Kultivierungen von *C. glutamicum*. Zusätzlich wurden physikalische Eigenschaften der Fermentationsbrühe wie Viskosität, Dichte und Oberflächenspannung gemessen, welche ähnlich zu Wasser gleicher Temperatur waren. Demnach war die Berücksichtigung der Medieneigenschaften für die experimentelle Charakterisierung des Pilotmaßstabsbioreaktor nicht notwendig. Durch Variation der Rührerdrehzahl und Begasungsraten konnte eine Bandbreite volumenspezifischer Leistungseinträge, Mischzeiten, volumenspezifischer Massentransferkoeffizienten ( $k_L a$ ) sowie Gas hold-up ( $\varepsilon_G$ ) erhalten werden, welche der Validierung anschließender Multiphasensimulationen dienten. Als Ergebnis wurde ein Betriebspunkt bei 300 rpm und

0.25 vvm gewählt, da diese Einstellungen mit einem spezifischen Leistungseintrag von  $2.2 \text{ kW m}^{-3}$  und einem  $k_{La}$  Wert von  $125 \text{ h}^{-1}$  ein realistisches Szenario eines späten Fed-Batch Prozesses repräsentieren, in dem kein Fluten des Rührers auftritt und genügend Sauerstoff zur Versorgung der Mikroorganismen zur Verfügung steht.

Im Anschluss wurde ein geeignetes Simulationssetup implementiert, um die Multiphasenströmung im Pilotmaßstab zu dem gewählten Betriebspunkt numerisch abzubilden. Durch die Einführung eines Skalierungsfaktors für die turbulente Dissipationsrate konnte der Rechenaufwand erheblich gesenkt werden, da gröbere Rechenetze verwendet werden konnten ( $1.12 \cdot 10^5 \text{ \#/m}^3$ ). Letztendlich betrug die Abweichung zwischen simulierten und experimentellen Werten weniger als 12 %.

Darüber hinaus konnte durch die Kombination dieses Setups mit einem Euler-Lagrange Ansatz die Momentaufnahme eines späten Fed-Batch Prozesses bestehend aus Glukose- und Sauerstoffprofilen dargestellt werden. Der kinetischen Ansatz von Roels diente dabei zur Beschreibung der Multisubstrataufnahme, welche über die extrazellulären Konzentrationen kontrolliert wurde und somit an die Euler-Phase geknüpft wurde. Die Bakterien wurden als masselose Partikel mittels der Lagrange'schen Beschreibungsweise simuliert. Die resultierenden Konzentrationsprofile wurden überlagert und in folgende Regime eingeteilt: geringe Glukosekonzentrationen ( $L_S$ ), transient (T) und ein geringe Sauerstoffkonzentrationen ( $L_{O_2}$ ). Die von den Bakterien wahrgenommenen Umgebungsbedingungen wurden aufgezeichnet und statistisch ausgewertet. Diese sogenannten *lifelines* liefern wertvolle Informationen über die Häufigkeit der Wechsel in bestimmte Regime, sowie die Aufenthaltszeiten der Bakterien innerhalb dieser Regime. Da Regime T nur 5 % des gesamten Volumens betrug und die Verweilzeiten in diesem Regime im Allgemeinen sehr kurz waren ( $< 1 \text{ s}$ ), kann T für das Design von Scale-Down (SD) Apparaten vernachlässigt werden. Üblicherweise richteten sich solche SD Anlagen aufgrund fehlender Detailinformationen über die Umgebungsbedingungen nach industriellen Mischzeiten. Über die Analyse der bakteriellen *lifelines* ist es jedoch möglich realistische Verteilungen der Regimewechsel sowie Aufenthaltszeiten innerhalb der Regime zu erhalten und so genauere Einstellungen für die SD Experimente zu verwirklichen. Infolgedessen wurden zwei Designs für SD Anlagen vorgeschlagen. Anhand der statistischen Auswertung für das größte Netz von  $1.12 \cdot 10^5 \text{ \#/m}^3$  wurden nur geringe Abweichungen in den Verweilzeiten von mehrheitlich unter 15 % im Vergleich zu zehnfach feineren Netzen bestimmt, was zu einer deutlichen Verringerung des nötigen Rechenaufwands führt. Der Multiphasenansatz wurde weiterhin in einer Fallstudie zur Simulation eines großskaligen Reaktors genutzt. Dabei konnten gute Übereinstimmungen der simulierten Prozessparameter wie  $k_{La}$  und  $\varepsilon_G$  mit den durch Korrelationen vorhergesagten Werten erzielt werden. Die Übertragbarkeit des vorhandenen Ansatzes von Pilot- auf Industriemaßstab wurde zudem über die identische Regimeverteilung des resultierenden Gradienten bestätigt.

In einer zweiten Fallstudie mit *P. putida* in einem  $54 \text{ m}^3$  Bioreaktor wurden weitere Informationen über die Entstehung von Heterogenitäten ermittelt. Eine einphasige CFD Studie wurde per *lifeline* analyse an ein Zellzyklusmodell von *P. putida* gekoppelt, welches Anpassungen der Replikation-

sphase ( $C_c$ ) abhängig von der Substratverfügbarkeit beschreibt. Kurz- und langfristige biologische Antworten wurden formuliert, sowie Subpopulationen unterschiedlicher  $C_c$ -Phasenlänge identifiziert. Zusätzlich wurde das Zellzyklusmodell zur Darstellung des Einflusses von  $\text{CO}_2$ -Stress und Substratverfügbarkeit auf die Dauer der Replikationsphase für *C. glutamicum* adaptiert. Dadurch kann zukünftig auch der Einfluss von  $\text{CO}_2$ -Stress auf *C. glutamicum* in großskaligen Fermentationen untersucht werden.

Zusammengefasst wird durch das Befolgen der in dieser Arbeit genannten Schritte die korrekte Vorhersage relevanter physikalischer und biologischer Parameter in Multiphasensystemen ermöglicht. Die empfohlenen Scale-Down Anlagen und biologischen Modelle haben das Potential über experimentelle und *in silico* Analysen realistische industrielle Fermentationsszenarien darzustellen. Demnach trägt diese Arbeit dazu bei *a priori* das Risiko suboptimaler Leistung in großskaligen Fermenter zu minimieren und gleichzeitig den Rechenaufwand zu reduzieren.



---

# 1 Introduction

## 1.1 The biotechnological market and challenges of production

Growth of global population, climate change, protection of environment or conquering diseases - the society of the 21<sup>st</sup> century has to face important challenges. Traditional sectors based on fossil fuels can no longer fulfill the needs of this growing population. Biotechnology offers a sustainable solution by increasing the productivity of both low-cost and high-value products lowering by-product and waste accumulation. The biotechnological market is constantly on the rise with the pharmaceutical market traditionally holding the major share. Worldwide sales in the biotechnological drug production increased up to 113 \$bn in 2017 for the top 20 biopharmaceuticals (Walsh, 2018). Also, the white biotech sector, driven by the production of biofuels, biomaterials, biochemicals, industrial enzymes or feed additives was expected to increase drastically by the end of 2020 with feed additives as key market (Festel, 2018). L-Lysine, a popular feed additive is globally produced by *Corynebacterium glutamicum* with 2.2 million tons per year and a registered growth rate of 10 % per year (Yokota & Ikeda, 2017). Manufacturing processes of such products generally involve large scale stirred tanks up to 500 m<sup>3</sup>. The development, however, is conducted in shake flasks or laboratory scale bioreactors, typically at a liquid volume < 10 L. Within this scale, optimal operating conditions are searched for to ensure the efficiency and productivity of the fermentation process. These optima are usually very specific concerning pH, temperature, dissolved oxygen, carbon or nitrogen source and feed strategy. Challenges arise when transferring these processes from laboratory to pilot scale and finally into a production facility. With the volume increase at each scale, operational conditions have to adapt to ensure optimal process performance. However, due to limited mixing and mass transfer within larger scales, this might not be possible. Concentration fluctuations of glucose, pH, oxygen or elevated carbon dioxide levels may arise and influence the organisms metabolism, which could result in deteriorated yields.

## 1.2 Motivation of this thesis

In order to predict the behaviour of a system or even improve it, the proper description and understanding of processes related to that system is crucial. Although large scale biotechnological

manufacturing processes exist for numerous products, the environment inside a bioreactor and potential consequences on microbial behaviour remain unclear. On one hand, little information on large scale production processes are available, since the facilities are owned by companies and therefore information are confidential. On the other hand, it is extremely difficult to gather detailed information inside a large scale reactor system due to high risk of contamination and unsuitable measurement techniques. In the recent years, computer aided techniques to study the bacterial environment gained momentum, as local conditions can be captured by the application of Computational Fluid Dynamics (CFD) (Werner et al., 2014). Thereby, the turbulent flow field of a stirred tank reactor is simulated enabling the prediction of various flow variables as well as reactor specific characteristics like power consumption or mixing times (Montante et al., 2005; Coroneo et al., 2011). Several possibilities to include the bacterial reaction towards fluctuating concentrations within a large scale bioreactor exist (Morchain et al., 2014; Pigou & Morchain, 2015). Latest research focuses on an Euler-Lagrange approach, which treats the liquid-phase motion in an Eulerian representation, but computes single massless particles to display the bacterial phase in a Lagrangian way (Lapin et al., 2004; Haringa et al., 2016; Kuschel et al., 2017). This method is a powerful tool to review the conditions to which the bacteria are exposed to. By tracking their path, the complete environmental (cell) history is recorded. Results of statistical evaluation can be coupled to biological models to display the formation of population heterogeneity or help to design scale down (SD) devices (Haringa et al., 2017a). These SD devices are laboratory scale bioreactors, which enable the installation of large scale conditions, allowing to measure microbial responses simultaneously. In contrast to traditional approaches relying on industrial mixing times for SD design (Neubauer & Junne, 2010; Käß et al., 2014; Heins et al., 2015), the Euler-Lagrange approach reflects the actual conditions encountered by the microorganisms.

Until now, these simulation of bacterial trajectories, so called *lifeline* analysis has been performed in single phase or with a carbon source as sole substrate neglecting the influence of oxygen. However, as most biotechnological processes are aerated it is necessary to include an oxygen balance in the simulation. In general, the conduction of multiphase simulations is rather complex and several aspects need to be considered like the modelling of the bubble size distribution, bubble breakage, bubble coalescence, interphase momentum exchange and grid size of the numerical mesh to keep a balance between simulation cost and accuracy of the obtained results.

To address these issues, in the presented thesis *Resolving heterogeneities in single and multiphase bioreactor systems - Predictive modelling tools towards successful scale-up* an experimentally validated multiphase pilot scale bioreactor system was investigated and heterogeneities occurring within a fed-batch fermentation process of *C. glutamicum* are displayed from the bacterial point of view. Furthermore, it suggest biological models as bacterial response towards fluctuating concentrations. A detailed overview of each chapter is given in the next section.

### 1.3 Objectives, strategies and thesis outline

The core aspects covered in this thesis are depicted for each chapter supported by several research questions (**RQn**), which will be answered in the respective chapter. **Chapter 2 - Theory** gives an overview of relevant background considering fundamental characteristics of numerical flow simulation, modelling of turbulence, agitation and mixing in stirred tanks as well as general problems which need to be solved to depict the complex flow of a multiphase system. Furthermore several models to include population heterogeneity are presented. **Chapter 3 - Characterisation of bioprocesses with *C. glutamicum* as model organism** describes the conduction of batch experiments with *C. glutamicum* in a laboratory scale stirred tank to determine organism specific consumption and production rates. The growth parameters serve to parameterise later numerical simulations. Additionally, media properties were examined and the following question arose:

**RQn3.1** How do viscosity, density and surface tension of the broth change compared to pure water? How will these properties affect the numerical simulation?

The following chapter, **Chapter 4 - Characterisation of a pilot scale bioreactor**, deals with the generation of experimental data to validate numerical simulations. Hereby, reactor and setup specific quantities like power consumption, mixing time, gas hold up and volumetric mass transfer coefficients are gathered which lead to the question:

**RQn4.1** What is a suitable operating point for the bioreactor?

Furthermore, the chapter addresses the complex issue of multiphase simulations and the questions were raised:

**RQn4.2** Which models are suitable to display the multiphase stirred tank pilot scale system? How well does the simulation reflect the experimental data?

**RQn4.3** Is it possible to reduce computational costs by reducing the grid density without loosing accuracy of the physical read outs?

Relating to chapter 4, **Chapter 5 - Simulated oxygen and glucose gradient** concentrates on the inclusion of glucose feed as well as glucose and oxygen consumption to the numerical simulation of the pilot scale reactor. Organism specific rates of chapter 3 were used to simulate a glucose and oxygen gradient. Moreover, bacterial trajectories or *lifelines* were simulated to display the environmental changes inside the fermenter from the bacterial point of view. The following research questions were targeted:

**RQn5.1** How does a multi substrate gradient consisting of glucose and oxygen concentration profiles for *C. glutamicum* look like and which different zones may be derived?

**RQn5.2** Which information are gained by statistically evaluating bacterial readouts from the simulation of *lifelines* in a multi substrate gradient? How can the results be used for process optimisation?

**RQn5.3** Are the concentration profiles influenced by the simplifications made in chapter 4 to reduce the mesh density? How big are the deviations in the final *lifeline* analysis?

The chapter couples numerical flow simulations to simple biological models to describe substrate consumption. Hereby, based on the work of Lapin et al. (2004) and Haringa et al. (2016) bacteria are treated as massless lagrangian particles and statistically evaluated to depict heterogeneity of a two phase flow system. A possible model to describe the bacterial response towards these concentration fluctuations is presented in **Chapter 6 - Cell cycle model**. The analyses of data obtained by single cell flow cytometry experiments of samples derived by continuous cultivations of *C. glutamicum* lead to the question:

**RQn6.1** How does the replication phase duration of *C. glutamicum* change for different substrate availability and carbon dioxide stress in a multiphase system?

As a preliminary study this was also examined in a single phase system dependent on substrate availability for *Pseudomonas putida*.

Heterogeneity of two large scale reactor systems is examined in **Chapter 7 - Heterogeneity analysis in large scale** exemplarily. In this chapter the findings of the biological response model from chapter 6 obtained for *P. putida* are connected to the single phase numerical simulations of a 54 m<sup>3</sup> stirred tank. Furthermore, the multiphase reactor setup of previous chapters is scaled up by a factor of 100 to display gradient formation in large scale as well as to include a basis for carbon dioxide mass transfer. Aspects examined in this chapter were:

**RQn7.1** How could the response of a *P. putida* culture towards substrate gradients within a large scale bioreactor look like and how does this influence the homogeneity of the population?

**RQn7.2** How does the obtained multiphase setup for *C. glutamicum* perform in large scale?

The final chapter, **Chapter 8 - Conclusion and outlook** discusses major findings and summarises the answers of the research questions. Suggestions for future work are also provided.

---

## 2 Theory

### 2.1 *Corynebacterium glutamicum*

*Corynebacterium glutamicum* was isolated in the 1950s in Japan, while searching for a glutamate producer to enhance flavours. It is a rod-shaped Gram-positive microorganism, which belongs to the phylum Actinobacteria. The cell length varies between 1.6 - 2.5  $\mu\text{m}$  (Neumeyer et al., 2012). It often grows in V-shaped pairs, as result of the snapping division (Letek et al., 2008). Because *C. glutamicum* is not only non-sporulating, non-endotoxic and generally regarded as safe (GRAS), but also grows fast and is easily cultivated, it is one of the most important platform for biotechnological applications (Leuchtenberger et al., 2005; Takors et al., 2007; Becker & Wittmann, 2012). Therefore, its metabolism has been extensively described in literature (Eggeling & Bott, 2005; Liebl, 2006; Yukawa & Inui, 2013; Becker & Wittmann, 2017) being able to produce carboxylic acids like L-lactate, succinate and acetate, while growing on carbon sources like glucose, fructose, sucrose or ribose under aerobic conditions. Marginal growth was also reported under anaerobic conditions but only in presence of nitrate (Takeno et al., 2007). As an industrial workhorse it is usually used for the production of organic acids, biofuels and polyamines, but most importantly for the production of amino acids like L-lysine or L-glutamate. The yearly production of lysine, which is used as feed additive for animals, is currently estimated to be 2.2 million tons (Yokota & Ikeda, 2017). Also, the annually L-glutamate production exceeds 3 million tons with product titers of  $100\text{ g L}^{-1}$  (Wendisch et al., 1997). The cultivation of *C. glutamicum* is generally conducted as aerated stirred fed-batch process in reactor volumes of up to  $500\text{ m}^3$  (Eggeling & Bott, 2015). The production in such huge fermenters, however, often suffer from deteriorated yields as described in the next section.

### 2.2 Scale up of fermentation processes

Manufacturing processes of low-cost and high quality products are usually performed in large-scale fermenters to decrease the economic burden. Being developed in laboratory scale tanks of 1 to 50 L, the challenge lies in the accurate transfer of these processes to a full scale production facility. An industrial production plant normally operates at a working volume  $>10\,000\text{ L}$  especially

for microbial processes. Most commonly, the geometric similarity is kept constant resulting in a constant tank height to tank diameter and tank diameter to impeller diameter ratio. While this is simple to realise, maintaining all other physical, chemical or biological factors is rather complicated. In fact a “1:1 approach” is simply impossible. For a single impeller systems, mixing time might be correlated very well to the agitation rate (Villadsen et al., 2011), however keeping the impeller speed constant leads to unreasonable high power consumption in large scale (Oldshue, 1966). On the contrary, if the volumetric power consumption ( $P/V$ ) is kept constant, high mixing times might lead to the formation of gradients. Gradient formation is mainly dependent on the growth characteristics of the organism. As different strains vary significantly in their growth kinetics, the substrate consumption rate is an additional factor which needs to be considered for process development and scale up. In essence, the time of carbon source consumption at carbon source concentrations equal to the half saturation concentration ( $c_S = K_S$ ) differs dramatically by orders of magnitude (25 to  $> 1000$  s) between various organisms, preventing the creation of a general scale up guideline (Bach, 2018).

Cultured in these fluctuating conditions heterogeneities may arise, due to cells differing in their metabolism, yields or quality of the product (Lara et al., 2006). Additionally, in case of an aerobic process, agitation and gassing rate need to be sufficient to maintain a specific volumetric oxygen mass transfer coefficient  $k_L a$  or dissolved oxygen level, to provide enough oxygen to the culture. Nevertheless, this might result in foaming issues, impeller flooding or increased shear stress. A proper scale up becomes even more complicated for multi-impeller systems. Therefore, scaling up of a fermentation process always remains a compromise between the individual scale up factors and needs to be adjusted dependent on the most relevant criteria for each special case.

The mixing time in a 30 m<sup>3</sup> stirred tank, agitated by four Rushton turbines was reported to be 125 s for a specific power input of 2 kW m<sup>-3</sup> (Vrábel et al., 2000), which is fourteen times higher than in pilot scale (Bach et al., 2017). For the same reactor, Larsson et al. (1996) described the occurrence of glucose gradients for a fermentation process of *Saccharomyces cerevisiae*. He tested the influence of different feeding positions or feeding at multiple positions. However, such changes evoke new challenges which need to be tackled like mechanical instability, inexact feeding and higher risk of contamination. Dissolved oxygen gradients were described by Steel & Maxon (1966) and Oosterhuis & Kossen (1984). These gradients might lower cell growth, product yield and increase by-product formation (Bylund et al., 1998). Furthermore, as a consequence of high pressures and poor mixing in large scale, partial pressures of carbon dioxide ( $p_{CO_2}$ ) might reach critical levels.

To investigate the cellular response to such fluctuating conditions, scale-down (SD) experiments are performed. Information gained by these experiments can elucidate intrinsic regulatory mechanisms and provide guidelines for strain and process engineering to minimise unwanted large scale impacts. Schilling et al. (1999) observed a reduced biomass and L-lysine production for the L-

lysine producing strain *C. glutamicum* DSM 5715 when cultivated under prolonged mixing times (10-130 s) in a 42 L bioreactor as a scale-down study. For the wild-type strain *C. glutamicum* ATCC13032, no significant growth reduction or by-product formation was measured, when cultivated in a scale-down experiment consisting of an aerated stirred tank reactor (STR) and a non-aerated plug flow reactor (PFR) module with a residence time in the PFR of 45-87 s. However, L-lactate and succinate were accumulated in the PFR, but subsequently re-assimilated in the STR (Käb et al., 2014). For the same strain oscillating  $\text{CO}_2/\text{HCO}_3^-$  level in a three compartment cascade bioreactor system resulting from installed  $p_{\text{CO}_2}$  gradients of 73-315 mbar led to the up-regulation of 66 genes (Buchholz et al., 2014b). Lemoine et al. (2016) observed a drastic growth and product reduction of a cadavarine producing strain, when cultivated in a three compartment scale-down (SD) device on complex media, mimicking a bottom-fed late fed-batch scenario.

However, these scale-down experiments usually rely on large scale mixing or circulation times. In order to obtain more advanced set-ups, residence times of bacterial cells in specific critical regimes might be used to design SD devices, which can be derived by computational fluid dynamics (CFD). This will be shown in the course of this thesis.

## 2.3 Dimensionless numbers

Due to their physical relevance several dimensionless numbers serve to characterise a system and may be calculated prior to CFD simulations. Additionally, these numbers enable the comparison of the results to other studies. The power number  $N_P$  is calculated from the power consumption  $P$ , the density  $\rho$ , agitation rate  $N$  and impeller diameter  $D_I$ :

$$N_P = \frac{P}{\rho N^3 D_I^5} \quad (2.1)$$

For many stirrer types the power number has already been calculated as a function of the Reynolds number  $Re$ , making it possible to estimate the power consumed by the agitation system. The  $Re$  represents the ratio of inertial to viscous forces and is expressed as:

$$Re = \frac{\rho N D_I^2}{\eta} \quad (2.2)$$

with  $\eta$  as dynamic viscosity of the liquid phase. Additionally the Froude number  $Fr$ , which describes the ratio of inertial to gravitational forces is often used to describe a system:

$$Fr = \frac{N^2 D_I}{g} \quad (2.3)$$

with  $g$  as gravitational acceleration. In a non aerated baffled tank operating in the turbulent regime ( $Re > 10^{-4}$ ), the power number becomes constant. At such conditions the inertial forces dominate and the effect of  $Re$  or  $Fr$  becomes negligible.

Aerated processes are usually characterised by the dimensionless flow number  $Fl$ :

$$Fl = \frac{Q_g}{N D_I^3} \quad (2.4)$$

with  $Q_g$  as gassing rate. The flow number is an indicator of loading or flooding regime (Nienow, 1998; Warmoeskerken & Smith, 1985) and critical flow numbers can be obtained from several correlations (Gezork et al., 2000; Rosseburg et al., 2018; Wiedmann, 1983). In the loading regime, the flow field is dominated by the momentum induced by the impeller, whereas in a flooding regime the momentum is induced by buoyancy driven flow.

The Eötvös number  $EO$  characterises the shapes of bubbles or drops moving in a surrounding fluid.  $EO$  is defined by the ratio gravitational forces to surface tension forces with  $d$  as bubble diameter and  $\sigma$  as surface tension:

$$EO = \frac{g (\rho_L - \rho_G) d^2}{\sigma} \quad (2.5)$$

The Schmidt number  $Sc$  describes the ratio between internal friction and diffusion rate.

$$Sc = \frac{\nu}{D} \quad (2.6)$$

with  $\nu$  as kinematic viscosity and  $D$  as diffusion coefficient.

## 2.4 Computational fluid dynamics for biotechnology

Computational fluid dynamics gain momentum in several fields amongst them the sector of biotechnology. To better understand how the complex flow within a bioreactor can be described, basics of numerical flow simulation and necessary simplifications are presented in the following sections.

### 2.4.1 Fundamentals of flow simulation

In principle, all kinds of flows can be described based on the fundamental equation of gas kinetics, the Boltzmann equation. However, in technical flows the inclusion of all physical effects is usually not necessary and several simplifications are helpful to reduce computational costs. Figure 2.1 gives a schematic overview of the hierarchy of basic flow equations. As the Knudsen number  $Kn$ , defining the ratio of the molecular mean free path length  $\lambda_m$  to a representative physical length

scale  $L$ , decreases to a value below  $10^{-2}$  ( $Kn < 10^{-2}$ ) the flow can be described macroscopically by the continuum mechanics. In the 19<sup>th</sup> century Claude-Louis Navier and George Gabriel Stokes formulated the Navier-Stokes Equations (NSE) for such flows. The mathematical model completes the Euler equations by the inclusion of viscosity and is only valid for Newtonian fluids of compressible or incompressible flows. In case of high Reynolds numbers ( $Re \gg 1$ ), friction is negligible and the general NSE simplify to the Euler equations. Furthermore, if the Mach number  $Ma$ , defining the ratio of fluid velocity to speed of sound, is small ( $Ma < 0.3$ ) the incompressible flow can be described semi-analytically as potential flow. Based on the general NSE in case of  $Ma < 0.3$ , the NSE for incompressible flows can be used. Additionally, if friction and heat transfer are negligible the flow can be described by potential equations, too. If friction and heat transfer can not be neglected but  $Re$  is very small ( $Re \ll 1$ ) the Stokes equations can be used.

Biotechnological applications are often conducted in the turbulent flow of stirred tanks ( $Re \gg 1$ ) under moderate temperatures (30 - 37 °C) and pressures (1 - 1.5 bar). Main components of the media, which is used to cultivate the bacteria are water and salts. Hence, the incompressible Navier-Stokes equations are generally used as model approach. Hereby, the volume occupied by the fluid in the vessel is described by a three-dimensional computational grid and the flow is characterised macroscopically by state variables. Physical relevant effects are described by the conservation laws for mass (eq. 2.7a), the three momentum equations (2.7b, 2.7c, 2.7d) and the energy conservation equation (2.7e) within an infinitesimally small volume element, resulting in a system of partial differential equations:

$$\frac{\partial u}{\partial x} + \frac{\partial v}{\partial y} + \frac{\partial w}{\partial z} = 0 \quad (2.7a)$$

$$\rho \left( \frac{\partial u}{\partial t} + u \frac{\partial u}{\partial x} + v \frac{\partial u}{\partial y} + w \frac{\partial u}{\partial z} \right) = -\frac{\partial p}{\partial x} + \eta \left( \frac{\partial^2 u}{\partial x^2} + \frac{\partial^2 u}{\partial y^2} + \frac{\partial^2 u}{\partial z^2} \right) \quad (2.7b)$$

$$\rho \left( \frac{\partial v}{\partial t} + u \frac{\partial v}{\partial x} + v \frac{\partial v}{\partial y} + w \frac{\partial v}{\partial z} \right) = -\frac{\partial p}{\partial y} + \eta \left( \frac{\partial^2 v}{\partial x^2} + \frac{\partial^2 v}{\partial y^2} + \frac{\partial^2 v}{\partial z^2} \right) \quad (2.7c)$$

$$\rho \left( \frac{\partial w}{\partial t} + u \frac{\partial w}{\partial x} + v \frac{\partial w}{\partial y} + w \frac{\partial w}{\partial z} \right) = -\frac{\partial p}{\partial z} + \eta \left( \frac{\partial^2 w}{\partial x^2} + \frac{\partial^2 w}{\partial y^2} + \frac{\partial^2 w}{\partial z^2} \right) \quad (2.7d)$$

$$\rho c_p \left( \frac{\partial T}{\partial t} + u \frac{\partial T}{\partial x} + v \frac{\partial T}{\partial y} + w \frac{\partial T}{\partial z} \right) = \lambda \left( \frac{\partial^2 T}{\partial x^2} + \frac{\partial^2 T}{\partial y^2} + \frac{\partial^2 T}{\partial z^2} \right) \quad (2.7e)$$

with  $u$ ,  $v$  and  $w$  as velocity components ( $u, v, w$ ) of a fluid particle in  $x, y$  or  $z$  direction ( $x, y, z$ ),  $p$  as pressure within the fluid and  $\eta$  as dynamic viscosity. As incompressible fluid, the density is assumed to be constant ( $\rho = const.$ ). The energy equation contains the temperature  $T$ , the thermal capacity  $c_p$  and the thermal conductivity  $\lambda$ . For biotechnological applications the temperature is controlled. Temperature gradients are neglected in this study and the process is assumed to be isotherm. So the NSE can be reduced to mass and momentum equations. Considering gravitation,

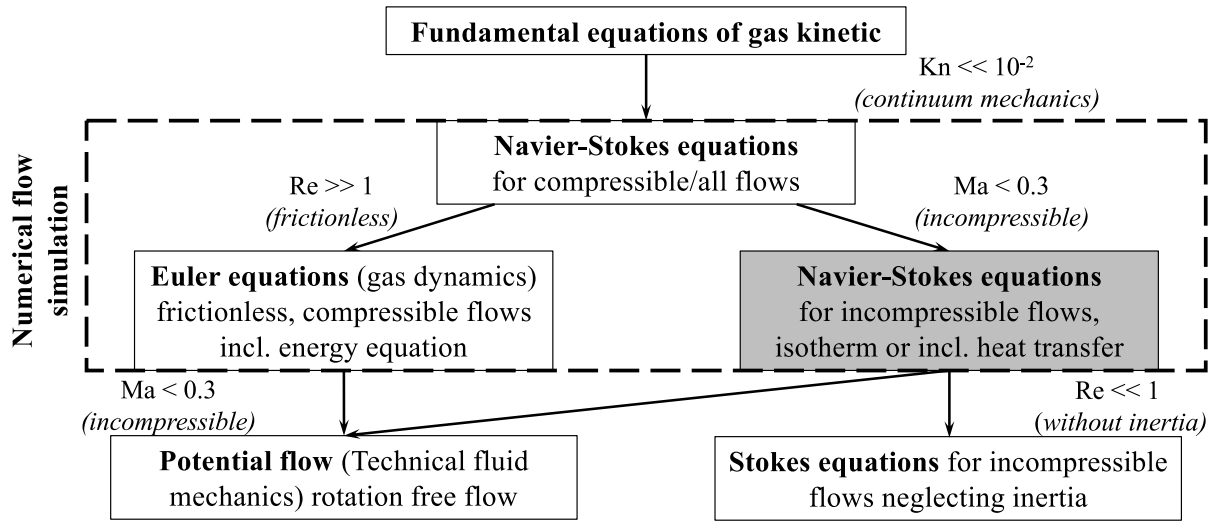


**Figure 2.1: Fundamental flow equations.** Schematic overview of flow equations. Modified to Laurien & Oertel jr. (2018). The relevant mathematical model for biotechnological applications is marked in grey.

the tensor notation with  $i, j = 1, 2, 3$  referring to the three velocities  $u, v, w$  and the coordinates  $x, y, z$ , respectively, can be written as:

$$\frac{\partial u_i}{\partial x_i} = 0 \quad (2.8a)$$

$$\rho \frac{\partial u_i}{\partial t} + \rho \frac{\partial (u_i u_j)}{\partial x_j} = - \frac{\partial p}{\partial x_i} + \eta \frac{\partial}{\partial x_j} \frac{\partial u_i}{\partial x_j} - \rho g_i \quad (2.8b)$$

(I)          (II)          (III)          (IV)          (V)

The left side of equation 2.8b describes the local (I) and convective (II) acceleration. Term (III) describes compressive forces, term (IV) frictional forces and term (V) gravitational forces with  $g_i$  as gravitational acceleration ( $g_1 = g_2 = 0; g_3 = 9.81 \text{ m s}^{-2}$ ).

## 2.4.2 Modelling of turbulence in stirred tanks

Although the NSE are generally valid for all kinds of flows, the practical applicability for technical systems is usually reduced to laminar flows. To capture all properties of a turbulent system a very high grid resolution is necessary to simulate the flow, which leads to immense computational costs. Alternatively, the turbulence is modelled to diminish the computational effort. Figure 2.2 (A) shows the hierarchy of turbulence models in terms of grid size and computational effort and figure 2.2 (B) displays the energy spectrum which is still captured by the respective model. The computationally cheapest approach are the Reynolds Average Navier-Stokes (RANS) models. Hereby, turbulence is already modelled at the integral (energy containing) scale  $L$ , which contains the largest eddy scales and concentrations of turbulent kinetic energy. The length scale  $L$  is con-

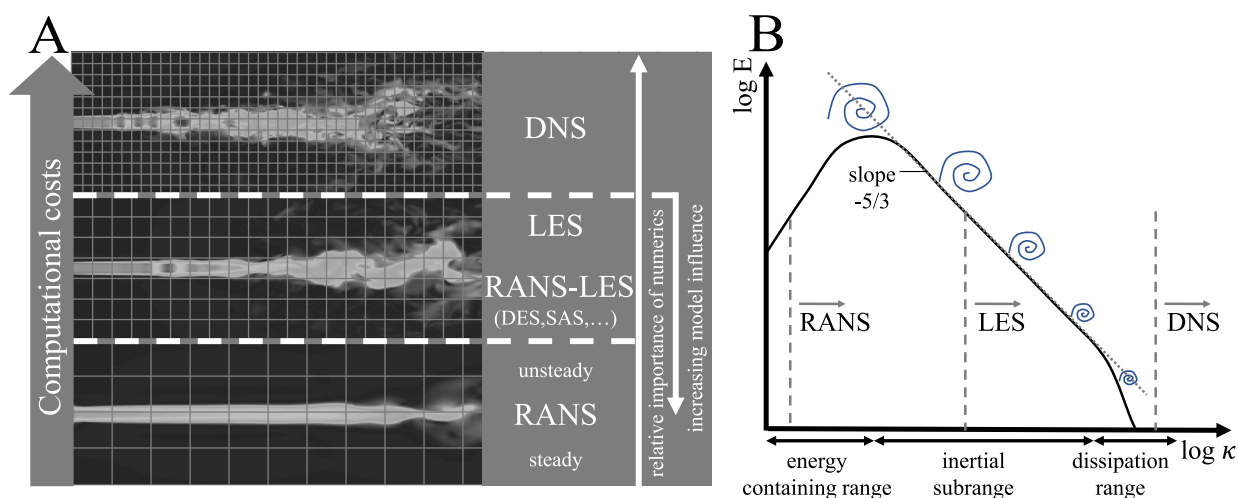


**Figure 2.2: Hierarchy of turbulence models and turbulent kinetic energy spectrum.** (A) Velocity distribution of a turbulent jet using RANS, LES and DNS. Modified to Rodriguez (2019). (B) Turbulent kinetic energy of isotropic turbulence with respect to the wavenumber  $\kappa$ . The level of computed and modelled scales in RANS, DNS and LES is shown. Adapted from Sagaut et al. (2006).

sidered as the size of the eddies containing most of the turbulent kinetic energy. These vortices decay to smaller ones in the inertial range, which is based on the Kolmogorov hypotheses (Kolmogorov, 1941) that correlate the inertial subrange energy spectrum  $E(\kappa)$  with the wavenumber  $\kappa$ , the turbulent dissipation rate  $\varepsilon$  and a constant  $C_\kappa$ :

$$E(\kappa) \sim C_\kappa \kappa^{-\frac{5}{3}} \varepsilon^{\frac{2}{3}} \quad (2.9)$$

with the mean value of turbulent kinetic energy obtained by:

$$\langle k \rangle = \int_0^\infty E(\kappa) d\kappa \quad (2.10)$$

The smaller eddies decay further and the turbulent kinetic energy is transferred to the mean flow by viscous effects until dissipation takes place at microscale  $\eta_\kappa$ , the Kolmogorov length scale:

$$\eta_\kappa = \left( \frac{\nu^3}{\varepsilon} \right)^{0.25} \quad (2.11)$$

with  $\nu$  as kinematic viscosity. This range is denoted as dissipation range in figure 2.2 (B). RANS models assume isotropy for the turbulence, whereas the flow in a stirred tank is anisotropic. It was shown, that the mean flow was predicted satisfactory by RANS models in two directions but over or underpredicted in the third direction (Coroneo et al., 2011; Bakker et al., 1997; Joshi et al., 2011). Furthermore, turbulent kinetic energy profiles were significantly underpredicted by RANS models (Murthy & Joshi, 2008). The unsteady RANS (URANS) approach bears the same

drawbacks, but is capable of resolving periodic flow features or moving parts of the flow. Much finer mesh resolution is necessary to perform a Large Eddy Simulation (LES), as large temporal and spatial scales are simulated, but small scales are modelled by a subgrid-scale. Resolving all but the smallest scale was shown to predict turbulent flow structures more accurately, especially the dissipative characteristics of a stirred tank, because smallest scales tend to be more isotropic than larger scales (Bakker & Oshinowo, 2004; Delafosse et al., 2009; Derksen & Van Den Akker, 1999; Hartmann et al., 2004; Jahoda et al., 2007).

However, LES needs very fine mesh resolution near the wall and is therefore very time consuming. Several hybrid models like detached-eddy simulation (DES) exist, which use LES away from the walls and RANS modelling near the wall to overcome limitations by RANS but offering increased insight in the solution of unsteady flows. By Direct Numerical Simulation (DNS) all turbulent structures are simulated and none are modelled. This is the most accurate approach, but requires high spatial and temporal resolution up to the Kolmogorov scale. Typically, DNS is only used in academia to investigate the properties of turbulence by replacing experimental approaches. Furthermore, it serves as basis to compare the quality of obtained results of computationally less demanding approaches like LES or RANS.

From a practical point of view, RANS models are still the most frequent choice to model technical flows because of the reduced computational demand, for stability reasons and easy handling. Especially for stirred multiphase flows, the computational demand increases drastically for other approaches. Therefore, the focus of this thesis is drawn to the description of RANS models.

The Reynolds-Averaged Navier-Stokes models solve ensemble-averaged (or time-averaged) Navier-Stokes equations by introducing averaged and fluctuating components. For instance the velocity  $u$  can be calculated by:

$$u(x, y, z, t) = \bar{u}(x, y, z) + u'(x, y, z, t) \quad (2.12)$$

with  $\bar{u}$  as mean value of the time interval  $\Delta t$  and  $u'$  as positive or negative fluctuation. To include the effect of turbulent fluctuations on the mean flow, equation 2.12 is inserted in the Navier-Stokes equations. After transformation and simplification this results in :

$$\frac{\partial \bar{u}_i}{\partial x_i} = 0 \quad (2.13a)$$

$$\rho \frac{\partial \bar{u}_i}{\partial t} + \rho \frac{\partial (\bar{u}_i \bar{u}_j)}{\partial x_j} = -\frac{\partial \bar{p}}{\partial x_i} + \frac{\partial}{\partial x_j} \left( \eta \frac{\partial \bar{u}_i}{\partial x_j} - \overline{\rho u'_i u'_j} \right) - \rho g_i \quad (2.13b)$$

The double average results in  $\overline{\bar{u}_i} = \bar{u}_i$  or  $\overline{\bar{u}_i \bar{u}_j} = \bar{u}_i \bar{u}_j$ . By definition the mean of the fluctuation is zero  $\overline{u'_i} = \overline{u'_j} = 0$ , resulting also in  $\overline{\overline{u'_i u'_j}} = \overline{u'_i u'_j} = 0$ . The additional six terms  $-\overline{\rho u'_i u'_j}$

( $i, j = 1, 2, 3$ ) were derived from terms (II) in eq. 2.8b, which contain fluctuations as consequence of turbulent mixing and are defined as Reynolds stress terms  $\tau_{ji}^{Re}$ . These fluctuations are unknown and have to be modelled.

Several models to compute the Reynolds stresses exist. The most common models are the  $k - \varepsilon$  models, which solve two additional transport equations and model the Reynolds stresses using the eddy viscosity approach.

In the standard formulation the transport equation for the turbulent kinetic energy  $k$  and the turbulent dissipation rate  $\varepsilon$  are :

$$\rho \frac{\partial k}{\partial t} + \rho \frac{\partial(k\bar{u}_j)}{\partial x_j} = \frac{\partial}{\partial x_j} \left( \left( \eta + \frac{\eta_t}{\sigma_k} \right) \frac{\partial k}{\partial x_j} \right) + G_k - \rho\varepsilon \quad (2.14a)$$

$$\rho \frac{\partial \varepsilon}{\partial t} + \rho \frac{\partial(\varepsilon\bar{u}_j)}{\partial x_j} = \frac{\partial}{\partial x_j} \left( \left( \eta + \frac{\eta_t}{\sigma_\varepsilon} \right) \frac{\partial \varepsilon}{\partial x_j} \right) + C_{1\varepsilon} \frac{\varepsilon}{k} G_k - C_{2\varepsilon} \rho \frac{\varepsilon^2}{k} \quad (2.14b)$$

(I) (II) (III) (IV) (V)

with term (I) describing the rate of change, term (II) transport by convection, term (III) transport by molecular and modelled turbulent diffusion and term (V) the dissipation per volume. The production term (IV) includes the Reynolds stress terms and can be expressed as:

$$G_k = -\overline{\rho u'_i u'_j} \frac{\partial u_i}{\partial x_j} \quad (2.15)$$

Hereby, the Reynolds stress terms are modelled by the turbulent viscosity (Boussinesq-approach) neglecting turbulent pressure:

$$-\overline{\rho u'_i u'_j} = \eta_t \left( \frac{\partial \bar{u}_i}{\partial x_j} + \frac{\partial \bar{u}_j}{\partial x_i} \right) \quad (2.16)$$

With the turbulent viscosity as :

$$\eta_t = \rho C_\eta \frac{k^2}{\varepsilon} \quad (2.17)$$

The constants for the standard  $k - \varepsilon$  (SKE) model are  $C_\eta = 0.09$ ,  $\sigma_k = 1.0$ ,  $\sigma_\varepsilon = 1.3$ ,  $C_{1\varepsilon} = 1.44$  and  $C_{2\varepsilon} = 1.92$ . Generally, the realizable  $k - \varepsilon$  model showed better performance in rotating flows and was therefore used in this study (Gimbun et al., 2009). The difference to the standard  $k - \varepsilon$  model is in the formulations of the turbulent viscosity and the transport equation for  $\varepsilon$ :

$$\rho \frac{\partial \varepsilon}{\partial t} + \rho \frac{\partial(\varepsilon\bar{u}_j)}{\partial x_j} = \frac{\partial}{\partial x_j} \left( \left( \eta + \frac{\eta_t}{\sigma_\varepsilon} \right) \frac{\partial \varepsilon}{\partial x_j} \right) + \rho C_{1\varepsilon} S \varepsilon - \rho C_{2\varepsilon} \varepsilon \frac{\nu \varepsilon^2}{k + \sqrt{\varepsilon}} \quad (2.18)$$

with  $C_1 = \max(0.43, \xi/(\xi + 5))$ ,  $\xi = Sk/\varepsilon$  and  $S = \sqrt{2S_{ij}S_{ij}}$  and the shear strain tensor:

$$S_{ij} = 0.5 \left( \frac{\partial u_i}{\partial x_j} + \frac{\partial u_j}{\partial x_i} \right) \quad (2.19)$$

The variable  $C_\eta$  to determine the turbulent viscosity is no longer constant in the realisable  $k - \varepsilon$  model but dependent on the mean strain and rotation rates, the angular velocity of the system rotation, and the turbulence fields ( $k$  and  $\varepsilon$ ). The constants for the realizable  $k - \varepsilon$  model are  $C_2 = 1.9$ ,  $\sigma_k = 1.0$  and  $\sigma_\varepsilon = 1.2$ .

The velocity changes rapidly and turbulences are subdued in the near wall zone due to no-slip conditions at the wall. Owing to these high solution gradients, the size of the grid cell nearest to the wall is very important. To compare near wall effects of several flows, the velocity  $u$  is made dimensionless ( $u^+$ ):

$$u^+ = \frac{u}{u_\tau}, \quad y_w^+ = \frac{y_w u_\tau}{\nu}, \quad u_\tau = \sqrt{\frac{\tau_w}{\rho}} \quad (2.20)$$

with  $y_w^+$  as dimensionless wall distance,  $y_w$  as actual wall distance,  $u_\tau$  as shear velocity,  $\nu$  as viscosity,  $\tau_w$  as wall shear stress and  $\rho$  as density of the medium.

If the viscous sublayer is completely resolved, the first grid cell needs to be  $y_w^+ = 1$ . This will significantly increase the mesh density and is only used in combination with low-Reynolds models (like  $k - \omega$ ). The application of a wall function is more common for high  $Re$  models (like SKE or RKE), especially if mixing in the middle of the domain is more important, rather than forces at the wall. Hereby, the first grid cell needs to be  $30 < y_w^+ < 300$ . In the viscous sublayer the flow is dominated by the molecular viscosity and is modelled as:

$$u^+ = y_w^+ \quad (2.21)$$

The near wall zone, the fluid layer above the viscous sublayer is modelled by the logarithmic wall function:

$$u^+ = 2.5 \ln y_w^+ + 5.5 \quad (2.22)$$

The first grid cell might be calculated by eq. 2.23 by inserting  $\tau_w$  in eq. 2.20 :

$$C_f = 0.058 Re^{-0.2}, \quad \tau_w = 0.5 C_f \rho u_\infty^2 \quad (2.23)$$

with the skin friction coefficient  $C_f$  of a flat plate (von Kármán, 1934) and  $u_\infty$  as the velocity distant to the wall. Other wall functions are applicable like the enhanced wall treatment option for low -  $Re$  flows or flows with complex near-wall phenomena, as well as the scalable wall functions.

### 2.4.3 Modelling of agitation and mixing in stirred tanks

A number of models to incorporate the motion of the impeller exist. Amongst them are steady state approaches like the Computational Snapshot (CS) model (Ranade & Van den Akker, 1994) the Inner-Outer (IO) model (Brucato et al., 1998) and the Multiple Reference Frame (MRF) model (Luo & Gosman, 1994). Hereby, the rigid body is subtracted from the fluid region and forces to impose the impeller motion are added either at the impeller or in the surrounding zone. In the CS approach impeller blades are fixed at a specific position and forces exerted by the impeller on the fluid are modelled. The IO and MRF models divide the mesh into two zones, one rotating frame containing the impeller and one stationary frame containing the baffles. By the separation into these zones, the impeller baffle interaction is accounted for. In contrast to the MRF method, the zones in the IO approach overlap, which requires an iterative matching of the solution obtained on the boundaries of the overlapping zones. The transient behaviour of the fluid motion can be modelled by the Sliding Mesh (SM) model (Murthy et al., 1994), however it is less favorable due to high computational costs (Dewan et al., 2006). The most frequently applied approach is the MRF method, as it showed adequate results compared to experimental Laser Doppler Anemometry (LDA) (Naude et al., 1998), with only small differences in fluid velocities and power draw compared to SM (Koh et al., 2003; Montante et al., 2001).

Mixing time studies generally showed better performance for single and multiple impeller systems applying LES methods compared to MRF-SKE or SM-SKE methods (Jahoda et al., 2007; Haringa & Mudde, 2018). In single impeller systems the mixing time was overpredicted by SM approaches (Jahoda et al., 2007; Zadghaffari et al., 2010) but good agreement with experimental data was shown for the MRF method provided, that the mesh resolution was sufficient. For multiple impeller systems the mixing time was over-estimated with both MRF-SKE and SM-SKE by 20 % and 26 % respectively (Jahoda et al., 2007). Kukuková et al. (2005) predicted only an overestimation of 8.6 % with MRF-SKE. For a three and four impeller system mixing time was overpredicted or fixed by tuning the turbulent Schmidt number  $Sc$  (Moštěk et al., 2005; Montante et al., 2005; Delafosse et al., 2014). Haringa et al. (2018b) reported an increase in mixing time with increasing mesh density, leading to poorer prediction of the mixing time. However, the study was conducted with large impeller spacings  $\Delta C = T$ , which exhibit complete parallel flow and thereby a pronounced inter-compartment plane. Furthermore, these mixing studies were conducted on frozen velocity and turbulence fields. Transient MRF performed with an URANS solver captures unsteady and rotational effects of the vortex (Gullberg & Sengupta, 2011), which might effect mixing times as well. Bach et al. (2017) reported good agreement with experimental mixing time for transient RANS simulations and a multiple reference frame approach. Moreover, as their study was conducted as multiphase simulation their results qualify the applicability of this approach to derive mixing times in two phase systems.

### 2.4.4 Modelling of two phase flows in stirred tanks

The majority of biotechnological applications is performed as aerobic fermentation, making it necessary to include a second phase in the simulation. Approaches for multiphase modelling are depicted in figure 2.3.

The Discrete Phase Model (DPM) follows the Euler-Lagrange approach. The fluid phase is treated as continuum and solved by the NSE, whereas the dispersed phase is solved by tracking a large number of particles. In case of a gas liquid flow these particles are bubbles which are calculated through the flow field. This approach is applicable for small gas volume fractions and becomes very computationally expensive for a large number of particles. For higher gas volume fractions the Euler-Euler approach is more suitable, treating the different phases as interpenetrating continua. Since a phase cannot be occupied by the other phase the sum of the volume fractions must add up to one. For each phase conservation equations are solved. The three common models are depicted in figure 2.3. The Volume of Fluid (VOF) is a surface-tracking technique designed for immiscible fluids, where the position of the interface between two fluids is of interest and therefore mostly applied for free-surface flows. For bubbly flows the Mixture and Eulerian model are better suited. In the mixture model, momentum equations for the mixture are solved and the dispersed phase is described by relative velocities, whereas the Eulerian model solves a set of  $n$  momentum and continuity equations for each phase. The mixture model is less computationally costly and used if the dispersed phase is wide distributed within the fluid phase. In the heterogeneous environment of a large scale stirred tank however, the dispersed phase is often concentrated, especially around the impeller. Additionally, interphase drag laws play an important role, which makes the Eulerian model a better choice to simulate a multiphase stirred tank. The basic equations for the two fluid model are shown in equation 2.24:

$$\frac{\partial \alpha_k}{\partial t} + \frac{\partial(\alpha_k \bar{u}_i^k)}{\partial x_i} = \Gamma_k \quad (2.24a)$$

$$\rho_k \left( \frac{\partial(\alpha_k \bar{u}_i^k)}{\partial t} + \rho \frac{\partial(\alpha_k \bar{u}_i^k \bar{u}_j^k)}{\partial x_j} \right) = -\alpha_k \frac{\partial \bar{p}}{\partial x_i} + \frac{\partial(\alpha_k \bar{\tau}_{ji}^k + \bar{\tau}_{ji}^{Re,k})}{\partial x_j} - \alpha_k \rho g_i + M_{i,k} \quad (2.24b)$$

with  $\alpha_k$  as the volume fraction of phase  $k$ ,  $\Gamma_k$  as source or sink term to describe mass transfer at the interface. As for single phase flows, the Reynolds stresses  $\bar{\tau}_{ji}^{Re,k} = -\rho_k \overline{\alpha_i'^k \alpha_j'^k}$  are modelled by either the mixture or dispersed formulation of the  $k - \varepsilon$ -model. The term  $M_{i,k}$  represents inter-phase momentum exchange.

The complexity of the interactions between the phases in aerated tanks makes it difficult to describe the dynamic behaviour of multiphase systems. Fundamental problems need to be tackled like: (i) interphase momentum exchange, (ii) modelling of bubble size distribution, (iii) modelling of

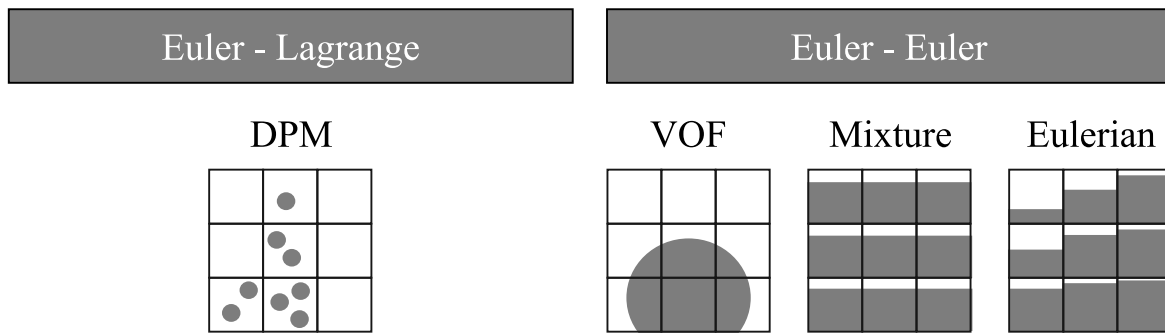


**Figure 2.3: Multiphase models.** The Discrete Phase Model (DPM) follows an Euler-Lagrange approach. The Volume of Fluid (VOF), Mixture and Eulerian model are Euler-Euler approaches.

bubble breakage, coalescence and daughter size distribution as well as (iv) the impact of grid size on the simulation results.

**(i) interphase momentum exchange:** Various forces act on bubbles in a bubbly turbulent flow like drag, lift, virtual mass force, turbulent dispersion or wall lubrication forces. As drag force was reported to be the most dominant contributor to momentum exchange in stirred tanks, a commonly accepted simplification is to reduce the momentum exchange to the impact of drag force (Scargiali et al., 2007). Unfortunately, drag coefficients are usually derived from measurements in stagnant laminar flows where bubbles are isolated due to the extreme dilution (Ishii & Zuber, 1979; Tomiyama et al., 1998). In turbulent flows containing large gas volume fractions the momentum boundary layers of bubbles interact, which results in crowding effects (Buffo et al., 2016; Ishii & Zuber, 1979) or the layer is affected by smaller eddies leading to decreasing bubble rise velocities (Bakker & Van den Akker, 1994; Brucato et al., 1998). If a bubble size distribution is simulated, typically only the Sauter diameter of the local distribution is used for drag force calculation.

**(ii) modelling of the bubble size distribution (BSD):** The bubble size distribution in a stirred tank is strongly heterogeneous. Assuming a fixed bubble diameter might lead to false interfacial area calculation and thereby false prediction of gas-liquid mass transfer. BSD are often described by Population Balance Equations (PBE), which consist of a complicated integro-partial differential equation. As an analytical solution is difficult to obtain, several approaches exist to solve the PBE numerically. The most widely explored methods include the Class Method and the Method of Moments. Two formulations may be applied for the Class Method. While the Kumar & Ramkrishna (1996) formulation is more accurate but computationally demanding, differences in accuracy can be corrected by a suitable choice of bin sizes in the Hagesaether et al. (2002) formulation. A range of 16 – 20 classes has been recommended by Haringa et al. (2017a) and Laakkonen et al. (2007a). However, the gain in accuracy was shown to be less pronounced if more classes than that were chosen (Laakkonen et al., 2007b). The PBE contain source terms to express the birth rates and death rates of bubbles of a specific size due to aggregation or break up, which need to be modelled.

**(iii) modelling of bubble breakage, coalescence and daughter size distribution (DSD):** As a consequence of turbulence and viscous stresses in a gas-liquid system, bubbles can break into smaller bubbles or coalesce over time. To describe the bubble dynamics, the inclusion of a suitable break up and coalescence model is necessary. Many break up models follow the kinetic theory of gases, leading to similar assumptions such as that breakage is caused by turbulent eddies smaller or equal to the size of the bubble, thereby bearing enough energy to overcome the resisting forces. The breakup frequency is provided by the collision rate between the particles and turbulent eddies multiplied by the collision efficiency. The collision efficiency terms, however, are based on different assumptions. For instance Lehr et al. (2002) assume that breakage occurs if the dynamic pressure of the eddy is larger than the capillary pressure, whereas other models assume that a critical value of eddy energy (Luo & Svendsen, 1996) or that the relative velocity of oscillations has to be exceeded (Alopaeus et al., 1999) to promote bubble breakage. Coalescence models are usually derived from similar assumptions and the models used by Luo & Svendsen (1996) and Alopaeus et al. (1999) or Prince & Blanch (1990), respectively, are based on the work of Coulaloglou & Tavlarides (1977). Lehr et al. (2002) investigated bubble collision with a high speed camera and proposed a model, where only gentle collisions lead to coalescence. The daughter size function describes the probability of the formation of a daughter particle of a specific volume from a mother particle. The DSD in the model of Luo & Svendsen (1996) is directly derived from the expression of the break up rate, whereas Alopaeus et al. (1999) used a simple  $\beta$ -distribution which was not dependent on physical properties of the system as in the other models. This simple expression requires significant less computational effort. Although the model by Luo & Svendsen (1996) is the most frequently used break up model, its practical applicability was questioned (Kálal et al., 2014). The authors thoroughly reviewed several break up models and concluded that the model by Alopaeus et al. (1999) predicted the BSD the best. The same approach was further used in several studies of Laakkonen, showing good agreement to experimental data (Laakkonen et al., 2007b).

**(iv) impact of the grid size:** The Reynolds-Average Navier-Stokes (RANS)  $k$ - $\varepsilon$  model was stated to underestimate the turbulent quantities locally in single and multiphase simulations, albeit giving satisfactory results of the total dissipated energy. Being less computational demanding, RANS is the preferred choice over other turbulence models. However, higher discretisation schemes and grid resolution are necessary for the accurate prediction of turbulent quantities. On the other hand, the velocity field or the power number by torque are less affected (Coroneo et al., 2011), legitimising the introduction of a scaling factor for turbulent quantities (Laakkonen et al., 2007b). This factor was based on experimental torque measurements and diminished the dependence of turbulent dissipation rate on grid size.

### 2.4.5 Modelling of population heterogeneity

As mentioned in section 2.2 concentration fluctuations within a large scale stirred tank may lead to the formation of population heterogeneities. In order to describe the microbial heterogeneity in a bioreactor, models are necessary to depict the microbial growth with different level of detail. Bailey (1998) classified microbial models into non-structured/structured and non-segregated/segregated approaches. The simplest models are non-structured/non-segregated approaches assuming average growth behaviour by a black box model approach (Nyholm, 1976). These models are usually used for process design, but fail to predict population heterogeneity or complex subcellular structures to identify bottlenecks. If subcellular levels like metabolic and transcriptional regulation, compartmentalisation or signal transduction are of interest, structured/non-segregated models are used (Nielsen et al., 1991; Shuler, 1999; Chassagnole et al., 2002). For these models the knowledge about the network structure is compulsory. The network can either be a metabolic or a gene regulatory network (GRN). GRNs can be further divided into continuous models, which are described by ordinary differential equations (Machado et al., 2012; Hardiman et al., 2009; Khodayari & Maranas, 2016), Boolean models (Wang et al., 2012; Davidich & Bornholdt, 2008) or probabilistic models (Chandrasekaran & Price, 2010; Qian & Elson, 2002; Turner et al., 2004). However, population heterogeneity can only be depicted by segregated models. The formation of subpopulations may result from small deviations in cellular metabolism and cell cycle dynamics or due to asymmetric division (Jahn et al., 2013), leading to differences according to their size and intracellular state. The PBE model framework presents a segregated approach, where the intracellular state can be represented with only few variables such as cell age (Nishimura & Bailey, 1981) or cell mass (Hjortso & Nielsen, 1995). Structured/segregated models reflect the most realistic approach to display microbial heterogeneity in large scale bioreactors, however, due to the complexity of cellular mechanisms they are limited in scale. As an alternative the focus was shifted to cell ensemble models, where the population is described by an ensemble of single-cell models, which differ according to key properties (Henson et al., 2002).

By coupling microbial models with the hydrodynamics in a stirred tank, populations heterogeneity within a large scale fermentation process can be depicted. Different approaches are possible. Some studies consider the coupling of a two-phase Euler-Euler approach using PBE with unstructured kinetic growth models to include microbial diversity (Morchain et al., 2014; Pigou & Morchain, 2015). The incorporation of a detailed intracellular reaction network, however, leads to computational extensive and intractable problems due to the high-dimensional distribution function, which needs to be solved. Additionally, no information about cell history is provided. With their pioneering work Lapin et al. (2004) presented a workaround by simulating individual cells choosing an Euler-Lagrange approach. The extracellular environment is still based on the continuous Euler approach, whereas a discrete cell ensemble (Lagrange) approach is applied to account for the

biophase. By the simulation of a sufficiently large number of individual cells, the behaviour of a bacterial population is approximated. Furthermore, the approach permits the analysis of bacterial *lifelines* in space and time. Simple Monod-like black box models can be applied in this agent-based modelling approach to account for spatially distributed substrate uptake (Haringa et al., 2016) and can be coupled to models describing a microbial response (Kuschel et al., 2017). More detailed kinetic models may be adopted (Lapin et al., 2006; Haringa et al., 2018a). Due to rapid bacterial responses to changing substrate concentrations in terms of substrate uptake rate, the bacterial consumption can be coupled to the continuous phase (Haringa et al., 2016). Hereby, only one-way coupling is considered, but the computational demand can be effectively reduced by a smaller number of simulated particles (Haringa et al., 2017b). In later studies this approach was used to derive scale down devices for process optimisation (Haringa et al., 2017a). However, the aforementioned studies neglected the influence of multiphase systems on bacterial heterogeneity.

---

### 3 Characterisation of bioprocesses with *C. glutamicum* as model organism

The market for biotechnological products is constantly on the rise and the portfolio is ever growing. Emerging fields are the production of amino and organic acids with bacterial systems or biopharmaceuticals with mammalian cells (Becker & Wittmann, 2012; Morrison & Lähteenmäki, 2017). *Corynebacterium glutamicum* is one of the most important platforms, being used for the production of more than 30 different chemicals (Leuchtenberger et al., 2005; Takors et al., 2007). However, for the production in industrial bioreactors the scale-up from smaller laboratory scales is crucial and tools to predict process performance *a priori* are of high interest. To parameterise these models cell specific growth, uptake and production rates were determined during a batch fermentation of *C. glutamicum*. Additionally, physical properties of the broth were analysed resulting in density and viscosity values similar to water. Smallest amounts of antifoaming agents ( $0.01 \text{ mL L}^{-1}$ ) already resulted in a surface tension reduction  $> 40 \%$  at thermodynamic equilibrium, whereas high biomass concentration of up to  $80 \text{ g L}^{-1}$  showed almost no effect. The dynamic surface tension measurement revealed furthermore that dwelling times of bubbles inside a bioreactor lie within the range of affected surface ages for these concentrations. However, the ambivalent behaviour of antifoam concerning  $k_{La}$  values shows the need of a thorough analysis to quantify these effects before considering a reduction of surface tension in numerical simulations.

#### 3.1 Introduction

The yearly production of lysine is currently estimated to be 2.2 million tons (Yokota & Ikeda, 2017). *Corynebacterium glutamicum* is used as workhorse to produce not only L-lysine but also L-glutamate in fed-batch processes of  $500 \text{ m}^3$  volume (Eggeling & Bott, 2015). However, industrial scale fermentations usually suffer from deteriorated yields due to the formation of substrate and gas gradients caused by limited mixing and mass transfer. To gain better knowledge of ratios inside the reactor, modelling tools have been used in the recent years to support scale-up processes. Prerequisite to develop such models is the knowledge about cell specific rates and physical properties of the broth. Cell specific growth rates  $\mu$ , biomass substrate yields  $Y_{XS}$  or substrate consumption rates  $q_S$  are needed to parameterise simple kinetic models like the well known Monod

model for saturated substrate consumption (Monod, 1949). Because fermentation processes with *C. glutamicum* are usually aerobic, also oxygen consumption rates  $q_{O_2}$  need to be determined. They can be incorporated in multisubstrate kinetic models in order to predict the formation of substrate and gas gradients (Roels, 1983).

Physical properties of the broth mainly influence the power consumption and gas-liquid mass transfer in stirred tanks. The behaviour of gas and liquid phase can be simulated by computational fluid dynamics. As density and viscosity of the broth have a high impact on mass and impulse balances, thorough experimental determination has to be performed. Viscosity quantifies the frictional force that arises between two adjacent layers which are in relative motion. With increasing process duration and thereby higher biomass concentrations, the viscosity of the broth may rise. Especially if the organism is sensitive to shear stress, cell disruption might contribute to elevated viscosity levels (Newton et al., 2017; Newton et al., 2016). As consequence rheometric properties might also change. If the shear force is still proportional to the shear rate, the fluid is characterised as Newtonian fluid with the viscosity as proportionality factor. Rheometric properties need to be included in numerical flow simulations in order to properly predict the flow behaviour.

In turbulent systems like stirred tanks, fast interface formation has to be considered. The interfaces between bubbles and the liquid have a strong impact on mass-transfer. Therefore, it is very important to measure the interfacial tension during the formation of the interface. Various methods exist to determine the surface tension (Tricot, 1997). Static methods measure the surface tension in thermodynamic equilibrium. These are very cheap and fast methods to characterise surface activity of an agent. Dynamic surface tension measurements determine the surface tension as function of the surface or interface age. The value reduces dependent on diffusion and absorption rate of the surfactant until the thermodynamic equilibrium is reached. As the dwelling time of bubbles within a stirred tank is limited, the interfacial gas-liquid area only exists for a certain time. Thereby, time dependent effects of a surfactant on bubbles within a bioreactor can be estimated.

In this chapter a batch fermentation of *C. glutamicum* was conducted as triplicate. Cell specific rates, yields and also physical properties of the broth were determined. The obtained data serve for later parametrisation of numerical simulations.

## **3.2 Material and methods**

### **3.2.1 Materials**

#### **3.2.1.1 Instruments and software**

A list of all instruments and software used in this work is provided in appendix A table A.1 and table A.2.

#### **3.2.1.2 Chemicals**

A list of chemicals used in this work is provided in appendix A table A.3.

#### **3.2.1.3 Buffers and solutions**

##### **Phosphate-buffered saline (PBS)**

The buffer consisted of 400 mM  $\text{Na}_2\text{HPO}_4/\text{NaH}_2\text{PO}_4$ , 150 mM NaCl and was adjusted to pH 7.2. PBS was used to wash the cells before staining.

##### **Staining buffer**

The staining buffer for fluorescence microscopy consisted of 0.68  $\mu\text{M}$  4',6-diamidino-2'-phenylindole (DAPI, SIGMA) and 0.2 M  $\text{Na}_2\text{HPO}_4$  (pH = 7.0).

##### **Sterilisation buffer**

Sterilisation buffer for the fermentation process contained 1 M  $\text{K}_2\text{HPO}_4$  and 1 M  $\text{KH}_2\text{PO}_4$ .

##### **Tris buffer**

Tris buffer consisted of 400 mM Tris and 4 mM  $\text{MgSO}_4$ . The pH value of the buffer was adjusted to 7.6 with 32% ( $\text{w v}^{-1}$ ) HCl.

#### **3.2.1.4 Media**

##### **2x TY complex media and agar plates**

Components of the 2xTY complex media listed in table 3.1 were dissolved in deionised water  $\text{dH}_2\text{O}$ . For solid cultures, 18 g  $\text{L}^{-1}$  agar was added prior to autoclaving (121 °C, 2 bar, 20 min).

**Table 3.1: Composition of 2xTY complex medium.** According to Russell & Sambrook (2001).

Component	Concentration [g L <sup>-1</sup> ]
Tryptone	16
Yeast extract	10
NaCl	5

### CGXII minimal media

For batch experiments CGXII minimal media containing 40 g L<sup>-1</sup> glucose was used to obtain high cell densities. CGXII media contained several stock solutions listed in table 3.2. Components for the trace element stock solution were dissolved in dH<sub>2</sub>O by adding 5 M HCl (pH = 1) and sterile filtered (0.2 µm). For the Biotin stock solution (1000x), 0.2 g Biotin was dissolved in 1 L dH<sub>2</sub>O and ≈ 5 mL 5 M HCl. After mixing, the solution was sterile filtered (0.2 µm) aliquoted and stored at -20 °C. By analogy the protocatechuic acid (PCA) solution was produced: 30 g PCA were dissolved in 1 L dH<sub>2</sub>O and ≈ 10 mL 5 M HCl. After mixing, the solution was sterile filtered (0.2 µm) aliquoted and stored at -20 °C. Stock solutions of MgSO<sub>4</sub> and CaCl<sub>2</sub> (1000x) were made by dissolving 250 g MgSO<sub>4</sub> and 10 g CaCl<sub>2</sub> in 1 L dH<sub>2</sub>O respectively. Solutions were autoclaved (121 °C, 2 bar, 20 min) and stored at 4 °C. A 50 % glucose stock solution contained 550 g glucose-monohydrate in 1 L dH<sub>2</sub>O, which was autoclaved at 121 °C and 2 bar for 20 min.

**Table 3.2: Composition of CGXII minimal medium.** Modified to Blombach et al. (2013).

Component	Stock concentration [g L <sup>-1</sup> ]	Final concentration [g L <sup>-1</sup> ]
(NH <sub>4</sub> ) <sub>2</sub> SO <sub>4</sub>		10
K <sub>2</sub> HPO <sub>4</sub>		1
KH <sub>2</sub> PO <sub>4</sub>		1
MgSO <sub>4</sub>	250	0.25
CaCl <sub>2</sub>	10	0.01
Biotin	0.2	0.0002
PCA	30	0.03
Glucose	500	40
Trace element stock solution (1000x)		
Fe(II)SO <sub>4</sub> · 7H <sub>2</sub> O	16.4	0.0164
MnSO <sub>4</sub> · H <sub>2</sub> O	10	0.01
CuSO <sub>4</sub> · 5H <sub>2</sub> O	0.2	0.0002
ZnSO <sub>4</sub> · 7H <sub>2</sub> O	1	0.001
NiCl <sub>2</sub> · 6H <sub>2</sub> O	0.02	0.00002

### 3.2.1.5 Bacterial strain

The wild-type strain (WT) *Corynebacterium glutamicum* ATCC13032 obtained from the American Type Culture Collection (ATCC, Manassas, VA, USA) was used for batch cultivations.

### 3.2.2 Seed train

The seed train as shown in figure 3.1 was conducted by streaking out cell material from a  $-70^{\circ}\text{C}$  glycerol stock on 2xTY agar medium (table 3.1). After incubation for two days at  $30^{\circ}\text{C}$ , a single colony was picked to inoculate the first preculture, consisting of 5 mL 2xTY medium in a glass tube. The first preculture was incubated for 14 h at  $30^{\circ}\text{C}$  on a shaker (Benchtop shaker AK85, Infors AG, Switzerland) at 120 rpm. The complete cell suspension was transferred into a baffled Erlenmeyer shaking flask (500 mL, working volume of 50 mL 2xTY medium). The second preculture was incubated for 8 h at  $30^{\circ}\text{C}$  on a shaker at 120 rpm. The optical density at a wavelength of 600 nm ( $\text{OD}_{600}$ ) was measured with a spectrophotometer (spectrophotometer DR2800, Hach Lange, Germany). The amount of preculture suspension to inoculate the reactor to  $\text{OD}_{600} = 1.0$  was calculated:

$$\text{OD}_{\text{preculture}} V_{\text{preculture}} = \text{OD}_{\text{main culture}} V_{\text{main culture}} \quad (3.1)$$

The cell suspension was pelleted (4000 g, 2 min,  $4^{\circ}\text{C}$ ) with a centrifuge (centrifuge 5430 R, Eppendorf, Germany). The supernatant was discarded and after two washing steps in 0.9 % ( $\text{w v}^{-1}$ ) NaCl solution, the pellet was resuspended in 50 mL CGXII and transferred to the main culture, thereby inoculating the fermenter to an  $\text{OD}_{600} = 1.0$ .

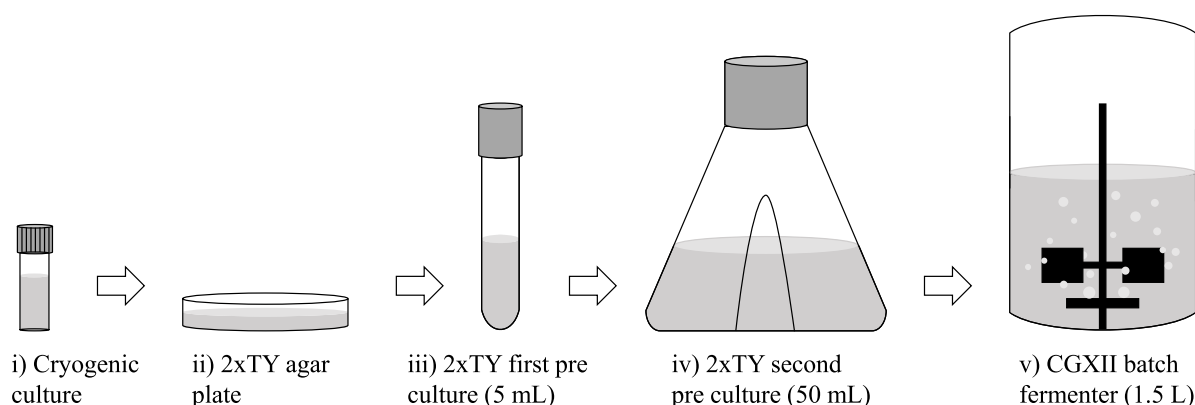


**Figure 3.1: Seed train.** (i) A cryo tube culture stored at  $-70^{\circ}\text{C}$  was thawed and cell suspension was streaked on (ii) 2xTY agar medium. After incubation for two days at  $30^{\circ}\text{C}$ , a single colony was transferred to a (iii) 5 mL 2xTY medium and incubated for 14 h at  $30^{\circ}\text{C}$  on a shaker at 120 rpm. (iv) The second preculture was inoculated with the complete cell suspension and incubated under the same conditions for 8 h. Finally the cell suspension was washed and the (v) stirred tank containing 1.5 L CGXII was inoculated to  $\text{OD}_{600} = 1$ . Batch fermentations were agitated and gassed at  $30^{\circ}\text{C}$  for 12 h.

### 3.2.3 Bioreactor cultivation

Batch fermentations were conducted as triplicates in a 3.7 L stainless steel stirred tank (STR) (KLF 2000, Bioengineering, Switzerland) with a working volume of 1.5 L. The tank was equipped with four baffles and one Rushton impeller. Gassing was enabled by a ring sparger close to the reactor bottom. The height of the reactor was 333 mm, the liquid filling height was  $H_L = 130$  mm, the tank diameter  $T_D = 125$  mm and the impeller diameter  $D_I = 60$  mm. Off bottom impeller spacing was set to 50 mm. The piping and instrumentation flowchart in figure 3.2 shows how the reactor was operated in batch mode. Air flow was set to  $1 \text{ L min}^{-1}$  and controlled by a mass flowmeter (V01, Model 3585, Analyt MTC Messtechnik GmbH, Germany). Before entering the reactor through the ring sparger, air was aseptically filtered (0.2  $\mu\text{m}$ ) (G01). The pressure was kept to 1.5 bar by controlling the exhaust gas flow (V02). During the fermentation process the exhaust gas composition was recorded by an off-gas analyser (BlueSens RS232, BlueSens GmbH, Deutschland). In order to remove the water in the exhaust gas and sterilise it, the exhaust gas was cooled by a heat exchanger (W01) and filtered (G02) prior to off-gas analysis. Additional to mechanical pressure relief, an overpressure valve was installed (VC01), releasing gas at  $p = 2.5$  bar. The pH was monitored by

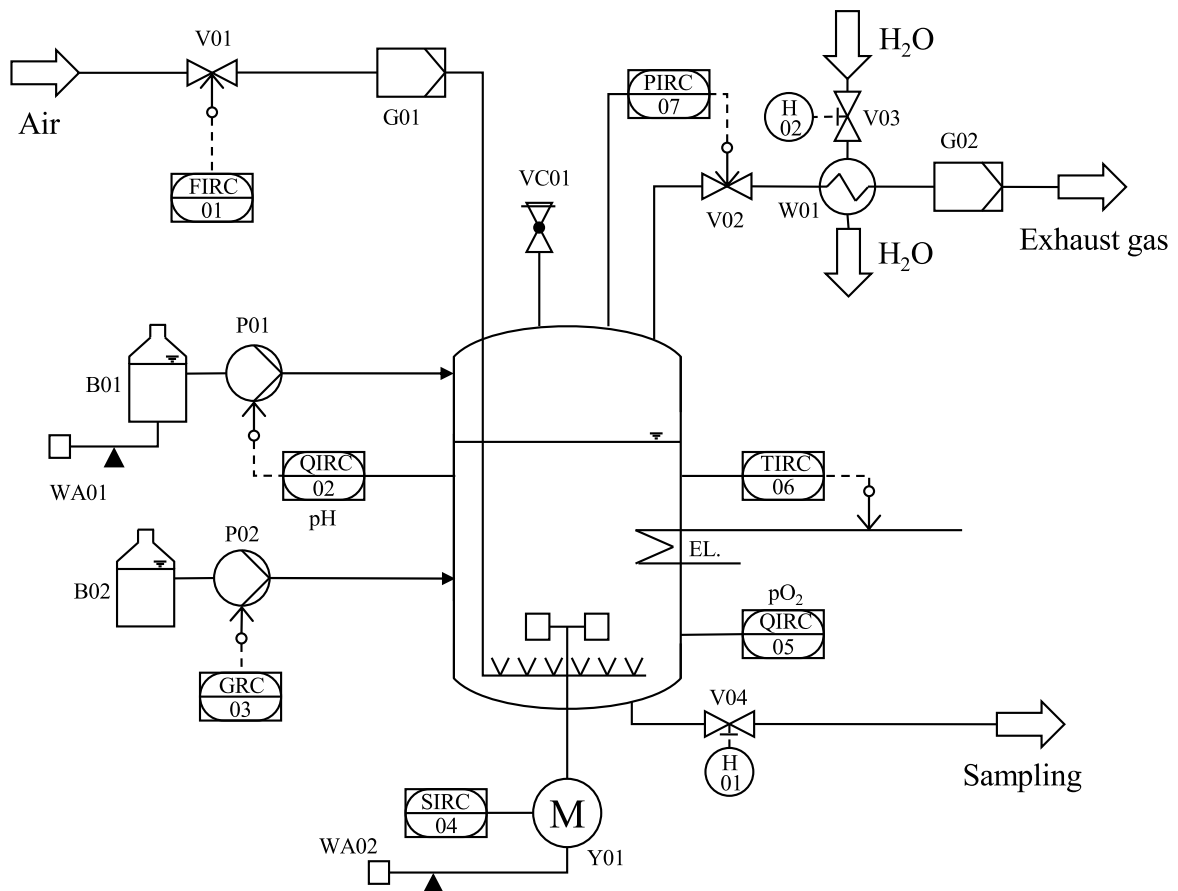


Figure 3.2: P&ID of the bioreactor in batch mode. EN ISO 10628:2000. Symbols are explained in the main text.

a pH probe (405-DPAS-SC-K8S, Mettler Toledo, Germany) and controlled (02) to keep pH = 7.4 by base addition (NH<sub>4</sub>OH) from a base reservoir (B01) enabled by a pump (P01, Watson-Marlow Fluid Technology Group, USA). Base consumption was balanced by a scale (WA01, Kern 572, Kern& Sohn, Germany). Antifoam (B02, Struktol® J 647, Schill&Seilacher, Germany) was injected via a controlled syringe pump (P02, Spritzenpumpe LA-30, HLL Landgraf Laborsysteme, Germany) (03). The dissolved oxygen (DO) was measured as percentage of air saturation by an oxygen probe (InPro 6800, Mettler-Toledo, Germany) and registered by the process control system (05). To keep the DO signal above 30 % agitation was controlled (04). The reactor mass was monitored throughout the process by a scale (WA02, Combics 3, Sartorius, Germany). Sampling was enabled by a manual valve (H01). Optical density and glucose concentrations were measured every hour. Density, cell dry weight, surface tension and viscosity were determined once in three hours. At a later process stage after about nine hours all samples were taken hourly for the second and third batch process. Temperature was monitored by a PT-100 sensor (PT-100 sensor, Bioengineering, Switzerland) and controlled (06) through direct contact to an electrical heating element and a water cooled cooling stick. The LabVIEW® 2009 SP1 software (National Instruments, USA) was used to for data recording and process control. Process duration was about 12 h.

### 3.2.4 Analytics

#### 3.2.4.1 Determination of biomass concentration

##### Optical density

Bacterial growth was monitored by measuring the turbidity of the liquid culture at OD<sub>600</sub> with a spectrophotometer (spectrophotometer DR2800, Hach Lange, Germany). For this purpose a sample was withdrawn from the bioreactor and diluted in 0.9 % (w v<sup>-1</sup>) NaCl solution to reach the linear range of the spectrophotometer (0.1 - 0.3). Samples were measured as triplicates. NaCl solution also served as reference.

##### Cell dry weight

Prior to the experiment, 1.5 mL glas vials (glas vials, VWR, Germany) were dried at 105 °C for two days, cooled to room temperature in a desiccator and weighted. Cell dry weight was determined as triplicates. Therefore, 1 mL of the biosuspension was centrifuged together with 1 mL dH<sub>2</sub>O in a 2 mL eppendorf tube at 20 000 g and 4 °C for 4 min. The additional water was used to remove all remaining biosuspension from the pipette tip. The supernatant was discarded, the cell pellet resuspended in 1 mL dH<sub>2</sub>O and centrifuged again. This washing step was performed twice, before the pellet was resuspended in 0.5 mL dH<sub>2</sub>O and transferred to the dried glass vials. The samples were dried at 105 °C for two days, cooled to room temperature in a desiccator and weighted.

The biomass weight was determined by subtracting the sample weight from the weight of the empty vial. A cell dry weight - optical density correlation factor was determined by fitting a linear correlation with  $\lambda$  as correlation factor:

$$\text{CDW} = \lambda_{\text{OD}} \text{OD}_{600} \quad (3.2)$$

### 3.2.4.2 Determination of glucose concentration

The photometric quantification of glucose is based on the enzymatic conversion of glucose to gluconate-6-phosphate by the hexokinase and glucose-6-phosphate-dehydrogenase (G6P-DH). NADPH forms as by-product, which can be measured via photometry at a wavelength of 365 nm. The glucose concentration  $c_S$  can be determined by Lambert-Beer law as follows:

$$c_S = \frac{\Delta E}{\varepsilon_{\text{NADPH}} d_c} \quad (3.3)$$

with  $\Delta E$  as difference of extinction with and without G6P-DH,  $d_c$  the diameter of the cuvette and  $\varepsilon_{\text{NADPH}} = 3.54 \text{ L mmol}^{-1} \text{ cm}^{-1}$  as specific constant for NADPH. In practice, 1-2 ml was taken from the cell suspension, centrifuged (20 000 g, 4 °C, 4 min) and the supernatant was transferred into a new tube, frozen at  $-20 \text{ °C}$  or measured directly as triplicates. The glucose measurement was performed in acrylic semi-micro cuvettes with an Ultrospec 2100 pro UV/Visible spectrophotometer (GE Healthcare Europe GmbH, Germany). Therefore 500  $\mu\text{L}$  Tris buffer (400 mM Tris, 4 mM  $\text{MgSO}_4$ , pH 7.6; see section 3.2.1.3), 100  $\mu\text{L}$   $\text{NADP}^+$  (4.4 mg  $\text{mL}^{-1}$ ), 100  $\mu\text{L}$  ATP (9.6 mg  $\text{mL}^{-1}$ ), 190  $\mu\text{L}$   $\text{dH}_2\text{O}$  and 100  $\mu\text{L}$  of the prediluted supernatant (concentration in the cuvette  $< 0.1 \text{ mM}$ ) were mixed. Subsequently the extinction at 365 nm was measured. After adding 10  $\mu\text{L}$  G6P-DH / hexokinase mix (Roche Diagnostics International Ltd) and incubation of the reaction mix for 10 min at room temperature, the final extinction was determined.

### 3.2.4.3 Determination of volumetric oxygen mass transfer coefficient

#### Steady-state (stationary) approach with Microorganisms

The volumetric oxygen mass transfer rate  $k_L a$  can be determined from the oxygen mass balance of the liquid phase within the bioreactor. The oxygen consumption is hereby balanced as follows:

$$V_L \frac{dc_{\text{O}_2,\text{L}}}{dt} = k_L a \Delta c_{\text{O}_2,\text{m}} V_L - Q_{\text{O}_2} V_L \quad (3.4)$$

with  $V_L$  as reactor liquid volume,  $\frac{dc_{\text{O}_2,\text{L}}}{dt}$  as oxygen accumulation rate,  $\Delta c_{\text{O}_2,\text{m}}$  as concentration

gradient and  $Q_{O_2}$  as volumetric oxygen uptake rate. During the cultivation, the change of oxygen accumulation rate and reactor volume is small and can be treated as pseudo stationary between two time steps. The oxygen accumulation rate is thereby set to zero resulting in equation 3.5.

$$k_L a = \frac{Q_{O_2}}{\Delta c_{O_2,m}} \quad (3.5)$$

The average logarithmic oxygen gradient can be calculated by:

$$\Delta c_{O_2,m} = \frac{H_{O_2}^{cp} p (y_{O_2}^{in} - y_{O_2}^{out})}{\ln \left( \frac{1 - \frac{E}{100}}{\frac{y_{O_2}^{out}}{y_{O_2}^{in}} - \frac{E}{100}} \right)} \quad (3.6)$$

with  $H_{O_2}^{cp}$  as Henry coefficient of oxygen,  $p$  as ambient pressure,  $y$  as molar gas fraction with subscript ( $O_2$ ) for oxygen for the incoming (in) and outgoing (out) gaseous phase and  $E$  (in %) as the liquid oxygen concentration.

The volumetric oxygen uptake rate  $Q_{O_2}$  is obtained by offgas analysis according to:

$$Q_{O_2} = \frac{p \dot{V}_{g,in}}{V_L R T} \left( y_{O_2,in} - \frac{1 - y_{O_2}^{in} - y_{CO_2}^{in}}{1 - y_{O_2}^{out} - y_{CO_2}^{out}} y_{O_2}^{out} \right) \quad (3.7)$$

with  $\dot{V}_{g,in}$  as gas volume flow,  $R$  as ideal gas constant and  $T$  as temperature under standard conditions ( $T = 294.15$  K,  $p = 1.01325 \cdot 10^5$  Pa). Subscript ( $CO_2$ ) denotes carbon dioxide.

### Dynamic approach without Microorganisms (desorption)

The volumetric mass transfer coefficient  $k_L a$  was measured with the dynamic gassing out method (Puthli et al., 2005; García-Ochoa & Gómez, 1998; Djelal et al., 2012; Sánchez Mirón et al., 2000). First, the liquid was deoxygenated by gassing with pure nitrogen. The second step included gassing with air until the liquid was saturated. The oxygen profile was monitored following the start of the air inflow by an optical oxygen probe (OXYBase WR-RS485-L5-OIW, PreSens, Germany) with the oxygen exchange cap (OEC-PS3-NAU-OIW, PreSens, Germany). Integration of equation 3.8 results in equation 3.9.

$$\frac{dc_{O_2,L}}{dt} = k_L a (c_{O_2,L}^* - c_{O_2,L}) \quad (3.8)$$

$$\ln \left( \frac{c_{O_2,L}^* - c_{O_2,L,2}}{c_{O_2,L}^* - c_{O_2,L,1}} \right) = -k_L a (t_2 - t_1) \quad (3.9)$$

with  $c_{O_2,L}$  as oxygen liquid and  $c_{O_2,L}^*$  as oxygen saturation concentration. Plotting the logarithm against the time, the  $k_L a$  value was directly calculated by the slope of the line. With a probe response time  $t_{63} < 3$  sec (time at which 63 % of the final value is reached)  $k_L a$  values  $< 480$  h<sup>-1</sup>

can be measured directly without considering a delay time according to the criteria of Van'T Riet (1979) and Zlokarnik (1999). Measurements were performed as triplicates in deionised water and in antifoam solutions containing 1.0 mL Struktol® J 647 .

#### 3.2.4.4 Determination of viscosity

Samples for viscosity measurement were frozen immediately with liquid nitrogen and stored until further analysis. Prior to measurement, the samples were thawed slowly on ice to prevent cell bursting. The rheometer (rheometer MCR 501, Anton Paar, Austria) with a spinning cone and a stationary plate was used to determine the viscosity of the samples. The distance between the moveable cone and the stationary plate was calibrated by setting zero gap. After the adjustment of the temperature to 30 °C, 300 µL sample was placed on the stationary plate. The measuring position was set to 0.1 mm distance to the stationary plate and the program was started. First the sample was spun for 10 s. After this, the cone spun with a rotational speed between 2 and 100 s<sup>-1</sup>, increasing in an interval of 3.5 s<sup>-1</sup>. Thereby, a constant shear rate was generated and the applied shear force was measured. Measurements were performed as triplicates. The principle is presented in figure 3.3. For Newtonian fluids the shear stress  $\tau_s$  is proportional to the applied shear rate  $\dot{\delta}$ . The viscosity  $\eta$  can then be calculated by equation 3.10.

$$\tau_s = \eta \dot{\delta} \quad (3.10)$$

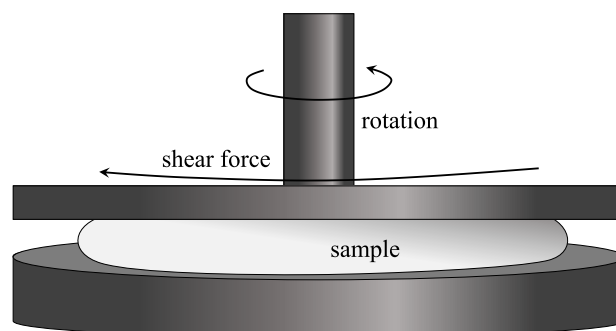


**Figure 3.3: Principle of viscosity measurement with a rheometer.** Sample is placed between the two plates and shear force is measured by applying rotational speed.

#### 3.2.4.5 Determination of surface tension

Surface tension can be measured by several methods with two of them applied in this work. The stationary method was used to measure the surface tension of the broth and different antifoam concentrations in water, whereas the dynamic method was only applied to the latter.

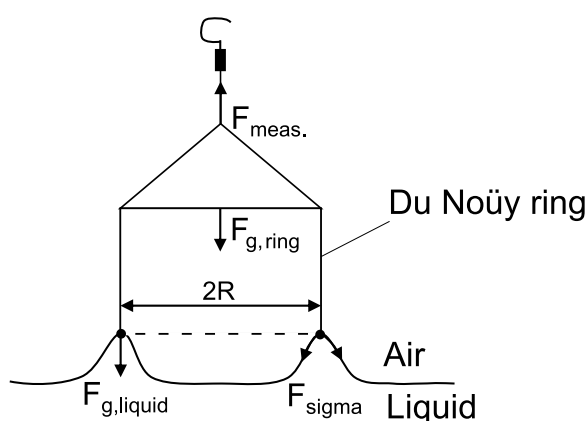


**Figure 3.4: Principle of the Du Noüy method.** Static surface tension measurement. The ring is lifted by the force  $F_{\text{meas.}}$ .  $F_{\text{g,ring}}$  and  $F_{\text{g,liquid}}$  denote the gravitational force of the ring and the liquid.  $F_{\text{sigma}}$  symbolises the force of surface tension.  $F_{\text{g,ring}}$  is compensated at the beginning of the measuring procedure.

The stationary surface tension measurement according to de Du Noüy ring method was performed with the tensiometer (STA1A, Sinterface Technologies, Germany). Thereby a platinum-indium ring was rinsed with ethanol and water and burned out in a Bunsen burner. Samples were heated to 30 °C, mixed prior to the measurement and 10 mL were transferred to a cleaned glass beaker. Then the ring was placed at a liquid-gas interface, so that the interface was horizontally directed and the ring completely wetted. The density was measured in advance and set in the program previous to the measurement. The automated surface tension measurement started by lifting up the submerged ring and registering the maximal applied force to lift the ring  $F_{\text{max}}$ . In figure 3.4 the principle of the measurement is shown.

As the ring's thickness is much smaller than the diameter, the inner and outer radius can be averaged to  $R$  with  $4\pi R$  corresponding to the wetted length of the ring. The surface tension  $\sigma$  is calculated by:

$$\sigma = \frac{F_{\text{max}}}{4\pi R\phi} \quad (3.11)$$

The correction factor  $\phi$  considers the ring geometry and the force to lift the liquid film beneath the ring  $F_{\text{g,liquid}}$ , which is raised when the ring pulls. Measurements were performed as triplicates.

The dynamic surface measurement of different antifoam (Struktol® J 647, Schill&Seilacher, Germany) concentrations ( $0.1 \text{ mL L}^{-1}$ ,  $1.0 \text{ mL L}^{-1}$ ,  $10 \text{ mL L}^{-1}$ ) was performed with a bubble pressure tensiometer (BP100, Krüss GmbH, Germany). Only the concentration with  $1.0 \text{ mL L}^{-1}$ , which resembles the concentration at the end of the batch process was measured as triplicate. The measurement setup is depicted in figure 3.5 (A). Approximately 10 mL of the sample was filled in a cleansed cylindrical glass bowl. The density of the sample was measured gravimetrically in advance. A capillary was positioned in 2 mm distance to the liquid surface of the sample. A magnetic stirrer prevented the accumulation of surface active material at the liquid surface prior to the mea-

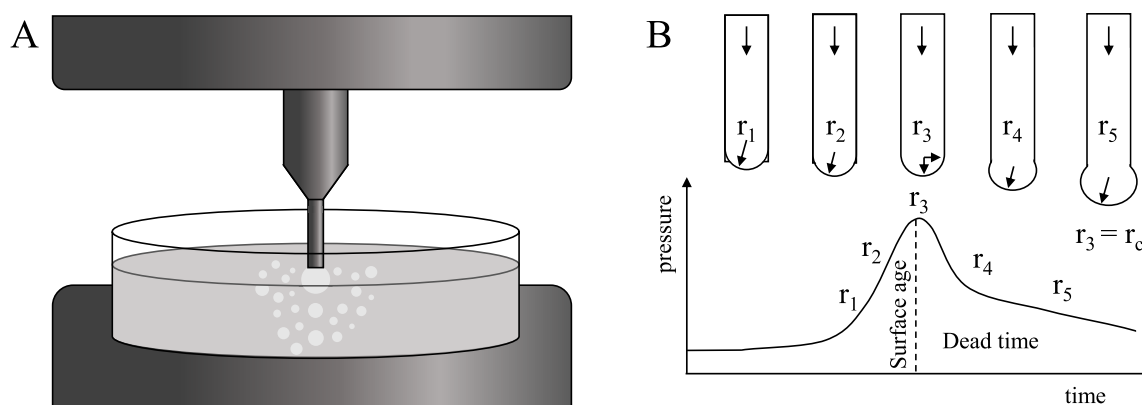


**Figure 3.5: Principle of the bubble pressure method.** Dynamic surface tension measurement. (A) Measurement setup. (B) Principle of the measurement. Pressure characteristics dependent on curvature radius ( $r_1 - r_5$ ) or surface age. Capillary radius is indicated as  $r_c$ . Figure modified to (Fainerman et al., 2004).

surement. The measurement started by immersing the capillary in the liquid. Bubbles were formed by the airflow through the capillary. Figure 3.5 (B) shows schematically the principle of the measurement. The internal pressure of a bubble forming at a capillary depends on the radius of the curvature  $r$  and the surface tension  $\sigma$  according to the Young Laplace equation. The radius of a forming bubble first decreases until it equals the radius of the capillary ( $r_3 = r_c$ ), before it increases again. At this point the internal pressure maximum is reached and with a known capillary radius the surface tension can be determined according to:

$$\sigma = \frac{(p_{\max} - p_0) r}{2} \quad (3.12)$$

with  $p_{\max}$  being the pressure at  $r = r_c$  and  $p_0$  as hydrostatic pressure. The surface tension is thereby coupled to a specific surface age, the time until  $p_{\max}$  is reached. By varying the speed to form the bubble, the surface tension can be expressed as a function of surface age. In this case the radius of the capillary was determined by a reference measurement with water.

### 3.2.4.6 Fluorescence microscopy

Freezing and thawing might damage the bacterial cell, leading to cell burst and DNA leakage. DNA is highly viscous and changes the viscosity of the broth. To exclude viscosity increase due to the sampling procedure, fluorescence microscopy was performed after samples were frozen and thawed. In short, biosuspension was centrifuged at 20 000 g and 4 °C for 4 min and washed in PBS after sampling. The pellet was first frozen in liquid nitrogen and then thawed on ice. Staining buffer was added (see 3.2.1.3), samples were incubated for 10 min in a dark room and subsequent microscopied.

### 3.2.4.7 Calculation of cell specific rates

Due to the constant volume of the batch fermentation the biomass concentration  $c_X$  can be expressed by the biomass mass balance after rearranging according to:

$$\frac{dc_X}{dt} = \mu c_X \quad (3.13)$$

with  $\mu$  as specific growth rate in ( $\text{h}^{-1}$ ). The maximal growth rate  $\mu_{\max}$  for the exponential growth phase can be obtained by linear regression:

$$\mu = \ln \left( \frac{c_{X,1}}{c_{X,0}} \right) \frac{1}{t_1 - t_0} \quad (3.14)$$

Similar to the biomass, the substrate concentration  $c_S$  can be expressed by the substrate mass balance according to :

$$\frac{dc_S}{dt} = -q_S c_S \quad (3.15)$$

with  $q_S$  as specific substrate consumption rate and can be calculated by equation 3.16. The biomass per substrate yield  $Y_{XS}$  is defined as:

$$Y_{XS} = \frac{\mu}{q_S} \quad (3.16)$$

and can be determined by linear regression according to:

$$Y_{XS} = \left( \frac{c_{X,1} - c_{X,0}}{c_{S,0} - c_{S,1}} \right) \quad (3.17)$$

For the oxygen mass balance applies by rearranging equation 3.4 :

$$\frac{dc_{O_2,L}}{dt} = k_L a \Delta c_{O_2,m} - Q_{O_2} \quad (3.18)$$

with the specific oxygen uptake rate  $q_{O_2} = \frac{Q_{O_2}}{c_X}$  follows for the biomass oxygen yield  $Y_{XO_2}$ :

$$Y_{XO_2} = \frac{\mu}{q_{O_2}} \quad (3.19)$$

Equivalent to oxygen, carbon dioxide mass balance can be rearranged and volumetric carbon dioxide emission rate  $Q_{CO_2}$  can be formulated as:

$$Q_{CO_2} = \frac{p \dot{V}_{g,in}}{V_L R T} \left( y_{CO_2}^{out} \frac{1 - y_{O_2}^{in} - y_{CO_2}^{in}}{1 - y_{O_2}^{out} - y_{CO_2}^{out}} - y_{CO_2}^{in} \right) \quad (3.20)$$

where the specific carbon dioxide rate is defined as  $q_{CO_2} = \frac{Q_{CO_2}}{c_X}$ .

An elemental carbon balance was performed in order to verify the consistency of the obtained experimental data and calculated rates. A simple black box model is set up with glucose being the sole carbon source and biomass and CO<sub>2</sub> as products.

$$c_{\text{glucose}} = c_{\text{biomass}} + c_{\text{CO}_2} \quad (3.21)$$

Furthermore the formation of by-products can be controlled by checking for uncovered carbon use. In- and out-flowing compounds were converted to  $C - mol$ .

### 3.3 Results and discussion

A batch fermentation with *C. glutamicum* was conducted to obtain cell specific rates and physical properties of the broth. The determined parameter serve for later parametrisation of numerical simulations.

#### 3.3.1 Process kinetics

To characterise the growth behaviour of *C. glutamicum* WT, a batch fermentation with glucose in CGXII media (see table 3.2) was carried out as triplicate (B1, B2, B3). The time course of biomass and glucose concentration for all three batch fermentations is displayed in figure 3.6, showing no significant differences. Concentrations are based on OD<sub>600</sub>-CDW correlation which resulted in a correlation factor  $\lambda_{\text{OD}} = 0.2669 \pm 0.0027$ . Hereby, B2 was excluded because of a measurement error in CDW determination. This factor is in fair agreement with Buchholz et al. (2013). Initial biomass concentration was about  $c_X = 0.246 \pm 0.014 \text{ g L}^{-1}$ . After a lag phase of approximately 3 h, cells grew exponentially until reaching stationary phase at 11 h. On average, a final biomass of  $c_X = 18.44 \pm 0.76 \text{ g L}^{-1}$  was reached. Glucose concentrations were determined by an enzymatic assay, considering a calibration curve. Initial glucose concentration was  $c_S = 41.66 \pm 0.72 \text{ g L}^{-1}$ . Glucose depletion occurred between 11 - 12 h, the end of the fermentation process.

Exponential growth rates were determined with  $\mu = 0.441 \pm 0.019 \text{ h}^{-1}$ , which are very similar to exponential growth rates by Buchholz et al. (2013). Biomass substrate yield resulted in  $Y_{\text{XS}} = 0.474 \pm 0.012 \text{ g}_{\text{CDW}} \text{ g}_S^{-1}$ , which is in good comparison to Buchholz et al. (2014b).

The pH was controlled to pH = 7.4 and the dissolved oxygen was controlled to be higher than 30 %. Because of increasing biomass and thereby elevated oxygen demand, the agitation rate was increased throughout the process to keep the dissolved oxygen above 30 %. If the system becomes more turbulent, bubble breakup is enhanced leading to an increased interphase exchange area. This

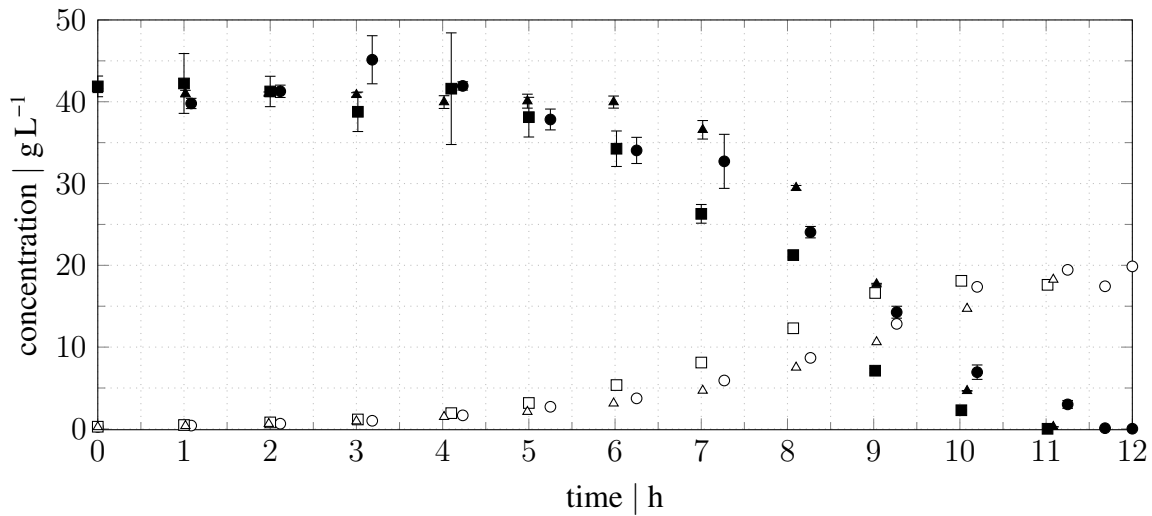


**Figure 3.6: Time course of  $c_X$  and  $c_S$ .** Biomass concentration  $c_X$  for B1 ( $\circ$ ), B2 ( $\square$ ) and B3 ( $\triangle$ ). Respective substrate  $c_S$  concentration are B1 ( $\bullet$ ), B2 ( $\blacksquare$ ) and B3 ( $\blacktriangle$ ).

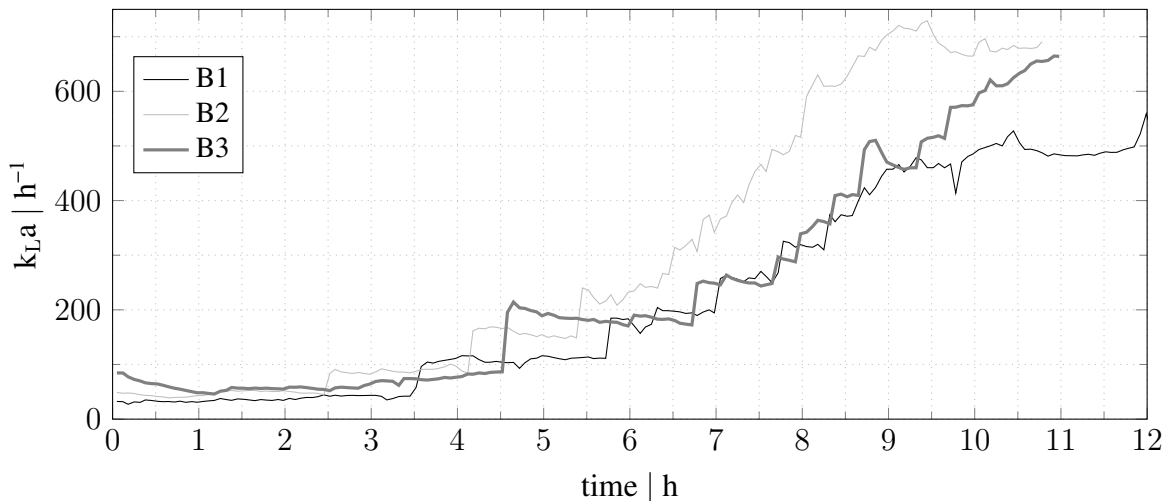


**Figure 3.7: Time course of  $k_L a$ .** The  $k_L a$  value for the three batch fermentations (B1, B2, B3) is shown for the whole process time.

is directly coupled to higher mass transfer coefficients. The  $k_L a$  values of the three fermentations as function of the process duration are shown in figure 3.7. On average  $k_L a$  values are about  $44 \text{ h}^{-1}$  at process start. Maximal values of  $600 - 700 \text{ h}^{-1}$  are reached at about 9 h. Afterwards glucose is depleted and the biomass concentration, agitation and consequently  $k_L a$  stay constant.

The biomass oxygen yield for the exponential phase was calculated with  $Y_{XO_2} = 0.043 \pm 0.0072 \text{ g}_{\text{CDW}} \text{ mmol}_{\text{O}_2}^{-1}$ . With a specific oxygen uptake rate of  $q_{O_2} = 10.16 \pm 0.929 \text{ mmol}_{\text{O}_2} \text{ g}_{\text{CDW}}^{-1} \text{ h}^{-1}$  and a specific carbon dioxide emission rate  $q_{\text{CO}_2} = 9.3 \pm 1.23 \text{ mmol}_{\text{O}_2} \text{ g}_{\text{CDW}}^{-1} \text{ h}^{-1}$  the respiratory quotient  $\text{RQ} = \frac{q_{\text{CO}_2}}{q_{\text{O}_2}}$  is close to the theoretical value of 1.0.

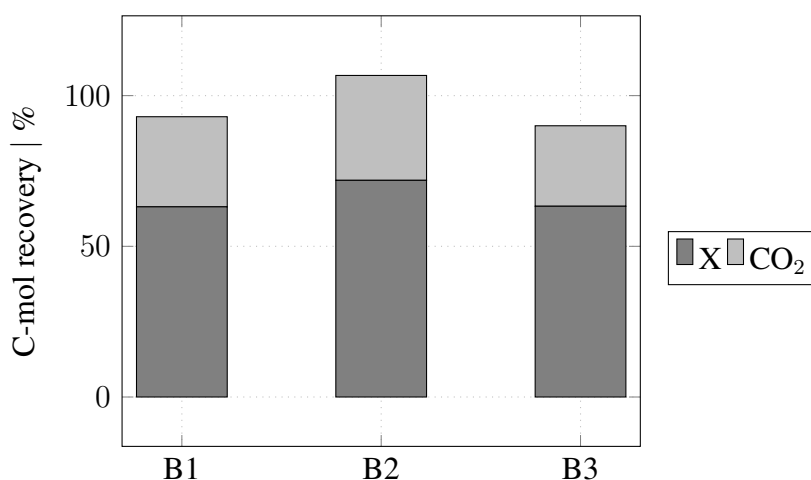


**Figure 3.8: Elemental carbon balance of the exponential phase.** The biomass (X) and carbon dioxide (CO<sub>2</sub>) content in C-mol recovery is shown as stacked bar plot for all three fermentation processes (B1, B2, B3).

The elemental carbon balance of the exponential phase is displayed in figure 3.8. Balances were calculated on basis of glucose as sole carbon source. The biomass content is shown in dark grey and the carbon dioxide content in light grey. In general, all three batches show similar results. The balance for the first process adds up to 93 %, the second up to 107 % and the third up to 90 % with a ratio of 2:1 for biomass compared to CO<sub>2</sub>. As high gassing rates used for this experiment led to stripping of CO<sub>2</sub>, the measurement of total inorganic carbon was not performed (Buchholz et al., 2014a). Considering that measurement inaccuracy of biomass and glucose measurements are likely to occur, a deviation of maximal 10 % is acceptable. Therefore, the consistency of the data and the determined rates was assumed. Furthermore, the formation of relevant amounts of by-product can be excluded Blombach et al. (2013) and Buchholz et al. (2014a).

### 3.3.2 Determination of broth viscosity

Prerequisite of viscosity measurements is, that cells stay intact during sampling and measurement procedure. If cells are disrupted, DNA will leak from the cell and modify the viscosity of the broth. Therefore, prior to viscosity measurements cells were stained with 4',6-diamidino-2'-phenylindole (DAPI) as explained in section 3.2.4.6 and examined via fluorescence microscopy. Figure 3.9 shows different samples of DAPI stained cells of *C. glutamicum* in the fermentation broth. As the DNA is still located within the cells, it was concluded, that the sampling and measurement procedure did not influence the cell structure. Therefore, an increase of viscosity due to DNA leakage after sampling was excluded. The viscosity of the broth containing different biomass concentrations was measured with a rheometer. Calibration was performed with water at different temperatures resulting in a correction factor of 1.9. The results of viscosity measurement serve for later parametrisation of the numerical flow simulations. However, those simulations are only

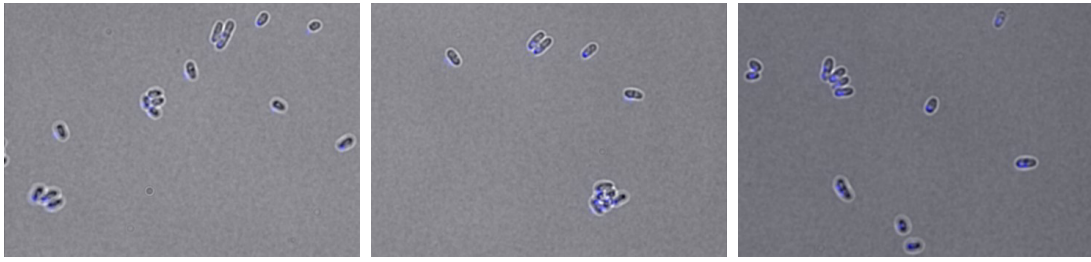


**Figure 3.9: Fluorescence microscopy of viscosity samples.** Viscosity samples were frozen and subsequently thawed on ice. The DAPI coloured DNA (blue) is located within the cells which shows that cells are still intact.

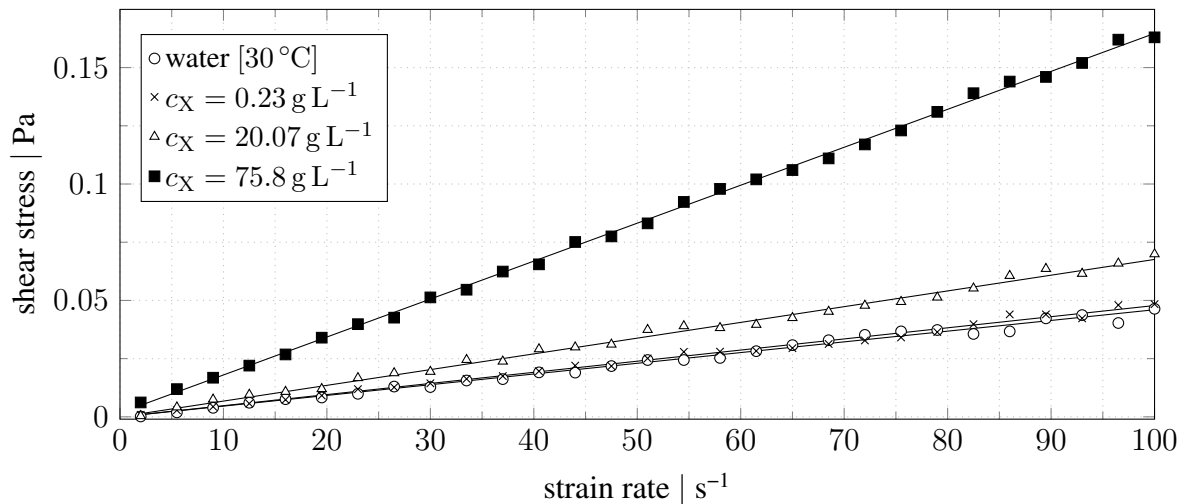


**Figure 3.10: Newtonian fluids.** Shear stress as function of the strain rate for water and different biomass concentrations. A linear correlation indicates a Newtonian fluid. Goodness for all fits was not less than  $R^2 = 0.99$ .

valid for Newtonian fluids if no other functions are implemented. Therefore, first it was tested if the broth was still a Newtonian fluid like water. Figure 3.10 shows the shear stress as function of the shear rate for water at 30 °C and different biomass concentrations at 30 °C. Because only  $c_X \approx 20 \text{ g L}^{-1}$  could be obtained by the batch fermentations, biomass of B3 was concentrated and resuspended in defined volumes of 0.9 % ( $\text{w v}^{-1}$ ) NaCl solution to obtain higher biomass concentrations. As indicated in section 3.2.4.4 Newtonian fluids have the property that the shear stress is proportional to the strain rate with the dynamic viscosity  $\eta$  as factor of proportionality. All samples in figure 3.10 exhibit a linear viscous behaviour, concluding that in case of *C. glutamicum* higher biomass concentration do not change the rheology.

To examine if the viscosity of the broth is influenced by increasing biomass concentrations, the viscosity of the broth was measured at different stages of the fermentation process. Figure 3.11 depicts the viscosity as function of the biomass concentration for the batch triplicates (B1, B2, B3). At fermentation start the viscosity is similar to water at 30 °C (0.0008 Pa s). The viscosity increases with increasing biomass concentration within the fermentation broth up to 0.0016 Pa s (B1). This lies in a similar range as reported by García-Ochoa & Gómez (2005) for *Candida bombicola*. The

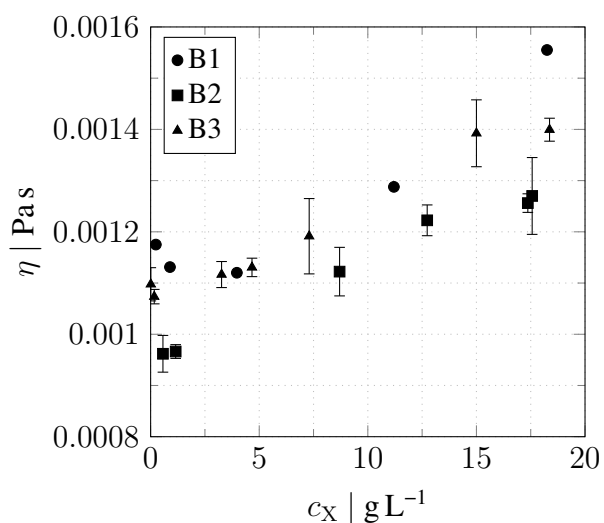


**Figure 3.11: Viscosity of the broth.** Viscosity of the three batch fermentations (B1, B2, B3) is shown as function of the biomass concentration  $c_X$  at 30 °C.

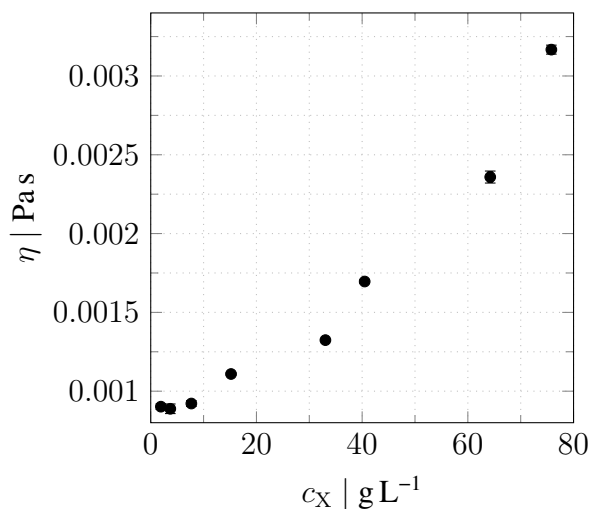


**Figure 3.12: Viscosity of different biomass concentrations.** Viscosity is shown as function of different biomass concentrations  $c_X$ . Biomass of B3 was concentrated and resuspended in NaCl to examine the influence of higher cell densities at 30 °C.

influence of higher biomass concentrations up to 80  $\text{g L}^{-1}$  on the viscosity at 30 °C is shown in figure 3.12. For low values of  $c_X$  of up to 20  $\text{g L}^{-1}$  reached in the fermentation, the viscosity does not differ from water at 30 °C. The viscosity increases steadily with increasing biomass and reaches a value of 0.003 Pa s for the maximal tested biomass concentration. While 80  $\text{g L}^{-1}$  reflects a very high concentration for a fermentation process, a viscosity of 0.003 Pa s equals the viscosity of milk at room temperature. Moreover, in the later chapters a numerical simulation of a fermentation process containing  $c_X \approx 35 \text{ g L}^{-1}$  is examined, which results in a viscosity of 0.001 25 Pa s, which is not more than water at 10 °C. Therefore, the influence of viscosity of a fermentation process of *C. glutamicum* on numerical simulation was neglected.

### 3.3.3 Determination of broth surface tension

The surface tension was measured with the static and the dynamic method as described in section 3.2.4.5. The static method was used to examine if the broth or high biomass concentrations influence the surface tension. The dynamic method was only applied for different antifoam concentrations to assess the dependency of surface age on the surface tension of the solution.

Results of the fermentation broth measured by the static method for all three batch fermentations are displayed in figure 3.13. Prior to the measurement, the density of the broth was determined gravimetrically to be  $1016 \pm 5.4 \text{ g L}^{-1}$  which is similar to water. As a batch fermentation was

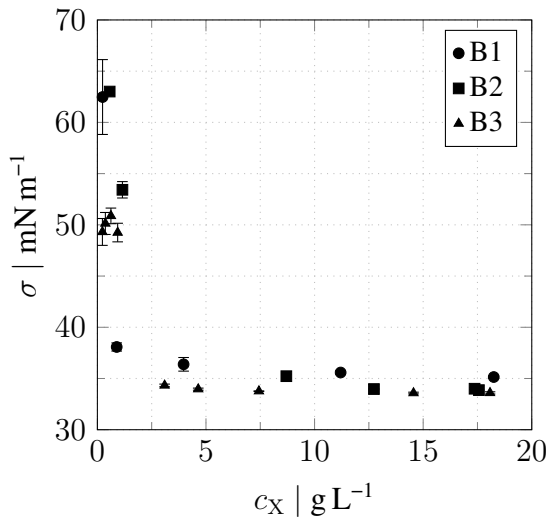


**Figure 3.13: Surface tension of the broth.** Surface tension of the three batch fermentations (B1, B2, B3) is shown as function of the biomass concentration  $c_X$  at 30 °C.

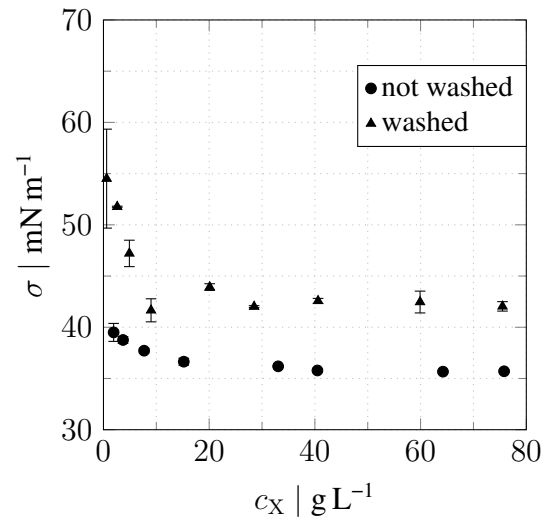


**Figure 3.14: Surface tension as function of biomass.** Surface tension of different biomass concentrations  $c_X$  is shown. Biomass was concentrated and resuspended in NaCl (not washed). An additional washing step was included to lower the antifoam concentration (washed).

conducted, the density did barely change for the complete process duration. Subsequent to the process start a surface tension of  $62.74 \pm 0.267 \text{ mN m}^{-1}$  was measured. This value is a bit smaller than the surface tension for water at 30 °C or CGXII media at 30 °C ( $71.85 \pm 0.275 \text{ mN m}^{-1}$ ). For longer process durations and thereby increasing biomass concentrations the surface tension dropped strongly and converged to a value of  $35 \text{ mN m}^{-1}$ . The biomass at the end of the process was concentrated and resuspended in defined volumes of 0.9 % ( $\text{w v}^{-1}$ ) NaCl solution. Figure 3.14 shows, that a biomass concentrations of  $80 \text{ g L}^{-1}$  also resulted in the same final value of  $35 \text{ mN m}^{-1}$  for the surface tension (not washed). Surprisingly, even smallest concentrations of biomass show a surface tension of  $\approx 40 \text{ mN m}^{-1}$ . Thus, the biomass concentration might have a negligible influence on the surface tension and other surface active agents like base or antifoam, which showed steadily increasing concentration with increasing process time, caused the drop in surface tension. This could explain the rapid drop of surface tension in figure 3.13. Because samples for the measurement in NaCl solution, displayed in figure 3.14 (not washed), were concentrated from biomass at process end, residual antifoam was still attached to the bacterial cells. To reduce the influence of agents, samples were washed in water and measured again (see figure 3.14 washed). It is clearly visible, that especially for low biomass concentrations the surface tension was significantly higher after the washing step, confirming the previously made assumptions. To search for the main contributor to surface tension reduction, different antifoam concentrations in water were measured. As displayed in figure 3.15, already smallest concentrations of  $0.01 \text{ mL L}^{-1}$  induce a drop in surface tension of  $30 \text{ mN m}^{-1}$  compared to water. Higher concentrations converge to the a value of  $33 \text{ mN m}^{-1}$ .

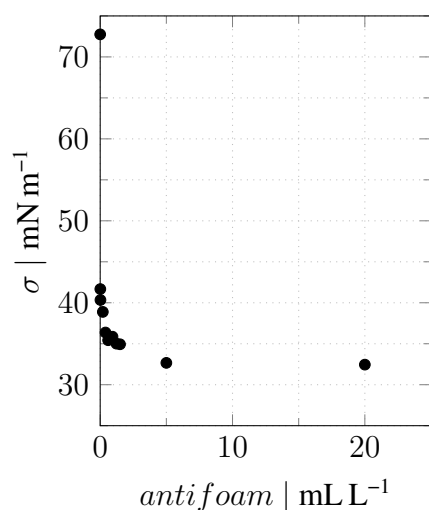


**Figure 3.15: Surface tension of antifoam solutions (static method).** The surface tension of different concentrations of antifoam (Struktol® J 647) was measured.

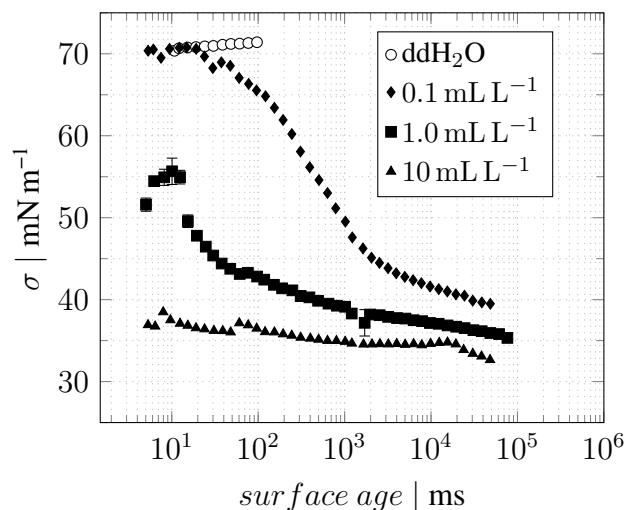


**Figure 3.16: Surface tension of antifoam solutions (dynamic method).** The surface tension of different concentrations of antifoam (Struktol® J 647) was measured.

Accordingly, it was concluded that the influence of biomass on the surface tension is negligible and already smallest concentration of antifoam affect the surface tension of the broth.

Nevertheless, with the static method, only the surface tension of the thermodynamic equilibrium can be determined. In essence, this implies that the interfacial area has to exist long enough until the surface concentration of the surfactant is equal to the concentration in the volume phase. However, the residence time of a bubble within the reactor is limited and depends on the bubble rise velocity, which is about  $0.25 \text{ m s}^{-1}$  in bubble columns (Heijnen & van't Riet, 1984). Considering a velocity reduction of  $\approx 35\text{-}50\%$  in the turbulent flow field of a stirred tank and assuming a reactor height of  $0.5\text{-}5 \text{ m}$ , dwelling times lie between  $3\text{-}40 \text{ s}$ , depending on the agitation rate (Poorte & Biesheuvel, 2002; Alves et al., 2004). In order to assess the influence of surface age on surface tension, a dynamic surface tension measurement was performed with a bubble pressure tensiometer. The results of the measurement are depicted in figure 3.16. Water at  $30^\circ\text{C}$  served as reference, resulting in  $\sigma \approx 71 \text{ mN m}^{-1}$  independent of the surface age. With  $\approx 70 \text{ mN m}^{-1}$  the surface tension for the smallest concentration of antifoam ( $0.1 \text{ mL L}^{-1}$ ) was similar to water within the first  $23 \text{ ms}$ . For longer surface ages of  $48 \text{ s}$  the surface tension decreased slowly to  $40 \text{ mN m}^{-1}$ . The measurement was stopped at this point. Due to the continuous accumulation of alkoxyated fatty acid originating from the antifoam at the interfacial area, the surface tension was reduced. Higher antifoam concentrations ( $1.0 \text{ mL L}^{-1}$ ) already lowered the surface tension to  $\approx 55 \text{ mN m}^{-1}$  for the first measurement point at  $5 \text{ ms}$ . Subsequent to a sharp drop at  $15\text{-}40 \text{ ms}$  the surface tension converged slowly and reached  $31 \text{ mN m}^{-1}$  after more than  $70 \text{ s}$ . The surface tension of a solution containing  $10 \text{ mL L}^{-1}$  was already reduced to  $37 \text{ mN m}^{-1}$  at measurement start. It converged to  $32 \text{ mN m}^{-1}$  after  $48 \text{ s}$  where the measurement was stopped. Consequently, the higher the initial

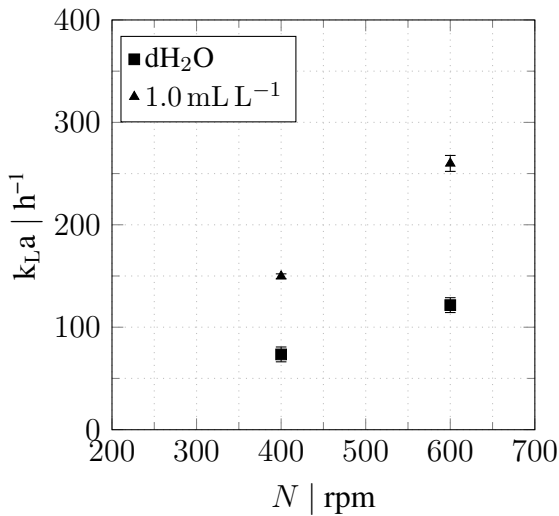


**Figure 3.17: Influence of antifoam on  $k_{L,a}$  values (lab scale).** The  $k_{L,a}$  is shown as function of the agitation rate  $N$  for water and an aqueous solution containing 1.0 mL Struktol® J 647. Measured at 0.5 vvm.

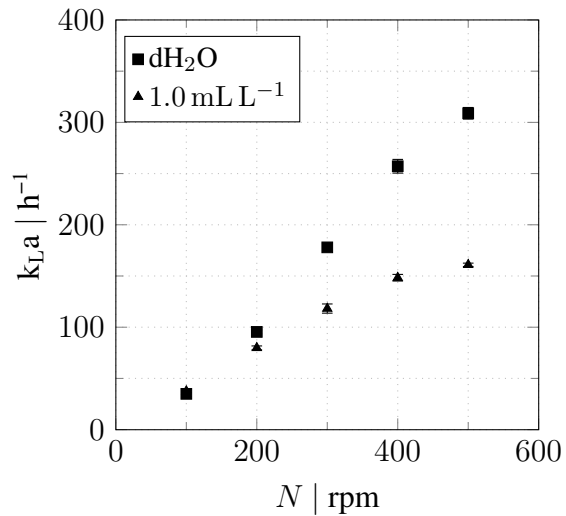


**Figure 3.18: Influence of antifoam on  $k_{L,a}$  values (pilot scale).** The  $k_{L,a}$  is shown as function of the agitation rate  $N$  for water and an aqueous solution containing 1.0 mL Struktol® J 647. Measured at 0.5 vvm.

antifoam concentration, the faster the interfacial area is covered with surfactant molecules which lowers the surface tension. The examined pilot scale bioreactor in the following chapter was operated with an antifoam concentration of 1.0 mL L<sup>-1</sup> at process end. With a gas velocity of  $\approx 0.15 \text{ m s}^{-1}$  average dwelling times of bubbles are about 7 s. So the surface tension of the broth influences bubble behaviour to some extent, as the value is reduced by almost 50% compared to pure media. According to most breakage models, a lower surface tension enhances bubble breakup (Kálal et al., 2014). Moreover, enhanced bubble breakup leads to the formation of smaller bubbles and thereby an increased interfacial area which is beneficial for species mass transfer between gas and liquid phase. To examine the effect of antifoam on volumetric oxygen mass transfer,  $k_{L,a}$  values for lab (2.5 L) and pilot scale (200 L) were measured. Figure 3.17 and 3.18 present a comparison between lab and pilot scale. While the addition of antifoam increased the  $k_{L,a}$  values in lab scale, it clearly showed a negative effect on  $k_{L,a}$  values in pilot scale. Both reactors had a similar  $H_L/T_D$  and  $T_D/D_I$  ratio and impeller spacing. However, they differ in the flow regimes for the current operational conditions. As a decreased surface tension is beneficial for bubble breakup but limits coalescence, the results for the pilot scale reactor are contradictory. Therefore, the sole assumption that antifoam only affects the surface tension might be too simple. Maia et al. (1999) reported similar contradictory results for various agitation and gassing rates leading to the assumption that beneath a positive effect on  $k_{L,a}$  values due to reduction of surface tension, coalescence is also enhanced and surface mobility is inhibited by antifoam leading in turn to a reduction of oxygen mass transfer rate. Hydrodynamic change by suppression of surface mobility as well as interfacial blockage by increasing mass transfer resistance was also reported by Kawase & Moo-Young (1990) and Yagi & Yoshida (1974). Additionally, different antifoam agents create different

effects (Benedek & Heideger, 1971; Schügerl et al., 1978). In the current pilot scale reactor setup coalescence effects are stronger compared to the lab scale reactor. The coalescence enhancing effect of antifoam might predominate over other effects in pilot scale leading to smaller  $k_L a$  values. However, a thorough analysis is needed to quantitatively describe mass transfer dependency on antifoam addition. Because of this ambivalent behaviour the reduction in surface tension due to antifoam addition was not included in numerical simulations.

### 3.4 Conclusion

A batch fermentation of *C. glutamicum* has been conducted to derive cell specific parameters and physical properties of the broth for later parametrisation of numerical simulations. The maximal growth rate during exponential growth phase was determined to be  $\mu_{\max} = 0.441 \pm 0.019 \text{ h}^{-1}$  and the biomass substrate yield  $Y_{XS} = 0.474 \pm 0.012 \text{ g}_{\text{CDW}} \text{ g}_{\text{S}}^{-1}$ . The oxygen balance resulted in a biomass oxygen yield of  $Y_{\text{XO}_2} = 0.043 \pm 0.0072 \text{ g}_{\text{CDW}} \text{ mmol}_{\text{O}_2}^{-1}$ . Thereby, the cell specific oxygen uptake rate of  $q_{\text{O}_2} = 10.16 \pm 0.929 \text{ mmol}_{\text{O}_2} \text{ g}_{\text{CDW}}^{-1} \text{ h}^{-1}$  was derived and the cell specific carbon dioxide emission rate  $q_{\text{CO}_2} = 9.3 \pm 1.23 \text{ mmol}_{\text{CO}_2} \text{ g}_{\text{CDW}}^{-1} \text{ h}^{-1}$  was calculated from the carbon dioxide balance. Accordingly, the respiratory quotient was obtained by  $RQ = \frac{q_{\text{CO}_2}}{q_{\text{O}_2}}$  and is close to the theoretical value of 1.0. The accuracy of the rates were furthermore confirmed by a nearly closed C-balance, which also excluded the formation of by-products.

Furthermore, physical properties of the broth were examined. The density of the broth was determined to be  $1016 \pm 5.4 \text{ g L}^{-1}$  and stayed constant during the process. With increasing biomass the viscosity increased to a value of  $0.0016 \text{ Pa s}$  at  $c_X \approx 20 \text{ g L}^{-1}$ . To obtain higher biomass concentrations, biomass was concentrated and resuspended in  $0.9 \%$  (w v<sup>-1</sup>) NaCl solution leading to a viscosity of  $0.003 \text{ Pa s}$  at  $c_X \approx 80 \text{ g L}^{-1}$ . In the later chapters a fermentation process containing  $c_X \approx 35 \text{ g L}^{-1}$  is examined by numerical simulation, which results in a viscosity of about  $0.00125 \text{ Pa s}$  which is not more than water at  $10^\circ\text{C}$ . Due to only slight increases, the influence of viscosity change within a fermentation process of *C. glutamicum* on numerical simulation will be neglected. The surface tension of the broth was found to be almost independent on the biomass concentration but was dominated by the addition of smallest amounts of antifoaming agents. At thermodynamic equilibrium, the surface tension was thereby reduced to  $35 \text{ mN m}^{-1}$  from initial  $71 \text{ mN m}^{-1}$ . Dynamic surface tension measurement revealed that the surface tension at surface ages  $> 20 \text{ ms}$  were influenced by antifoaming agents of  $0.1 \text{ mL L}^{-1}$  whereas higher concentrations  $> 1.0 \text{ mL L}^{-1}$  already showed a reduction in surface tension at measurement start. However,  $k_L a$  measurements showed that the sole simplification of the impact of antifoam to a reduction of surface tension is invalid and a thorough analysis is needed to quantify these effects.

---

## 4 Characterisation of a pilot scale bioreactor

Maintaining process performances during scale-up is not an easy task, especially for aerated systems. The transition from laboratory to a full scale production facility is usually hampered due to limited mixing and mass transfer. Only few correlations exist to estimate physical parameters in gassed systems. Besides, their validity is restricted to specific reactor geometries and operating regimes. In the recent years, CFD gain momentum for such predictions especially to provide detailed information on environmental conditions inside a fermenter. However, two phase flow simulations are complex and current approaches published in literature are mostly not validated by experimental data. In this study, a 300 L pilot scale reactor has been characterised experimentally to find best operating conditions within a loading regime. First, single phase (SP) simulations were conducted to test the reactor setup and to determine an appropriate range of grid size. A thorough multiphase study (MP) followed, which showed, that higher grid resolution for MP is needed. Due to considerable computational costs, grid dependence of the turbulent dissipation rate was reduced by introducing a scaling factor in breakage, coalescence, drag and mass transfer functions. Amongst several models for the description of the latter, a suitable approach was implemented resulting in very good agreement with experimental data. Even the coarsest resolution with  $1.12 \cdot 10^5 \text{ \#}/m^3$  was sufficient enough to display the experimental data.

### 4.1 Introduction

False assumptions during scale-up may be costly in terms of diminished yields and productivities. First of all, the correct determination of physical parameters is required. Among these are the volume specific power input, oxygen transfer coefficient, gas hold-up and mixing time. These can be estimated by correlations predicting mean values for distinct reactor setups (Moucha et al., 2003; Van'T Riet, 1979; Vasconcelos et al., 1995). Albeit, resolving local differences can not be accomplished. By contrast, the use of CFD allows the prediction of these parameters without neglecting local differences within the bioreactor. However, only few multiphase studies exist. On the one hand, the validity of several multiphase models has never been proven due to the lack of experimental data. While the experimental effort to determine global parameters in large scale is immense, achieving local resolutions is almost impossible. However, prerequisite of correct determination of local parameters by CFD is the validation of global values. On the other hand,

the complexity of the interactions between the phases in aerated tanks makes it difficult to describe the dynamic behaviour of multiphase systems. Fundamental problems need to be tackled. An extensive evaluation of simulation strategies for two phase flows is given in chapter 2.4.4.

In this study, a multi-impeller pilot scale bioreactor is characterised to find suitable operating conditions considering gassing and mixing to display a late fed-batch process of a *C. glutamicum* culture. By using CFD, first a single phase study is conducted to evaluate reactor setup and necessary grid resolution. Subsequently, the two phase flow within the stirred tank is simulated, process relevant parameters are validated experimentally and the influence of grid size is investigated also for multiphase. Additionally, a novel approach of scaling turbulent dissipation rate is used to reduce the effect of discretisation scheme and grid size on the simulation output.

## 4.2 Experimental measurements

### 4.2.1 Bioreactor setup

Measurements were performed in a pilot scale multi impeller stirred bioreactor with a reaction volume of 200 L. The tank was equipped with four baffles and three Rushton turbines. All geometric measures are displayed in figure 4.1 and table 4.1. For gassed experiments air was introduced through a ring sparger. Experiments were carried out in deionised water with the properties listed in table 4.1. For better comparison the density and viscosity were chosen similar to water, as measurements of the broth in the previous chapter resulted in no significant difference. Because of the ambivalent behaviour of antifoaming agents the influence on surface tension was neglected as discussed before.

### 4.2.2 Power consumption

The total value of power input was measured by electrical measurement method performed directly in the motor by an inhouse made wattmeter with the digital control instrument SP670 (Schwille Elektronik, Germany). The power draw  $P$  for the direct current motor can be obtained by:

$$P = U I \quad (4.1)$$

where  $U$  is the supplied voltage and  $I$  the current intensity. The LabView software (National Instruments, USA) was used for data acquisition and impeller speed controlling. To account for the actual power consumption, power due to losses must be considered. Energy losses of the agitation system measured only in air were therefore subtracted from the measurements with fluid.

Measurements were carried out for several agitation speeds (100 rpm - 500 rpm) and gassing rates (0 vvm, 0.25 vvm, 0.5 vvm, 1 vvm). The sampling rate was set to 10 kHz. The average of 1000 samples was taken to record the signal every 100 ms for a duration of 15 min. The mean power draw from the recorded signal was then taken for further analysis.

### 4.2.3 Mixing time

Mixing time was determined by pulse-response experiments. The tracer solution (75 ml of a 6 M di-potassium phosphate,  $K_2HPO_4$ ) solution was injected into the bioreactor containing deionised water ( $dH_2O$ ) at a height of  $\approx 0.5$  m. A pressure of 6 bar was used to inject the tracer within 25 ms (Buchholz et al., 2014b). The response curves of various reactor conditions (agitation speed: 100 rpm - 500 rpm and gassing rate: 0 vvm, 0.25 vvm, 0.5 vvm, 1 vvm) were recorded with conductometers (LF 521, Wissenschaftlich-Technische Werkstätten GmbH, Germany) at a fixed temperature of 30 °C. Starting from a nonhomogeneous state, mixing time  $\tau_{95}$  is defined as the time reaching 95 % homogeneity. The normalized tracer concentration  $c_t/\bar{c}_t$  with  $\bar{c}_t$  as vessel average is then between 0.95 and 1.05. Average mixing times were derived from triplicates of each experimental condition.

### 4.2.4 Gas hold-up

Gas hold-up was measured with a self constructed ultrasonic device consisting of an ultrasonic probe (HC-SR04 Distance Sensor Module, Aukru, China) which was connected to an Arduino Board (Nano V3, Arduino, Italien) containing a microcontroller (ATmega328, Arduino, Italien). The probe was installed at the top of the reactor. Distance to the liquid surface of the non-agitated and non-gassed reactor served as reference state which was less than 50 mm. Gas hold-up was measured for several agitation speeds (100 rpm - 500 rpm) and gassing rates (0 vvm, 0.25 vvm, 0.5 vvm, 1 vvm) by recording the change of the liquid height at 30 °C. The signal was recorded for 5 min with a sampling rate of 10 s<sup>-1</sup>.

### 4.2.5 Measurement of $k_L a$

The volumetric mass transfer coefficient  $k_L a$  was measured with the dynamic gassing out method as previously described in chapter 3.2.4.3. Measurements were performed in deionised water at several agitation speeds (100 rpm - 500 rpm) and gassing rates (0 vvm, 0.25 vvm, 0.5 vvm, 1 vvm). Each operation condition was measured as triplicate at 30 °C.

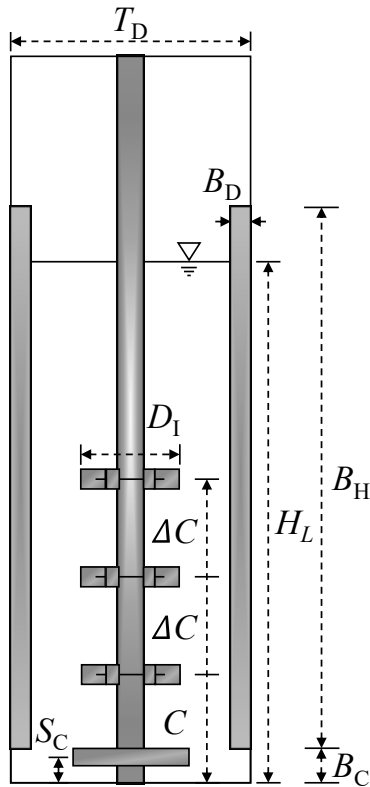


**Figure 4.1: Pilot scale reactor geometry.** Tank was equipped with four baffles and three Rushton turbines. Liquid filling height is marked with a triangle.

**Table 4.1: Pilot scale geometry, operational conditions and media properties.** The tank was operated at varies agitation and gassing rates. Measures are displayed in figure 4.1. Subscripts L and G stand for liquid and gas, respectively.

Description	Symbol	Unit	
Tank height (liquid level)	$H_L$	1.06	m
Tank diameter	$T_D$	0.488	m
Impeller diameter	$D_I$	0.2	m
Off-bottom impeller clearance	$C$	0.22	m
Impeller spacing	$\Delta C$	0.21	m
Baffle length	$B_H$	1.1	m
Baffle diameter	$B_D$	0.04	m
Off-bottom baffle clearance	$B_C$	0.07	m
Off-bottom sparger clearance	$S_C$	0.056	m
Media density	$\rho_L$	995.7	$\text{kg m}^{-3}$
Media viscosity	$\eta_L$	0.0008	Pa s
Media surface tension	$\sigma_L$	0.0712	$\text{N m}^{-1}$
Gas density (air)	$\rho_G$	1.1	$\text{kg m}^{-3}$
Temperature	$\vartheta$	30	$^{\circ}\text{C}$
Agitation rate	$N$	100 - 500	rpm
Gassing rate	$Q_g$	0 - 1	vvm

## 4.3 Numerical simulations

### 4.3.1 General setup

Details of the geometry as well as operating conditions and liquid properties are given in 4.2.1. Baffles and blades were assumed as zero-thickness walls. Structured hexahedral meshes of the full  $2\pi$  three dimensional domain were adopted. Different grid sizes were considered, depending on the simulation setup (see table 4.2, 4.3). Orthogonal quality and aspect ratio were not less than 0.4 or higher than 12 respectively. The multiphase simulation (MP) for mesh 4 (MPM4) was not included in the following results part but was discussed at the end of section 4.4.2.2.

Numerical simulation were conducted with the commercial software ANSYS<sup>®</sup> Fluent 18.1 using the realizable  $k-\varepsilon$  (RKE) RANS turbulence model and MRF to account for agitation. Simulations were carried out on 4 cores (Intel<sup>®</sup> Core<sup>™</sup> i7) or on 16 cores (Intel<sup>®</sup> Xeon<sup>™</sup> CPU E5-2650 v3). In case of higher mesh densities simulations were run at the bwUniCluster (Intel<sup>®</sup> Xeon<sup>™</sup> E5-2670,

bwUniCluster, Germany), the FORHLR II (Intel® Xeon™ E5-2660 v3 processors, FORHLR II, Germany) or the High-Performance Computing Center Stuttgart (HLRS) (Intel® Xeon™ CPU E5-2680 v3, Cray XC40, High-Performance Computing Center Stuttgart, Germany). All simulations were performed in transient mode with a pressure based solver.

### 4.3.2 Single phase simulations

Spatial discretisation was set to second order upwind scheme for continuity and momentum as well as for  $k$  and  $\varepsilon$  equations in single phase simulations. Standard wall functions were employed. No-slip boundary conditions were applied for all walls except for the top of the reactor, which was set to no-shear to mimic a free surface. Agitation rate was set to  $N = 5 \text{ s}^{-1}$ . Temporal discretisation was second order implicit. Convergence of the flow field was declared when the residuals remained  $< 10^{-5}$  within each time step. In order to reach that criterium, time step size has been varied depending on the mesh density (see table 4.2). Radial velocity, energy dissipation rates, torque and volume integrated energy dissipation rate were averaged for 15 s. To investigate mixing performance a tracer was introduced in the impeller region of the second impeller with equal properties of the bulk fluid. The tracer concentration was recorded at three different vertical positions in the reactor: at the bottom  $P(0 | 0.03 | 0.115)$ , in the middle  $P(0 | 0.518 | 0.115)$  and at the top  $P(0 | 1.06 | 0.115)$ .

**Table 4.2: Setup for Single Phase Simulations.**

Grid size as number of numerical cells per volume for all simulation setup in (single phase (SP)). Agitation speed  $N$  in rounds per second and timestep size  $\Delta t$  in seconds.

Mesh	grid size # $\text{m}^{-3}$	$N$ $\text{s}^{-1}$	$\Delta t$ s
SPM1	8.77E+05	5	0.00500
SPM2	1.76E+06	5	0.00500
SPM3	3.69E+06	5	0.00333
SPM4	1.02E+07	5	0.00050

**Table 4.3: Setup for Multiphase Simulations.**

Grid size as number of numerical cells per volume for all simulation setup in (multiphase (MP)). Agitation speed  $N$  in rounds per second and timestep size  $\Delta t$  in seconds.

Mesh	grid size # $\text{m}^{-3}$	$N$ $\text{s}^{-1}$	$\Delta t$ s
MPM1	1.12E+05	5	0.0050
MPM2	4.53E+05	5	0.0005
MPM3	2.04E+06	5	0.0005
(MPM4)	(4.24E+06)	(5)	(0.0005)

### 4.3.3 Multiphase simulations

Polydispersed multiphase flow was simulated by the Eulerian model including a discrete Population Balance Model (PBM), which allows the prediction of local bubble size distribution (BSD).

The setup is mainly based on Kuschel & Takors (2020) and contained a scaling factor for turbulent dissipation rate  $\varepsilon$  in bubble break up, bubble coalescence, bubble drag and for the calculation of the mass transfer coefficient  $k_L$ . This scaling factor was introduced to overcome the underprediction of turbulent energy dissipation due to insufficient grid resolution. It is based on the assumption, that mixing energy (power calculated from impeller torque  $P_t$  with subscript (t) for torque and gassed power input  $P_{\text{pneum}}$ ) converts to turbulent energy and dissipates to heat in the liquid phase ( $P_\varepsilon$ ). Hence local energy dissipation was linearly scaled to  $\varepsilon_{sc}$  by the factor  $f_{sc}$  described in equation 4.2 resulting in 4.3 introducing the subscript (sc) as scaled quantity.

$$f_{sc} = \frac{P_{\text{total}}}{P_\varepsilon} = \frac{P_{\text{pneum}} + P_t}{P_\varepsilon} \quad (4.2)$$

$$\varepsilon_{sc} = f_{sc} \varepsilon_{\text{local}} \quad (4.3)$$

Hereby,  $P_t$  was calculated according to equation 4.18.  $P_{\text{pneum}}$  and  $P_\varepsilon$  were calculated as follows (Roels & Heijnen, 1980):

$$P_{\text{pneum}} = \Phi_g R T \ln \left( \frac{p_0}{p} \right) \quad (4.4)$$

$$P_\varepsilon = \int \alpha_L \rho_L \varepsilon dV \quad (4.5)$$

with  $\Phi_g$  as molar flow,  $R$  as universal gas constant,  $T$  as temperature,  $p_0$  as standard pressure,  $p$  as actual pressure,  $\alpha_L$  and  $\rho_L$  as liquid volume fraction and density. The agitation rate was set to  $N = 5 \text{ s}^{-1}$ . Breakup was described by the Laakkonen breakup kernel (Laakkonen et al., 2007b), which was implemented via user defined function. However, for stability reasons and simplicity not the original function but a simple sine function has been used to fit the error function:

$$arg = \sqrt{C_2 \frac{\sigma}{\rho_L \varepsilon_{sc}^{\frac{2}{3}} d_i^{\frac{5}{3}}} + C_3 \frac{\eta_L}{\sqrt{\rho_L \rho_G} \varepsilon_{sc}^{\frac{1}{3}} d_i^{\frac{4}{3}}}} \quad (4.6a)$$

$$x = \begin{cases} \frac{2}{\sqrt{\pi}} \sin(\sin(arg)) & arg \leq 1 \\ \sin(arg^{\frac{2}{3}}) & 1 < arg \leq 2 \\ 1 & 2 < arg \end{cases} \quad (4.6b)$$

$$g(d_i) = C_1 \varepsilon_{sc}^{\frac{1}{3}} (1 - x) \quad (4.6c)$$

Here  $g(d_i)$  stands for the breakage rate of bubbles with diameter  $d_i$  and  $\eta_L$  for the liquid dynamic viscosity. Values for  $C_1$ ,  $C_2$  and  $C_3$  were proposed by Laakkonen et al. (2007b) to be 2.52, 0.04 and 0.01, respectively. The goodness of the fit is discussed in section 4.4.2.2.

Turbulent collision frequencies were calculated based on the coalescence kernel originating from Coulaloglou & Tavlarides (1977) with the algebraic correction of Alopaeus et al. (1999) and Prince & Blanch (1990) and implemented via user defined function:

$$h(d_i, d_j) = C_4 \varepsilon_{sc}^{\frac{1}{3}} (d_i + d_j)^2 (d_i^{\frac{2}{3}} + d_j^{\frac{2}{3}})^{\frac{1}{2}} \lambda(d_i + d_j) \quad (4.7)$$

with  $C_4$  suggested by Laakkonen et al. (2007b) to be 2.65. The model for coalescence efficiency  $\lambda(d_i + d_j)$  was also taken from Prince & Blanch (1990) with  $C_5 = 5.17$  as proposed by Laakkonen et al. (2007b) with  $\sigma$  as surface tension:

$$\lambda(d_i + d_j) = \exp \left( -C_5 \frac{\rho_L^{\frac{1}{3}} \varepsilon_{sc}^{\frac{1}{3}}}{\left(\frac{1}{d_i} + \frac{1}{d_j}\right)^{\frac{5}{6}} \sigma^{\frac{1}{2}}} \right) \quad (4.8)$$

The daughter size distribution was also modelled according to Laakkonen et al. (2007b).

The Hagesaether formulation (Hagesaether et al., 2002) for the discrete method with 23 bubble classes was used to describe particle size distribution. The Ramkrishna formulation was proposed to provide more accurate results (Kumar & Ramkrishna, 1996). However, it can be very slow due to the large number of integration points. Whereas the Hagesaether formulation requires fewer integration points, the difference in accuracy can be corrected by a suitable choice of bin size.

The correlation of Tomiyama et al. (1998) for isolated bubbles in slightly contaminated systems was implemented via user defined function to account for bubble drag coefficient  $C_{D,0}$ :

$$C_{D,0} = \max \left\{ \min \left( \frac{24}{Re} (1 + 0.15 Re^{0.687}), \frac{72}{Re} \right), \frac{8}{3} \frac{Eo}{Eo + 4} \right\} \quad (4.9)$$

with  $Eo$  as Eötvös number defined as:

$$Eo = \frac{g (\rho_L - \rho_G) d^2}{\sigma} \quad (4.10)$$

As Tomiyama drag closure was obtained for bubbles in quiescent fluids, effective (eff) viscosity  $\eta_{\text{eff}}$  (Bakker & Akker, 1994; Brucato et al., 1998) and swarm effects (Ishii & Zuber, 1979) were also included to consider drag modification under turbulent conditions.

$$Re_{\text{eff}} = \frac{\rho_L d |u_L - u_G|}{\eta_{\text{eff}}}, \quad \eta_{\text{eff}} = \eta_L + C_5 \rho_L \varepsilon_{sc}^{\frac{1}{3}} d^{\frac{4}{3}} \quad (4.11)$$

with  $C_5 = 0.02$  as proposed by Bakker & Akker (1994) and  $u$  as liquid or gas velocity.

The bubble swarm function accounts for the crowding effect and was included via drag coefficient  $C_D$ :

$$C_D = f(\alpha_D) C_{D,0}(Re_{\text{eff}}), \quad f(\alpha_G) = \begin{cases} (1 - \alpha_G)^{C_6} & \alpha_G \leq 0.8 \\ 1 & \alpha_G > 0.8 \end{cases} \quad (4.12)$$

with  $C_6$  to be -1.3 as proposed by Buffo et al. (2013). For the simulation of dispersed phase turbulence the mixture model was included. The Schmidt number was set from 0.7 to 0.2 as recommended by Montante et al. (2005) to improve mixing times. The gassing rate was set to 0.25 vvm. Gassing was enabled by setting the top surface of the ring sparger to velocity inlet boundary condition. The default value for turbulence intensity was kept and the hydraulic diameter was set to 0.056 m. The initial bubble diameter was calculated with 10 mm according to the correlation of Gaddis & Vogelpohl (1986).

$$d = \left[ \left( \frac{6 d_0 \sigma}{\rho_L g} \right)^{\frac{4}{3}} + \left( \frac{81 \eta_L Q_g}{\pi g \rho_L} \right) + \left( \frac{135 Q_g^2}{4 \pi^2 g} \right)^{\frac{4}{5}} \right]^{\frac{1}{4}} \quad (4.13)$$

with  $d_0$  as nozzle diameter,  $\sigma$  as surface tension,  $\eta_L$  as dynamic viscosity and  $Q_g$  as gassing rate.

Degassing boundary condition was applied at the top of the reactor. The expansion of the fluid was considered by increasing the liquid height according to the experimental gas hold-up. All walls were no-slip boundaries for liquid and free-slip for gas except for the impellers, which were also modeled with no-slip boundaries for gas to account for the accumulation of gas in the trailing vortices behind the blades. The agitation rate was set to  $N = 5 \text{ s}^{-1}$ . Spatial discretization was set to second order upwind for continuity and momentum as well as for  $k$  and  $\varepsilon$  equations. Transient formulation was also set to second order implicit with a time step size of  $\Delta t = 0.0005 \text{ s}$ . Convergence of the flow field was declared when the residuals remained  $< 10^{-4}$  within each time step and a steady gas volume fraction was reached.

Mixing performance in multiphase was performed identical to single phase simulations (see section 4.3.2). The overall volumetric oxygen mass transfer coefficient was calculated according to equation 4.17. All functions were implemented as user defined function (UDF) into the Fluent code.

#### 4.3.4 Validation parameters

Simulated data have been validated with overall experimental gas hold-up,  $k_L a$  value, power input and mixing time. The overall gas hold-up was calculated by volume-averaging the local gas hold-up with  $i$  as control variable according to :

$$\bar{\alpha}_G = \frac{\sum \alpha_{G,i} V_i}{\sum V_i} \quad (4.14)$$

with  $V_i$  and  $\alpha_{G,i}$  as local volume and gas hold up. Similarly, the  $k_L a$  value has been calculated. To account for the mass transfer coefficient  $k_L$ , different values for  $C_{k_L}$  are proposed (0.301 (Kawase et al., 1992), 0.4 (Linek et al., 2004), 0.46 (Laakkonen et al., 2007b), 0.5 (Laakkonen et al., 2006), 0.523 (Linek et al., 2004) and 0.592 (Prasher & Wills, 1973)).

$$k_{L,i} = C_{k_L} \sqrt{D_{O_2}} \left( \frac{\rho_{L,i} \varepsilon_i}{\eta_{L,i}} \right)^{0.25} \quad (4.15)$$

with  $D_{O_2}$  as diffusion coefficient of oxygen in water.

The local interfacial surface area  $a_{I,i}$  was calculated with the local sauter diameter  $d_{S,i}$  assuming sphere shaped bubbles:

$$a_{I,i} = \frac{6 \alpha_{G,i}}{d_{S,i}} \quad (4.16)$$

The overall  $k_L a$  was then expressed by:

$$\overline{k_L a} = \frac{\sum k_{L,i} a_{I,i} V_i}{\sum V_i} \quad (4.17)$$

The power input from torque  $P_t$  was calculated by:

$$P_t = 2 \pi N M \quad (4.18)$$

with  $M$  as rotational momentum in Nm. Also, the overall sauter diameter was calculated and compared to data from literature:

$$\bar{d}_S = \frac{\sum d_{S,i} \alpha_{G,i} V_i}{\sum \alpha_{G,i} V_i} \quad (4.19)$$

## 4.4 Results and discussion

A pilot scale bioreactor was characterised experimentally in terms of power input, gas hold up, mixing time and mass transfer rate. A loading regime was determined for numerical simulations. Data were furthermore used to validate single and multiphase simulations.

#### 4.4.1 Experimental measurements

##### Power consumption

The results for power input measurements for four different gassing rates and five different agitation rates are displayed in figure 4.2.

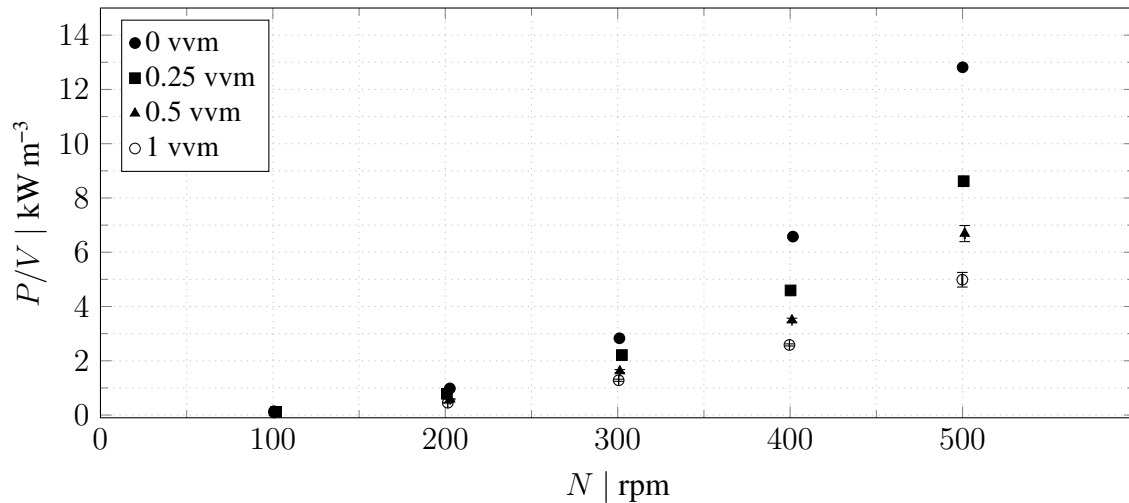


**Figure 4.2: Power input as function of agitation rate.** The power input by electrical power measurement is shown for different operating conditions.

The power consumption increases exponentially with agitation rate for both, ungasged and gasged conditions. For non aerated conditions and 100 rpm the power consumption was about  $0.1 \text{ kW m}^{-3}$ , whereas for 500 rpm the maximum power consumption of  $12.8 \text{ kW m}^{-3}$  was obtained. In general, gasged power consumption is always smaller than ungasged power consumption. Only 68 % of the non-aerated power consumption were reached for 0.25 vvm, 53 % for 0.5 vvm and 39 % for 1 vvm, respectively. This power reduction is caused by the formation of cavities behind the impeller blades, as well as by different fluid densities under aerated conditions (van't Riet & Smith, 1973). For single impellers many authors have extensively studied this effect (Warmoeskerken & Smith, 1981; Oosterhuis & Kossen, 1981; Yawalkar et al., 2008). The difference between aerated and unaerated power consumption becomes less pronounced for lower stirrer speeds. This may be due to the poor gas dispersion of smaller agitation rates. If the power number  $N_P$  of the ungasged case is calculated and plotted against the Reynolds number, the typical profile of a Rushton turbine is visible as shown in figure 4.3. Normally, for baffled tanks a  $N_P$  of 5 per Rushton turbine for a fully turbulent flow ( $Re > 10^4$ ) can be expected in single phase (Rushton & Costich, 1950; Doran, 2013). However, having three Rushton turbines in this study, results in a  $N_P$  of  $\approx 13.5$ . Only for multi-impeller systems with complete parallel flow higher  $N_P$  can be obtained.

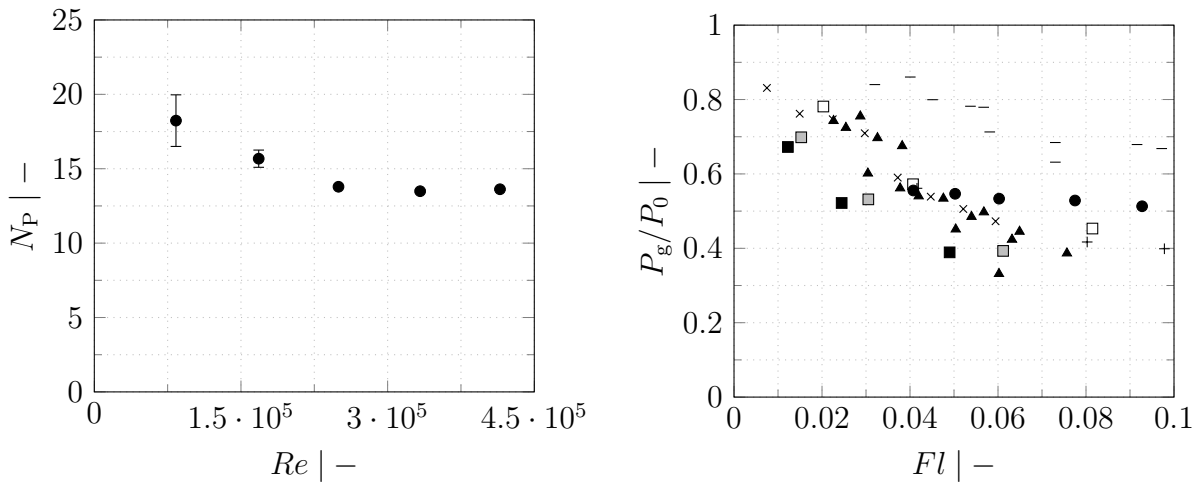


**Figure 4.3: Power number as function of Reynolds number.** The ungasged power number for different agitations rates (100 rpm - 500 rpm) is shown.

**Figure 4.4: Power ratio as function of flow number.** This study:  $\square$  300,  $\blacksquare$  400 and  $\blacksquare$  500 rpm for gassing rates (0.25, 0.5, 1 vvm). Literature:  $\times$  Taghavi et al. (2011),  $+$  Vrabel et al. (2000),  $-$  Nienow & Lilly (1979),  $\bullet$  Markopoulos & Pantouflas (2001),  $\blacktriangle$  Karcz et al. (2004).

The stirrer spacing of this pilot scale bioreactor lies in the transition from merging to parallel flow according to Chunmei et al. (2008) and Xueming et al. (2008), causing a reduction in power consumption. This phenomenon will be further discussed in 4.4.2.

To compare the data with other studies, the power ratio of gassed power and ungasged power consumption is often plotted as function of the flow number  $Fl$ . Figure 4.4 shows exemplarily the power ratio of aerated (0.25, 0.5, 1 vvm) and non-aerated power consumption for 300, 400 and 500 rpm as well as data from literature. There exist no data for the exact same setup, however, for similar agitations systems the power ratio ranges from 0.35 to 1 depending on the impeller type and aeration rate. The power ratio decreases with increasing aeration rate for all studies. While the results of Nienow & Lilly (1979) for the measured dual impeller system are in general a bit higher, the results of this study are in good agreement with the other authors. Especially for 300 rpm the power ratio fits very well with dual Rushton system of Taghavi et al. (2011), Markopoulos & Pantouflas (2001), Karcz et al. (2004) as well as the triple impeller system of Vrabel et al. (2000). While the flow number includes effects of rotational speed and gassing rate, differences between the authors usually arise from deviating impeller setup like blade number or thickness.

Discrepancies between the individual agitation rates are also reported in Cui et al. (1996) who concluded that the flow number alone may not be sufficient enough to describe the power ratio, because gassed power consumption varies considerably at the same flow number. Instead, he suggested to plot  $(1 - P_g/P_0)$  over  $Q_g N^{0.25} D^{-2}$  and thereby showed that the  $Q_g N^{0.25} D^{-2}$  correlated better under various operating conditions, making it possible to obtain a critical  $Fl$ . However, he

**Table 4.4: Determination of flooding regime.** for various operating conditions, critical flow numbers of several authors ([1] Zwietering, [2] Dickery, [3] Zlokarnik, [4] Mikulcova (a), [5] Mikulcova (b), [6] (Rosseburg et al., 2018), [7] (Gezork et al., 2000)) are listed. Correlations from authors [1-5] are summarized in Wiedmann (1983). The Correlation of Mikulcova includes a positive (a) or a negative (b) factor. Flooding regimes are highlighted in grey.

$Q_g$ [vvm]	$N$ [rpm]	$Fl$ [–]	[1]	[2]	[3]	[4]	[5]	[6]	[7]
0.25	100	0.061	0.003	0.024	0.225	0.036	0.055	0.027	0.075
0.25	200	0.031	0.012	0.047	0.637	0.145	0.218	0.106	0.299
0.25	300	0.020	0.027	0.071	1.170	0.325	0.491	0.240	0.674
0.25	400	0.015	0.048	0.094	1.802	0.578	0.873	0.426	1.198
0.25	500	0.012	0.075	0.118	2.518	0.904	1.364	0.665	1.872
0.5	100	0.123	0.003	0.024	0.225	0.036	0.055	0.027	0.075
0.5	200	0.061	0.012	0.047	0.637	0.145	0.218	0.106	0.299
0.5	300	0.041	0.027	0.071	1.170	0.325	0.491	0.240	0.674
0.5	400	0.031	0.048	0.094	1.802	0.578	0.873	0.426	1.198
0.5	500	0.025	0.075	0.118	2.518	0.904	1.364	0.665	1.872
1	100	0.245	0.003	0.024	0.225	0.036	0.055	0.027	0.075
1	200	0.123	0.012	0.047	0.637	0.145	0.218	0.106	0.299
1	300	0.082	0.027	0.071	1.170	0.325	0.491	0.240	0.674
1	400	0.061	0.048	0.094	1.802	0.578	0.873	0.426	1.198
1	500	0.049	0.075	0.118	2.518	0.904	1.364	0.665	1.872

also showed that in a multi-impeller system each impeller has an individual loading and flooding regime, which is furthermore dependent on the stirrer spacing. Unfortunately, power consumption of individual impellers could not be measured in this study. To determine impeller flooding the correlations of various authors were compared as summarized in table 4.4. The critical flow numbers when flooding occurs are highlighted in grey. According to all authors the impellers are flooded with a gassing rate of 1 vvm and 100 rpm. The correlation of Zwietering even predicts a flooding regime for 400 rpm. For 0.5 vvm and 0.25 vvm most authors predict a flooding regime for 100 rpm, whereas for 200 rpm two authors predict flooding for 0.5 vvm and only Zwietering predicts flooding for 0.25 vvm.

These correlations were derived from single impeller measurements. The critical flow number in a system with dual Rushton turbines can be different for each turbine (Taghavi et al., 2011). However, since no correlation for a triple impeller system exists and also stirrer spacing has an influence on the critical  $Fl$ , the correlations mentioned in table 4.4 give a good overview about operating conditions which could cause a flooding regime.

## Gas hold up

Another possibility to determine a flooding regime is to plot the gas hold up as a function of the Froude number  $Fr$ . In figure 4.5 the results of the three different gassing rates expressed as superficial gas velocity are presented. The gas hold up increases with increasing  $Fr$  and superficial gas velocity. For a superficial gas velocity of  $0.0044 \text{ m s}^{-1}$  gas hold up rises from 1.2 % to 5.2 % and for  $0.0087 \text{ m s}^{-1}$  from 2.5 % to 8.1 %. A maximal gas hold up of 10 % was reached for the highest superficial gas velocity and Froude number. The black circle indicate the transition from loading to flooding regime, which can be determined by the change in slope of the graphs (Rosseburg et al., 2018). For a high agitation rate, the gaseous phase is dispersed efficiently by the Rushton turbines leading to an homogeneous regime. Only a small increase in gas hold up with increasing stirrer frequencies was observed. If the agitation rate decreases insufficient momentum induced by the stirrer leads to a sudden drop in gas hold up, because the gas phase is not properly dispersed anymore. A heterogeneous regime consisting of bubble agglomerates forms, which will pass the turbines due to higher buoyancy. Consequently, flooding of the impeller could occur up to a  $Fr = 0.26$  (about 200 rpm) for 0.25 vvm. Most of the correlations shown in table 4.4 predict a bit smaller transition point. For 0.5 vvm and 1 vvm flooding could occurs up to a  $Fr = 0.34$  which lies between 200 rpm and 300 rpm and is also a bit higher predicted as most of the correlations. More measurement points would lead to a better determination of the transition point and therefore a better determination of the flooding regime. However, the current results can be helpful to choose an operating point in order to avoid impeller flooding.

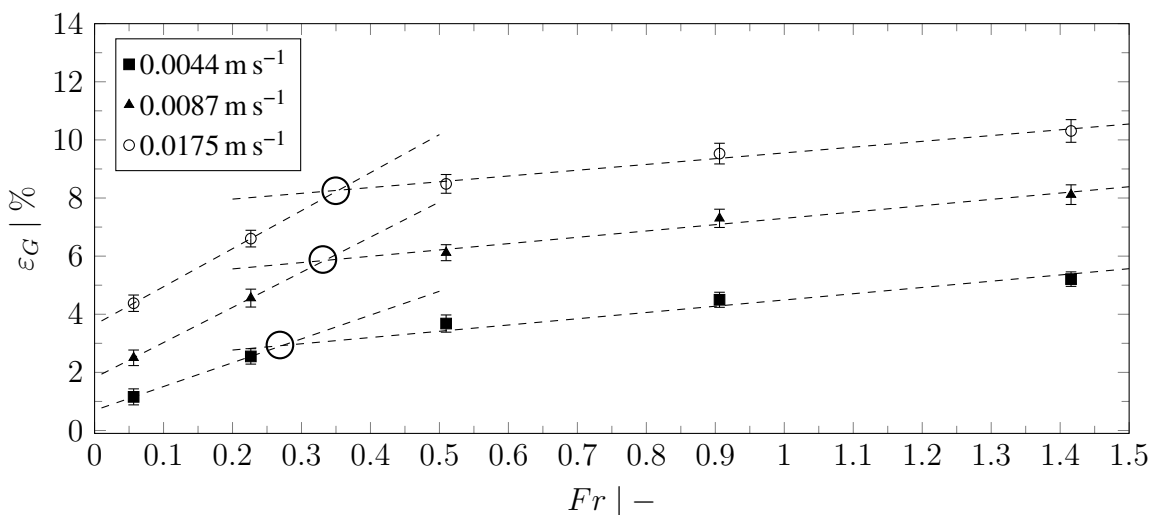


**Figure 4.5:** Gas hold up as function of  $Fr$ . The gas hold up of the three different gassing rates expressed as superficial gas velocity ( $0.25 \text{ vvm} \hat{=} 0.0044 \text{ m s}^{-1}$ ,  $0.5 \text{ vvm} \hat{=} 0.0087 \text{ m s}^{-1}$ ,  $1 \text{ vvm} \hat{=} 0.0175 \text{ m s}^{-1}$ ) is shown for different agitation rates (100 rpm - 500 rpm) expressed as  $Fr$ . Black circles indicate a change of slope if a linear function (dashed line) was fitted to correlate the data.

Gas hold up was furthermore correlated to the impeller power consumption ( $P_G/V$ ) per unit volume and superficial gas velocity  $v_S$  (Rushton & Bmbinet, 1968; Shewale & Pandit, 2006).

$$\varepsilon_G = K \left( \frac{P_G}{V} \right)^\gamma v_S^\zeta \quad (4.20)$$

Values for the constants  $K$ ,  $\gamma$  and  $\zeta$  were obtained by regression of experimental data in the complete dispersion regime ( $N \geq 300$  rpm) with  $K = 0.250$  [0.020, 0.522],  $\gamma = 0.201$  [0.104, 0.298] and  $\zeta = 0.625$  [0.537, 0.713]. Values in brackets indicate the 95 % confidence interval. The small amount of data points results in a wide parameter range. The goodness of fit was calculated with  $R^2 = 0.99$ . The results are displayed in figure 4.6. Moucha et al. (2003) reported a correlation for  $\varepsilon_G$  with a value for  $\gamma$  ( $\gamma = 0.54$ ) higher compared to this study but a value for  $\zeta$  ( $\zeta = 0.58$ ), which is in good agreement with the results presented here. Differences may result from deviations in sparger geometry or the significant bigger impeller spacing chosen by Moucha et al. (2003).

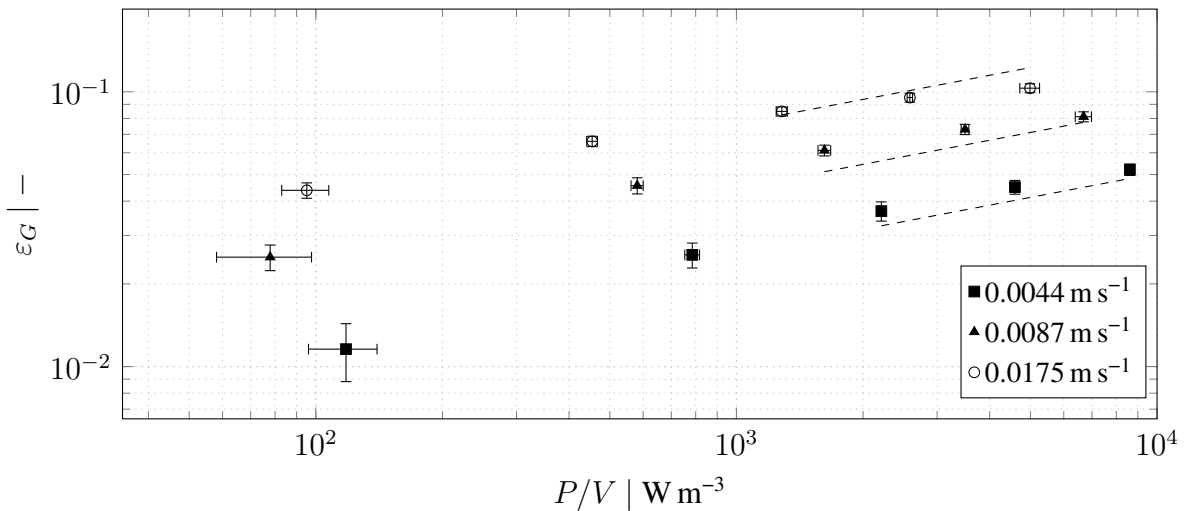


**Figure 4.6: Gas hold-up as function of power consumption.** The gas hold up is shown for different gassing rates expressed as superficial gas velocity (0.25 vvm  $\hat{=}$  0.0044 m s<sup>-1</sup>, 0.5 vvm  $\hat{=}$  0.0087 m s<sup>-1</sup>, 1 vvm  $\hat{=}$  0.0175 m s<sup>-1</sup>). As the first six data points did not lie in a complete dispersion regime, they were excluded from parameter fitting.

### Mixing time

The results of mixing time measurements are displayed in figure 4.7 as function of the  $Re$ . For non aerated experiments (black circle) the mixing time decreases with increasing  $Re$  due to better dispersion and diffusion at higher turbulence. At 100 rpm ( $Re \approx 8.4 \cdot 10^4$ ) the mixing time is about 37 s and decreases up to 7 s at 500 rpm ( $Re \approx 4.1 \cdot 10^5$ ) before it slowly reaches a constant value independent of  $Re$ . Similar behaviour was obtained for a superficial gas velocity of 0.0044 m s<sup>-1</sup> (0.25 vvm, black squares). The influence of gassing becomes evident at higher superficial gas ve-

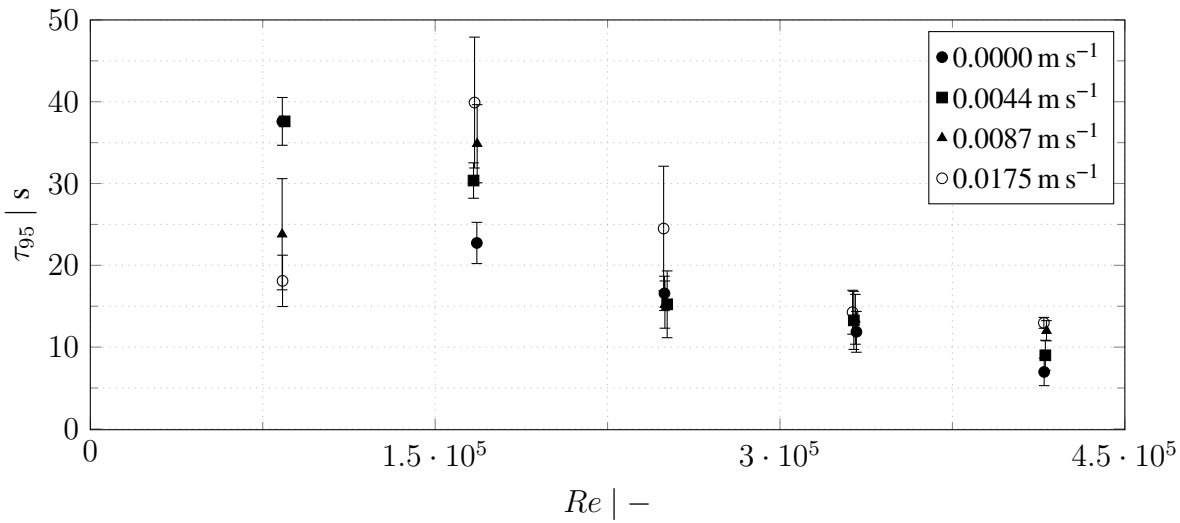


**Figure 4.7: Mixing time as function of  $Re$ .** The mixing time of the different gassing rates expressed as superficial gas velocity ( $0.25 \text{ vvm} \hat{=} 0.0044 \text{ m s}^{-1}$ ,  $0.5 \text{ vvm} \hat{=} 0.0087 \text{ m s}^{-1}$ ,  $1 \text{ vvm} \hat{=} 0.0175 \text{ m s}^{-1}$ ) is shown for different agitation rates (100 rpm - 500 rpm) expressed as  $Re$ .

locities of  $0.0087 \text{ m s}^{-1}$  and  $0.0175 \text{ m s}^{-1}$  (0.5 vvm and 1 vvm). Clearly mixing time increases from about 24 s to 35 s for 0.5 vvm and from 18 s to 40 s for 1 vvm when switching from 100 rpm to 200 rpm ( $Re \approx 1.7 \cdot 10^5$ ). In fact the mixing time at  $Re \approx 1.7 \cdot 10^5$  is even higher than in the non-aerated case. At higher  $Re$ , a decrease in mixing time was observed, converging to the same mixing time as the other cases. Considering the results from the gas hold up measurements, the transition point from flooding to loading regime was at an agitation rate between  $Re \approx 1.7 \cdot 10^5$  and  $Re \approx 2.5 \cdot 10^5$  (200 rpm and 300 rpm) for higher gassing rates and about 200 rpm for smaller gassing rates. From most of the correlations in table 4.4 a bit smaller transition point was predicted. This behaviour is reflected in the mixing time experiments as well. For  $0.0087 \text{ m s}^{-1}$  and  $0.0175 \text{ m s}^{-1}$  impeller flooding leads to smaller mixing times for an agitation rate of 100 rpm ( $Re \approx 8.4 \cdot 10^4$ ) compared to the lower gassing rates. Under these conditions, the flow field is dominated by the momentum induced by the rising gas fraction, forming large scale vortices. The reactor almost behaves like a bubble column leading to decreased mixing times. As the momentum induced by the impeller becomes stronger due to increasing stirrer frequency, the inhomogeneous flow of the gaseous phase is homogenised by the Rushton turbines. The flow field transforms from large scale vortices to the well-known radial flow pattern with circulation loops above and below the impeller of a Rushton turbine. Less large scale vortices first lead to poor mixing performance. With increasing  $Re$ , however, the momentum induced by the impeller is dominant and the gaseous phase plays a minor role. Mixing performance in this regime is almost independent from the Reynolds number. Similar results were obtained by Rosseburg et al. (2018) and Groen (1994). Rosseburg et al. (2018) presented a thorough mixing study in a large scale acrylic reactor operating at higher  $Re$  and smaller gassing rates than in this study. There are not many correlations to determine mix-

**Table 4.5: Comparison with mixing time correlation.** Experimental data of this study are compared to the mixing time correlation of Vasconcelos et al. (1995), choosing the geometric similarity as 100. The percentage error is shown.

Agitation	0 vvm	0.25 vvm	0.5 vvm	1 vvm
100 rpm	-16.35	23.13	59.18	374.52
200 rpm	4.57	30.29	40.95	85.76
300 rpm	11.83	-4.65	-17.98	46.28
400 rpm	7.55	-5.12	-19.96	-8.70
500 rpm	-25.99	-32.44	-15.36	-12.10

ing time in a multi impeller multiphase system. Vasconcelos et al. (1995) provided a correlation for a pilot scale dual impeller system operated in the loading regime. A comparison of the data in this study and the data obtained by the correlation are displayed in table 4.5 as percentage error. With up to 16 % the results of this study are in fair agreement with the calculated values for single phase mixing time. Only the percentage error at 500 rpm is quite high, but considering that small measurement errors at these short mixing times already have a big impact, the results are still comparable. As the gassing rate increases the deviations increase as well. While for higher agitation rates the differences are still acceptable even for high gassing rates, a substantial difference is visible at smaller agitation rates. These operational conditions were shown to cause a flooding regime. However, the correlation of Vasconcelos et al. (1995) is not suitable to predict mixing times for flooding regimes, leading to this huge differences.

If the mixing time is plotted as function of the actual power consumption the flooding effect becomes more obvious. In figure 4.8 a decrease in mixing time with increasing power consumption is observed for every superficial gas velocity. Only for the smallest power consumption of about  $0.07 \text{ kW m}^{-3}$  -  $0.1 \text{ kW m}^{-3}$  at 100 rpm mixing performance is better in the aerated case compared to a higher power consumption. As the agitation rate increases, power consumption gets higher and mixing performance first deteriorates, especially for the higher gassing rates. After a certain power consumption is reached mixing performance improves converging into the same value for all cases for higher power consumptions. Again this shows that the transition point from flooding to loading lies between 100 rpm and 300 rpm depending on the gassing rate. The obtained results are in good agreement with the single phase mixing experiments of Bach et al. (2017). In his study, several mixing experiments were performed in a 200L reactor, geometrical similar to the one in this study. He furthermore stated, that mixing time is rather dependent on the power input, than on the type of fluid, meaning less dependent on the viscosity or density of the fluid. This is also reflected in the data of this study, provided, that the reactor is operating in the loading regime.

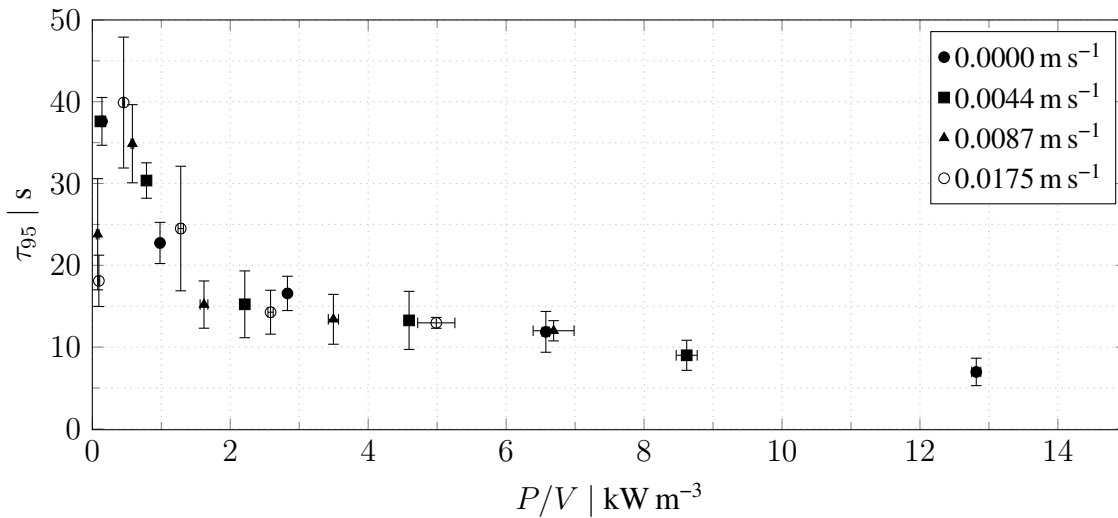


**Figure 4.8: Mixing time as function of the power consumption.** The mixing time for various agitation and gassing rates is presented.

### Mass transfer coefficient

The mass transfer coefficient is shown as a function of power consumption in figure 4.9 in double logarithmic scale. As expected, the mass transfer coefficient increases with increasing agitation rate, as well as with increasing superficial gas velocity. Values for  $k_L a$  range from  $0.008 \text{ s}^{-1}$  to  $0.056 \text{ s}^{-1}$  for 0.25 vvm and from  $0.01 \text{ s}^{-1}$  to  $0.086 \text{ s}^{-1}$  for 0.5 vvm. Highest  $k_L a$  were obtained for 1 vvm with  $0.022 \text{ s}^{-1}$  for the smallest power consumption and  $0.114 \text{ s}^{-1}$  for the highest agitation rate.

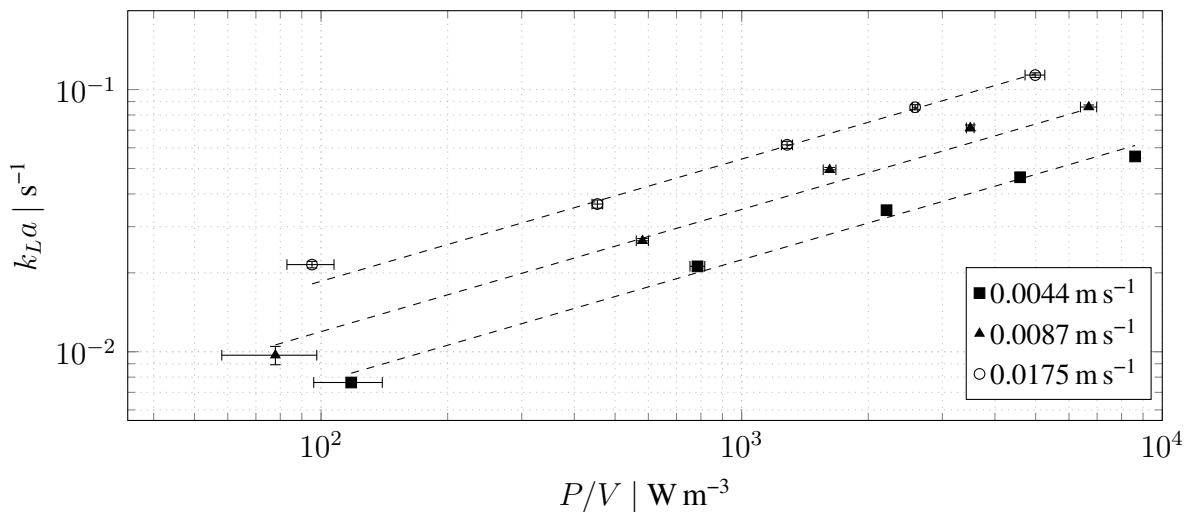


**Figure 4.9: Volumetric mass transfer coefficient as function of power consumption.** The volumetric mass transfer coefficient for oxygen is shown for different gassing rates expressed as superficial gas velocity (0.25 vvm  $\hat{=}$   $0.0044 \text{ m s}^{-1}$ , 0.5 vvm  $\hat{=}$   $0.0087 \text{ m s}^{-1}$ , 1 vvm  $\hat{=}$   $0.0175 \text{ m s}^{-1}$ ).

Dashed lines in figure 4.9 indicate fitted correlations according to the equation:

$$k_{L}a = K \left( \frac{P_G}{V} \right)^{\gamma} v_S^{\zeta} \quad (4.21)$$

with  $P_G/V$  as volumetric power consumption in  $\text{W m}^{-3}$  and  $v_S$  as superficial gas velocity in  $\text{m s}^{-1}$ . The parameters  $K$ ,  $\gamma$  and  $\zeta$  were fitted with  $K = 0.0287$  [0.0179, 0.0395],  $\gamma = 0.466$  [0.441, 0.491] and  $\zeta = 0.638$  [0.549, 0.727]. Values in brackets indicate the 95 % confidence interval. The goodness of fit was calculated with  $R^2 = 0.985$ . The parameters are in good agreement with the values for ion-free water obtained by Van't Riet (1979) with  $K = 0.026$ ,  $\gamma = 0.4$  and  $\zeta = 0.5$ .

Summarising, a multi-impeller 300 L pilot scale bioreactor was characterised in terms of power consumption, gas hold up, mixing time and oxygen mass transfer rate at various gassing and agitation rates. Critical flow numbers for the transition from loading to flooding regime were determined. Knowledge of these parameters is a prerequisite for optimal process performance, especially during scale up. Low power consumption, short mixing times, sufficient gas hold up and proper gas dispersion to obtain high  $k_{L}a$  values are favourable operating conditions for a fermentation process with *C. glutamicum*. As discussed in this section, impeller flooding was expected for all gassing rates at 100 rpm and for most gassing rates at 200 rpm. Although flooding leads to shorter mixing times at smaller power consumption (see figure 4.8), poor gas dispersion leads to insufficient  $k_{L}a$  values. Generally, the reactor should be operated in a loading regime, preferably at low power consumption. Therefore, in this study a agitation rate of 300 rpm and 0.25 vvm is suggested. At this conditions, power consumption and mixing time are in a reasonable range. Moreover,  $k_{L}a$  is sufficient to supply the culture with enough oxygen, but produce local limitation zones, reflecting the scenario of a late fed-batch fermentation. The experimental data furthermore served for validation purposes of numerical simulations.

#### 4.4.2 Numerical simulations

Numerical simulations were performed in single and in multiphase as described in 4.3. A single phase mesh study was conducted to evaluate the dependency of the simulation result on the grid size, as well as to compare model results of the current setup with experimental data. The same reactor setup was furthermore used for multiphase simulations with different simulation setups (see 4.3.3) in order to achieve the best agreement with experimental data. The effect of grid size was also evaluated throughout the study.

#### 4.4.2.1 Single phase simulations

In order to examine when mesh independence was reached a mesh study was performed for single phase simulations. The simulations were carried out at  $N = 5 \text{ s}^{-1}$  with MRF model to account for agitation as explained in 4.3.2. Flow variables like radial velocity  $u_{\text{rad}}$  and turbulent dissipation rate  $\varepsilon$  were tracked for 15 s at several positions indicated in figure 4.10.

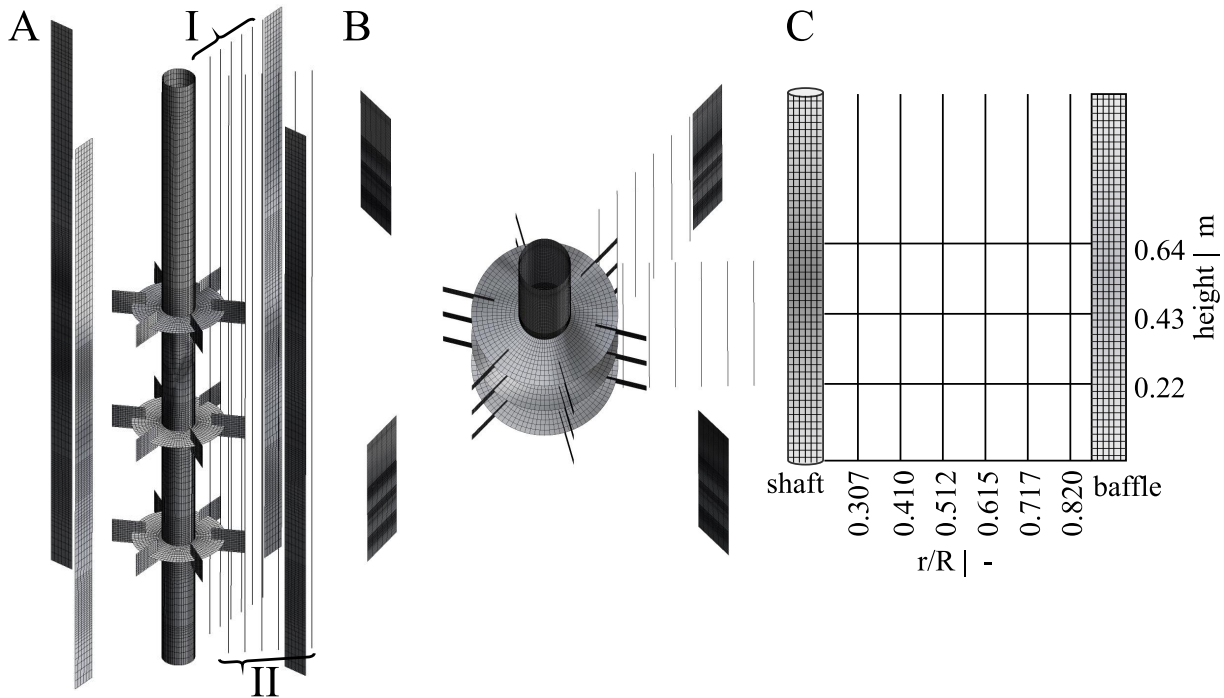


**Figure 4.10: Position of the lines for tracking flow variables.** (A, B) The flow variables  $u_{\text{rad}}$  and  $\varepsilon$  were tracked for 15 s at the indicated positions (shaft to baffle) I: Line 1 - 6, II: Line 7 - 14. (C) Tangentially averaged profiles were recorded at each stirrer plane as indicated (bottom to top): plane 1-3. With modifications to Kuschel & Takors (2020).

Lines 1-6 were positioned in the impeller discharge stream between impeller blade and baffle, whereas lines 7-14 were shifted  $45^\circ$  towards the middle between two impeller blades. The lines in figure 4.10 (C) indicate a plane at each impeller height. The axial profiles of the normalised radial velocity at the 12 different lines are displayed in figure 4.11. Highest radial velocities were obtained in the impeller discharge stream at a height of about 0.2 m, 0.4 m and 0.6 m. A ratio of  $u_{\text{rad}}/u_{\text{tip}}$  of  $\approx 0.4$  or  $\approx 0.5$  is only reached in the near impeller region at  $r/R$  of 0.307 or 0.410. The ratio between radial (rad) velocity and tip speed (tip) is rather small compared to single impeller profiles of 0.7 - 0.8 from literature (Murthy & Joshi, 2008; Chara et al., 2016). In multi-impeller systems the radial velocity might be underestimated by the current turbulence model to some extent (Devi & Kumar, 2013), yet a slightly merging flow field affects the radial velocity in the discharge stream. Figure 4.12 (A) clearly shows the typical flow field of radially pumping Rushton turbines with circulation loops above and below the impeller. However, if  $90^\circ$  offset of the plane in 4.12

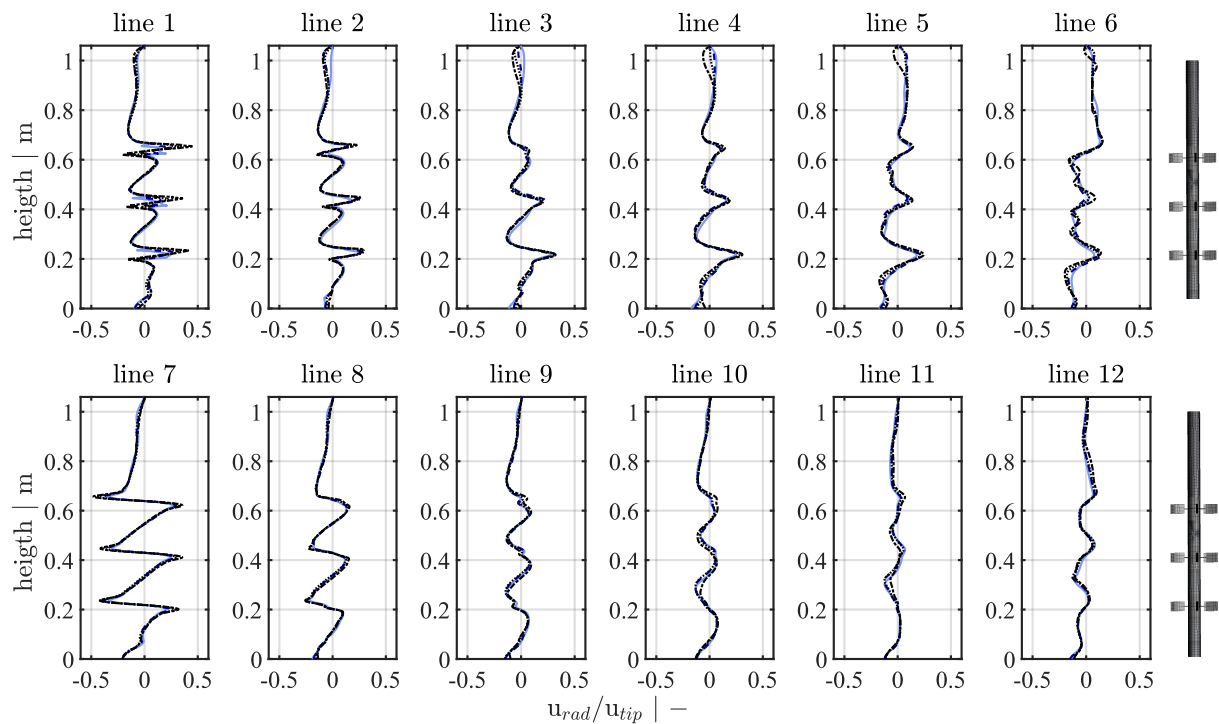


**Figure 4.11: Normalised radial velocity at various positions (SP).** The position of the different lines is indicated in figure 4.10 (A, B). The normalised radial velocity  $u_{rad}/u_{tip}$  is shown for different mesh densities: SPM1 —, SPM2 - - -, SPM3 ····, SPM4 - · - · (see table 4.2).

(A) (see figure 4.12 (B)) is regarded, no distinct flow field of separate radial pumping Rushton turbines is visible, but rather an overlap of the vortices caused by each impeller. The current stirrer spacing lies in the transition from merging to parallel flow (Chunmei et al., 2008) and will lead to reduced radial velocities compared to a single Rushton turbine or a complete parallel flow. Reduced velocity ratios have also been shown in other studies of a dual Rushton turbine system (Micale et al., 1999; Li et al., 2012). With the exception of line 1, the axial profiles at various positions indicate that mesh independence for radial velocity is already reached for SPM1.

Figure 4.13 shows the tangentially averaged profiles of the radial velocity at each stirrer plane. As already mentioned for the axial profiles, the velocity in the discharge stream for this case is much smaller than the tip speed. Additionally, by tangentially averaging the velocity, the velocity profile of the whole  $360^\circ$  geometry was taken into account. Compared to distinct position of the axial profiles, this shows that the velocities differ depending on the examined angle. This might be caused by the nature of the MRF model in combination with the asymmetric reactor geometry (four baffles but six impeller blades). Velocity profiles are higher close to the impeller vicinity. Also the bottom impeller seems to cause larger velocities in the discharge stream than the middle and the top impeller. The profiles of each grid size are comparable for the bottom and the middle impeller, however for the top impeller some deviations especially for the finest mesh are visible. No significant differences were detectable for the axial profiles. However, if absolute radial velocities

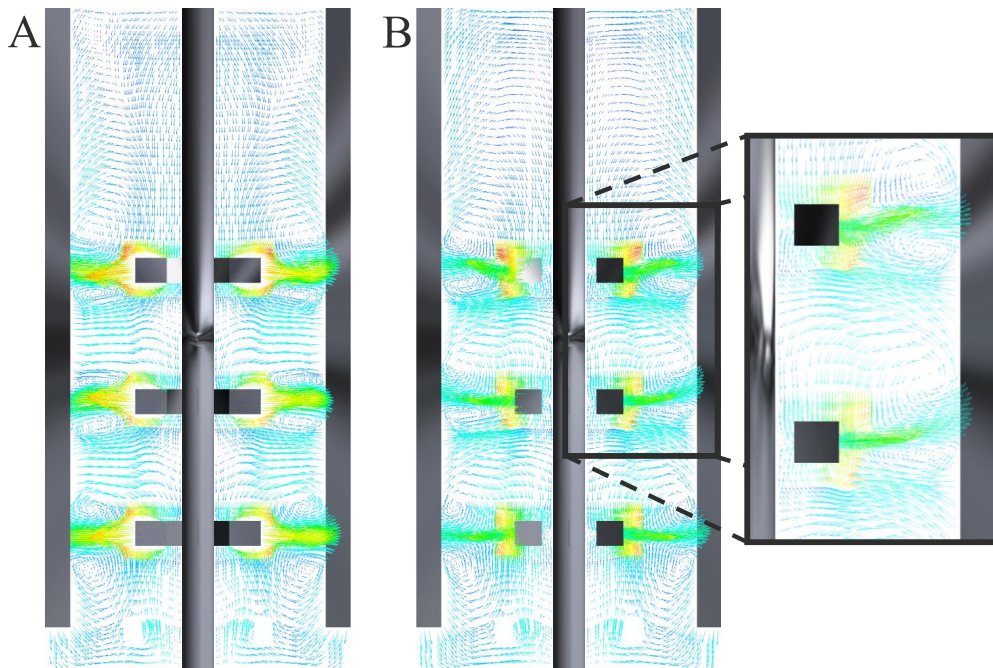


**Figure 4.12: Merging flow field.** Exemplary flow field of SPM3. (A) Parallel flow field. (B) Merging flow field at  $90^\circ$  offset from the plane in (A).

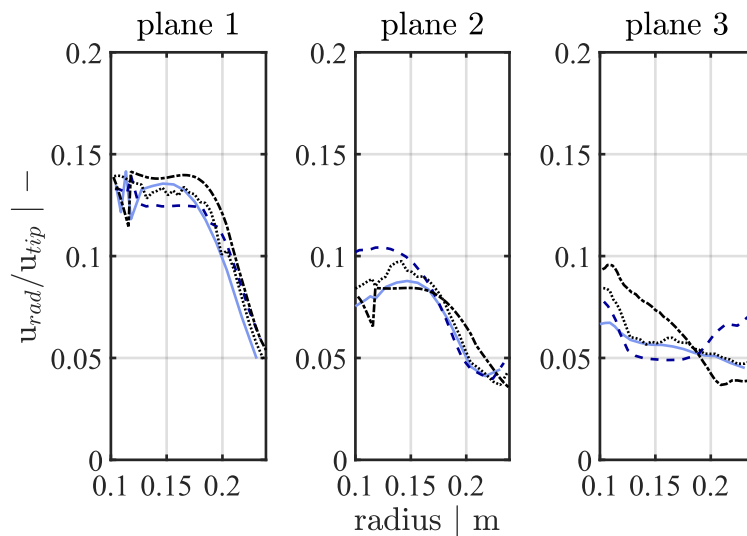


**Figure 4.13: Tangentially averaged profiles of the normalised radial velocity (SP).** The position of the different stirrer planes is indicated in figure 4.10 (C). The normalised radial velocity  $u_{rad}/u_{tip}$  is shown for different mesh densities: SPM1 —, SPM2 - - -, SPM3 ····, SPM4 - · - · (see table 4.2). Plane 1-3: bottom, middle, top impeller.

are averaged for  $360^\circ$ , differences may occur due to partly opposing flow directions of the irregular merging flow field. In general, this also leads to smaller overall radial velocities. Still deviations between the meshes are in an acceptable range.

Obviously, mesh dependence is more severe for the turbulent dissipation rate  $\varepsilon$  (Haringa et al., 2018b). Figure 4.14 shows  $\varepsilon$  normalised to the agitation rate and the impeller diameter. Huge dif-

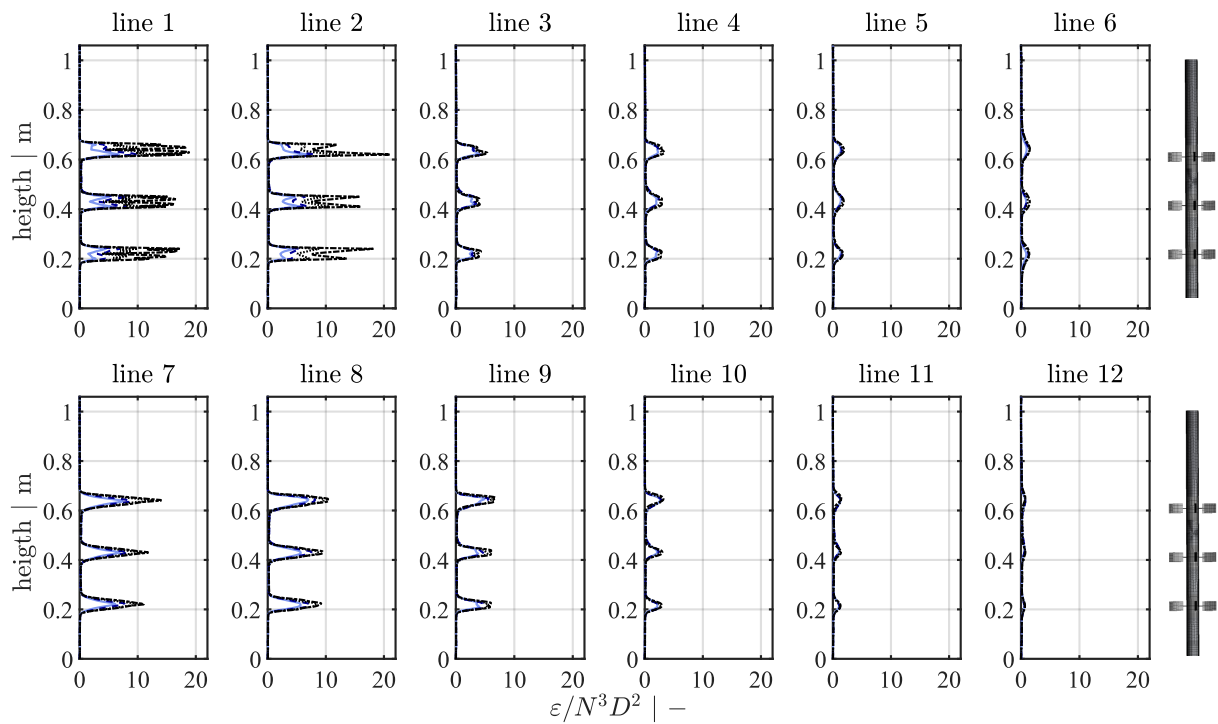


**Figure 4.14: Normalised turbulent dissipation rate at various positions (SP).** The position of the different lines is indicated in figure 4.10 (A, B). The normalised turbulent dissipation rate  $\varepsilon / N^3 D^2$  is shown for different mesh densities: SPM1 —, SPM2 - - -, SPM3 ····, SPM4 - · - · (see table 4.2).

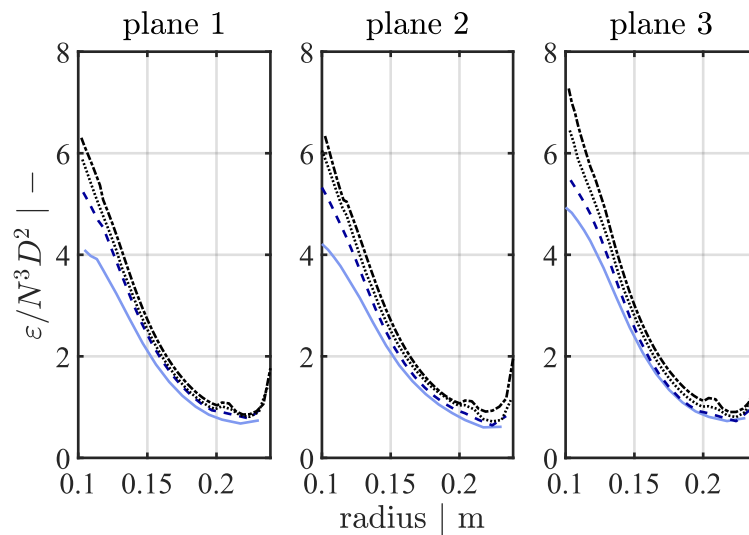


**Figure 4.15: Tangentially averaged profiles of the normalised turbulent dissipation rate (SP).** The position of the different stirrer planes is indicated in figure 4.10 (C). The normalized turbulent dissipation rate  $\varepsilon / N^3 D^2$  is shown for different mesh densities: SPM1 —, SPM2 - - -, SPM3 ····, SPM4 - · - · (see table 4.2). Plane 1-3: bottom, middle, top impeller.

ferences between the meshes are visible, especially in the near impeller zone within the impeller discharge stream. So locally, mesh independence is not reached with mesh SPM3 and an additional mesh would be necessary to see if SPM4 results in mesh independent values for  $\varepsilon$ . However, pro-

files of the tangentially averaged turbulent dissipation rate seem to be more in accordance between the individual meshes (see figure 4.15), indicating that the URANS model is capable to predict the overall dissipation rate (Delafosse et al., 2008).

**Table 4.6: Comparison of integral predicted energy dissipation with expected power input in single phase.** Power draw from torque and power from dissipation were calculated according to equation 4.18 and 4.5. The grid size can be found in table 4.2.

Mesh	$N_{P,t,top}$	$N_{P,t,mid}$	$N_{P,t,bot}$	$N_{P,t,tot}$	$N_{P,\varepsilon}$	dev. [%]
SPM1	3.80	2.52	2.72	9.04	7.50	16.97
SPM2	4.04	3.57	3.65	11.26	10.28	8.71
SPM3	4.24	3.71	3.82	11.77	11.26	4.36
SPM4	4.67	4.06	4.23	12.96	12.76	1.48

A comparison of the power consumption reflects these results. Table 4.6 lists the calculated power number obtained by torque (t) for the top, middle and bottom impeller of each mesh and compares the total power number with the power number by integral predicted energy dissipation. Already for mesh SPM3 the deviation between the two values is less than 5 %. So even if the mesh shows some deviations in  $\varepsilon$  locally, the global power consumption calculated by torque is in good agreement with the power calculated from energy dissipation.

The predicted values are also consistent with the experimental data. As shown in figure 4.3, the power number obtained for  $Re \approx 2.5 \cdot 10^5$  (300 rpm) is  $\approx 13.6$  yielding a deviation of only 5 % to the simulated values. So the current setup was suitable to represent the experimental data. The potential of numerical simulation to represent power consumption measurements by torque have been reported before (Taghavi et al., 2011).

Mixing time simulations were performed by introducing a tracer in a predefined volume as explained in 4.3.2. The profile of the normalised tracer concentration is exemplarily shown for SPM4 in figure 4.16. The tracer concentration was measured at three fixed points. Before mixing is complete, a relatively high concentration will be detected every time the bulk passes the measurement point. These concentration peaks are separated periodically with the circulation time as period (Nienow, 1997). Accordingly, the circulation time can be estimated as depicted in figure 4.16. A comparison of all meshes is given in table 4.7.

Differences between the mixing times obtained by SPM1 to SPM4 are rather small with maximal 7 %. Unlike reported by Haringa et al. (2018b), there is no trend visible in increasing mixing time depending on the grid size. A reason for this discrepancy could be, that compartmentalisation in this reactor setup is less severe than reported by Haringa et al. (2018b), due to smaller impeller

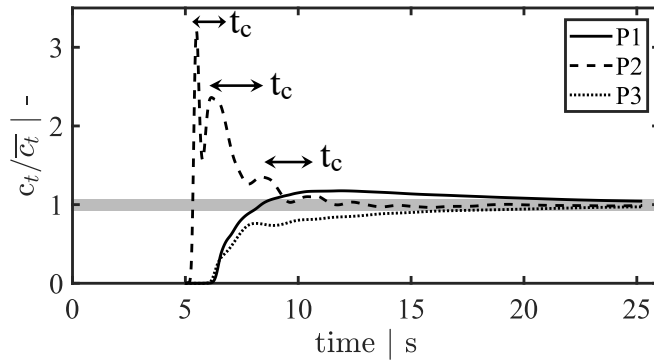


**Figure 4.16: Mixing time profile.** Profile of the normalized tracer concentration at the indicated positions P1-3 (see chapter 4.3.2) for mesh SPM4. Calculated circulation time  $\approx 1.7$  s.

**Table 4.7: Mixing time in single phase.** The grid size can be found in table 4.2. The variable  $\tau_{95}$  is the time reaching 95% homogeneity.

Mesh	$\tau_{95}$ [s]
SPM1	19.6
SPM2	18.8
SPM3	20.3
SPM4	19.2

spacing and therefore the slightly merging flow field. Consequently, the formation of an inter-compartment zone between the vortices of two Rushton turbines is less pronounced. Additionally, this effect is emphasised by the tracer injection point. The injection point was chosen at medium height between two intercompartment zones, rather than at the reactor top, to make it comparable to experimental data. This may have led to a less mesh dependent distribution of the tracer because only one instead of two intercompartment zones had to be passed by the tracer solution.

With about 20 s, simulated mixing time is in general a bit higher than the experimental mixing time ( $\approx 16.5$  s). Overshooting of mixing time by the current turbulence models was reported by Haringa et al. (2018b) due to the previously described intercompartment zones. So even if compartmentalisation is less pronounced in this case, the mixing time is still overpredicted by  $\approx 20\%$ . To reduce that overshooting, tuning of the turbulent Schmidt number is recommended in literature (Delafosse et al., 2014; Haringa et al., 2017b; Montante et al., 2005).

#### 4.4.2.2 Multiphase simulations

A range for an appropriate grid size was obtained from single phase simulations. In the further analysis similar mesh densities were used for multiphase simulations. Multiphase simulations were conducted with the Eulerian model including a PBM approach as explained in 4.3.3. To overcome the underprediction of turbulent energy dissipation due to insufficient grid resolution but still keep reasonable computational costs a scaling factor for  $\varepsilon$  was introduced in breakup, coalescence, drag and mass transfer functions. The functions were implemented as user defined functions. Different models were tested to find a suitable setup to properly display experimental data.

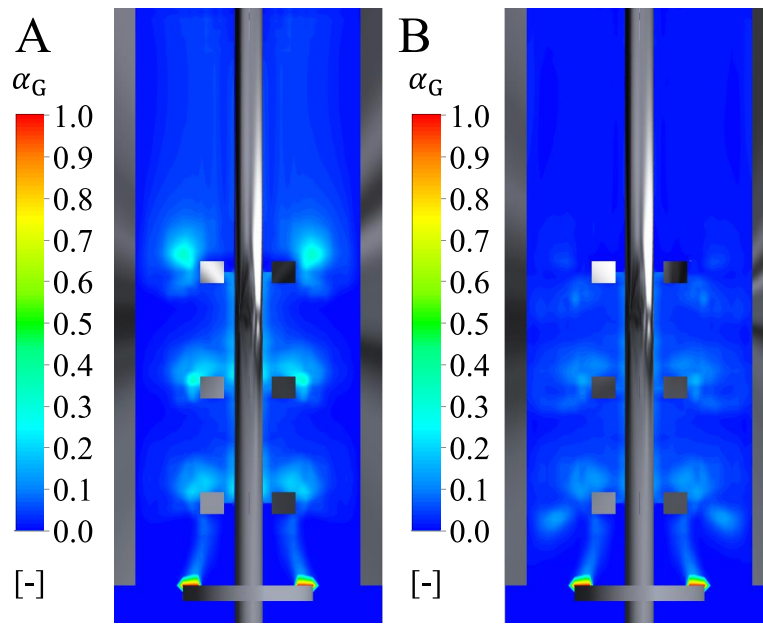


**Figure 4.17: Drag dependent gas volume fraction.** (A) Tomiyama drag model slightly contaminated (Tomiyama et al., 1998). (B) Tomiyama drag model slightly contaminated including turbulent and swarm effects (Bakker & Akker, 1994; Brucato et al., 1998). MPM2 is shown exemplarily.

Bubble break up was simulated with the model by Laakkonen et al. (2006). However, for stability reasons and simplicity not the original break up function but a simple sine function was implemented to fit the error function. The results of both functions are almost identical with a root mean square of  $R^2 = 0.99$ . Slight differences were only visible for small bubble diameters and small values for  $\varepsilon$ , where the original function predicts a bit higher values than the substitute function.

Unfortunately, the drag coefficients in the drag closures of the current Fluent version are derived from measurements in stagnant laminar flows where bubbles are isolated due to the extreme dilution (Ishii & Zuber, 1979; Tomiyama et al., 1998). In turbulent flows with larger gas fractions the momentum boundary layers of bubbles interact, which results in crowding effects (Buffo et al., 2013) or the layer is affected by smaller eddies leading to decreasing bubble rise velocities (Bakker & Akker, 1994; Brucato et al., 1998). Therefore, a drag closure containing effective viscosity, swarm effects and the previously described scaling factor was implemented (see section 4.3.3). A comparison of the simulated gas volume fraction using the drag closure by Tomiyama et al. (1998) (A) and the closure used in this study (B) for MPM2 is shown in figure 4.17.

By neglecting the impact of effective viscosity on drag force, bubbles left the impeller discharge stream too early (see figure 4.17 (A)). In this case, the gas volume fraction accumulated mainly in the trailing vortices of the impellers, whereas a better gas distribution was reached by including turbulent effects (see figure 4.17 (B)). The replacement of the molecular viscosity by the effective viscosity in the drag closure leads to smaller effective Reynolds numbers  $Re_{\text{eff}}$  and thereby to higher drag coefficients. Higher drag coefficients furthermore result in better gas retention and

**Table 4.8: Determination of the scaling factor in multiphase.** The scaling factor was calculated from total power input  $P_{total}$  and  $P_\varepsilon$  according to equation 4.2. The grid size can be found in table 4.3.

Setup	$\frac{P_{total}}{V} \left[ \frac{kW}{m^3} \right]$	$\frac{P_\varepsilon}{V} \left[ \frac{kW}{m^3} \right]$	$f_{sc} [-]$
MPM1	1.864	0.980	1.90
MPM2	2.321	1.521	1.53
MPM3	2.190	1.687	1.30

**Table 4.9: Comparison of different  $k_L a$  models.** Different models for the mass transfer coefficient  $k_L$  as described in section 4.3.4 were tested and compared to the experimental value of  $125 \pm 4 \text{ h}^{-1}$ . The constants for the  $k_L$  model were taken from [1] (Kawase et al., 1992), [2] (Linek et al., 2004), [3] (Laakkonen et al., 2007b), [4] (Laakkonen et al., 2006), [5] (Linek et al., 2004) and [6] (Prasher & Wills, 1973)). All values are displayed in  $[\text{h}^{-1}]$ .

Setup	$k_L a$ [1]	$k_L a$ [2]	$k_L a$ [3]	$k_L a$ [4]	$k_L a$ [5]	$k_L a$ [6]
MPM1	116	155	178	203	229	437
MPM2	115	154	177	201	227	433
MPM3	122	163	187	213	241	459

distributions. By optical assessment during gas hold up measurements the scenario in figure 4.17 (B) was considered as more realistic. However, complete optical access to the reactor was difficult.

Multiphase simulations including all user defined functions, were conducted until convergence of the flow field (residuals remained  $< 10^{-4}$  within each time step) and a steady gas volume fraction was reached. The scaling factor was calculated according to the ratio of total power consumption and integral power due to energy dissipation. The results are depicted in table 4.8. The scaling factor was included in all UDFs by  $f_{sc}$  and all flow equations were solved again till convergence criteria were reached. Power consumption did change less than 3 % after inclusion of  $f_{sc}$ .

To account for the volumetric mass transfer coefficient  $k_L a$ , different values for the constant  $C_{k_L}$  in the  $k_L$  model are proposed as described in 4.3.4. After inclusion of the calculated factor (table 4.8), scaled  $k_L a$  values were simulated. The results are displayed in table 4.9. The constant  $C_{k_L} = 0.301$  of Kawase et al. (1992) showed the best agreement with the experimental value of  $125 \pm 4 \text{ h}^{-1}$  and was therefore chosen for all further simulations.

The third mesh used in multiphase simulations still showed a deviation of  $\approx 30 \%$  between  $P_{total}$  and  $P_\varepsilon$  (see table 4.8), whereas for a comparable mesh density the 'power gap' in single phase was less than 8%.  $P_\varepsilon$  is mostly dependent on the turbulent dissipation rate, so sensitive flow variables such as  $u_{rad}$  and  $\varepsilon$  were checked for mesh dependency in multiphase, equally to single phase simulations.

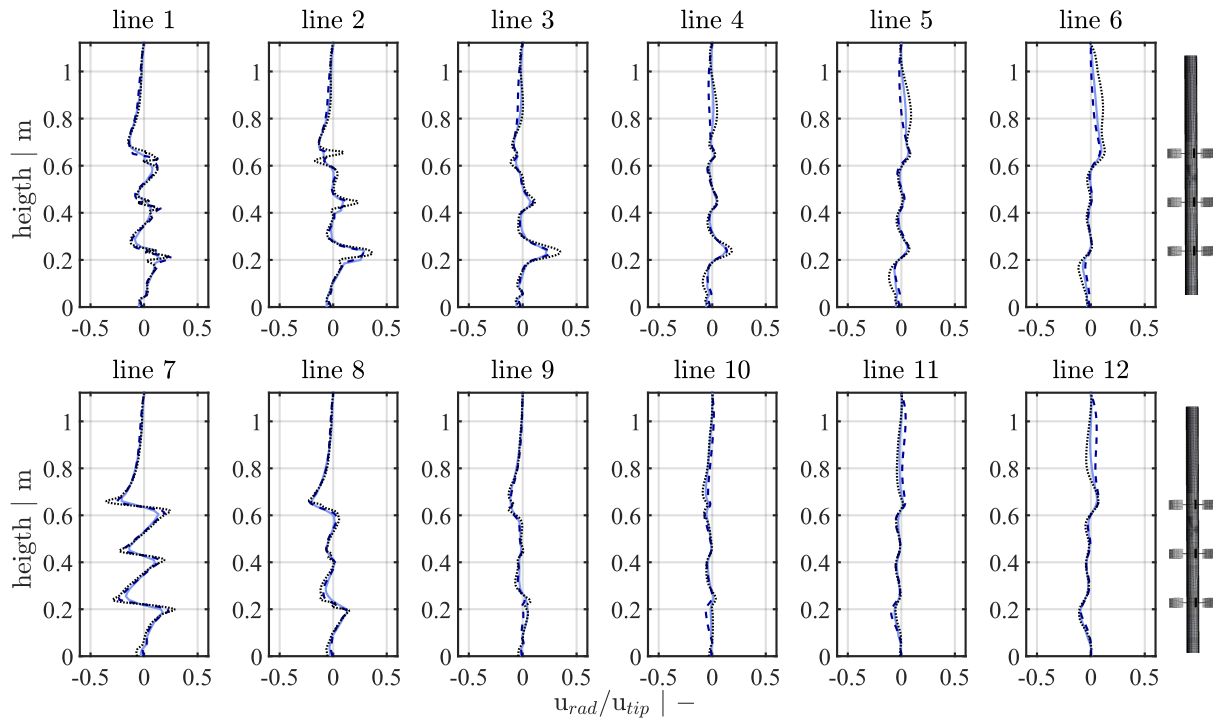


**Figure 4.18: Normalised radial velocity at various positions (MP).** The position of the different lines is indicated in figure 4.10 (A, B). The normalised radial velocity  $u_{rad}/u_{tip}$  is shown for different mesh densities: MPM1 —, MPM2 - - -, MPM3 ···· (see table 4.3). With modifications to Kuschel & Takors (2020).

The flow variables were recorded for 15 s at several positions (see figure 4.10). Averaged profiles of the radial velocity are displayed in figure 4.18 for the three meshes. As discussed previously for SP simulations, the ratio of radial velocity and tip speed is much smaller compared to single impeller measurements. The current turbulence model tends to underestimate the radial velocity for the multi impeller system (Devi & Kumar, 2013), yet the presence of a gas phase as well as the slightly merging flow field affect the radial velocity in the discharge stream (Chunmei et al., 2008).

Already MPM1 shows good agreement with the finer meshes, except for some regions in the impeller discharge stream. Here, MPM3 exhibits slightly higher values than the other meshes. However, tangentially averaged profiles of the radial velocity at the three stirrer planes show good conformity (see figure 4.19). Profiles diverge only in the near wall zone.

Obviously, mesh dependency is more significant for the turbulent dissipation rate  $\varepsilon$  (Haringa et al., 2018b). Huge differences between the meshes in the normalised turbulent dissipation rate exist especially in the near impeller zone (see figure 4.20). Unlike SP simulations also tangentially averaged profiles differ (see figure 4.21). To diminish the dependency of  $\varepsilon$  on grid size in the current models for breakage, coalescence, drag and mass transfer due to insufficient mesh resolution, the above mentioned scaling factor was introduced.

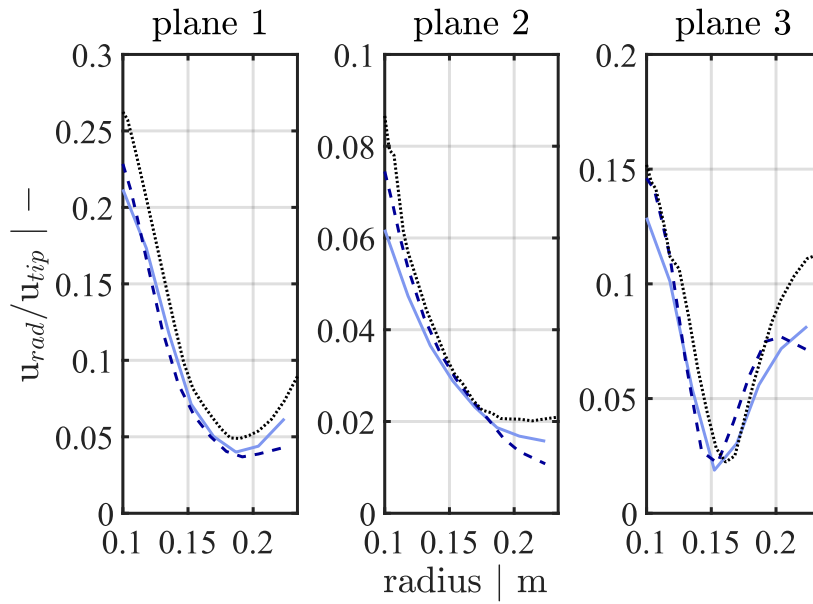


**Figure 4.19: Tangentially averaged profiles of the normalised radial velocity (MP).** The position of the different stirrer planes is indicated in figure 4.10 (C). The normalised radial velocity  $u_{rad}/u_{tip}$  is shown for different mesh densities: MPM1 —, MPM2 - - -, MPM3 ···· (see table 4.3). Plane 1-3: bottom, middle, top impeller. With modifications to Kuschel & Takors (2020).

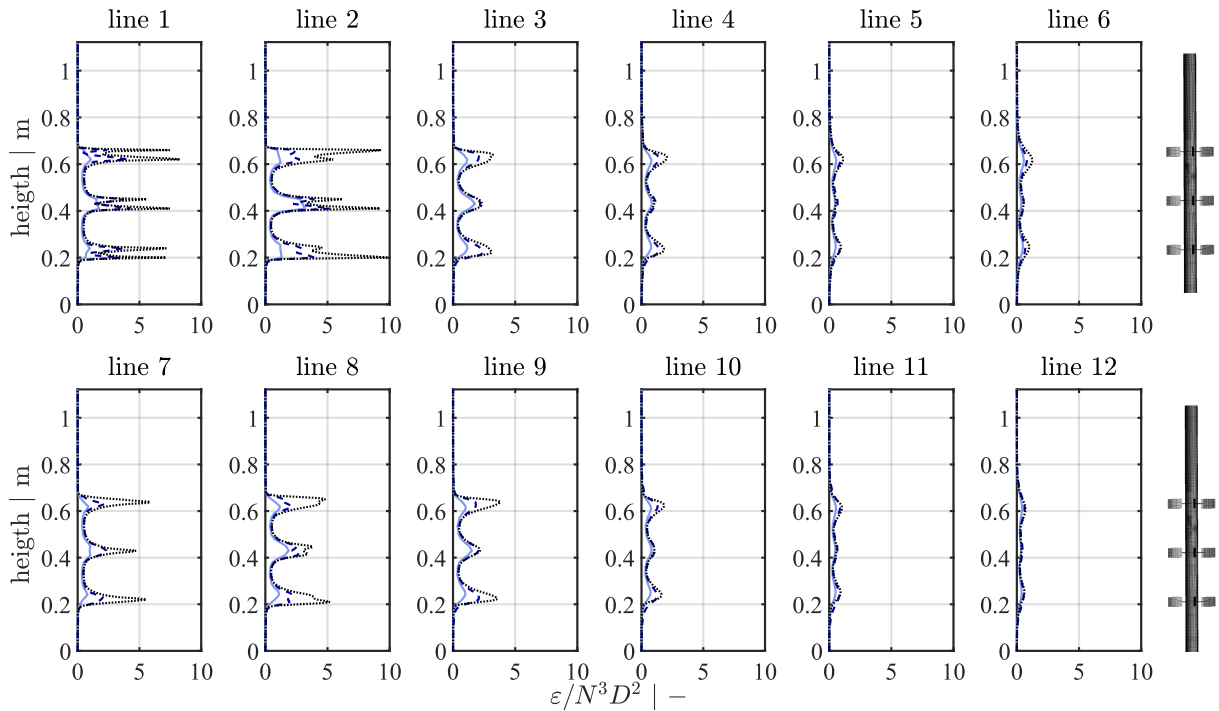


**Figure 4.20: Normalised turbulent dissipation rate at various positions (MP).** The position of the different lines is indicated in 4.10 (A, B). The normalised turbulent dissipation rate  $\varepsilon/N^3 D^2$  is shown for different mesh densities: MPM1 —, MPM2 - - -, MPM3 ···· (see table 4.3). With modifications to Kuschel & Takors (2020).

The results of the simulation with the complete setup are exemplarily shown for mesh MPM3 in figure 4.22. As concluded from single phase simulations and the radial velocity profile, vortices

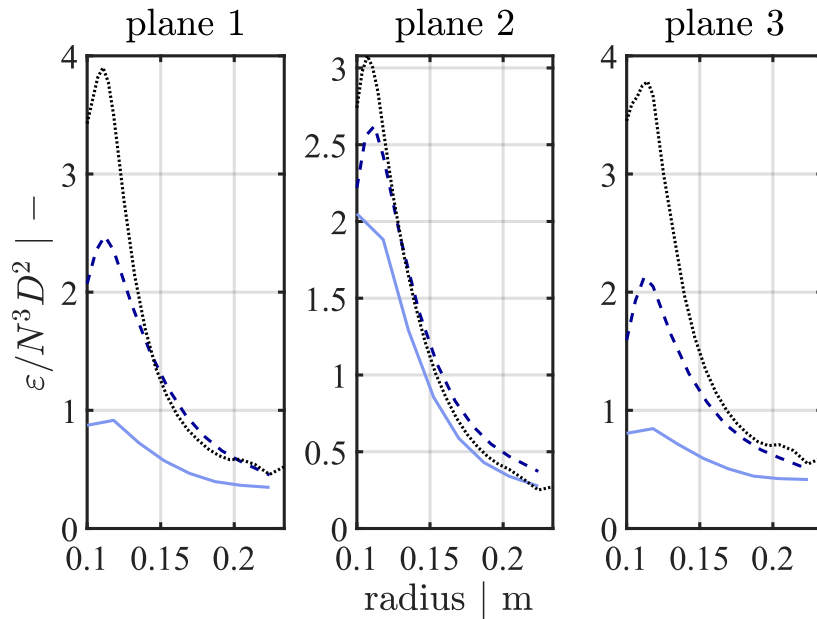


**Figure 4.21: Tangentially averaged profiles of the normalised turbulent dissipation rate (MP).** The position of the different stirrer planes is indicated in 4.10 (C). The normalized turbulent dissipation rate  $\varepsilon / N^3 D^2$  is shown for different mesh densities: MPM1 —, MPM2 ---, MPM3 ···· (see table 4.3). Plane 1-3: bottom, middle, top impeller. With modifications to Kuschel & Takors (2020).

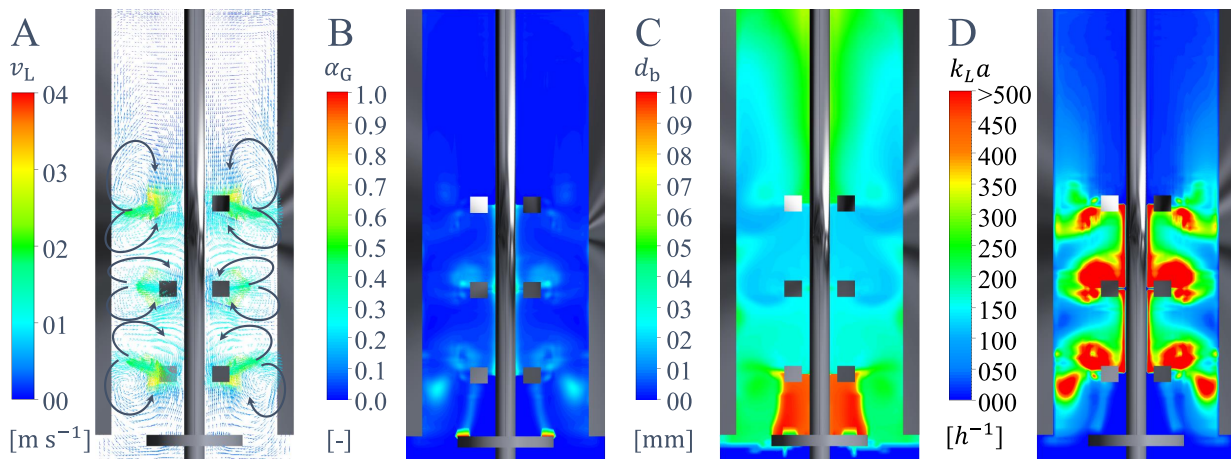


**Figure 4.22: Results of multiphase simulations of MPM3.** (A) Flow field, (B) gas volume distribution, (C) BSD and (D) distribution of  $k_L a$  values for MPM3 are shown exemplarily. With modifications to Kuschel & Takors (2020).

caused by each impeller overlap also in multiphase due to proximate impeller spacing (see figure 4.22 (A)). Additionally, the effect is enhanced by the upwards motion of the gas, leading to no distinct flow fields of separate radial pumping Rushton turbines. With a Froude number of  $N^2 D / g = 0.52$  and a Flow number of  $Q_g / N D^3 = 0.02$ , no flooding was expected according to critical Flow numbers of Rosseburg et al. (2018) and others (Wiedmann, 1983) as discussed in section 4.4.1. The presumption is confirmed by the simulated gas volume fraction, showing a loading regime for the first impeller (see 4.22 (B)). Bubbles with the initial diameter of 10 mm were disrupted by the first impeller and broke into smaller bubbles of about 4 – 5 mm (see 4.22 (C)).

Smallest bubbles (2 – 3 mm) were observed in the impeller discharge stream of the middle and upper impeller. As they moved upwards to the liquid surface bubble diameter increased. Largest bubbles were found around the impeller shaft close to the reactor top, where coalescing effects are dominant. Experimental data by Laakkonen et al. (2007b) revealed a similar tendency. The distribution of local  $k_L a$  values mirror the results of gas volume fraction and bubble size distribution. Highest values of over  $500 \text{ h}^{-1}$  were obtained in the impeller discharge stream, where the combination of a large gas volume fraction and a small bubble diameter lead to an enhanced mass transfer exchange area (see 4.22 (D)).

The experimental values of the power number, gas hold up,  $k_L a$  and mixing time were extensively discussed in section 4.4.1 and compared to data from literature. Table 4.10 shows the results of multiphase simulations with the complete setup compared to the experimental data. The power input by torque is well predicted by the simulation, especially mesh 3 shows a deviation of no more than 2.8 %.

The experimental (3.6 %) and simulated (3.2 %, mesh MPM3) gas hold up are in good comparison, especially if experimental noise is considered. Predictions by mesh MPM1 (2.7 %) and 2 (2.6 %) are still acceptable. As  $f_{sc}$  scales  $\varepsilon$  proportionally, deviations between the prediction precision of the three meshes may exist due to the non-linear character of the breakage, coalescence, drag and  $k_L a$  function. Additionally, gas hold up is directly dependent on the velocity profile which was shown to differ slightly in close proximity to the impeller. Compared to literature, Laakkonen et al. (2007b) presented with 2.4 % a smaller gas hold up than results obtained by simulation of this study. However, the authors used only one instead of three Rushton turbines. Therefore, smaller power input and gas hold up can be expected.

**Table 4.10: Simulated and experimental data in multiphase.** Comparison of simulated data and experimental validation. Experimental bubble diameter was taken from Laakkonen et al. (2007b). With modifications to Kuschel & Takors (2020).

Setup	$N_P$ [-]	$\alpha_G$ [%]	$k_L a$ [ $\text{h}^{-1}$ ]	$\tau_{95}$ [s]	$d_b$ [mm]
MPM1	9.50	2.7	116	17	3
MPM2	11.82	2.6	115	13.9	3
MPM3	11.18	3.2	122	13.1	3.4
exp	$10.88 \pm 0.11$	$3.6 \pm 0.3$	$125 \pm 4$	$15.2 \pm 4$	1.2 - 4.1

Highly accurate values for  $k_L a$  prediction were obtained. In fact, even mesh MPM1 reached a prediction quality no less than 92.8 %. The non-linear nature of the  $k_L a$  closure may also serve as explanation for deviations between the meshes in this case.

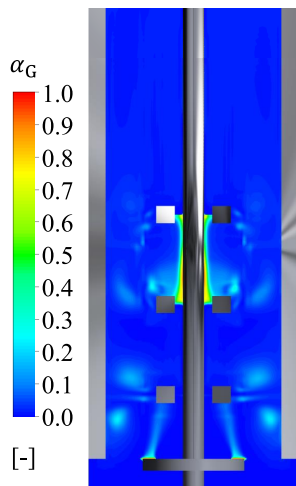


**Figure 4.23: Gas volume distribution of MPM4.**

**Table 4.11: Simulated and experimental data of MPM4.** Comparison of simulated parameters and experimental validation. Experimental bubble diameter was taken from Laakkonen et al. (2007b).

Parameter	MPM4	exp
$N_P$ [-]	11.6	$10.88 \pm 0.11$
$\alpha_G$ [%]	2.8	$3.6 \pm 0.3$
$k_L a$ [ $h^{-1}$ ]	94	$125 \pm 4$
$\tau_{95}$ [s]	13.4	$5.2 \pm 4$
$d_b$ [mm]	3.7	1.2 -4.1

Results from SP simulations showed that mixing time was overestimated by  $\approx 20\%$ . Mixing time was simulated by tuning  $Sc$  from 0.7 to 0.2, which is a common choice in single phase (Delafosse et al., 2014; Montante et al., 2005). However, the effect is less incisive in MP, where the upwards motion of the gas breaks the mass-exchange barrier of the inter impeller zone (Haringa et al., 2017b). Mixing time between mesh MPM2 and mesh MPM3 does not change anymore. Considering the standard deviation of mixing experiments every mesh gives acceptable results.

Bubble diameter was not measured experimentally. Comparison is therefore performed with a study by Laakkonen et al. (2007b) testing different operating conditions. Laakkonen et al. (2007b) measured sauter mean diameters of about 1.2 mm - 4.1 mm for similar settings, which is in good agreement with the results of this study.

To check if finer grid sizes would result in the same values, a fourth mesh was simulated with the mesh size described in table 4.3. The simulation turned out to be very unstable, so time step size was adjusted resulting in high computational demand to reach a steady gas volume fraction. The gas volume fraction is depicted in figure 4.23. Clearly, the second stirrer shows a flooding regime, which could not be confirmed optically for the experimental setup. However, as described before, a complete optical access was difficult. The standard wall function for the realisable RANS  $k-\varepsilon$  model assumes a suitable size for the first layer of grid cells. The dimensionless wall distance  $y_w^+$  needs to be in the range  $30 < y_w^+ < 300$  according to the Fluent user guide. If the distance is too high, the wall is not properly resolved, whereas the model is invalid for too low distances. Calculating the actual wall distance  $y_w$  according to equations 2.20 and 2.23 for that range and taking  $1.5 \text{ m s}^{-1}$  as average velocity for the gas phase around the reactor shaft results in a minimal wall distance of  $y_w = 4.5 \text{ mm}$ . With 4 mm the actual distance of MPM4 is already smaller than the valid range, leading to the conclusion that results from MPM4 may be false. This is furthermore

supported by the bad agreement of simulation results with experimental data as shown in table 4.11. Differences may be caused by the predicted flooding regime, which could not be observed experimentally, leading to a smaller overall gas hold up and an underprediction of the  $k_{L}a$  value by 25 %.

Summarising, simulated values fit the experimental data very well. Even for mesh MPM1 deviations are acceptable.

## 4.5 Conclusion

A multi impeller pilot scale bioreactor was characterised in terms of power consumption, gas hold up, mixing time and oxygen mass transfer rate at agitation rates of 100 - 500 rpm and gassing rates between 0 - 1 vvm. Complete dispersion regimes were only obtained for  $Fr > 0.3$ . Reactor flooding occurred for 100 - 200 rpm at 0.5 - 1 vvm. While shorter mixing times in this scenario are beneficial, small  $k_{L}a$  values may lead to a complete oxygen limitation of a fermentation process. To account for operation conditions within a loading regime an agitation rate of 300 rpm and 0.25 vvm was chosen for numerical simulations. Under these conditions a culture of *C. glutamicum* will not be oxygen limited but local limitation zones will arise, reflecting a late fed-batch scenario. First single phase simulations (SP) were performed. Flow fields of different mesh sizes revealed the occurrence of merging circulation loops, caused by each radial pumping Rushton turbine for the current setup. Locally, mesh dependency was more severe for the turbulent dissipation rate  $\varepsilon$  than for the radial velocity  $u_{rad}$ , but SPM3 and SPM4 were in good agreement considering global values for  $\varepsilon$ . This is mirrored by the comparison of power consumption by torque and power from dissipation rate which is  $< 5\%$  already for SPM3. Mixing time was underpredicted in SP by 20 % suggesting a tuning of the turbulent Schmidt number. A similar grid size range was chosen for multiphase (MP) simulations. Amongst several models for the description of a two-phase flow of a stirred, multi-impeller bioreactor a suitable approach was implemented and validated by experimental data. Considering experimental noise, the influence of mesh granularity for the given simulation setup was shown to be less than 12 % (except for  $\alpha_G$  of MPM1 and 2 with  $< 21\%$ ) for the prediction of process relevant parameter by defining a scaling factor for epsilon. This factor was simply based on the power gap of the power introduced to the reactor and integral dissipated energy. Experimental data were only needed for validation purposes. Consequently, a grid size of  $1.12 \cdot 10^5 \text{ \#}/m^3$  is suggested to be sufficient to represent the actual conditions in the bioreactor. Likewise, similar mesh densities have been used in stirred two-phase flow simulations (Bach et al., 2017; Haringa et al., 2017a). The obtained model setup was furthermore used to simulate a multiphase double gradient as described in the next chapter.

---

## 5 Simulated oxygen and glucose gradient

The successful transfer of a fermentation process from lab to industrial scale requires the prevention of any performance losses. No general approach to accurately predict process performance exists but there are excellent methods like bacterial lifeline analysis that could help to understand the microbial environment and to unravel potential risks. In the previous chapter (4) a multiphase multi-impeller stirred tank in pilot scale was simulated and process relevant parameters were validated by experimental data. This chapter focuses on the depiction of a pseudo-stationary double gradient of a late fed-batch scenario of *C. glutamicum* where oxygen is not process limiting, albeit present only in small concentrations. The same pilot scale reactor setup and settings described in the previous chapter were used. So-called *lifelines*, records of bacterial cells experiencing different levels of glucose and oxygen were identified and used to design SD devices. To tackle the problem of computational costs, grid size was evaluated throughout the different simulation stages. Most remarkably, by using the introduced scaling factor also the coarsest approach of chapter 4 with a mesh density of  $1.12 \cdot 10^5 \text{ \#}/m^3$  was sufficient to properly resolve the double gradient and predict biological readouts.

### 5.1 Introduction

The increasing environmental consciousness of our society has created the need to switch to sustainable circular processes using renewable resources. Low-value, high volume products like amino or organic acids are mostly produced by microorganisms with *Corynebacterium glutamicum* being an established host. However, for the production in industrial bioreactors the scale-up from smaller laboratory scales is crucial and usually suffers from limited mixing and mass transfer. Diminished productivities, conversion yields or product purities are often recorded as a result of emerging substrate or gas gradients (Bylund et al., 1998; Enfors et al., 2001; Garcia-Ochoa & Gomez, 2009; Hewitt & Nienow, 2007; Junker, 2004; Junne et al., 2012; Neubauer et al., 2013; Schmidt, 2005; Vrabel et al., 2001). Population heterogeneities may occur, which could be the reason for underperformance of the bioprocess. To tackle this problem, several scale down analysers, laboratory scale systems mimicking the heterogeneous environment, have been developed (Ka et al., 2014; Loffler et al., 2016). However, they often rely on industrial mixing times and the assumption of certain concentration profiles. Computational fluid dynamics has proven to be

a valuable tool to provide detailed information on environmental conditions inside a fermenter (Lapin et al., 2006; Morchain et al., 2014; Pigou & Morchain, 2015). In the recent years, substrate gradients in fed-batch production scale have successfully been simulated and the influence of concentration fluctuations on microorganisms has been evaluated in comprehensive statistical analysis (Haringa et al., 2016; Haringa et al., 2017a; Kuschel et al., 2017). Coupled with kinetic or mechanistic models, an approach to determine the degree of heterogeneity and to design scale-down (SD) analysers is provided, thereby enabling predictions about productivity in large-scale bioreactors. Yet the influence of oxygen as substrate is often neglected due to the complexity of two-phase flow simulations.

The previous chapter provides a detailed, validated study on multiphase simulations in a stirred pilot scale bioreactor. In the current chapter (a) a pseudo-stationary double gradient occurring during a late fed-batch fermentation of a *C. glutamicum* is depicted using the multiple substrate kinetic proposed by Roels (1983). Furthermore, (b) microbial responses to fluctuating environmental conditions were evaluated by cellular lifelines analysis and (c) the influence of grid size is assessed throughout every simulation state to get proper physical and biological readouts. Moreover, (d) lessons learned are drawn for optimised design of scale down devices.

## 5.2 Simulation setup

The setup from chapter 4.3.3 was used to simulate a multiphase substrate and oxygen gradient. To evaluate the impact of micro-environmental heterogeneities, a bacterial lifeline analysis was performed. The effect of grid size was assessed for the three different meshes MPM1, MPM2 and MPM3 introduced in the previous chapter.

### 5.2.1 Inclusion of the reaction

Glucose feed, oxygen mass transfer and bacterial reaction were included in setup 4.3.3 after convergence criteria and a steady gas volume fraction were reached. Glucose feed was enabled by a source term in a small region at the fermenter top with a feeding rate  $F = 0.076 \text{ g}_S \text{ g}_{CDW}^{-1} \text{ h}^{-1}$ , assuming a cell concentration of  $c_X = 36.5 \text{ g}_{CDW} \text{ L}^{-1}$  and an average growth rate of  $\bar{\mu} = 0.035 \text{ h}^{-1}$ .

Oxygen mass transfer was included via UDF with the volumetric mass transfer coefficient  $k_L a$  calculated by equation 4.17. The transfer rate was then obtained by:

$$\frac{dc_{O_2}}{dt} = k_L a (c_{O_2}^* - c_{O_2}) \quad (5.1)$$

with  $c_{O_2,L}$  as liquid oxygen concentration and  $c_{O_2}^*$  as oxygen saturation concentration calculated by the Henry's law. The Henry constant  $H_{O_2}^{cp} = 1.2 \cdot 10^5 \text{ mol m}^{-3} \text{ Pa}^{-1}$  at 30 °C was calculated by :

$$H_{O_2}^{cp} = H_{O_2}^{cp,\Theta} \exp \left( C_{\text{Sander}} \left( \frac{1}{T} - \frac{1}{T^\Theta} \right) \right) \quad (5.2)$$

with  $H^{cp,\Theta}$  as reference value at 25 °C taken from Sander (2015).

The kinetic proposed by Roels (1983) was used to account for multisubstrate consumption:

$$\mu = \mu_{\max} \min \left( \frac{c_S}{c_S + K_S}; \frac{c_{O_2}}{c_{O_2} + K_{O_2}} \right) \quad (5.3)$$

with  $\mu$  as growth rate and  $K_S$  and  $K_{O_2}$  as half saturation concentrations. Glucose and oxygen consumption were implemented via UDF. Specific growth parameters of *C. glutamicum* ATCC13032 were obtained from batch experiments (see chapter 3.3.1) resulting in a maximal growth rate of  $\mu_{\max} = 0.441 \text{ h}^{-1}$ , a biomass glucose yield of  $Y_{XS} = 0.474 \text{ g}_{\text{CDW}} \text{ g}_S^{-1}$  and a biomass oxygen yield of  $Y_{XO_2} = 0.043 \text{ g}_{\text{CDW}} \text{ mmol}_{O_2}^{-1}$ . The  $K_S$  value for *C. glutamicum*  $K_S = 3.6 \cdot 10^{-3} \text{ g}_S \text{ L}^{-1}$  was taken from Lindner et al. (2011). Since similar cytochrome *bd* activity has been reported (Kita et al., 1984; Kusumoto et al., 2000), the value for  $K_{O_2}$  was taken from *E.coli* with  $K_{O_2} = 2 \cdot 10^{-3} \text{ mmol}_{O_2} \text{ L}^{-1}$ . Transient simulations were performed until a steady-state concentration profile of glucose and oxygen was reached, thereby reflecting a 'snap-shot' of a late fed-batch scenario in pilot-scale. Because the rate of mixing and mass transfer is an order of magnitude higher than the reaction, the reaction was coupled to the continuous liquid phase. This simplification will be discussed in section 5.3.1. Although steady-state concentration was reached, the flow field showed a periodically changing behaviour. To facilitate comparability between the meshes, power input by torque, velocity profiles and turbulent dissipation rate were tracked at several positions. The simulation was stopped when average values of the examined parameters were reached.

Classification of the glucose and oxygen gradients into specific regimes followed the growth rate substrate dependency depicted in figure 5.1. The growth rate is shown as function of the dimensionless substrate concentration  $c_M/K_M$  of a single substrate Monod kinetic for either glucose or oxygen. If  $c_M/K_M \leq 0.5$  (corresponding to  $x = c_M/(c_M K_M) \leq 0.33$ )  $\mu$  is proportional to  $c_M$ , which refers to a low concentration ( $L_S$  for low glucose or  $L_{O_2}$  for low oxygen) regime. If  $c_M/K_M > 9$ ,  $\mu$  reaches 90 % of  $\mu_{\max}$  and the function can be approximated by a function of zero order. This regime was defined as  $H_S$  and  $H_{O_2}$ , because  $\mu$  was independent of a change in substrate concentration. The range in between refers to a transient regime ( $T_S$  and  $T_{O_2}$ ).

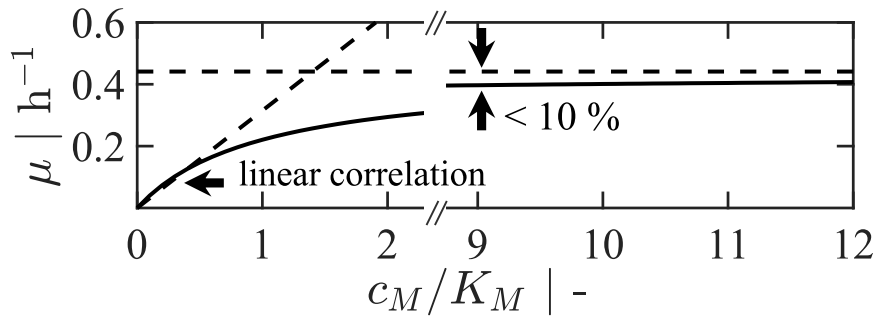


**Figure 5.1: Single substrate Monod kinetic.** Single substrate Monod kinetic  $\mu = f(c_M/K_M)$  to define regimes (solid line). M can either stand for glucose or oxygen. If  $c_M/K_M \leq 0.5$  the Monod kinetic was approximated by a function of first order, if  $c_M/K_M > 9$  the Monod kinetic can be replaced by a function of zero order defining low and high concentration regimes respectively (dashed lines). The region in between was defined as transient regime. With modifications to Kuschel & Takors (2020).

## 5.2.2 Particle tracking

Bacteria were introduced as massless Lagrange particles ( $St \ll 1$ ). The discrete random walk model was enabled. For each mesh 120,000 bacteria were tracked for 260 s. Average growth rates of Euler and Lagrange simulation were compared to proof statistical relevance. During particle tracking concentrations and flow field were fixed. The position, the encountered glucose and oxygen concentration for each bacterium were recorded every 15 ms. Further analysis was performed in MATLAB® (MATLAB R2019a, The MathWorks, Inc., USA). This so called *lifeline* analysis is used to analyse heterogeneities within the bioreactor and was published in various papers (Haringa et al., 2016; Haringa et al., 2017a; Kuschel et al., 2017)

## 5.2.3 Statistical evaluation

The recorded signal was smoothed by applying a moving average filter with a filter window based on the Lagrangian timescale as recommended by Haringa et al. (2017a). This filtering step was necessary to filter out unrealistic turbulent fluctuations, caused by the discrete random walk model. Haringa et al. (2017a) also suggested a second filter step to remove rapid consecutive low-amplitude crossings which was enabled by a median filter. The processed trajectories were then analysed according to their regime transitions. Regime classification of glucose and oxygen gradients into low, transient and high concentration regimes was explained in section 5.2.1. By overlapping concentration profiles of glucose and oxygen (see figure 5.4) it is obvious, that high glucose concentrations are located within a low oxygen regime and vice versa. As the multisubstrate kinetic by Roels (1983) suggests that the growth rate is determined by the limiting substrate, regimes for the double gradient were defined as follows:  $L_S$  for low glucose regime,  $L_{O_2}$  for low oxygen regime and a transient regime T. The regime T includes higher concentrations of both

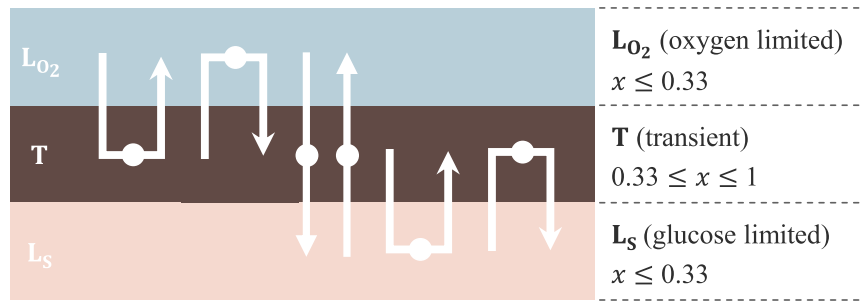


**Figure 5.2: Regime transition patterns.**  $L_{O_2}TL_{O_2}$ : Particle starts and ends in low oxygen regime with a dwelling time in the transient area.  $TL_{O_2}T$ : Reverse event starting in the transient area with retention in low oxygen regime.  $L_{O_2}TL_S$ : Particle traverses all regimes from low oxygen to low glucose.  $L_STL_{O_2}$ : Reverse movement from low glucose to low oxygen.  $TL_S T$ : Circulation from transient over low glucose back to transient area.  $L_S TL_S$ : Reverse event from low glucose to transient back to low glucose regime. The second capital letter always indicates the area in which the retention time  $\tau$  was measured and  $x = c_M/(c_M K_M)$ . With modifications to Kuschel & Takors (2020)

substrates and therefore higher growth rates can be expected. Each bacterium will linger in such a regime for a specific time and will traverse the regime borders with a specific frequency. The frequency and duration of these transitions were then further analysed according to the transition patterns displayed in figure 5.2.

## 5.3 Results and discussion

### 5.3.1 Pseudo-stationary double gradient

A pseudo-stationary double gradient of a late fed-batch scenario was obtained by coupling the reaction to the continuous liquid phase. The compartmentalisation arises due to different timescales of the simulation. The time  $\tau_{\text{dep}}$  needed to shift a half-saturated culture to substrate depletion was estimated to be  $\tau_{\text{dep}} = K_S/(q_{S,\text{max}} c_X) = 0.38$  s for either oxygen or glucose by assuming a substrate limited single Monod kinetic ( $c_S \rightarrow 0$ ). Since the timescale for the reaction rate is an order of magnitude smaller than mixing ( $\tau_{95} = 15.2 \pm 4$  s) or circulation time ( $\tau_{95} = 2.9 \pm 0.75$  s), the formation of a substrate gradient is likely to occur. Figure 5.3 shows the spatial distribution of the growth rate for all three meshes resulting in an average growth rate of about  $0.0335 \text{ h}^{-1}$ . Strikingly high growth rates ( $\mu > 0.24 \text{ h}^{-1}$ ) were attained proximate to the top impeller, whereas the rest of the reactor exhibited rather growth limited zones. The reason for spatially distributed growth rates is elucidated in figure 5.4 (A) and (B). Glucose and oxygen gradients of MPM3 are displayed exemplarily. Gradients of MPM1 and MPM2 were similar. Small differences in gradient formation between the meshes result from slight deviations in the overall physical parameters like  $k_L a$  or  $\tau_{95}$ .

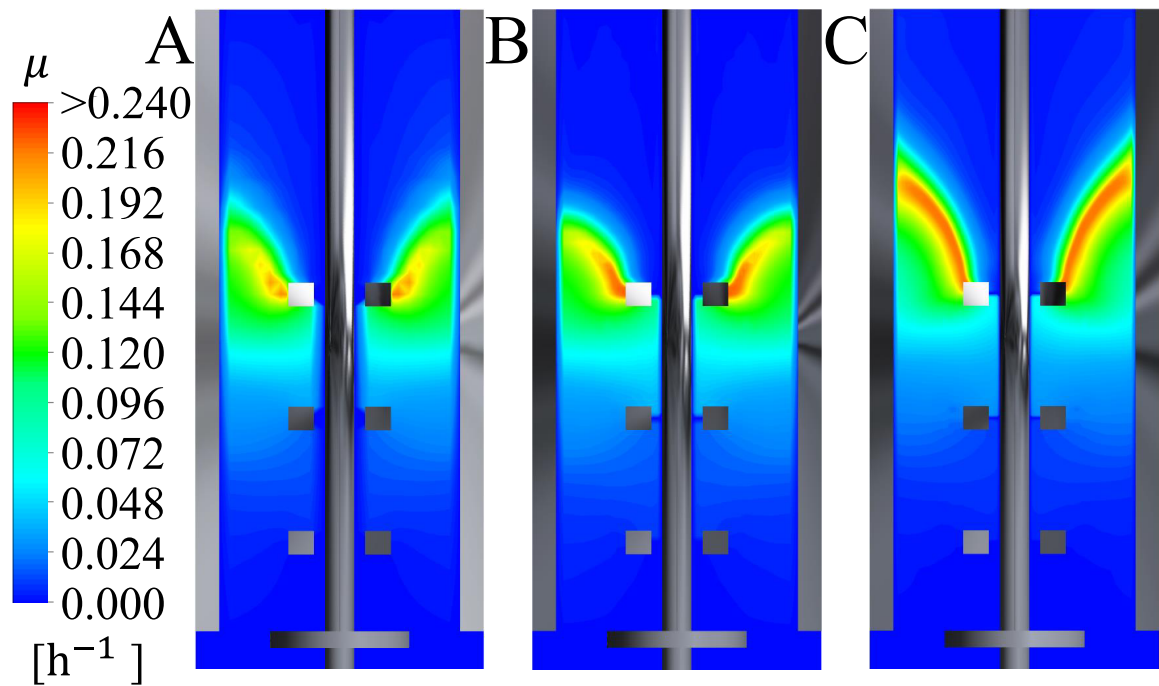


**Figure 5.3: Local distribution of simulated growth rates.** (A) MPM1, (B) MPM2 and (C) MPM3. With modifications to Kuschel & Takors (2020).

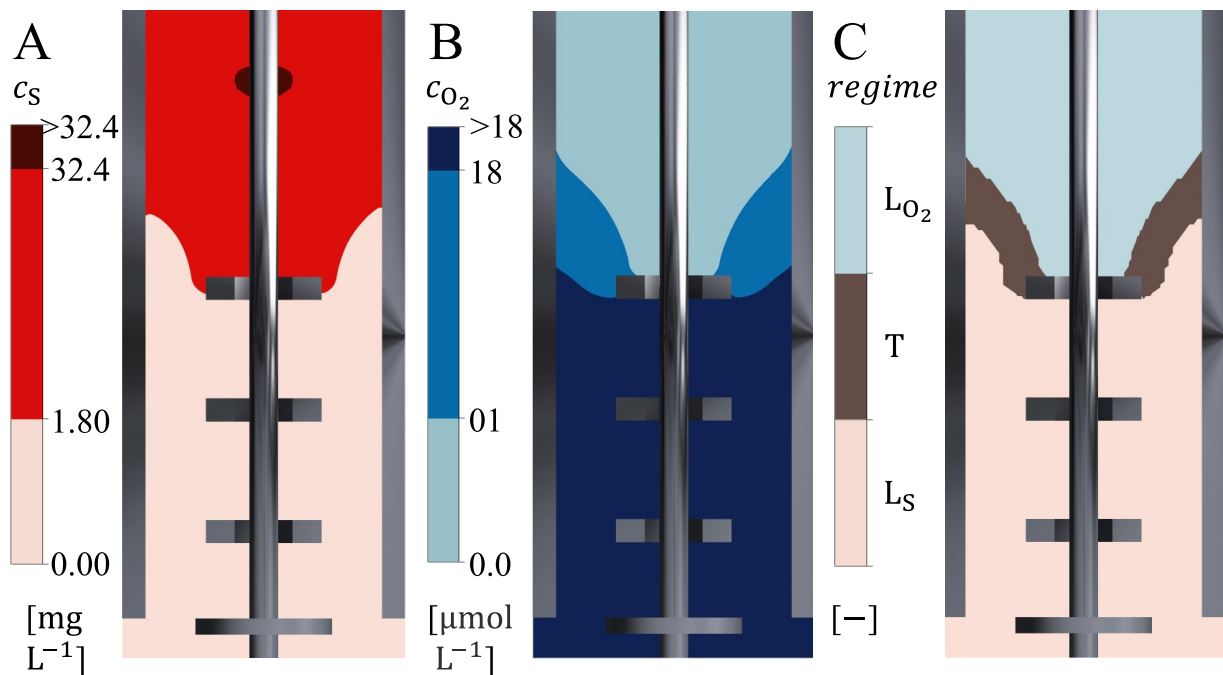


**Figure 5.4: Spatial concentration profiles of glucose and oxygen.** Concentration profiles derived from MPM3 of (A) glucose, fed from the top and (B) oxygen, introduced by a ring sparger close to reactor bottom. Colouration from dark to light colours indicate high, transient or low concentrations. Overlapping both gradients results in (C) the regimes with low glucose  $L_S$ , transient T and low oxygen  $L_{O_2}$  concentrations. With modifications to Kuschel & Takors (2020)

Regime discretisation was dependent on growth rate – substrate correlation as explained in section 5.2.1. High glucose ( $H_S$ ) concentrations were only detectable close to the feed port, the bulk was glucose-poor ( $L_S$ ). A transient zone ( $T_S$ ) was defined in between. The opposite scenario attuned for oxygen: a high oxygen concentration ( $H_{O_2}$ ) was located in the bulk spreading from reactor bottom to the top impeller, followed by a small transient zone ( $T_{O_2}$ ) and an oxygen limited zone in the upper part of the reactor ( $L_{O_2}$ ) (see figure 5.4 (B)). This reverse gradient formation leads to high growth rates around the first impeller. As the growth rate follows the limiting substrate and high glucose or oxygen concentrations were rather tainted by limitation zones, the regime classification was reduced to a low oxygen  $L_{O_2}$ , a transient T and a low glucose  $L_S$  regime (see figure 5.4). The transient zone T was predicted to be less than 5 % of the of the total volume according to the simulation with MPM3, which was in good agreement with the other two meshes (MPM1: 3.7 %; MPM2: 3.3 %).

### 5.3.2 Statistical lifeline analysis

The Lagrangian analysis approach by Haringa et al. (2016) was applied as previously described. So called *lifelines*, trajectories of 120,000 massless cells of a *C. glutamicum* population were studied. Therefore, concentration profiles of glucose and oxygen encountered by individual cells were recorded for 260 s and the resulting potential growth rate was calculated applying the Roels multi-substrate kinetic. The Lagrangian average growth rate ( $\mu = 0.0291\text{h}^{-1}$ ) was comparable between all meshes and is in good agreement with the Eulerian approach ( $\mu = 0.0335\text{h}^{-1}$ ), ensuring that a sufficient number of particles was used. A lifeline is displayed exemplarily for 25 s in figure 5.5 (D). The normalised glucose and oxygen concentrations are depicted in figure 5.5 (A) for 200 s. The profiles reflect the results of the previous section: High glucose concentrations are coupled to low oxygen concentrations and vice versa. Elevated growth rates can only be obtained if both substrates are present in moderate concentrations as demonstrated in figure 5.5 (B). The profiles were translated into regime transitions patterns for further analysis. Figure 5.5 (C) illustrates several of these pattern marked in red. The pattern  $TL_S T$  may serve as an example for interpretation: After 18 s a bacterial cell moves from moderate glucose and oxygen concentrations (T) to low glucose levels  $L_S$ . It lingers there for about 40 s, before it traverses back to moderate levels (T). In the following, the retention time  $\tau$  refers to the residence period in the middle regime (second capital letter, here  $L_S$ ). In general, the residence time in the transient regime (T) is quite short. All bacterial lifelines were scanned for such transition patterns to obtain the frequency distribution as a function of  $\tau$ . Six transition strategies were evaluated and compared between the three meshes. Total frequency of the event, average and maximal residence times (corresponding to the limit, within which 99 % of the values were located) were calculated (see table 5.1).

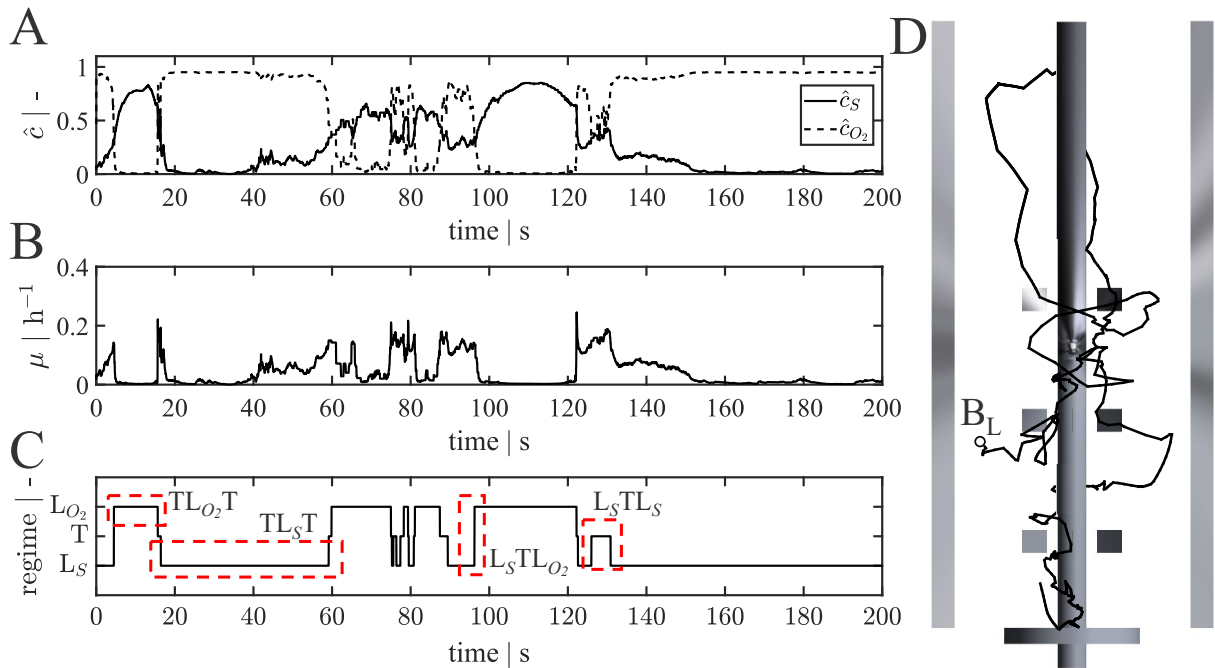


**Figure 5.5: Time course of glucose and oxygen profiles.** Profiles of (A) normalised ( $\hat{c} = c_M/c_M K_M$ ) glucose and oxygen concentration and (B) the resulting growth rate of a bacterial lifeline recorded for 200 s. (C) The profiles were translated to low glucose  $L_S$ , low oxygen  $L_{O_2}$  and a transient regime T. (D) Bacterial lifeline in the bioreactor for 25 s. With modifications to Kuschel & Takors (2020).

**Table 5.1: Regime transition statistics.** Total frequency, average  $\bar{\tau}$  and maximal  $\tau_{\max}$  retention time are listed for each regime transition pattern for MPM3. With modifications to Kuschel & Takors (2020).

Regime transition	frequency [%]	$\bar{\tau}$ [s]	$\tau_{\max}$ [s]
$L_S T L_S$	10.06	0.36	1.05
$T L_S T$	31.36	5.50	75.66
$T L_{O_2} T$	26.47	2.99	13.47
$L_{O_2} T L_{O_2}$	4.62	0.38	1.23
$L_S T L_{O_2}$	15.99	0.20	0.81
$L_{O_2} T L_S$	11.50	0.33	1.20

Additionally, the regime transitions distribution of MPM3 is presented in figure 5.6. Noteworthy, long retention times are obtained for the pattern  $T L_S T$ . Bacteria can linger up to 76 s in  $L_S$ , whereas the average residence time in the glucose limited zone is only 5.5 s. With about 31 %  $T L_S T$  is also the most frequent regime transition. A possible explanation can be concluded from figure 5.4. Particles can be caught in the trailing vortices of the Rushton turbines causing a circulation within the low glucose regime.  $T L_{O_2} T$  is the second most frequent pattern (26 %) with shorter residence times than in  $T L_S T$ . Maximal and average residence times are only 13.5 s and 3 s respectively.

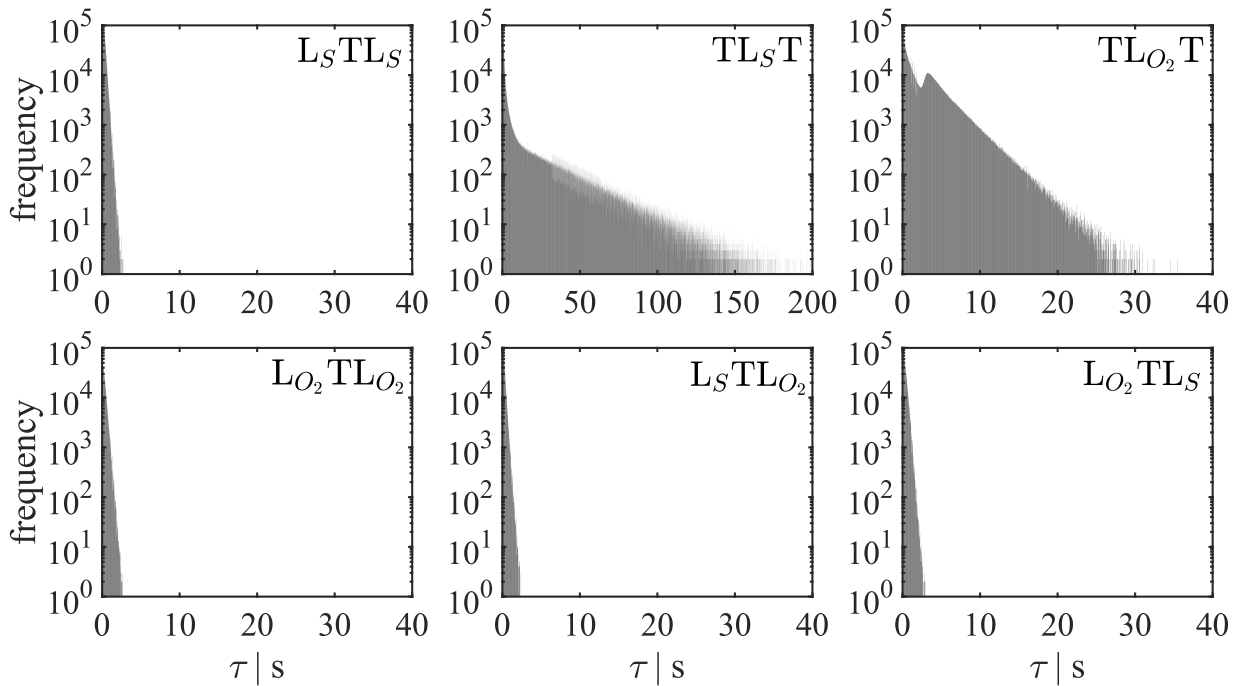


**Figure 5.6: Frequency distribution of regime transition strategy.** Regime transition strategy as function of the retention time  $\tau$ . The six possible patterns are shown as semi-log plot. With modifications to Kuschel & Takors (2020).

All patterns with the dwelling time in the transient regime exhibit a rapid decay after less than 1.5 s. On average bacteria spend less than 0.4 s within this regime, which is in the time scale of  $\tau_{\text{dep}}$ . Due to the nature of the fermentation setup the transient zone forms only in a small region at the top impeller, where the velocity of the particles is very high. This leads to the fast crossings of zone T. A comparison of average residence time prediction by the simulation with MPM3 for transition  $L_S T L_S$  and  $L_S T L_{O_2}$  results in a deviation of about 1 % for MPM2 and about 7 % for MPM1 (see figure 5.7). For the rapid transition  $L_{O_2} T L_{O_2}$  differences between the meshes were in the range of 14 - 17 % and up to 35 % for the transition  $L_{O_2} T L_S$ . For the longer dwelling times, the deviations of MPM1 and MPM2 compared to mesh MPM3 were around 10 - 14 % ( $T L_S T$ ) and 16 - 31 % ( $T L_{O_2} T$ ), respectively. Such lifeline analyses provide valuable information about concentration fluctuations encountered by microorganisms and are currently of high interest for the design of SD analysers (Haringa et al., 2017a) in order to identify population heterogeneities in bioreactors. As measurements from biological scale-down experiments are usually error-prone a deviation of maximal 35 % between the meshes is considered tolerable. MPM1 only possess 1/10 of the grid size of MPM3. In other words, less computational power is required to qualify cellular performance in large scale bioreactors.

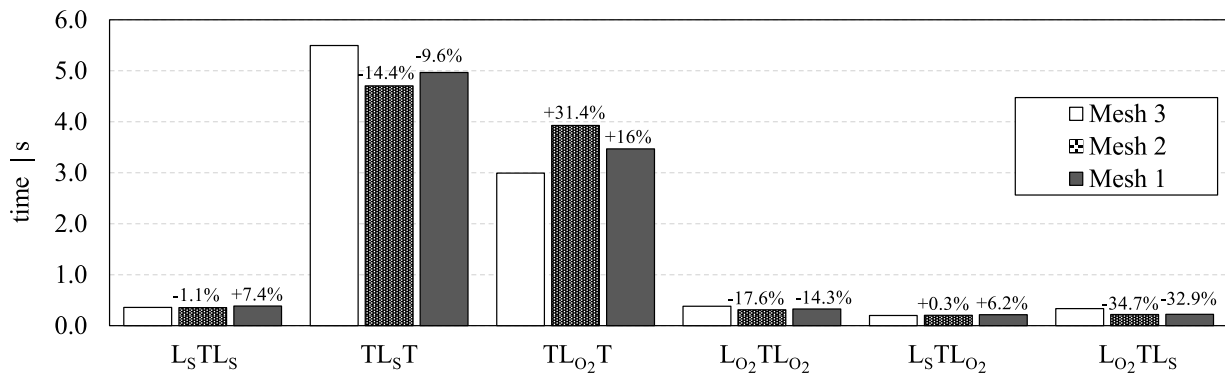


**Figure 5.7: Comparison of residence time prediction.** Comparison of average residence time prediction  $\bar{\tau}$  for the three simulated meshes. Deviations of MPM1 and MPM2 compared to MPM3. With modifications to Kuschel & Takors (2020).

### 5.3.3 Simplified design of scale-down devices

The results for the current substrate limited fed-batch scenario show that the volume of moderate substrate concentrations, here called transient zone, (see section 5.3.1) is with less than 5 % so small that the influence on bacterial behaviour is questionable. This is furthermore confirmed by rapid transitions through that regime with a dwelling time of maximal 1.2 s. Within this time instantaneous metabolic responses may occur. However, profound effects on the bacterial population are rather unlikely, since massive transcriptional responses after stress exposure periods >35 seconds were observed for *E. coli* (Löffler et al., 2016). Still, the initiation of transcriptional response may have started and will proceed upon transition into well-mixed zones of the bioreactor (Nieß et al., 2017). In case of *C. glutamicum*, by-product formation (lactate) starts as metabolic response to oxygen limitation. The later consumption of lactate in oxygen rich regimes, however, will cause no change in the energetic state of the cell. Thereby, *C. glutamicum* has proven its robustness regarding the exposure to large scale stress conditions (Käß et al., 2014). Accordingly, the transient zone may be excluded, considering only a glucose and oxygen limited regime for further analysis. As such, the Euler-Lagrangian analysis was simplified by neglecting related regime patterns finally yielding the two-compartment readouts L<sub>S</sub>L<sub>O<sub>2</sub></sub>L<sub>S</sub> and L<sub>O<sub>2</sub></sub>L<sub>S</sub>L<sub>O<sub>2</sub></sub>. For the first pattern an average retention time of 3.4 s and a maximal retention time of 15 s was obtained. Longer residence times in glucose limited regimes were found (5.7 s) for the second transition pattern, that can expand to a maximal dwelling time of 80.5 s.

In general, these analyses serve as basis to design wet-lab scale-down devices, where the regimes can be translated into a multi-compartment set-up. Figure 5.8 (A) and (B) illustrate simplified designs of such devices. The first set-up consist of two stirred tanks, which are connected by a PFR. As indicated key limitations are installed in the STR, whereas the PFR is used to realise the T zone. Additionally, each STR is supplied by either TL substrate or oxygen to raise limiting levels. The fre-

frequency of the regime changes may be controlled by the ratio of the volumes of the different tanks. Pumping between both STR and the PFR follows the travelling paths  $L_S TL_{O_2}$ ,  $L_S TL_S$ ,  $L_{O_2} TL_S$ ,  $L_{O_2} TL_{O_2}$  with the average dwelling times to determine the pumping rates. How many percent of the frequency change are covered by the scale-down device may be optional to the experimentalist. For instance, the case in figure 5.8 (B) illustrates the simplified version neglecting the impact of the transient regime T. Furthermore, residence times and design volumes for industrial scale bioreactors will differ.

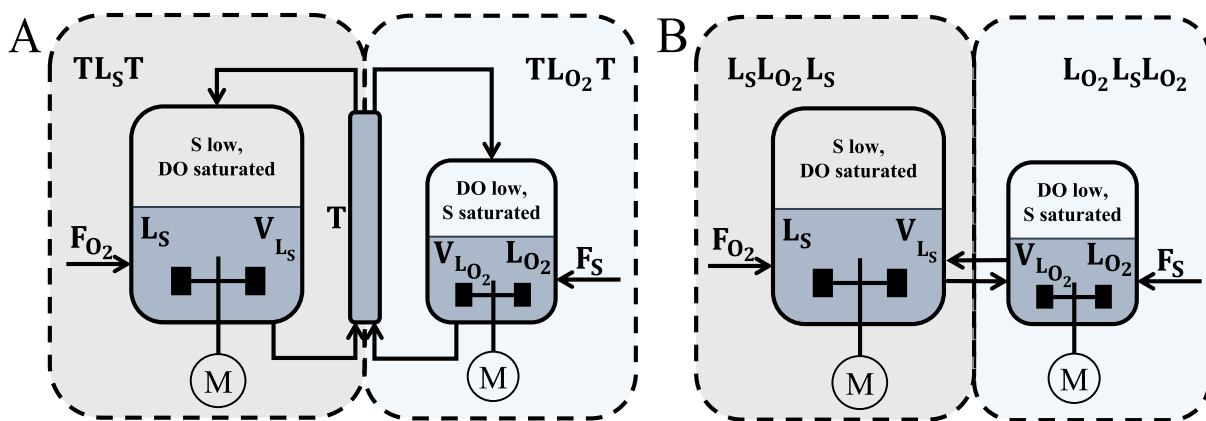


**Figure 5.8: Examples of simplified scale-down devices.** (A) and (B) Examples of simplified scale down devices . With modifications to Kuschel & Takors (2020).

## 5.4 Conclusion

The scaling factor approach by Laakkonen et al. (2007b), which was introduced in the previous chapter, was successfully applied to simulate substrate and oxygen gradients for the three different mesh sizes. This 'snap-shot' double gradient may occur during a substrate limited late fed-batch process of *C. glutamicum*, where oxygen is still present, albeit in low concentrations within specific regions.

Interestingly, concentration profiles of relatively coarse mesh granularity were still in good agreement with the finest mesh. Bacterial lifeline analysis further revealed that biologically relevant readouts such as regime changes were based well on a mesh density of  $1.12 \cdot 10^5 \text{ \#/m}^3$ , still giving accurate residence time distributions with mostly less than 15 % deviation compared to 10-fold finer mesh resolution. Consequently, the use of this scaling approach opens the door for large scale applications with less computational effort. In other words, the sensitivity of simulation results is primarily decoupled not only for physical parameter but also for the readout of biological criteria such as regime changes as part of lifeline analysis.

The double gradient consisted of a glucose limited zone  $L_S$ , a small regime of moderate concentrations  $T$  and an oxygen limited zone  $L_{O_2}$ . It may be surprising that the inclusion of a second substrate and thereby a second phase in a biotechnical setup finally leads to a rather simple compartmentalisation. In essence, this reflects the complex interplay of two phase mixing applications, mass transfer and bacterial substrate consumption. Careful consideration is required for each individual scenario. However, by introducing the gas phase in the lower reactor part and feeding at the reactor top, the occurrence of a small  $T$  zone but large  $L_S$  and  $L_{O_2}$  zones is rather a common than a rare event. Hence, the presented approach may serve as a representative example and deserves to be tested for other cases.

---

## 6 Cell cycle model

The physiological state of a bacterial cell is influenced by its surrounding environment. External stress such as varying concentrations within a large scale bioreactor is a key factor to induce the formation of population heterogeneity. The individual cells within a population can differ according to growth phenotypes and cell cycle pattern (Müller et al., 2010). Hence, the heterogeneous environment of a large scale fermenter might affect the homogeneity of a bacterial population, yielding subpopulations that co-exist next to each other. To describe the formation of subpopulations based on cell cycle dynamics a model is needed which depicts the bacterial replication process. This study aimed to develop a cell cycle model for *Corynebacterium glutamicum* AC13032. The replication phase duration was derived as a function of growth rate and partial pressure of carbon dioxide (*C. glutamicum*). Additionally, based on the work of Lieder et al. (2016), a model describing the replication phase as a function of the growth rate for *Pseudomonas putida* KT2440 was obtained. Combined with the CFD approach from the previous chapters, heterogeneity in terms of subpopulations containing one, two or more chromosomes as described in chapter 7 can be displayed.

### 6.1 Introduction

The bacterial cell cycle of a cell using binary fission can be divided into three parts; the initiation of replication ( $B_c$ -phase), the time required for replication ( $C_c$ -Phase) and the time between replication and cell division ( $D_c$ -phase). The duration of those cell cycle phases varies with growth conditions and nutrient availability (Bipatnath et al., 1998). The  $C_c$  and  $D_c$  period have been described as decreasing with increasing growth rates and reach a constant value for well growing cells. The  $B_c$  period minimises for increasing growth rates (Cooper & Helmstetter, 1968). Furthermore, the duration of the cell cycle phases seems to be adjusted up-on oxygen stress conditions. The more severe the oxygen stress factor, the faster DNA replication takes place implying a reduced  $C_c$  phase, but prolonging  $B_c$  and  $D_c$  phases to cope with stress while maintaining a constant growth rate (Lieder et al., 2016). In order to grow with shorter doubling times (shorter times than the combined  $C_c$  and  $D_c$  phase duration), it has been shown for some bacteria that they are capable of multifork replication (Skarstad et al., 1986; Youngren et al., 2014; Lieder et al., 2016). Then, initiation of replication already starts in the preceding generations. Also for *C. glutam-*

*icum* uncoupled DNA synthesis has been suggested (Neumeyer et al., 2012). To determine the  $C_c$  phase duration experimentally, the *oriC / ter* (origin of replication to terminus of replication) ratio needs to be measured using quantitative PCR (Skarstad et al., 2012). As this method is quite time consuming, fluorescence-activated cell scanning has proven to be a much faster approach. With the help of single cell analysis, the DNA content of thousands of bacteria is measured to generate DNA content histograms of the population. Cooper & Helmstetter (1968) developed a model, which describes bacterial replication and division cycle. Skarstad et al. (1985) extended this model to determine the duration of the cell cycle phases as result of a specific DNA content distribution for a population of *E. coli B/r*. Thus, the cell cycle durations can be determined by parameter estimation using the experimentally obtained DNA histograms. The model was successfully applied for other organisms, too (Lieder et al., 2016).

In the following sections the dependency of cell cycle dynamics on environmental conditions for *Pseudomonas putida* KT2440 and *Corynebacterium glutamicum* AC13032 is described. The case dealing with *P. putida* is mainly dependent on the work of Lieder et al. (2016) and describes the replication phase duration as function of the growth rate, whereas the cell cycle model obtained for *C. glutamicum* considers an additional stress factor. The effect of elevated partial pressures of carbon dioxide on cell cycle dynamics was also examined because carbon dioxide showed an influence on the growth behaviour of *C. glutamicum* (Blombach et al., 2013). Data for *C. glutamicum* were obtained from chemostat experiments with several growth rates and partial pressure of carbon dioxide which were analysed by flow cytometry. Cultivation and data analysis is described in Eilingsfeld et al. (2020).

## 6.2 Model setup

An overview of the cell cycle model is given in figure 6.1. The method requires the measurement of single cells via flow cytometry analysis. The DNA content of thousands of bacteria was detected to obtain a distribution of cells containing a specific DNA content. Thereby, subpopulations with one, two or more chromosomes were identified. The samples were derived from various chemostat experiments, where different growth rates and partial pressures of carbon dioxide were installed. Data acquisition, analysis and processing is described in Eilingsfeld et al. (2020). With the help of the cell cycle model  $C_c$  and  $D_c$  phase duration was estimated by fitting the model to the experimentally obtained DNA content distribution in MATLAB (MATLAB R2019a, The MathWorks, Inc., USA). The doubling time was set according to the installed growth rate. As the experimental data contained some noise, the standard deviation for the frequency distribution was also estimated. In the end a function for the replication phase duration dependent on the installed environmental conditions was obtained.

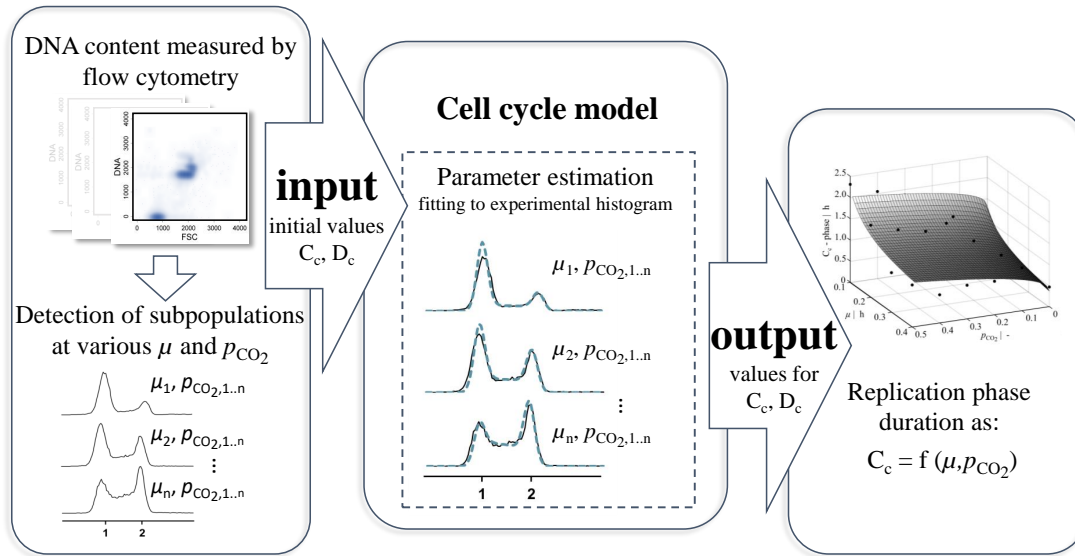


**Figure 6.1: Cell cycle model overview.** DNA histograms of several chemostat experiments installing different growth rates  $\mu$  and partial pressures of carbon dioxide  $p_{CO_2}$  were measured and served as input for the cell cycle model. Parameters were varied until the model fitted the experimental data best. In the end a function to describe replication phase dependent on  $\mu$  and  $p_{CO_2}$   $C_c = f(\mu, p_{CO_2})$  was derived.

A step by step description of the model is given in the following. The basic structure of the cell cycle model is presented in figure 6.2. The upper row (A - C) describes the scheme for a standard fork division cycle and the lower row (E - F) for a multifork division cycle. The model consists of an age distribution  $n(a)$  (figure 6.2 A and D), giving the frequency of cells in an specific age as:

$$n(a) = \ln 2 \cdot 2^{1-a} \quad 0 \leq a \leq 1 \quad (6.1)$$

It is assumed that cells grow from age zero to age one. For a standard fork division cycle, the cell cycle starts with the  $B_c$  phase. At the cell age  $a_1$  the initiation of replication phase  $C_c$  begins until the termination age  $a_2$  is reached. The time for cell division is denoted as  $D_c$  phase. For a multifork cell division cycle overlapping  $C_c$  phases may lead to a termination event of the previous generation within one doubling time before the initiation of the next cycle starts. As a consequence of binary fission, there are twice as much new born cells ( $a = 0$ ) compared to dividing cells ( $a = 1$ ). The function was normalised as follows:

$$\int_0^1 n(a) da = 1 \quad 0 \leq a \leq 1 \quad (6.2)$$

According to Cooper & Helmstetter (1968) the movement of the replication fork and therefore the DNA accumulation rate  $\frac{dG(a)}{da}$  is constant between initiation and termination. The DNA synthesis is described as a step function with the discontinuities initiation and termination. The initiation

and termination age is calculated by equation 6.3. Here  $a_1$  and  $a_2$  account for the events when initiation and termination occur. The parameter  $x$  refers to the integral number of division cycles in which replication  $C_c$  and division  $D_c$  ( $C_c + D_c$ ) take place,  $\tau_d$  describes the doubling time.

$$a_1 = (x \tau_d - (C_c + D_c))/\tau_d \quad (6.3a)$$

$$a_2 = (\tau_d - D_c)/\tau_d \quad (6.3b)$$

The theoretical chromosome content per cell  $G$  in the three intervals was calculated by equation 6.4.

$$G(a) = k_d(F_1 a + F_3) + a_1 k_d(F_1 - F_2) + a_2 k_d(F_2 - F_3) \quad 0 \leq a \leq a_1 \quad (6.4a)$$

$$G(a) = k_d(F_2 a + F_3) + 2a_1 k_d(F_1 - F_2) + a_2 k_d(F_2 - F_3) \quad a_1 \leq a \leq a_2 \quad (6.4b)$$

$$G(a) = k_d(F_3 a + F_3) + 2a_1 k_d(F_1 - F_2) + 2a_2 k_d(F_2 - F_3) \quad a_2 \leq a \leq 1 \quad (6.4c)$$

With  $k_d$  as DNA synthesis rate  $k_d = \frac{\tau}{2C}$  and  $F_i$  as number of replication forks in the  $i$ th interval (Skarstad et al., 1985; Fossum et al., 2007). The course of the theoretical DNA content for standard fork cell division is shown in figure 6.2 B. For a standard cell cycle division, the cells start with one chromosome, then DNA replication follows until the cells contain two chromosomes. For a multifork division cycle, initiation may already have started in the previous generation leading to overlapping replication phases (see figure 6.2 E).

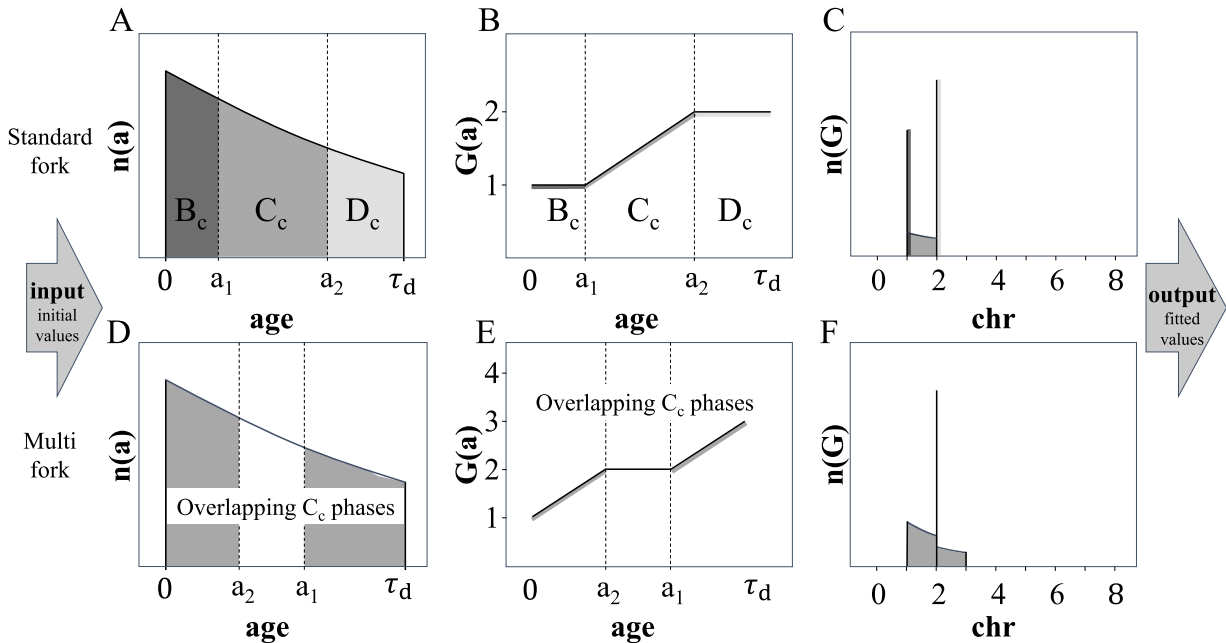


**Figure 6.2: Principle of the cell cycle model.** Upper row: standard fork division cycle. Lower row: multifork division cycle. (A, D) Age distribution with the x-axis as cell age (from 0 up to  $\tau_d$ ) and the y-axis as frequency of cells in a specific age  $n(a)$ . Initiation  $a_1$  and termination  $a_2$  age are shown exemplarily. (B, E) Accumulated DNA  $G(a)$  per cell as function of the cell age. (C, F) Frequency distribution of cells  $n(G)$  containing a specific chromosome number.

Linking the age distribution  $n(a)$  to the cellular accumulation of DNA  $n(G)$  results in the theoretical DNA histogram. In intervals of ongoing DNA synthesis, the fraction of a culture having an age between  $a$  and  $a + \Delta a$  equals the fraction having DNA contents between  $G$  and  $\Delta G$ .

$$n(G)dG = n(a)da \quad (6.5a)$$

$$n(G) = \frac{n(a)}{\frac{dG}{da}} \quad (6.5b)$$

Substituting  $n(a)$  and  $\frac{dG}{da}$  through equation 6.1 and the derivation of 6.4 results in equation 6.6.

$$n(G) = 2 \frac{\ln 2}{k_d F_1} e^{\frac{-\ln 2}{k_d F_1} [G - k_d F_3 - a_1 k_d (F_1 - F_2) - a_2 k_d (F_2 - F_3)]} \quad G_0 \leq G \leq G_1 \quad (6.6a)$$

$$n(G) = 2 \frac{\ln 2}{k_d F_2} e^{\frac{-\ln 2}{k_d F_2} [G - k_d F_3 - 2a_1 k_d (F_1 - F_2) - a_2 k_d (F_2 - F_3)]} \quad G_1 \leq G \leq G_2 \quad (6.6b)$$

$$n(G) = 2 \frac{\ln 2}{k_d F_3} e^{\frac{-\ln 2}{k_d F_3} [G - k_d F_3 - 2a_1 k_d (F_1 - F_2) - 2a_2 k_d (F_2 - F_3)]} \quad G_2 \leq G \leq G_3 \quad (6.6c)$$

Here, only the replicating cells are considered. Cells with constant DNA level (one chromosome and two chromosomes) have to be calculated separately. In Skarstad et al. (1985) a delta function  $\delta(x)$  to depict the DNA distribution is used. The exponential function can be substituted by  $f_i \cdot \delta(G - G_i)$ , in which  $G_i$  is the cellular DNA content and  $f_i$  the fraction of cells in the  $i$ th interval. This fraction is calculated by equation 6.7.

$$\int_{a_{i-1}}^{a_i} n(a) da = 1 \quad i = 1, 2, 3; \quad a_0 = 0; \quad a_3 = 1 \quad (6.7)$$

In an exponentially growing culture there are slight differences of individual doubling times. Therefore a biological variation of 5 % was considered, so that in total 30 individual cells with individual doubling time were included (Skarstad et al., 1985). The histograms for the individual cells were calculated, weighted and added up channel by channel to get a resulting DNA histogram for the whole culture. The theoretical DNA distribution was then convoluted with a normal distribution by assuming that the methodological variation of each DNA value can be represented by a normal distribution (see equation 6.8). The methodological variation of each DNA ( $n(G_j)$ ) value can be represented by a normal distribution  $y_{\text{sim}}(x_i)$  in channel  $x_i$ :

$$y_{\text{sim}}(x_i) = \sum_{j=1}^m n(G_j) \frac{1}{\sigma \sqrt{2\pi}} e^{-0.5 \left( \frac{x_i - x_j}{\sigma} \right)^2} \quad (6.8)$$

with  $n(G_j)$  as number of cells in channel  $x_j$  and  $m$  as the total number of channels taken into account when calculating the convolution in channel  $x_j$ .

Parameter estimation was performed as least square fit by minimising the sum of the squares of the residuals between experimental ( $y_{\text{exp}}$ ) and simulated histograms ( $y_{\text{sim}}$ ). The measure of goodness of the fit was chosen referring to the work of Skarstad et al. (1985) with  $m$  individual data points of  $y_{\text{exp}}$  and  $y_{\text{sim}}$  :

$$s = \sqrt{\frac{\sum_{j=1}^m (\sqrt{y_{\text{exp}}} - \sqrt{y_{\text{sim}}})^2}{m - 1}} \quad (6.9)$$

For the parameter estimation a patternsearch algorithm in MATLAB was applied upfront to narrow the parameter space. Subsequently, a parameter estimation was performed by discretising the obtained parameter space. The 99 % confidence interval was determined for each parameter.

Parameter estimation for cell cycle durations of *P. putida* was based on the work of Lieder et al. (2016). Here, the replication phase  $C_c$  was determined for chemostat experiments installing different growth rates ( $\mu = [0.1, 0.2, 0.3, 0.4, 0.5, 0.6] \text{ h}^{-1}$ ). Thus, the cell cycle duration was determined as function of the growth rate.

The  $C_c$ -phase duration for *C. glutamicum* was determined for different growth rates ( $\mu = [0.1, 0.2, 0.3, 0.4] \text{ h}^{-1}$ ) as well as different partial pressure of carbon dioxide ( $p_{\text{CO}_2} = [0.04\%, 10\%, 20\%, 30\%, 40\%, 50\%]$ ) with  $p_{\text{CO}_2} = 0.04\%$  denoted as reference process. Data acquisition for the *C. glutamicum* case is described in Eilingsfeld et al. (2020). Furthermore, a function  $C_c = f(\mu, p_{\text{CO}_2})$  was determined.

## 6.3 Results and discussion

The results of replication phase estimation by the previously described cell cycle model are displayed for the following two cases. The first case shows the fitted histograms for *P. putida* based on the work of Lieder et al. (2016). A function for the replication phase dependend on substrate availability  $C_c = f(\mu)$  was derived from flow cytometry data of chemostat experiments installing six different growth rates as described in 6.2. The second case deals with the cell cycle modification of *C. glutamicum* due to varying substrate availability and different partial pressures of carbon dioxide. Data were obtained by chemostat experiments installing respective conditions. Bioreactor cultivations and flow cytometry data analysis are described in Eilingsfeld et al. (2020). A function was fitted to calculate the replication phase duration  $C_c = f(\mu, p_{\text{CO}_2})$ .

### 6.3.1 Cell cycle phases of *P. putida*

The results of parameter estimation for replication phase duration of *P. putida* are displayed in figure 6.3 (A). Here, the frequency distribution of a specific DNA content or number of chromo-

some equivalents obtained by flow cytometry data analysis is shown for six distinct growth rates. Experimental histograms are drawn as solid lines and fitted histograms as dashed lines. For small growth rates ( $\mu = 0.1 \text{ h}^{-1}$ ) most cells within the population contain one chromosome. With increasing growth rate ( $\mu = 0.3 \text{ h}^{-1}$ ) the distribution is shifted to a state where most cells within the population are either replicating cells or contain two chromosomes. Multiphase replication started for cells growing between  $\mu = 0.3 \text{ h}^{-1}$  and  $\mu = 0.4 \text{ h}^{-1}$  because the histograms showed a shift towards more than two chromosomes equivalents and the estimated sum of  $C_c$  and  $D_c$  was higher than the doubling time (for more information see Lieder et al. (2016)).

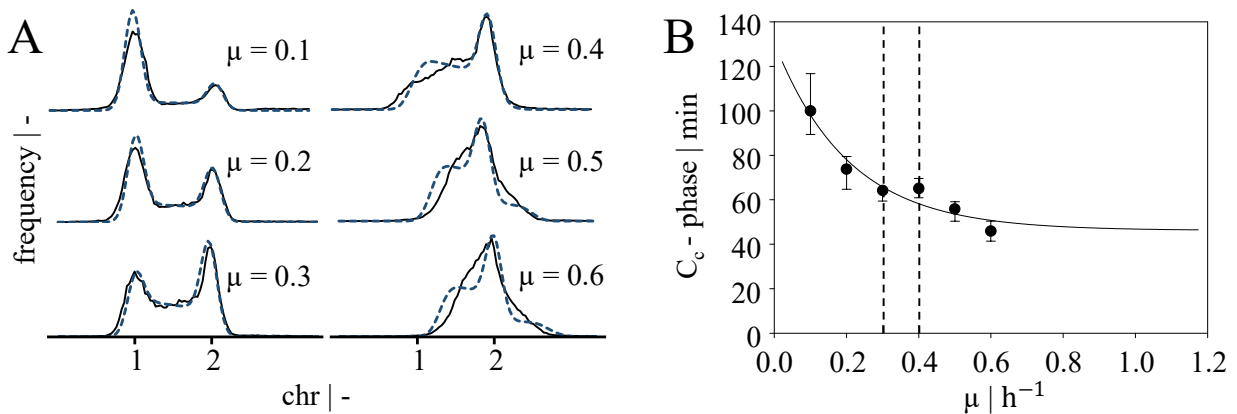


**Figure 6.3: Cell cycle phases for *P. putida*.** A) Experimental (solid line) and simulated (dashed line) frequency distribution of cells having a specific chromosome content chr (here one or two chromosomes). B) Replication phase duration  $C_c$  as function of the growth rate  $\mu$ . Transition between standard and multifork replication is marked with two dashed lines.

Figure (B) displays the fitted correlation for the replication phase  $C_c$  dependent on the growth rate  $\mu$ . The function  $C_c = f(\mu)$  was fitted by the following equation proposed by Keasling et al. (1995):

$$C_c = C_{c,\min} \left( 1 + a_{\text{fit}} e^{\frac{b_{\text{fit}}}{\tau_d}} \right) \quad (6.10)$$

with  $C_{c,\min} = 46.2 \text{ min}$  as the minimal  $C_c$ -period and  $a_{\text{fit}} = 1.83$  and  $b_{\text{fit}} = 3.38$  as parameter to fit the experimental data (Kuschel et al., 2017). The fit resulted in a squared residual of  $R^2 = 0.94$ . The replication phase duration decreases from about 100 min with increasing growth rate and converges to a constant value of 46.2 min. As the DNA polymerase activity is limited, DNA replication can not be further accelerated and multifork replication starts in order to enable short doubling times and thereby fast cell growth. The transition point between  $\mu = 0.3 \text{ h}^{-1}$  and  $\mu = 0.4 \text{ h}^{-1}$  is marked as dashed lines. The minimal obtained replication phase duration for *P. putida* is longer compared to *E. coli* (40 min) due to the 1.3 times higher genome size of *P. putida*. The obtained function can be combined with CFD to describe heterogeneity within a large scale bioreactor. More information are given in chapter 7.

### 6.3.2 Cell cycle phases of *C. glutamicum*

The results of the parameter estimation for cell cycle phases of *C. glutamicum* are listed in table 6.1. The replication ( $C_c$ ) and division ( $D_c$ ) phases were fitted for different environmental conditions as described in 6.2. The standard deviation of the resulting Gaussian distribution was also fitted and was less than 20 % except for two samples. The time prior to initiation of replication ( $B_c$  phase) was calculated as  $B_c = \tau_d - C_c - D_c$ . Irrespectively of the carbon dioxide content, all samples showed decreasing duration of cell cycle phases with increasing growth rate. This trend was also shown for *E. coli* and *P. putida* (Helmstetter, 1996; Lieder et al., 2016). In fact, the  $B_c$  period diminished for higher doubling rates. The duration of the  $B_c$  phase is coupled to a critical cell mass, which is reached much faster under nutrient rich conditions (Donachie, 1968). If the duration of replication and cell division is longer than the actual doubling time, the cells start to perform multifork replication as described in section 6.1. A stagnant replication duration and thereby the start of multifork replication was shown to occur at a growth rate of  $\mu = 0.4 \text{ h}^{-1}$  for *E. coli* and *P. putida*. As the doubling time under reference conditions for a growth rate of  $\mu = 0.4 \text{ h}^{-1}$  for *C. glutamicum* is also slightly smaller than the sum of  $C_c$  and  $D_c$  phase, multifork replication is also suggested to start for  $\tau_d < 1.7\text{h}$  for *C. glutamicum*. The generally shorter replication phases of *C. glutamicum* ( $C_c(\mu = 0.2 \text{ h}^{-1}) \approx 0.62 \text{ h}$ ) compared to *E. coli* ( $C_c(\mu = 0.2 \text{ h}^{-1}) \approx 1.66 \text{ h}$ ) and *P. putida* ( $C_c(\mu = 0.2 \text{ h}^{-1}) \approx 1.3 \text{ h}$ ) for identical doubling rates may be attributed to the smaller genome size (Koppes et al., 1978). While the genome size for *E. coli* K12 is 4.6 Mb and 6.18 Mb for *P. putida* KT2440, *C. glutamicum* possesses with 3.3 Mb a 1.4 times smaller genome than *E. coli* K12. However the division phase of *C. glutamicum* ( $D_c(\mu = 0.2 \text{ h}^{-1}) \approx 2.28 \text{ h}$ ) seems to be elevated compared to other organisms under reference conditions (*E. coli* ( $D_c(\mu = 0.2 \text{ h}^{-1}) \approx 0.28 \text{ h}$ ), *P. putida* ( $C_c(\mu = 0.2 \text{ h}^{-1}) \approx 1.0 \text{ h}$ )). A possible explanation for this might be the occurrence of the V-snapping division for *C. glutamicum* (Letek et al., 2008), where cells grow as pairs tending to stick together for a long time period.

Remarkably, replication phases of the carbon dioxide stressed samples are significantly higher compared to the reference sample. While the replication phases for  $p_{\text{CO}_2} = 0.04\%$  range from  $C_c = 1 \text{ h}$  to  $C_c = 0.5 \text{ h}$  for  $\mu = 0.1$  to  $\mu = 0.4 \text{ h}^{-1}$ , replication phases are prolonged by factor two for partial pressures of carbon dioxide of 10%. With increasing  $p_{\text{CO}_2}$ , the duration of replication phase increases furthermore up to  $C_c = 2.3 \text{ h}$  for  $p_{\text{CO}_2} = 50\%$  and  $\mu = 0.1 \text{ h}^{-1}$ . For higher growth rates at elevated  $p_{\text{CO}_2}$ , the replication reached a minimal time of  $C_c \approx 1 \text{ h}$ . As a consequence, carbon dioxide stress seems to decelerate the DNA synthesis process. Carbon dioxide can diffuse into the cells and lower the intracellular pH value (Gutknecht et al., 1977). A reduced pH may inhibit the speed of the DNA polymerase to some extent (Eckert & Kunkel, 1993; Sabatino et al., 1988). This would furthermore explain the occurrence of multifork replication already at a growth rate of  $\mu = 0.2 \text{ h}^{-1}$  (here  $C_c + D_c > \tau_d$ ).

**Table 6.1: Results of cell cycle phases for *C. glutamicum*.** Replication ( $C_c$ ) and division ( $D_c$ ) phase for different growth rates ( $\mu = [0.1, 0.2, 0.3, 0.4] \text{ h}^{-1}$ ) and partial pressures of carbon dioxide ( $p_{\text{CO}_2} = [0.04\%, 10\%, 20\%, 30\%, 40\%, 50\%]$ ) with  $p_{\text{CO}_2} = 0.04\%$  as reference determined by the model. The time before initiation of replication  $B_c$  was calculated accordingly. The parameter  $s$  is a measure of goodness of fit (Skarstad et al., 1985).

Sample	$C_{c,\text{fit}}$ [ $C_{c,\text{min}}$ , $C_{c,\text{max}}$ ] in [h]	$D_{c,\text{fit}}$ [ $D_{c,\text{min}}$ , $D_{c,\text{max}}$ ] in [h]	$B_{\text{calc}}$ [ $B_{\text{min}}$ , $B_{\text{max}}$ ] in [h]	$s$
REF_0.1	1.06 [0.99, 1.08]	5.37 [5.23, 5.44]	0.51 [0.40, 0.71]	1.26
REF_0.2	0.62 [0.52, 0.71]	2.28 [2.24, 2.39]	0.56 [0.37, 0.71]	3.01
REF_0.3	0.48 [0.48, 0.48]	1.81 [0.80, 1.81]	0.02 [0.02, 1.03]	1.42
REF_0.4	0.48 [0.48, 0.48]	1.28 [1.28, 1.40]	0.00 [0.00, 0.00]	1.23
p10_0.1	1.57 [1.52, 1.68]	4.91 [4.79, 4.99]	0.45 [0.26, 0.62]	3.53
p10_0.2	1.01 [0.98, 1.10]	2.48 [2.45, 2.51]	0.00 [0.00, 0.03]	1.98
p10_0.3	0.97 [0.92, 1.02]	1.36 [1.32, 1.39]	0.00 [0.00, 0.08]	3.55
p10_0.4	1.02 [0.95, 1.07]	1.15 [1.13, 1.21]	0.00 [0.00, 0.00]	3.57
p20_0.1	1.69 [1.61, 1.81]	3.82 [3.75, 3.87]	1.42 [1.26, 1.58]	3.17
p20_0.2	1.62 [1.51, 1.62]	1.76 [1.71, 1.82]	0.09 [0.02, 0.24]	2.44
p20_0.3	1.40 [1.35, 1.40]	1.42 [1.40, 1.48]	0.00 [0.00, 0.00]	2.89
p20_0.4	0.80 [0.79, 0.85]	1.38 [1.36, 1.42]	0.00 [0.00, 0.00]	2.00
p30_0.1	1.87 [1.87, 1.87]	3.99 [3.99, 3.99]	1.07 [1.07, 1.07]	1.19
p30_0.2	1.37 [1.36, 1.45]	2.24 [2.21, 2.30]	0.00 [0.00, 0.00]	1.62
p30_0.3	1.91 [1.78, 2.00]	1.18 [1.12, 1.27]	0.00 [0.00, 0.00]	5.24
p30_0.4	0.80 [0.80, 0.87]	1.22 [1.18, 1.24]	0.00 [0.00, 0.00]	3.01
p40_0.1	2.05 [1.89, 2.07]	4.44 [4.35, 4.50]	0.44 [0.37, 0.69]	1.86
p40_0.2	1.50 [1.50, 1.53]	2.40 [2.37, 2.40]	0.00 [0.00, 0.00]	1.91
p40_0.3	0.74 [0.68, 0.79]	1.95 [1.95, 2.06]	0.00 [0.00, 0.00]	2.26
p40_0.4	0.67 [0.63, 0.74]	1.51 [1.46, 1.55]	0.00 [0.00, 0.00]	3.25
p50_0.1	2.31 [2.20, 2.47]	4.29 [4.16, 4.40]	0.33 [0.06, 0.56]	2.28
p50_0.2	1.70 [1.57, 1.78]	2.19 [2.14, 2.24]	0.00 [0.00, 0.00]	2.53
p50_0.3	0.94 [0.84, 1.00]	2.09 [2.00, 2.15]	0.00 [0.00, 0.00]	5.35
p50_0.4	1.00 [0.98, 1.00]	1.09 [1.07, 1.12]	0.00 [0.00, 0.00]	2.11

Alternatively, cells might increase ATP consuming transporter activity to apply countermeasures against decreasing intracellular pH values. Consequently, maintaining constant intracellular pH could also lead to increased cellular maintenance demands (Eigenstetter & Takors, 2017).

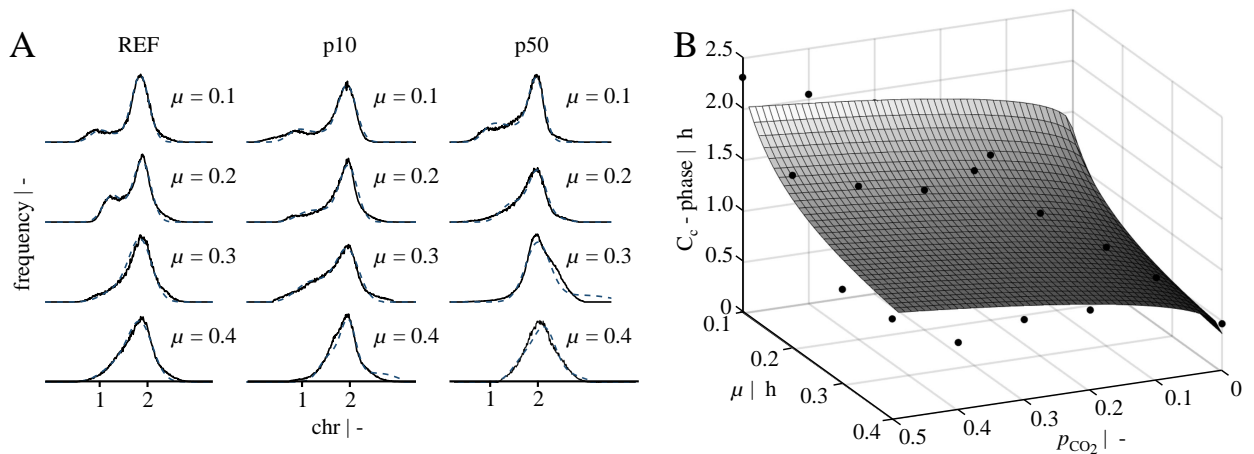


**Figure 6.4: Cell cycle phases for *C. glutamicum*.** A) Experimental (solid line) and simulated (dashed line) frequency distributions of cells having a specific chromosome content chr (here one or two chromosomes). Histograms for  $p_{\text{CO}_2} = 0.04\%$  (reference),  $p_{\text{CO}_2} = 10\%$  and  $p_{\text{CO}_2} = 50\%$  are exemplarily shown for all growth rates. B) Replication phase duration  $C_c$  as function of the growth rate  $\mu$  and partial pressure of carbon dioxide  $p_{\text{CO}_2}$ . Black dots indicate fitted values of table 6.1.

The parameter fit is depicted in figure 6.4 (A). Experimental and theoretical histograms for three different partial pressure of carbon dioxide  $p_{\text{CO}_2} = 0.04\%$  (reference),  $p_{\text{CO}_2} = 10\%$  and  $p_{\text{CO}_2} = 50\%$  are exemplarily shown for all growth rates. The parameter  $s$  in table 6.1 describes the goodness of each fit. The values for  $s$  are in the same range as shown in Skarstad et al. (1985). So the model reflects the experimental histograms very well.

A function for the replication phase dependent on growth rate and partial pressure of carbon dioxide  $C_c = f(\mu, p_{\text{CO}_2})$  was fitted to the values in table 6.1 via weighted least square fit with the parameter  $s$  as weighting factor. The surface plot of the obtained phenomenological model is shown in figure 6.4 B. The following function was obtained:

$$C_c = a_{\text{fit}} \frac{1}{\mu} + b_{\text{fit}} \frac{1}{p_{\text{CO}_2}^{c_{\text{fit}}}} \quad (6.11)$$

with  $a_{\text{fit}} = 0.1228$  [0.09999, 0.1455],  $b_{\text{fit}} = -0.422$  [-0.7584, -0.0857] and  $c_{\text{fit}} = 0.1546$  [-0.04751, 0.3567] as fitted parameter and a squared residual of  $R^2 = 0.9$ . Numbers in brackets indicate the 95 % confidence interval of the fit. As already discussed above, the  $C_c$  period decreases with increasing growth rate but increases with increasing  $p_{\text{CO}_2}$ .

## 6.4 Conclusion

External stress may lead to the division of a population into subpopulations possessing different properties. With the help of the cell cycle model subpopulations differing in their DNA content have been described for two cases. For *P. putida* the replication phase duration as function of growth rate was obtained on basis of the work of Lieder et al. (2016). The replication phase  $C_c$  was shown to decrease with increasing growth rate. Furthermore, the occurrence of multifork replication was shown to start for growth rates between  $0.3 \text{ h}^{-1} < \mu \leq 0.4 \text{ h}^{-1}$ . Similar results were obtained for *C. glutamicum*. The  $C_c$  period also showed a decrease with increasing growth rate but an increase with increasing partial pressures of carbon dioxide  $p_{\text{CO}_2}$ , showing that  $p_{\text{CO}_2}$  stress slows down the replication process. Noteworthy, in order to cope with the installed growth rate, multifork replication for *C. glutamicum* under elevated  $p_{\text{CO}_2}$  conditions was initiated already for growth rates of  $\mu = 0.2 \text{ h}^{-1}$  whereas under reference conditions *C. glutamicum* showed similar behaviour compared to *P. putida*. Combined with CFD the derived functions for the  $C_c$  period may help to describe population heterogeneity in large scale bioreactors.



---

## 7 Heterogeneity analysis in large scale

The occurrence of spatial substrate distribution triggers cellular adaptations to changing environmental conditions and may finally lead to the formation of a heterogeneous culture within an industrial scale bioreactor. Yet, this complex topic is not completely understood and improvements in strain engineering, reactor design and fermenter operation can be achieved if more information about cellular response towards concentration gradients in large scale reactors becomes available. In this chapter, heterogeneity in a single and multiphase scenario of an industrial fed-batch fermentation was examined in two separate case studies performed with the help of computational fluid dynamics. The first case depicts a glucose gradient in a 54 m<sup>3</sup> bioreactor occurring during a fed-batch scenario of *Pseudomonas putida* KT2440. A bacterial lifeline analysis combined with the cell cycle model of chapter 6 resulted in at least 72 % of the bacterial population showing quick metabolic responses and 10 % being likely to undergo massive transcriptional changes. Moreover, two types of responses were formulated: a short term response in terms of altered ATP consumption leading to 52.9 % with higher ATP maintenance demands than the average and a long term response of cells possessing different cell cycle strategies. For the latter subpopulations of cells with distinct replication phase durations were identified. The second case deals with a scale-up of the multiphase simulation from chapter 4 and 5 up to a total volume of 22 m<sup>3</sup>, where a late fed-batch phase of *Corynebacterium glutamicum* ATCC13032 was examined. Identical compartmentalisation was found for large scale, which suggest similar scale-down devices to examine the influence of limitation zones in large scale on bacterial behaviour. Furthermore, first approaches for carbon dioxide balancing were considered. Both cases show exemplarily the importance of the integration of biological readouts into scale-up considerations.

### 7.1 Introduction

The conservative strategy of scale-up relies on the calculation of physical parameters according to previously determined correlations (Mersmann et al., 1975; Van't Riet, 1979; Nienow, 1997; Moucha et al., 2003). In single phase, these predictions are usually very precise, whereas in multiphase special considerations have to be taken into account. For instance, mixing times in loading regimes will quite differ from mixing times in flooding regimes (Vasconcelos et al., 1995;

Alves & Vasconcelos, 1995). Additionally, the correct prediction of overall physical parameter does not necessarily lead to consistent process performance. In fact a simple “1:1 approach”, keeping all parameters constant at the same time is typically not possible. Due to decreased mixing quality vertical and radial oxygen gradients as well as carbon source gradients might arise causing local limitations zones and thereby reduced production performance. Only few industrial scale data are available owing to high experimental costs or because data are intellectual property of the companies. A brief summary is given in chapter 2 section 2.2.

To shed light on the complex interplay of physical, chemical and biological factors, approaches in the recent years include computational fluid dynamics as aiding tool for scale-up considerations (Haringa et al., 2016; Haringa et al., 2017a). In the previous chapters organism specific parameters as well as physical parameters of a fermentation process have been collected to setup such simulations or to validate the results. A pilot scale reactor was examined in multiphase, a suitable simulation setup was found and a gradient of oxygen and glucose occurring during a late fed-batch of *C. glutamicum* was depicted (Kuschel & Takors, 2020). Furthermore, a sufficient grid density was determined not only to describe physical parameters but also biological readouts. The chapter aims to display techniques to include the influence of organisms specific behaviour into scale-up considerations exemplarily for two distinct case studies. The first case deals with a single phase simulation of a fermentation process of *P. putida* in a 54 m<sup>3</sup> bioreactor. It presents an example to include a biological response towards changing substrate availability in form of modified replication phase durations. This case combines computational fluid dynamics with the cell cycle model from chapter 6 to account for substrate induced population heterogeneity within a large scale fermentation and is based on Kuschel et al. (2017). The second case presents a scale-up of the multiphase pilot scale simulation of chapter 4 and 5. The compartmentalisation for identical biological kinetic but slightly different operational conditions is described and the basis of carbon dioxide mass balance is included.

## **7.2 Material and methods**

The reactor setup for two case studies is described in the following. The first case study was conducted for a fermentation scenario of *Pseudomonas putida* KT2440 in a 54 m<sup>3</sup> bioreactor and is based on Kuschel et al. (2017). The second case study describes a fed-batch process with *Corynebacterium glutamicum* ATCC13032 and results from the scale-up of the pilot scale reactor in chapter 4 and 5 up to a volume of 22 m<sup>3</sup>.

### 7.2.1 Case 1: Single phase with *P. putida*

#### Geometry and reactor setup

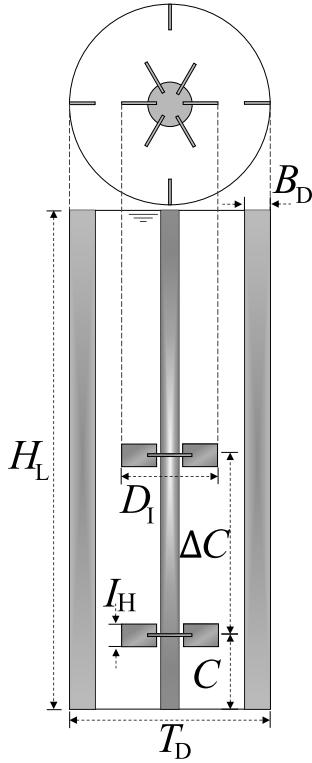


**Table 7.1: Setup of the 54 m<sup>3</sup> reactor.** Geometry of the 54 m<sup>3</sup>, operational conditions, media properties and organism specific parameters are listed in the table. Measures are displayed in figure 7.1. Modified to Kuschel et al. (2017).

Description	Symbol	Unit
Liquid height	$H_L$	7.7 m
Tank diameter	$T_D$	3 m
Impeller diameter	$D_I$	1.3 m
Off-bot. impeller clearance	$C$	0.9 m
Impeller clearance	$\Delta C$	3 m
Baffle diameter	$B_D$	0.3 m
Impeller height	$I_H$	0.27 m
Media density	$\rho_L$	995.7 kg m <sup>-3</sup>
Media viscosity	$\eta_L$	0.0008 Pa s
Temperature	$\vartheta$	30 °C
Agitation rate	$N$	100 rpm
Feeding rate	$F$	0.738 kg <sub>S</sub> kg <sub>CDW</sub> <sup>-1</sup> h <sup>-1</sup>
Biomass concentration	$c_X$	10 kg <sub>CDW</sub> m <sup>-3</sup>
Yield (biomass/substrate)	$Y_{XS}$	0.4 kg <sub>CDW</sub> kg <sub>S</sub> <sup>-1</sup>
Half saturation constant	$K_S$	0.01 kg <sub>S</sub> m <sup>-3</sup>
Growth rate (max)	$\mu$	0.59 h <sup>-1</sup>

**Figure 7.1: Geometry of the 54 m<sup>3</sup> reactor.** Tank was equipped with four baffles and two turbines containing eight (bottom) and six blades (top).

The reactor geometry was originally derived from Haringa et al. (2016) and was slightly modified for this study. A schematic diagram is depicted in figure 7.1, dimensions are listed in table 7.1. With a total volume of 54 m<sup>3</sup> the setup consisted of four baffles and two Rushton impellers equipped with eight (bottom) and six blades (top) blades. The feeding rate was set to half of the maximum uptake rate  $q_{S,max}$ . Media properties as well as operational conditions are also listed in table 7.1. This study deals with a large scale single phase simulation, therefore no gassing was installed and aeration, gas transfer as well as oxygen uptake were neglected. A simple Monod kinetic served to mimic substrate consumption in the liquid phase. Growth parameters of *Pseudomonas putida* can be extracted from table 7.1.

## Simulation setup

Numerical simulations were conducted using the commercial software ANSYS® Fluent 17.0 . A grid size of 445,000 polyhedral cells resulted in the same circulation times as achieved by Haringa et al. (2016), therefore no further mesh refinement was performed. Inner geometries were modelled in 3D. The flow field was approximated by the RANS standard k- $\epsilon$  model including sliding mesh motion to account for the impeller rotation. Standard wall functions were employed. All surfaces were set to no-slip boundary conditions, except for the frictionless top area, which mimicked a free surface. Simulations were performed in transient mode with a time step size of  $\Delta t = 0.01$  s. Glucose was fed from the reactor top until a steady glucose concentration was reached. Transport, turbulence and glucose concentration equation were disabled, and further analysis was performed on frozen flow field similar to chapter 5.2.2. In total, 120,000 bacterial cells were introduced as massless Lagrangian particles and tracked over 260 s. Based on the ergodic theorem, tracking 1,560,000 bacteria for 20 s (the approximate circulation time) results in the same average values. The discrete random walk (DRW) model was enabled. The position and encountered glucose concentration were recorded every 30 ms.

## Statistical evaluation

Potential growth profiles of each bacterium were calculated from recorded glucose profiles and smoothed by a moving average filter as well as an additional 1D filter to remove rapid sequential regime transitions smaller than 0.09 s. Both filtering steps caused deviations from the raw data of less than 5 %. The filtered signal was translated into regime transitions. Regimes were classified according to the replication strategy of *P. putida* at a specific growth rate. For further information on growth specific cell cycle dynamics see chapter 6. Following regimes were defined: a standard forked replication regime S for  $\mu \leq 0.3 \text{ h}^{-1}$ , the transition area T ( $0.3 < \mu < 0.4 \text{ h}^{-1}$ ), and a multifork replication regime M for  $\mu \geq 0.4 \text{ h}^{-1}$ . Six specific regime transition patterns were defined as indicated in figure 7.2. A growth rate distribution was derived by averaging the obtained growth rates of each lifeline for 20 s. Combined with the cell cycle model described in chapter 6 (equation 6.10) the growth profiles were translated into a distribution of potential  $C_c$ -phase duration. Additionally, Adenosine triphosphate (ATP) consumption was estimated according to Pirt's law (Pirt, 1965):

$$q_{\text{ATP}} = \frac{\mu}{Y_{\text{XATP}}} + m_{\text{ATP}} \quad (7.1)$$

with  $m_{\text{ATP}} = 3.96 \text{ mmol}_{\text{ATP}} \text{ g}_{\text{CDW}}^{-1} \text{ h}^{-1}$  as nongrowth-associated maintenance and  $Y_{\text{ATP}} = 0.0118 \text{ g}_{\text{CDW}} \text{ mmol}_{\text{ATP}}^{-1}$  as growth associated maintenance for *P. putida* (Duuren et al., 2013).

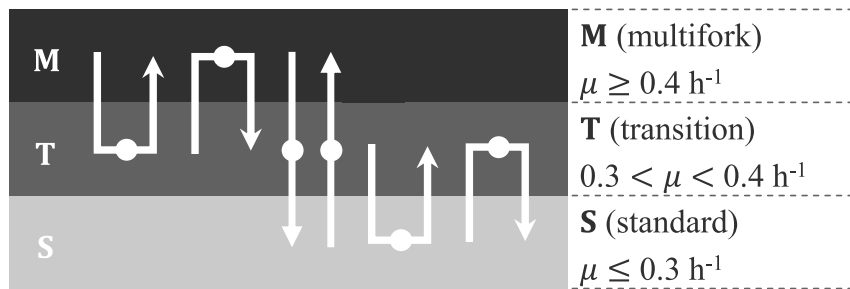


**Figure 7.2: Regime transition patterns for the 54 m<sup>3</sup> reactor.** MTM: Particle starts and ends in multifork regime with a dwelling time in the transition area. TMT: Reverse event starting in the transition area with retention in multifork regime. MTS: transition from multi to standard fork regime with retention time in transition area. STM: Particle traverses all regimes from low standard to multifork. TST: Circulation from transition over standard fork back to transition area. STS: Reverse movement from standard to transition back to standard fork regime. The second capital letter always indicates the area in which the retention time  $\tau$  was measured.

### 7.2.2 Case 2: Multiphase with *C. glutamicum*

#### Scale-up of reactor geometry and gradient simulation

The volume of the pilot scale bioreactor from chapter 4 was scaled by factor 100. Scale-up criteria were chosen to be a constant height to diameter ( $H_1/T_D = 2.17$ ) ratio as well as the same impeller diameter to reactor diameter ( $D_1/T_D = 0.41$ ) ratio. The gas volume flow per liquid volume per minute was kept to 0.25 vvm. Choosing superficial gas velocity as scale-up criterium would have resulted in a gas volume flow per liquid volume per minute of 0.05 vvm which was considered too low for a large scale *C. glutamicum* fermentation. A comparison between both setups is provided in table 7.2. The agitation rate was set to 100 rpm allowing for low power consumption but no flooding according to the critical flow numbers of Rosseburg et al. (2018) and Gezork et al. (2000) as well as Zlokarnik and Mikulcova summarized in Wiedmann (1983) with  $Fl$  being 0.062.

As no experimental gas hold up measurements for the industrial scale were available, a simulation with a very coarse mesh was conducted upfront to determine the gas hold up. Consequently, the liquid volume was increased by 9.16 %. The number of numerical cells with  $1.12 \cdot 10^5 \text{ \#}/m^3$  was chosen according to chapter 4 and 5. All other settings were exactly as described in chapter 4.4.2 (Multiphase Simulations). However, for stability reasons simulations were performed with the first order upwind scheme and a time step size of  $\Delta t = 0.0001 \text{ s}$ . Before switching to transient mode a steady solution was obtained until residuals were  $< 10^{-4}$  to accelerate simulation procedure. Transient simulations were performed until a steady overall gas volume fraction was reached. A scaling factor for the turbulent dissipation rate  $\varepsilon$  (see chapter 4.3.3) was included and the simulation was run until steady overall values were reached again. The reactions were included according to the guidelines described in chapter 5.2.1. Additionally to oxygen mass transfer and consumption,

carbon dioxide production and mass transfer was considered. Because the respiratory quotient ( $RQ$ ) of *C. glutamicum* was almost equal to one (see chapter 3.3.1), carbon dioxide production was implemented equally to oxygen consumption. Carbon dioxide mass transfer was implemented similar to oxygen mass transfer. A Henry coefficient of  $H_{CO_2}^{cp} = 2.89 \cdot 10^4 \text{ mol m}^{-3} \text{ Pa}^{-1}$  at  $30^\circ\text{C}$  was calculated from equation 5.2 taking the reference value at  $25^\circ\text{C}$  from Sander (2015). The mass transfer coefficient for carbon dioxide  $k_{LaCO_2}$  could be estimated from  $k_{LaO_2}$  according to the penetration theory of Higbie (1935) and the surface renewable model of Danckwerts (1951):

$$k_{LaCO_2} = k_{LaO_2} \sqrt{\frac{D_{CO_2}}{D_{O_2}}} \quad (7.2)$$

with  $D_{CO_2} = 2.0 \cdot 10^{-9} \text{ m}^2 \text{ s}^{-1}$  and  $D_{O_2} = 2.4 \cdot 10^{-9} \text{ m}^2 \text{ s}^{-1}$ . Reaction was initially simulated on steady flow field until a steady average concentration was reached. Then a transient solution was obtained until the average concentration reached a constant value and local values showed an oscillating behaviour.

**Table 7.2: Measures of the different scales.** Pilot scale and industrial scale conditions are listed.

Scale	$V_L$ [m <sup>3</sup> ]	T [m]	H [m]	D [m]
Pilot (exp)	0.198	0.488	1.06	0.2
Industrial	19.8	2.265	4.915	0.93

## 7.3 Results and discussion

The following results are divided in two case studies. The first study investigates a single phase large scale fed-batch fermentation with *P. putida*. Possible bacterial responses to environmental conditions are formulated by the inclusion of the cell cycle model. This case is based on Kuschel et al. (2017). The second case depicts a large scale multiphase gradient of a fed-batch scenario with *C. glutamicum* by scaling-up the bioreactor from chapter 4. Here, also the carbon dioxide balance is included.

### 7.3.1 Case 1: *P. putida*

A pseudostationary glucose gradient with an average glucose concentration of  $20 \text{ mg L}^{-1}$  was obtained. Theoretical growth rates for every numerical cell (Eulerian approach) were calculated resulting in an average growth rate of  $\bar{\mu} = 0.294 \text{ h}^{-1}$ . This is identical to expected growth rate

for the set feed rate ( $\bar{\mu} = 0.295 \text{ h}^{-1}$ ) ensuring no occurrence of mass imbalances. The glucose gradient depicted in figure 7.3 (A) is coloured by the potential cell cycle strategy of *P. putida* at a specific growth rate. Higher potential growth rates and therefore complexer replication strategies are obtained close to the feed port, whereas low glucose concentrations close to the reactor bottom lead to possible standard fork regimes. The corresponding flow field is presented in figure 7.3 (B). Around each impeller the typical flow field of a radial pumping Rushton turbine is visible. Compared to previous studies (chapter 4 and 5), the impeller spacing is high enough to obtain a parallel flow field, with the distinct inter impeller zone between the turbines. Figure 7.3 (C) shows two exemplary lifelines for 20 s with L1 crossing all regimes and L2 remaining in the standard fork regime. As the effect of oxygen was neglected in this study for simplicity, the underlying gradient was not expected to perfectly reflect the real experiment. However, with the help of such lifeline analysis it is possible to examine the effect of cell history or lag phases of the bacteria and thereby to determine a degree of heterogeneity within the reactor. The following section provides a statistical analysis of such lifelines.

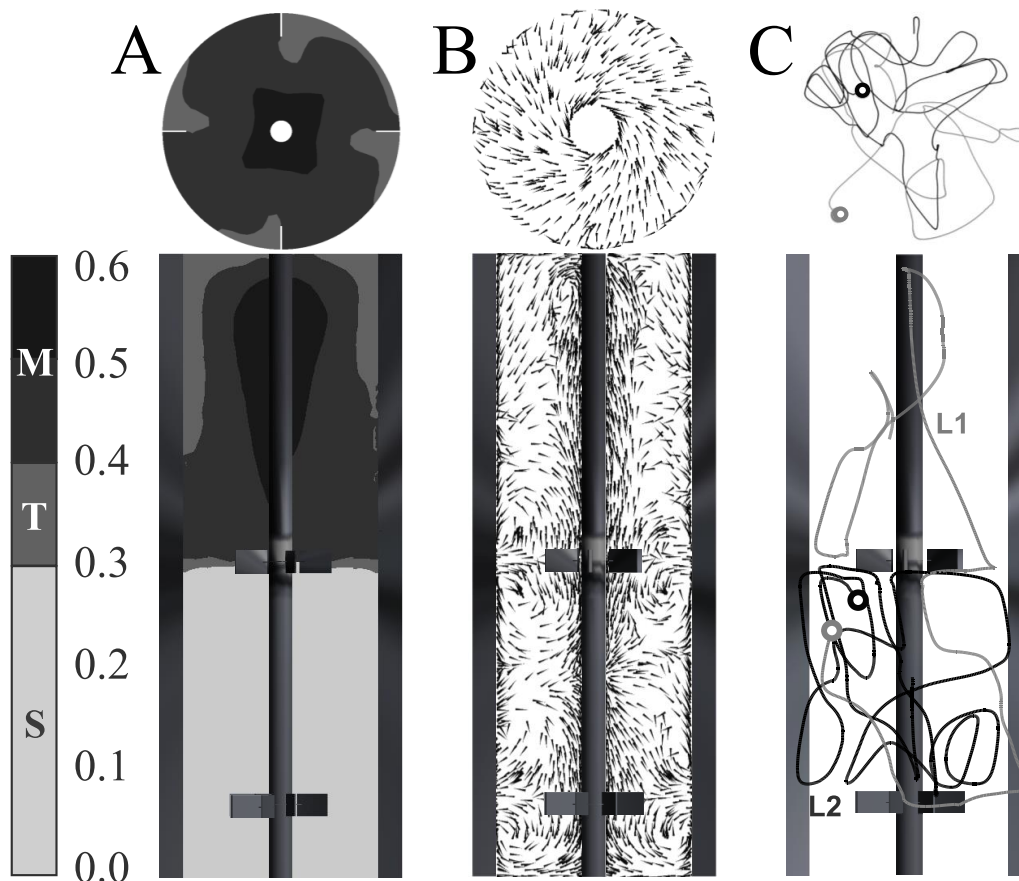


**Figure 7.3: Large scale ( $54 \text{ m}^3$ ) single phase gradient and lifelines.** A) Average glucose gradient calculated for 150 s, colored by regime classification strategy: standard forked replication regime S ( $\mu \leq 0.3 \text{ h}^{-1}$ ) in light grey, transition area T ( $0.3 < \mu < 0.4 \text{ h}^{-1}$ ) in grey, and multifork replication regime M for ( $\mu \geq 0.4 \text{ h}^{-1}$ ) in dark grey, B) Average flow field. C) Exemplary lifelines. Modified to Kuschel et al. (2017).

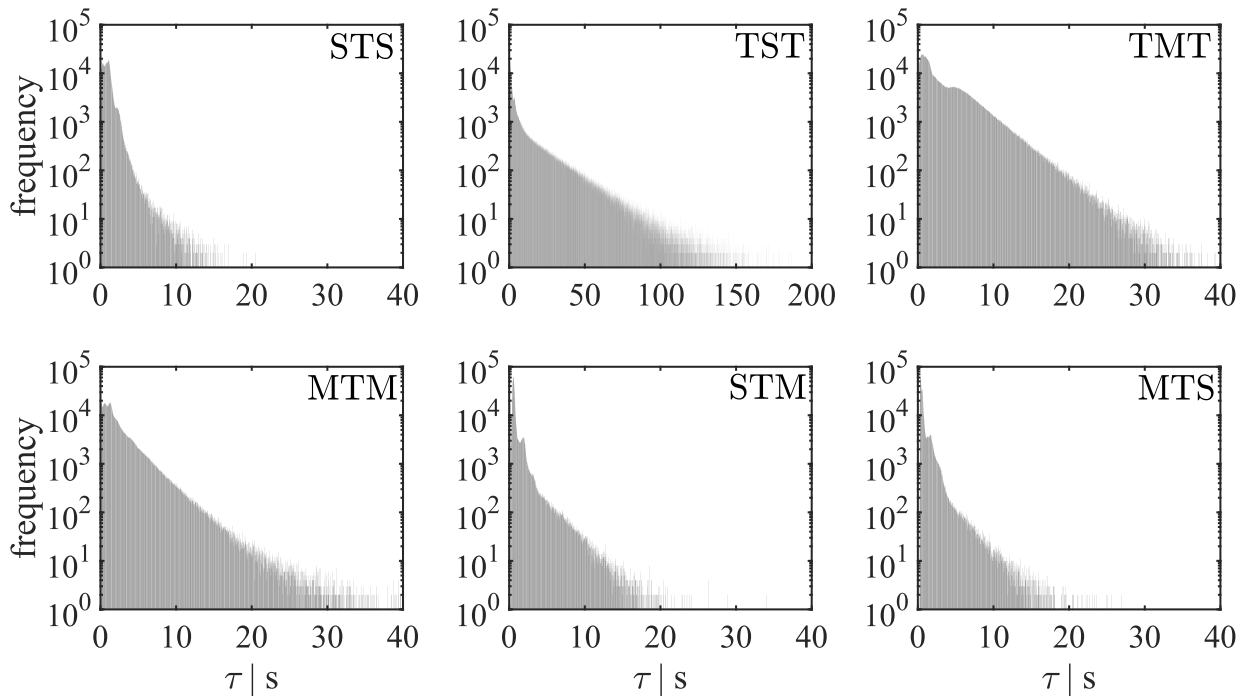


**Figure 7.4: Frequency distribution of regime transition strategy for the 54 m<sup>3</sup> reactor.** Regime transition strategy as function of the retention time  $\tau$ . The six possible patterns are shown as semi-log plot. The second capital letter always indicates in which regime  $\tau$  was measured. With modifications to Kuschel et al. (2017).

Paths of 120,000 bacterial cells were tracked for 260 s and growth rates for the recorded glucose profiles were calculated resulting in an average growth rate of  $\bar{\mu} = 0.269 \text{ h}^{-1}$  (Lagrangian approach). A deviation of only 8.5 % compared to the Eulerian approach assures that an adequate amount of particles was used. Processing of the lifelines is described only briefly. See also chapter 5 for further explanation. The growth profiles were filtered and translated into replication modulus curves according to the regime thresholds as explained in section 7.2.1. Considering the previous example, L1 in figure 7.3 (C) was exposed to high variations in glucose concentration, being likely to suffer metabolic consequences. In contrast, metabolic shifts for L2 were small and effects on the cell cycle could be excluded. Hence, within that given timescale bacteria sensed completely different environmental conditions and may start different metabolic or even transcriptomic programs finally initiating different replication strategies. Each adjustment will cost energy and could have an impact on process performance.

To evaluate the exposure times in the different regimes and the frequency of these transitions, all lifelines were evaluated according to the six regime transition patterns depicted in figure 7.2. The frequency distribution as function of the retention time in this regime  $\tau$  is presented in figure 7.4, table 7.3 lists the corresponding average  $\bar{\tau}$  and maximal  $\tau_{\max}$  retention times. In general, a strong decay after maximal 10 - 20 s and an average retention time of 1 - 3 s is visible for all transition patterns except for TST which showed dwelling times up to 73.5 s. In fact, the reason can be

**Table 7.3: Regime transition statistics for the 54 m<sup>3</sup> reactor.** Average  $\bar{\tau}$  and maximal  $\tau_{\max}$  retention times are listed for each regime transition pattern. The maximum  $\tau_{\max}$  was defined as the limit, within which 99 % of the values were located. With modifications to Kuschel et al. (2017).

Regime transition	$\bar{\tau}$ [s]	$\tau_{\max}$ [s]
STS	0.99	3.7
TST	8.54	73.5
TMT	3.53	16.25
MTM	2.45	13
STM	0.95	6.6
MTS	0.88	5.5

deduced from the flow field and the regime distribution (see figure 7.3). The radial pumping Rushton turbines cause large circulation loops above and below each impeller. Consequently, cells are trapped in the loops of the lower impeller provoking a long residence time in the substrate limited zone. As a result average retention times for the TST pattern are the longest  $\bar{\tau}_{TST} = 8.54$  s.

The afore mentioned statistics provide valuable information about the cellular history enabling the evaluation of the degree of heterogeneity within the fermentation process. When cells pass regimes of different concentrations they will adapt accordingly. While metabolic adaptations are known to be very rapid  $< 30$  s, fundamental transcriptional changes were measured by plug flow experiments after stress exposure times  $> 70$  s (Löffler et al., 2016). Considering these findings for regime analysis, all travellers from moderate to low substrate regimes were involved being prepared to switch from multi to standard fork replication (TS). During the observation window, 72.6 % of all cells carried out that move once and lingered more than 30 s in regime S, whereas 14.7 % stayed more than 70 s in regime S. By analogy, the transition from maximal to moderate substrate concentrations (MTS) resulted in 55.5 % to performing this move with retention times in moderate concentrations (regime T and S) longer than 30 s and 10.4 % with dwelling times more than 70 s respectively. Furthermore, two possible types of responses can be deduced.

Firstly, an instantaneous response occurring immediately after the stimulation such as a concentration fluctuation was considered. The response is assumed to be spatially coupled to the stimulus and includes all metabolic responses for instance glucose uptake or ATP production. The distribution of energy level is displayed in figure 7.5 (A). With an average ATP consumption rate of  $q_{\text{ATP,mean}} = 29.31 \text{ mmol}_{\text{ATP}} \text{ g}_{\text{CDW}}^{-1} \text{ h}^{-1}$  the values are obviously not evenly distributed, but rather exhibit an individual distribution according to the gradient. While only 6.3 % of all cells consumed ATP with  $q_{\text{ATP,mean}} = 29.31 \pm 2 \text{ mmol}_{\text{ATP}} \text{ g}_{\text{CDW}}^{-1} \text{ h}^{-1}$ , 40.8 % showed an reduced and 52.9 % an

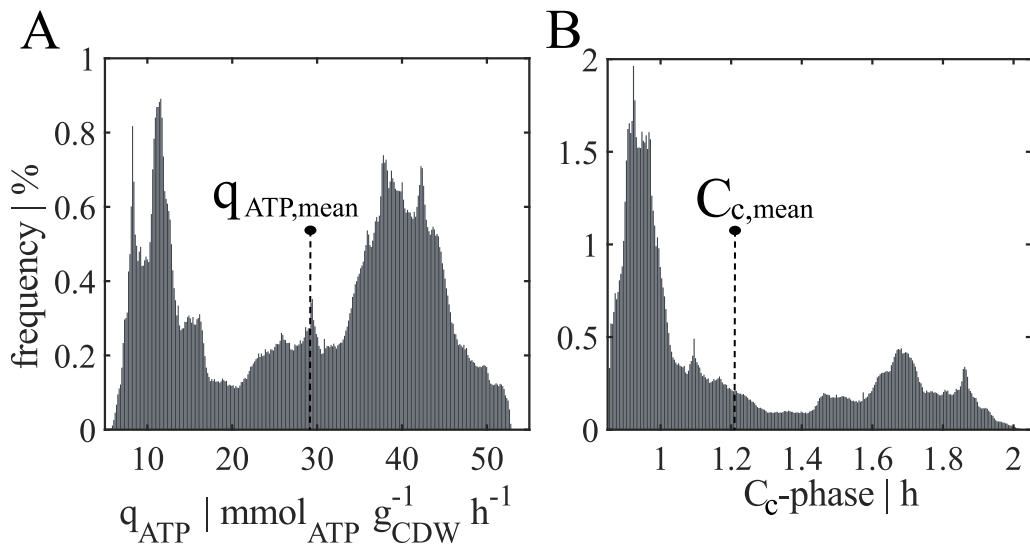


**Figure 7.5: Distribution of energy level and C-phase duration for the 54 m<sup>3</sup> reactor.** A) Frequency of cells with a specific ATP consumption rate ( $q_{\text{ATP}}$ ) tracked for 20 s. Average value of  $q_{\text{ATP,mean}} = 29.31 \text{ mmol}_{\text{ATP}} \text{ g}_{\text{CDW}}^{-1} \text{ h}^{-1}$ . B) Frequency of cells having a specific duration of replication (C-phase). Average C-phase duration of  $C_{\text{c,mean}} = 1.21 \text{ h}$ . Counts were divided into 300 bins. With modifications to Kuschel et al. (2017).

increased energy demand compared to the mean value. Moreover, the ATP consumption was 1.5 times the mean value for 12.2%. The distribution will slightly differ if the effect of non-growth associated maintenance on large scale fluctuations was considered (Löffler et al., 2016).

Secondly a delayed response several seconds till minutes after stimulation was examined. Although spatially decoupled from the stimulus, a specific trigger time was assumed to initiate a transcriptomic or proteomic program, in this case a modified growth rate or cell cycle duration. Consequently, as described in section 7.2.1, a distribution for the replication phase duration was derived ranging from  $C_{\text{c,min}} = 0.86 \text{ h}$  to  $C_{\text{c,max}} = 2.05 \text{ h}$ . With an average duration of  $C_{\text{c,mean}} = 1.21 \text{ h}$  only 22.3% possessed the mean replication phase of  $C_{\text{c,mean}} = 1.21 \pm 0.2 \text{ h}$ , whereas about 30% showed longer  $C_{\text{c}}$ -periods of more than 1.41 h. Shorter replications durations ( $< 1.01 \text{ h}$ ) were determined for 47.7%. Moreover, about 56.1% of the cells were identified to be rapidly growing cells with growth rates  $\mu > 0.3 \text{ h}^{-1}$ . These cells might have already started to adjust their cell cycle to multifork replication. In fact, considering the different growth phenotypes from figure 7.5 (B), three subpopulations might be formulated: (i) short  $C_{\text{c}}$ -phase durations of  $0.94 \pm 0.08 \text{ h}$ , (ii) slow growing cells with  $C_{\text{c}}$ -phase durations of  $1.68 \pm 0.1 \text{ h}$  and (iii) a transition state of  $C_{\text{c}}$ -phases ranging from 1.1 to 1.5 h. In summary, an approach is presented to mimic the scenario of a (fed)-batch fermentation by the superposition of subpopulations containing different growth rates and  $C_{\text{c}}$ -phase durations.

### 7.3.2 Case 2: *C. glutamicum*

A scale-up of the pilot scale reactor from chapter 4 was performed by numerical flow simulations. Hereby, the reactor was scaled by a factor 100 up to 19.8 m<sup>3</sup>. Scale-up criteria and the setup for the multiphase simulation is described in section 7.2.2. Criteria had been chosen in order to have geometric similarity and an identical number of numerical cells per volume compared to the pilot scale reactor, which has proofed good agreement with experimental data. Global physical parameters of the pilot and large scale simulations are compared in table 7.4. The scaling factor for the turbulent dissipation rate for industrial scale was calculated with 1.65.

**Table 7.4: Results of the different scales in multiphase.** Pilot scale (experimental and numerical) and industrial scale results are listed.

Scale	$N_P$ [-]	$\alpha_G$ [%]	$k_L a$ [ $h^{-1}$ ]	$\tau_{95}$ [s]	$d_b$ [mm]
Pilot (exp)	10.88±0.11	3.6±0.3	125±4	15.2±4	1.2 -4.1
Pilot (num)	9.5	2.7	116	17	3
Industrial	9.0	8.8	225	55	5.85

The power number was calculated with  $N_P = 9.0$  for the large fermenter which is about 5 % smaller than in the pilot scale. Since both scales were operated in the turbulent regime, power numbers differ only slightly. Although P/V was not chosen as scale up criterium, pilot and large scale power consumptions are in the range of typical industrial scale bioreactors of up to 5 kW m<sup>-3</sup>. Volumetric power consumption of simulated pilot (1884 W m<sup>-3</sup>) and large scale (1441 W m<sup>-3</sup>) differed by 30 %.

Increased gassing rates result in a 3.26 times higher gas volume fraction of 8.8 % in large scale compared to 2.7 % in pilot scale (num). Since the numerical value for pilot scale was underestimated (see chapter 4.4.2.2), the comparison with experimental data is considered more appropriate. Consequently, the large scale gas volume fraction is only 2.4 times higher compared to the experimental gas volume fraction of 3.6 % in pilot scale. Differences in gas volume distribution for pilot (A) and large (B) scale are depicted in figure 7.6, showing significant higher gas volume fraction for large scale as reflected in the overall gas hold up. Furthermore, a flooding regime seems to be predicted by CFD for the first impeller. While the correlations of Rosseburg et al. (2018) and Gezork et al. (2000) as well as Zlokarnik and Mikulcova summarized in Wiedmann (1983) clearly predict no flooding for a flow number of  $Fl = 0.062$ , impeller flooding is suggested by Zwietering and Dickery (Wiedmann, 1983). Unfortunately, it is not possible to verify the predictions, due to the lack of experimental data.

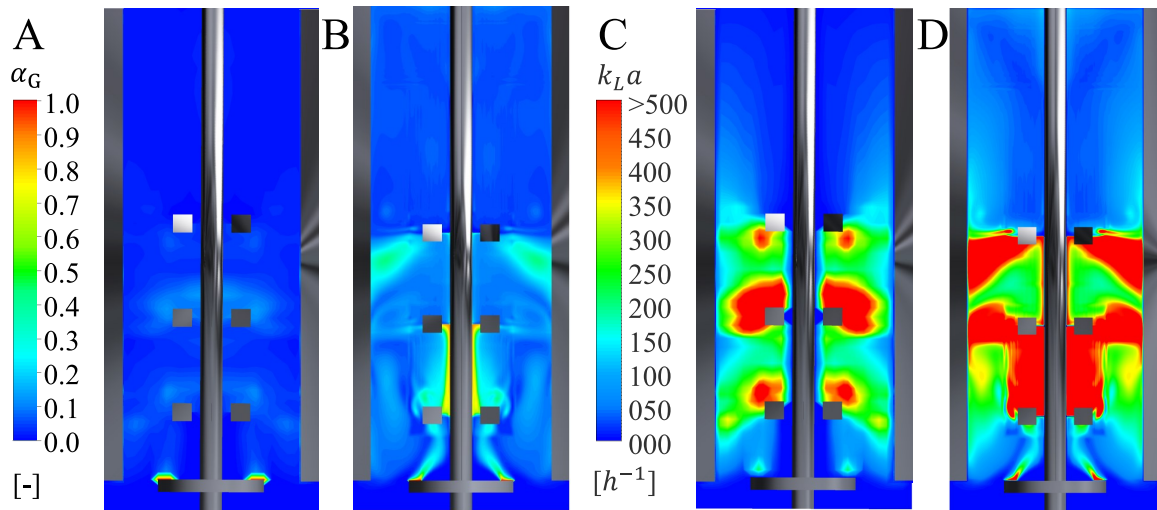


**Figure 7.6: Comparison of pilot and large scale gas hold up and mass transfer coefficient.** A) Gas volume distribution of the pilot scale reactor, B) Gas volume distribution of the large scale reactor, C) Distribution of volumetric mass transfer coefficient in pilot scale, D: Distribution of volumetric mass transfer coefficient in large scale. With modifications to Kuschel & Takors (2020).

However, gas hold up for the large scale might be compared to pilot scale by calculating the theoretical gas hold up from the correlation (equation 4.20) fitted in chapter 4.4.1.

$$\varepsilon_G = 0.25 \left( \frac{P_G}{V} \right)^{0.2} (\text{vvm H})^{0.625} \quad (7.3)$$

With a power ratio of  $1441 \text{ W m}^{-3}$  and the increased liquid level for large scale, the correlation 7.3 predicts a gas hold up of 9.4 %. Compared to the numerical simulation with a gas hold up of 8.8 %, only small deviation of 7 % is obtained.

Similar considerations can be made for the  $k_{L,a}$  value. Figure 7.6 shows, that local  $k_{L,a}$  values are notably higher for large (D) compared to pilot (C) scale, which is reflected by the higher overall  $k_{L,a}$  of  $225 \text{ h}^{-1}$  for industrial scale (see table 7.4). If large scale and the numerical simulation with the pilot scale reactor are compared, the overall  $k_{L,a}$  is 1.94 times higher for large scale. Likewise, a comparison between simulated large scale and experimental pilot scale values yields a ratio of 1.80. Elevated  $k_{L,a}$  values in industrial scale result from significantly increased gas volume fractions. To check the validity of numerical results for the industrial scale bioreactor, the overall  $k_{L,a}$  was compared with values obtained by the correlation (see equation 7.4) fitted in chapter 4.4.1. Thereby, a  $k_{L,a}$  value of  $256 \text{ h}^{-1}$  was calculated, resulting in minor deviation of 14 %.

$$k_{L,a} = 0.0287 \left( \frac{P_G}{V} \right)^{0.466} (\text{vvm H})^{0.638} \quad (7.4)$$

Summarizing,  $\varepsilon_G$  and  $k_{L,a}$  calculated by CFD are in fair agreement to the values obtained by the experimental correlation.

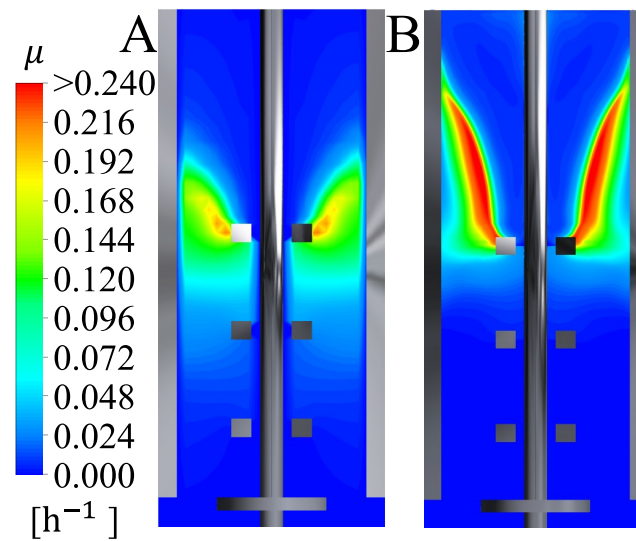


**Figure 7.7: Comparison of theoretical growth rates in pilot and large scale.** A) Pilot scale growth distribution, B) Large scale growth distribution. With modifications to Kuschel & Takors (2020)

Because of the high computational demand mixing time could only be determined on frozen flow field. The simulation resulted in a  $\tau_{95} = 55$  s. As the flow field is transient this is only an approximation and the real value might differ. Unfortunately, no experimental data are available to verify the results. The overall sauter diameter is with  $d_b = 5.85$  mm almost twice as big as in pilot scale. The higher gas volume fraction may lead to increased coalescing effects which results in increased bubble diameters. However, due to the lack of experimental data validation is not possible.

The aim of this study was furthermore to simulate a double gradient consisting of inhomogeneous glucose and oxygen concentrations, as already shown in chapter 5. The kinetic by Roels (1983) was also applied in large scale to account for multisubstrate consumption. Even though  $k_L a$  value and mixing time differ significantly for pilot and industrial scale, the obtained growth profiles seem to be very similar as presented in figure 7.7. The highest growth rates of  $0.24 \text{ h}^{-1}$  are obtained in the previously mentioned transient area T (see chapter 5), whereas the conditions in the lower and upper part of the reactor lead to almost no growth at all. As the glucose and oxygen profiles were comparable to pilot scale they are not shown here or discussed in the following. Accordingly, regime classification for the industrial scale reactor can be performed identically to the pilot scale reactor, with a low oxygen regime in the upper part, a small transition area spreading cone shaped from the upper impeller to the liquid surface and a low glucose regime in the lower part. Consequently, scale-down devices might be designed likewise as proposed in chapter 5.3.3 only with modified dwelling times which can be obtained by a thorough lifeline analysis in large scale.

Moreover, the simulation was extended by the carbon dioxide mass balance resulting in a triple gradient of glucose, oxygen and carbon dioxide profiles. Oxygen and carbon dioxide profiles of gas and liquid phase are shown in figure 7.8. The oxygen concentration in the gas phase is depicted

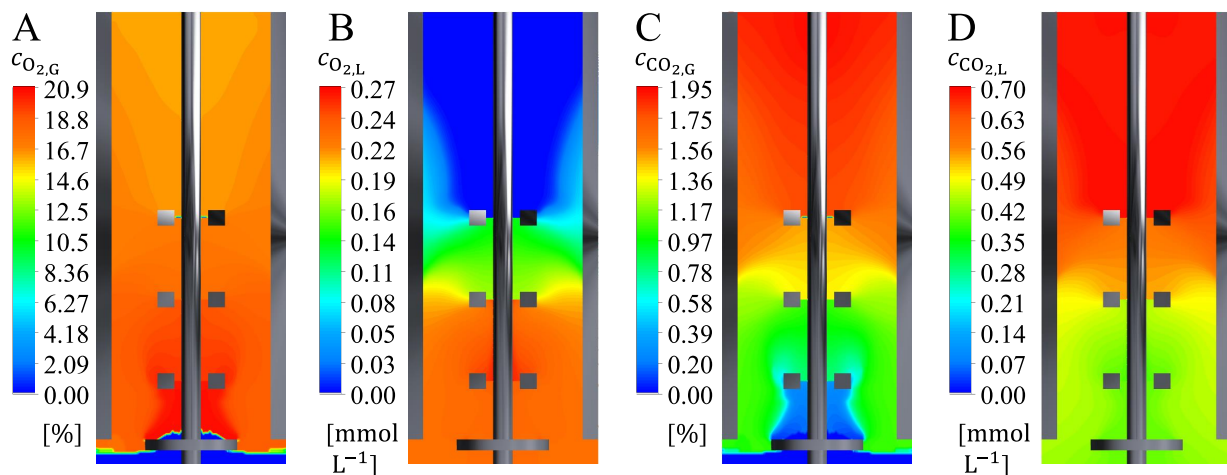


**Figure 7.8: Oxygen and carbon dioxide local distribution in large scale.** A) Oxygen content in the gas phase, B) Oxygen liquid concentration, C) Carbon dioxide content in the gas phase and D: Carbon dioxide liquid concentration.

in figure 7.8 (A). The entering gas contains the set oxygen content of  $\approx 21\%$ . As the gas rises from the reactor bottom to the liquid surface the oxygen content within the air reduces to a value of  $\approx 18\%$ . The liquid oxygen concentration profile is similar to the gas phase (B). Highest concentrations of  $0.27 \text{ mmol L}^{-1}$  are obtained in the lower part of the reactor around the first impeller, where bubbles with high oxygen content leaving the sparger are disrupted. The concentration decreases with increasing reactor height and an oxygen limitation zone forms in the upper part of the reactor. The glucose feed port is located in the upper part of the reactor, thus oxygen consumption rates are elevated there causing an oxygen depletion. The carbon dioxide profile shows the reverse behaviour: the gas entering the reactor contains only  $0.04\%$  carbon dioxide, whereas carbon dioxide is transferred into the bubbles while they rise to the liquid surface until the carbon dioxide content is about  $2\%$ . Liquid carbon dioxide concentration profiles are similar to the gas profile. In the lower part of the reactor the concentration is about  $0.42 \text{ mmol L}^{-1}$ . Due to high volumetric mass transfer rates proximate to the impeller, carbon dioxide is transferred into the uprising gas fraction. The accumulation of carbon dioxide in the upper part of the reactor with concentrations up to  $0.7 \text{ mmol L}^{-1}$  is caused by strongly decreased volumetric mass transfer rates in the respective part (see figure 7.6) on the one hand and decreased driving force concentration differences on the other hand.

A carbon dioxide content of  $2\%$  in the exhaust gas and a concentration  $c_{\text{CO}_2}$  of  $0.7 \text{ mmol L}^{-1}$  seems rather small for a large scale fermentation. Additionally, mass transfer at the liquid surface is neglected here, which would furthermore reduce the carbon dioxide concentration in the upper part of the reactor. Typically, exhaust gas contents with volumetric fractions of  $5 - 20\%$  or higher are expected for microbial or mammalian cultivations (Blombach & Takors, 2015). Dissolved  $c_{\text{CO}_2,L}$  levels of about  $8.18 \text{ mmol L}^{-1}$  for an aerated ( $0.1 \text{ vvm}$ ),  $1.5 \text{ bar}$  pressured, stirred batch cultivation of *C. glutamicum* were measured in the late exponential phase (Blombach et al., 2013; Blombach

& Takors, 2015). Although the biomass concentration was only  $7 \text{ g}_{\text{CDW}}\text{L}^{-1}$ , which is about five times smaller than the biomass concentration used in this study, the growth rate was determined with  $\mu = 0.4 \text{ h}^{-1}$  which is about 12 times higher than the resulting average growth rate of this process. Consequently, the overall  $c_{\text{CO}_2}$  production was significantly higher compared to this study. Furthermore, gassing rates of 0.1 vvm for the laboratory reactor are significantly smaller than for large scale conditions with 0.25 vvm. The increased gas volume fraction in large scale leads to stripping effects of carbon dioxide which prevented an accumulation of  $c_{\text{CO}_2,\text{L}}$ . On top of that, this effect is enhanced by longer bubble dwelling times in large scale. For simplicity also pH gradients were neglected. In fact, a pH shift towards acid conditions, could lead to elevated local carbon dioxide concentrations. As  $c_{\text{CO}_2,\text{L}}$  concentrations were very low for the current feeding strategy and operational conditions, a lifeline analysis analogous to case 1 by inclusion of the cell cycle model of chapter 6 was not performed. However, a basis for the inclusion of carbon dioxide as well as primary local carbon dioxide conditions within a industrial scale bioreactor are provided.

Summarizing, a large scale glucose, oxygen and carbon dioxide gradient was simulated by scaling-up the pilot scale bioreactor of the validated study conducted in chapter 4 and 5. Glucose and oxygen limitation zones were identified to be analogous to pilot scale compartmentalisation for identical glucose feeding strategies, but different gassing and mixing conditions.

## 7.4 Conclusion

Two case studies to describe heterogeneity in an industrial scale fermenter were conducted with the help of computational fluid dynamics.

In the first study a fed-batch scenario of *P. putida* was investigated assuming homogeneous oxygen concentrations. Glucose feed and immediate substrate consumption in the liquid phase led to spatial substrate heterogeneity. A previously developed cell cycle model was applied to classify this heterogeneous environment within the bioreactor into regimes of different potential cell cycle strategies such as standard (S), transient (T) and multifork (M) replication regimes. By bacterial lifeline analysis, average retention times of 1 to 8.5 s and maximal retention times of 4 to 73.5 s in a specific regime for certain regime transitions were approximated. Based on the findings of Löffler et al. (2016) 72 % of all cells were identified to show quick metabolic responses and 10 % being likely to undergo massive transcriptional changes. Linked to STR-PFR scale-down experiments further investigations may be conducted. Moreover, a short and long term response was framed. A distribution of different ATP consumption rates was obtained as instantaneous response resulting in an inhomogeneous population of 40.8 % with reduced and 52.9 % with increased energy demand compared to the mean value of  $q_{\text{ATP,mean}} = 29.31 \pm 2 \text{ mmol}_{\text{ATP}} \text{ g}_{\text{CDW}}^{-1} \text{ h}^{-1}$ . A delayed response in

terms of replication phase distribution was defined, resulting in the formulation of three subpopulations as follows: (i) short  $C_c$ -phase durations of  $0.94 \pm 0.08$  h, (ii) slowly growing cells with  $C_c$ -phase durations of  $1.68 \pm 0.1$  h and (iii) a transition state of  $C_c$ -phases ranging from 1.1 to 1.5 h.

The second case dealt with the depiction of an industrial scale multiphase simulation of a fed-batch scenario with *C. glutamicum*. As large scale data are rare, those studies are usually sole predictions and not validated by experimental data. This approach however makes use of the simulation setup as well as numerical requirements of a previously validated study in pilot scale to display glucose and oxygen conditions for a snap-shot scenario of a large scale fed-batch fermentation. The large scale overall gas hold up and  $k_L a$  value showed minor deviations of only 7% and 14%, respectively, compared to the calculated values of the experimentally obtained correlations. Even though mixing and gassing conditions were different to pilot scale, growth profiles of the large scale scenario exhibited high similarity to the pilot scale local growth rate distribution, suggesting the same compartmentalisation strategy of low oxygen, transient and low glucose regimes for scale-down designs. The simulation setup has been furthermore extended by the carbon dioxide balance leading to non-critical carbon dioxide concentrations of only  $0.7 \text{ mmol L}^{-1}$  for the current feeding and operational setup, due to low growth and high gassing rates. However, the aim of this study was to provide a basis for the inclusion of carbon dioxide mass balance and display environmental heterogeneity in industrial scale fermentations. Additionally, it outlines the need to include organism specific considerations in terms of substrate consumption and regime formation into scale-up strategies instead of solely focussing on scale up for physical parameter. By bacterial lifeline analysis this study could be furthermore extended for biological readouts to consider dwelling times in critical concentration regimes for the scale-up strategy. Moreover, by the consideration of higher growth rates, carbon dioxide concentrations may reach a critical level to function as stress factor for a culture of *C. glutamicum*. Thus, the heterogeneity analysis may then be extended by carbon dioxide induced cell cycle modifications. As such, the implementation could be performed analogous to case 1 including the cell cycle model obtained for *C. glutamicum* as described in chapter 6.

The two cases reflect the need to not only scale a reactor for physical parameters, but integrate biological readouts into scale-up considerations for individual cases. Only the combination of both enables the detection of possible hot spots or limitation zones. A lifeline analysis may furthermore serve as basis for the design of scale-down devices or as *in silico* method to directly investigate biological readouts.

## 8 Conclusion and outlook

This chapter summarizes all results that were achieved in the course of this thesis and provides conclusions under consideration of the objectives and motivation formulated in chapter 1. Posed research questions are addressed and future perspectives are given.

The main intention of this work was to provide supporting tools for large scale characterisation to minimise the risk of suboptimal scale-up. Each chapter contributes to the prediction of industrial scale performance *a priori*. A graphical overview is given in figure 8.1.

### Chapter 3 - Characterisation of bioprocesses with *C. glutamicum* as model organism

In chapter 3 several batch fermentations of *C. glutamicum* were conducted to derive **cell specific rates** and physical **properties of the broth** as indicated in figure 8.1. The maximal growth rate  $\mu_{\max}$ , the biomass substrate yield  $Y_{XS}$  and the biomass oxygen yield were determined in exponential phase. Furthermore, the cell specific oxygen uptake rate  $q_{O_2}$  and the cell specific carbon

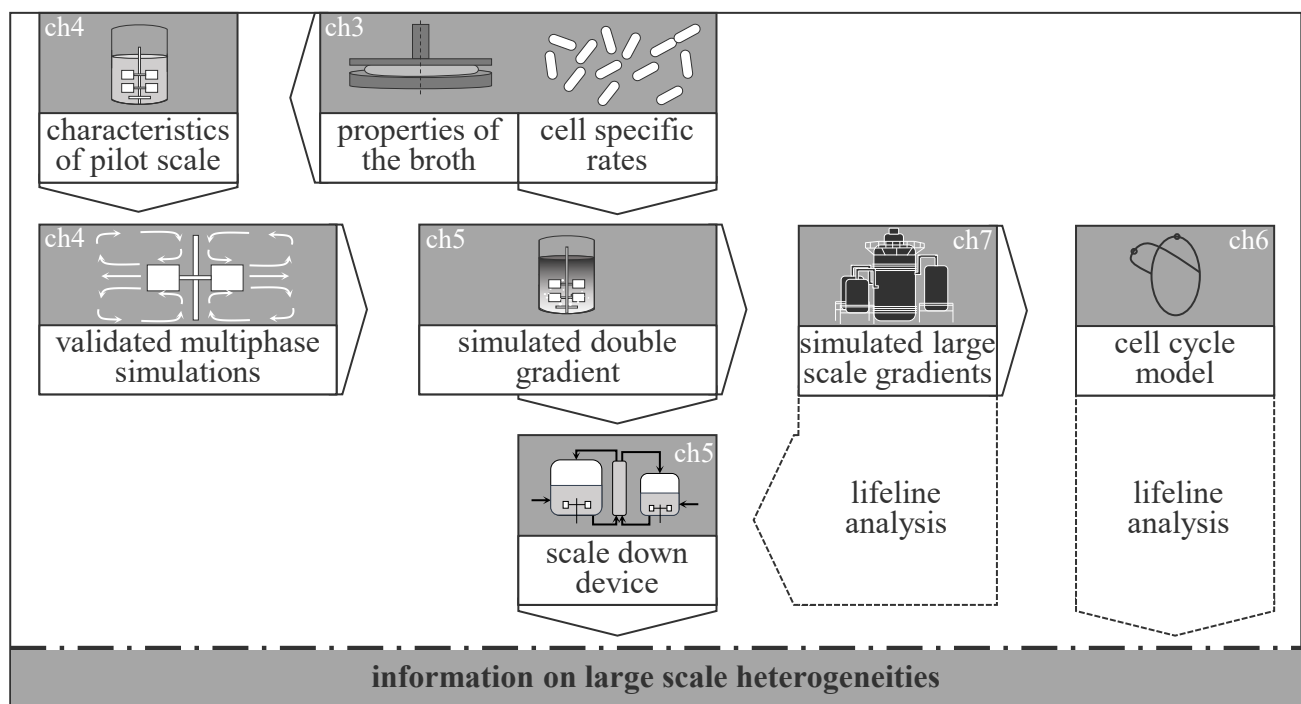


**Figure 8.1: Schematic overview of workpackages achieved in this study.** Explanations of the graphics are given in the main text. The abbreviation ch indicates the respective chapter in which the results are found.

dioxide emission rate  $q_{\text{CO}_2}$  were calculated leading to a respiratory quotient ( $RQ$ ) close to the theoretical value of 1.0. A nearly closed C-balance excluded the formation of by-products and confirmed the accuracy of the determined rates. The examination of the broth led to the answer of the first research question:

**RA3.1** For the investigated case of *C. glutamicum* viscosity and density were similar to water and thereby chosen as such for further experiments and numerical simulations. Since the surface tension was only slightly dependent on biomass, effects were not included in numerical simulations.

Although biomass did have a minor impact, a significant drop in surface tension to  $30 \text{ mN m}^{-1}$  was measured by the addition of antifoaming agents. However, due to contradictory effects on  $k_L a$  values, the sole simplification of the impact of antifoam to a surface tension reduction is invalid and future research should focus on a thorough analysis to quantify and include these effects in numerical simulations.

#### Chapter 4 - Characterisation of a pilot scale bioreactor

Using the findings of chapter 3 regarding the physical properties of the broth, a **pilot scale** bioreactor was **characterised** in chapter 4. Since the simulation of turbulent two phase flows is rather complex and large scale data were not available, the conducted experiments served for parameter **validation** of the performed **multiphase simulations** (see figure 8.1). The measurement of power consumption, mixing time, gas hold up and  $k_L a$  values within a range of agitation rates of 100 to 500 rpm and gassing rates of 0 to 1 vvm was basis to decide on a suitable operating point:

**RA4.1** An operating point of 300 rpm and 0.25 vvm was considered appropriate, as it reflects a typical volumetric power consumption of  $2.2 \text{ kW m}^{-3}$  of large scale applications.

In addition to power considerations, no flooding was predicted to occur under these conditions and the resulting  $k_L a$  of  $125 \text{ h}^{-1}$  was sufficient to supply enough oxygen to a late fed-batch culture with biomass concentrations of about  $35 \text{ g L}^{-1}$ .

Furthermore, the chapter presents a numerical setup to simulate the pilot scale bioreactor, answering the question of a suitable setup:

**RA4.2** The Eulerian PBM, as well as the RKE turbulence model including the MRF model were suitable to simulate the polydispersed multiphase flow of the agitated tank. The extension of the Tomiyama et al. (1998) drag model by turbulent drag modification and swarm effects, finally resulted in good agreement of numerical simulations with experimental data.

Moreover, the transferability of the bubble breakup, coalescence and daughter size model by Laakkonen et al. (2007b) to a multiple impeller pilot scale reactor setup was shown.

---

The reduction of computational costs was a central aspect of this thesis, as summarized by the following answer:

**RA4.3** The inclusion of a scaling factor showed good accordance of predicted to experimental process parameters already for a grid size of  $1.12 \cdot 10^5 \text{ \#}/\text{m}^3$ , thereby reducing computational costs.

Considering experimental noise, deviations of simulated values were  $< 12 \%$  compared to experimental data, with one exception. The difference between experimental and simulated gas hold up was determined with  $< 21 \%$  for the two coarser grid sizes. Still, since significant reduction of computational costs is obtained, this deviation is acceptable. Nevertheless, coarser mesh densities might cause higher deviations in the velocity profiles or incorrect prediction of the power consumption by torque, which is not covered by the scaling approach and thereby not recommended. As an increase in turbulence generally requires the refinement of grid size, further studies using higher agitation rates should be conducted to determine minimal density.

## Chapter 5 - Simulated oxygen and glucose gradient

The combination of cell specific rates from chapter 3 and multiphase setup from chapter 4 enabled the **simulation** of a substrate and oxygen gradient in chapter 5 as indicated in figure 8.1. This 'snap-shot' **double gradient** may occur during a substrate limited late fed-batch process of *C. glutamicum*, where oxygen is still present, albeit in low concentrations within specific regions. These regions can be classified into defined regimes, answering the first research question of this chapter:

**RA5.1** A multi substrate gradient consisting of glucose and oxygen shows highest glucose concentrations close to the feed port at the reactor top and lowest at the bottom, whereas opposite profiles attune for oxygen. A double gradient can be classified in regimes of low glucose ( $L_S$ ), a transient (T) and low oxygen regime ( $L_{O_2}$ ).

The regimes of the double gradient resulted from a simplification by overlaying gradients for each substrate. Before, regimes for a single substrate were classified in a regime of linear coupled growth-substrate dependency, a transient regime and a regime where fluctuations in substrate concentrations show negligible effects on growth. The regimes were thereby denoted as low (L), transient (T) and high (H) concentration regime for either glucose or oxygen, respectively.

Besides regime classification, statistical evaluation of simulated bacterial trajectories or so-called *lifelines*, records of bacterial cells experiencing different levels of glucose and oxygen, were focus of this chapter and the advantage of this analysis was depicted:

**RA5.2** The statistical *lifelines* analysis revealed the frequency of all regime transitions and average dwelling times in specific regimes. The results may be well used to design wet-lab scale-up simulators.

Lacking detailed information on the environment inside a bioreactor, traditionally, these **scale-down** (SD) devices are based on industrial mixing times. However, the imposed conditions may not reflect the concentration fluctuations encountered by the microorganisms. For the current double gradient a simplification was proposed as a result of the *lifelines* analysis: As both, the average dwelling time in the transient regime (T) was very short ( $< 1$  s) and the volume of T was rather small ( $< 5\%$  of the total volume) compared to the other regimes, regime T can also be neglected for the design of a SD. Two designs were proposed in section 5.3.3.

Since some deviations in process parameter for the examined grid densities were observed, a core question of the thesis was how much the scaling approach for epsilon introduced in chapter 4 influences gradient and *lifelines* analysis:

**RA5.3** Concentration profiles and therefore the growth rate distribution as shown in figure 5.3 were nearly equal based on a mesh density of  $1.12 \cdot 10^5 \text{ \#}/m^3$  compared to 10-fold finer mesh resolution. Moreover, bacterial *lifelines* analysis revealed, that biological readouts such as regime changes, still generated accurate dwelling time distributions with mostly less than 15% deviation between the meshes.

Consequently, the use of this scaling approach opens the door for large scale applications with reduced computational effort.

## Chapter 6 - Cell cycle model

As outlined in RA5.2 such analysis may be used to design SD, which can furthermore unravel basic regulatory systems, mark the suitability of a strain for large scale and provide guidelines for strain and process engineering. However, by coupling *lifelines* analysis to a biological response model, further information on large scale heterogeneities can be retrieved. A **cell cycle** model for *C. glutamicum* was developed in chapter 6 as displayed in figure 8.1. The model describes cell cycle adaption as response towards varying substrate availability or potential growth rates and partial pressure of carbon dioxide. The influence on *C. glutamicum* is summarized in the following:

**RA6.1** The replication phase duration ( $C_c$ ) of *C. glutamicum* decreased with increasing growth rate, but higher partial pressures of carbon dioxide ( $p_{CO_2}$ ) slowed down the replication process.

In fact, the  $C_c$  period was doubled for  $p_{CO_2}$  of 50% compared to the reference state ( $p_{CO_2} = 0.04\%$ ). Moreover, to cope with the installed growth rate, multifork replication for *C. glutamicum* was initiated already for growth rates of  $\mu = 0.2 \text{ h}^{-1}$  under elevated  $p_{CO_2}$  conditions, whereas multifork replication did not start for growth rates  $\mu < 0.4 \text{ h}^{-1}$  under reference conditions.

As a preliminary study, a function for the  $C_c$  period was also determined for *P. putida* based on the work of Lieder et al. (2016). The replication phase  $C_c$  for *P. putida* decreased with increasing

---

growth rate and multifork replication started for growth rates between  $0.3 \text{ h}^{-1} < \mu \leq 0.4 \text{ h}^{-1}$ . The obtained function was furthermore coupled to a **large scale simulation** as presented in chapter 7.

### Chapter 7 - Heterogeneity analysis in large scale

Since a late fed-batch scenario of *P. putida* assuming homogeneous oxygen concentrations was reflected, a single phase simulation was conducted. Based on the cell cycle model introduced in chapter 6, the gradient was classified in regimes of potential cell cycle strategies such as standard (S), transient (T) and multifork (M) replication regimes. Bacterial *lifelines* analysis for *P. putida* was performed to answer the question of bacterial response towards fluctuating concentrations and the formation of heterogeneity:

**RA7.1** The *lifelines* analysis for *P. putida* resulted in average retention times up to 8.5 s and maximal retention times up to 73.5 s in a specific regime for certain regime transitions. A short and long term response was framed, resulting in an inhomogeneous ATP consumption as well as the classification into subpopulations.

Inhomogeneous ATP consumption was depicted as instantaneous response showing 40.8 % with reduced and 52.9 % with increased energy demand compared to the mean value of  $q_{\text{ATP,mean}} = 29.31 \pm 2 \text{ mmol}_{\text{ATP}} \text{ g}_{\text{CDW}}^{-1} \text{ h}^{-1}$ . Cell cycle adaption as delayed response resulted in the formulation of three subpopulations as follows: (i) short  $C_c$ -phase durations of  $0.94 \pm 0.08 \text{ h}$ , (ii) slowly growing cells with  $C_c$ -phase durations of  $1.68 \pm 0.1 \text{ h}$  and (iii) a transition state of  $C_c$ -phases ranging from 1.1 to 1.5 h.

As indicated in figure 8.1 (dashed lines), a prospective would be to perform such *lifelines* analysis for a culture of *C. glutamicum* in large scale. To provide a basis, the pilot scale setup of chapter 4 was adapted to simulate an industrial case of *C. glutamicum* including carbon dioxide balance, which answers the question of suitability of the chosen approach for large scale:

**RA7.2** Overall process parameters like gas hold up and  $k_L a$  value were in fair comparison to results obtained by the fitted correlation of chapter 4. Although gassing and mixing conditions for pilot and large scale differed, regime assignments were identical to the examined pilot scale case.

The results show the transferability of the numerical approach from chapter 4 to larger scales. Since regime assignments were identical to the examined pilot scale case, the same SD design as recommended in chapter 5 is suggested. Large scale dwelling times in the specific regimes, however, are likely to be much longer. Additional to the design of a SD simulator, a large scale simulation of *C. glutamicum* with elevated growth rates can be connected to the derived cell cycle model to reveal further heterogeneities in large scale. In this case cell cycle adaptations upon substrate and  $p_{\text{CO}_2}$  stress for an industrial case can be displayed.

In summary, this work facilitates the *a priori* prediction of large scale heterogeneities. A framework is presented which includes validated multiphase simulations, the depiction of a glucose-oxygen double gradient and the subsequent steps necessary to gain insights in large scale conditions, namely the design of scale-down devices and the coupling of large scale simulations with biological response models. Applicability was shown for case studies with *C. glutamicum* and *P. putida* as major production hosts in industrial biotechnology. Although literature indicates only small influence of glucose and oxygen variations on *C. glutamicum*, scale-down devices so far focused on physical readouts like mixing times. In contrast, the presented methodology in this work enables the use of biological readouts, meaning the frequency and duration of defined concentration fluctuations experienced by the microorganisms. Specific transition patterns may be implemented in scale-down devices which reflects a more realistic large scale scenario. Additionally, compared to existing CFD studies yielding scale-down designs, for the first time a multiphase system was considered. Furthermore, the given cell cycle model was connected to single phase simulations with *P. putida* and adapted for the use with *C. glutamicum*. Similar modelling approaches can be linked to multiphase simulations to retrieve *in silico* results in parallel to experimental evaluation by scale-down devices. Consequently, both paths can be adapted for the application with different microorganisms used in large scale production and further occurring stress factors.

---

## Bibliography

- Alopaeus, V., Koskinen, J. & Keskinen, K. I. (1999). "Simulation of the population balances for liquid-liquid systems in a nonideal stirred tank. Part 1 Description and qualitative validation of the model". In: *Chemical Engineering Science* 54.24, pp. 5887–5899.
- Alves, S. S., Maia, C. I. & Vasconcelos, J. M. (2004). "Gas-liquid mass transfer coefficient in stirred tanks interpreted through bubble contamination kinetics". In: *Chemical Engineering and Processing: Process Intensification* 43.7, pp. 823–830.
- Alves, S. S. & Vasconcelos, J. M. T. (1995). "Mixing in gas-liquid contactors agitated by multiple turbines in the flooding regime". In: *Chemical Engineering Science* 50.14, pp. 2355–2357.
- Bach, C. (2018). "Modelling of gradients in large scale bioreactors". PhD thesis.
- Bach, C., Yang, J., Larsson, H., Stocks, S. M., Gernaey, K. V., Albaek, M. O. & Krühne, U. (2017). "Evaluation of mixing and mass transfer in a stirred pilot scale bioreactor utilizing CFD". In: *Chemical Engineering Science* 171, pp. 19–26.
- Bailey, J. E. (1998). "Mathematical modeling and analysis in biochemical engineering: Past accomplishments and future opportunities". In: *Biotechnology Progress* 14.1, pp. 8–20.
- Bakker, A., Laroche, R. D., Wang, M. H. & Calabrese, R. V. (1997). "Sliding mesh simulation of laminar flow in stirred reactors". In: *Chemical Engineering Research and Design* 75.1, pp. 42–44.
- Bakker, A. & Akker, H. E. Van den (1994). "Gas-liquid contacting with axial-flow impellers". In: *Chemical engineering research & design* 72.4, pp. 573–582.
- Bakker, A. & Oshinowo, L. M. (2004). "Modelling of turbulence in stirred vessels using large eddy simulation". In: *Chemical Engineering Research and Design* 82.9, pp. 1169–1178.
- Bakker, A. & Van den Akker, H. E. (1994). "A computational model for the gas-liquid flow in stirred reactors". In: *Chemical Engineering Research and Design* 72.A4, pp. 594–606.
- Becker, J. & Wittmann, C. (2012). "Bio-based production of chemicals, materials and fuels - *Corynebacterium glutamicum* as versatile cell factory". In: *Current Opinion in Biotechnology* 23.4, pp. 631–640.
- Becker, J. & Wittmann, C. (2017). "Industrial Microorganisms: *Corynebacterium glutamicum*". In: *Industrial Biotechnology: Microorganisms*. Wiley Online Books 1, pp. 183–220.
- Benedek, A. & Heideger, W. J. (1971). "Effect of additives on mass transfer in turbine aeration". In: *Biotechnology and Bioengineering* 13.5, pp. 663–684.
- Bipatnath, M., Dennis, P. P. & Bremer, H. (1998). "Initiation and velocity of chromosome replication in *Escherichia coli* B / r and K-12". In: *Journal of Bacteriology* 180.2, pp. 265–273.
- Blombach, B., Buchholz, J., Busche, T., Kalinowski, J. & Takors, R. (2013). "Impact of different CO<sub>2</sub>/HCO<sub>3</sub><sup>-</sup> levels on metabolism and regulation in *Corynebacterium glutamicum*". In: *Journal of Biotechnology* 168.4, pp. 331–340.

- Blombach, B. & Takors, R. (2015). “CO<sub>2</sub> intrinsic product, essential substrate, and regulatory trigger of microbial and mammalian production processes”. In: *Frontiers in Bioengineering and Biotechnology* 3, pp. 1–11.
- Brucato, A., Ciofalo, M., Grisafi, F. & Micale, G. (1998). “Numerical prediction of flow fields in baffled stirred vessels: A comparison of alternative modelling approaches”. In: *Chemical Engineering Science* 53.21, pp. 3653–3684.
- Buchholz, J., Graf, M., Blombach, B. & Takors, R. (2014a). “Improving the carbon balance of fermentations by total carbon analyses”. In: *Biochemical Engineering Journal* 90, pp. 162–169.
- Buchholz, J., Graf, M., Freund, A., Busche, T., Kalinowski, J., Blombach, B. & Takors, R. (2014b). “CO<sub>2</sub>/HCO<sub>3</sub><sup>-</sup> perturbations of simulated large scale gradients in a scale-down device cause fast transcriptional responses in *Corynebacterium glutamicum*”. In: *Applied Microbiology and Biotechnology* 98.20, pp. 8563–8572.
- Buchholz, J., Schwentner, A., Brunnenkan, B., Gabris, C., Grimm, S., Gerstmeir, R., Takors, R., Eikmanns, B. J. & Blombach, B. (2013). “Platform engineering of *Corynebacterium glutamicum* with reduced pyruvate dehydrogenase complex activity for improved production of l-lysine, l-valine, and 2-ketoisovalerate”. In: *Applied and Environmental Microbiology* 79.18, pp. 5566–5575.
- Buffo, A., Marchisio, D. L., Vanni, M. & Renze, P. (2013). “Simulation of polydisperse multiphase systems using population balances and example application to bubbly flows”. In: *Chemical Engineering Research and Design* 91.10, pp. 1859–1875.
- Buffo, A., Vanni, M., Renze, P. & Marchisio, D. (2016). “Empirical drag closure for polydisperse gas – liquid systems in bubbly flow regime : Bubble swarm and micro-scale turbulence”. In: *Chemical Engineering Research and Design* 113, pp. 284–303.
- Bylund, F., Collet, E., Enfors, S. & Larsson, G. (1998). “Substrate gradient formation in the large-scale bioreactor lowers cell yield and increases by-product formation”. In: *Bioprocess Engineering* 18.3, pp. 171–180.
- Chandrasekaran, S. & Price, N. D. (2010). “Probabilistic integrative modeling of genome-scale metabolic and regulatory networks in *Escherichia coli* and *Mycobacterium tuberculosis*”. In: *Proceedings of the National Academy of Sciences of the United States of America* 107.41, pp. 17845–17850.
- Chara, Z., Kysela, B., Konfrst, J. & Fort, I. (2016). “Study of fluid flow in baffled vessels stirred by a Rushton standard impeller”. In: *Applied Mathematics and Computation* 272, pp. 614–628.
- Chassagnole, C., Noisommit-Rizzi, N., Schmid, J. W., Mauch, K. & Reuss, M. (2002). “Dynamic modeling of the central carbon metabolism of *Escherichia coli*”. In: *Biotechnology and Bioengineering* 79.1, pp. 53–73.
- Chunmei, P. A. N., Jian, M. I. N., Xinhong, L. I. U. & Zhengming, G. A. O. (2008). “Investigation of fluid flow in a dual Rushton impeller stirred tank using particle image velocimetry”. In: *Chinese Journal of Chemical Engineering* 16.5, pp. 693–699.
- Cooper, S. & Helmstetter, C. E. (1968). “Chromosome replication and the division cycle of *Escherichia coli* B/r”. In: *Journal of Molecular Biology* 31.3, pp. 519–540.

- 
- Coroneo, M., Montante, G., Paglianti, A. & Magelli, F. (2011). “CFD prediction of fluid flow and mixing in stirred tanks: Numerical issues about the RANS simulations”. In: *Computers and Chemical Engineering* 35.10, pp. 1959–1968.
- Coulaloglou, C. A. & Tavlarides, L. L. (1977). “Description of interaction processes in agitated liquid-liquid dispersions”. In: *Chemical Engineering Science* 32.11, pp. 1289–1297.
- Cui, Y., Lans, R. G. van der & Luyben, K. C. A. (1996). “Local power uptakes in gas liquid systems with single and multiple Rushton turbines.” In: *Chemical Engineering Science* 51.1, pp. 2631–2636.
- Danckwerts, P. V. (1951). “Significance of liquid-film coefficients in gas absorption”. In: *Industrial & Engineering Chemistry* 43.6, pp. 1460–1467.
- Davidich, M. & Bornholdt, S. (2008). “The transition from differential equations to Boolean networks: A case study in simplifying a regulatory network model”. In: *Journal of Theoretical Biology* 255.3, pp. 269–277.
- Delafosse, A., Morchain, J., Guiraud, P. & Liné, A. (2009). “Trailing vortices generated by a Rushton turbine: Assessment of URANS and large Eddy simulations”. In: *Chemical Engineering Research and Design* 87.4, pp. 401–411.
- Delafosse, A., Collignon, M. L., Calvo, S., Delvigne, F., Crine, M., Thonart, P. & Toye, D. (2014). “CFD-based compartment model for description of mixing in bioreactors”. In: *Chemical Engineering Science* 106, pp. 76–85.
- Delafosse, A., Liné, A., Morchain, J. & Guiraud, P. (2008). “LES and URANS simulations of hydrodynamics in mixing tank: Comparison to PIV experiments”. In: *Chemical Engineering Research and Design* 86.12, pp. 1322–1330.
- Derksen, J. & Van Den Akker, H. E. (1999). “Large eddy simulations on the flow driven by a Rushton turbine”. In: *AIChE Journal* 45.2, pp. 209–221.
- Devi, T. T. & Kumar, B. (2013). “Comparison of flow patterns of dual rushton and CD-6 impellers”. In: *Theoretical Foundations of Chemical Engineering* 47.4, pp. 344–355.
- Dewan, A., Buwa, V. & Durst, F. (2006). “Performance optimizations of grid disc impellers for mixing of single-phase flows in a stirred vessel”. In: *Chemical Engineering Research and Design* 84.8, pp. 691–702.
- Djelal, H., Larher, F., Martin, G. & Amrane, A. (2012). “Continuous culture for the bioproduction of glycerol and ethanol by *Hansenula anomala* growing under salt stress conditions”. In: *Annals of Microbiology* 62.1, pp. 49–54.
- Donachie, W. D. (1968). “Relationship between cell size and time of initiation of DNA replication [36]”. In: *Nature* 219.5158, pp. 1077–1079.
- Doran, P. M. (2013). “Mixing”. In: *Bioprocess Engineering Principles*. Second Edition. London: Academic Press. Chap. 8, pp. 255–332.
- Duuren, J. van, Puchařka, J., Mars, A. E., Bücken, R., Eggink, G., Wittmann, C. & Martins Dos Santos, V. (2013). “Reconciling in vivo and in silico key biological parameters of *Pseudomonas putida* KT2440 during growth on glucose under carbon-limited condition.” In: *BMC biotechnology* 13.1, p. 93.

- Eckert, K. A. & Kunkel, T. A. (1993). "Effect of reaction pH on the fidelity and processivity of exonuclease-deficient Klenow polymerase". In: *Journal of Biological Chemistry* 268.18, pp. 13462–13471.
- Eggeling, L. & Bott, M. (2005). *Handbook of Corynebacterium glutamicum*. CRC Press.
- Eggeling, L. & Bott, M. (2015). "A giant market and a powerful metabolism: l-lysine provided by *Corynebacterium glutamicum*". In: *Applied Microbiology and Biotechnology* 99.8, pp. 3387–3394.
- Eigenstetter, G. & Takors, R. (2017). "Dynamic modeling reveals a three-step response of *Saccharomyces cerevisiae* to high CO<sub>2</sub> levels accompanied by increasing ATP demands". In: *FEMS Yeast Research* 17.1, pp. 1–11.
- Eilingsfeld, A., Kuschel, M. & Takors, R. (2020). "Impact of high levels of carbon dioxide on population heterogeneity of *Corynebacterium glutamicum*". In: *paper in preparation* 0.0, p. 0.
- Enfors, S., Jahic, M., Rozkov, A., Xu, B., Hecker, M. & Ju, B. (2001). "Physiological responses to mixing in large scale bioreactors". In: *Journal of Biotechnology* 85.2, pp. 175–185.
- Fainerman, V. B., Makievski, A. V. & Miller, R. (2004). "Accurate analysis of the bubble formation process in maximum bubble pressure tensiometry". In: *Review of Scientific Instruments* 75.1, pp. 213–221.
- Festel (2018). *Economic Aspects of Industrial Biotechnology*. Springer, Berlin, Heidelberg.
- Fossum, S., Crooke, E. & Skarstad, K. (2007). "Organization of sister origins and replisomes during multifork DNA replication in *Escherichia coli*". In: *The EMBO Journal* 26.21, pp. 4514–4522.
- Gaddis, E. S. & Vogelpohl, A. (1986). "Bubble formation in quiescent liquids under constant flow conditions". In: *Chemical Engineering Science* 41.1, pp. 97–105.
- García-Ochoa, F. & Gómez, E. (1998). "Mass transfer coefficient in stirred tank reactors for xanthan gum solutions". In: *Biochemical Engineering Journal* 1.1, pp. 1–10.
- García-Ochoa, F. & Gómez, E. (2005). "Prediction of gas-liquid mass transfer coefficient in sparged stirred tank bioreactors". In: *Biotechnology and Bioengineering* 92.6, pp. 761–772.
- García-Ochoa, F. & Gomez, E. (2009). "Bioreactor scale-up and oxygen transfer rate in microbial processes: An overview". In: *Biotechnology Advances* 27.2, pp. 153–176.
- Gezork, K. M., Bujalski, W., Cooke, M. & Nienow, A. W. (2000). "The transition from homogeneous to heterogeneous flow in a gassed, stirred vessel". In: *Chemical Engineering Research and Design* 78.3, pp. 363–370.
- Gimbun, J., Rielly, C. D. & Nagy, Z. K. (2009). "Modelling of mass transfer in gas-liquid stirred tanks agitated by Rushton turbine and CD-6 impeller: A scale-up study". In: *Chemical Engineering Research and Design* 87.4, pp. 437–451.
- Groen, D. J. (1994). "Macromixing in Bioreactors." PhD thesis.
- Gullberg, P. & Sengupta, R. (2011). *Axial fan performance predictions in CFD, comparison of MRF and sliding mesh with experiments*. Tech. rep. SAE Technical Paper.
- Gutknecht, J., Bisson, M. A. & Tosteson, F. C. (1977). "Diffusion of carbon dioxide through lipid bilayer membranes". In: *Journal of General Physiology* 69.6, pp. 779–794.

- 
- Hagesaether, L., Jakobsen, H. A. & Svendsen, H. F. (2002). "A model for turbulent binary breakup of dispersed fluid particles". In: *Chemical Engineering Science* 57.16, pp. 3251–3267.
- Hardiman, T., Lemuth, K., Siemann-Herzberg, M. & Reuss, M. (2009). "Dynamic modeling of the central metabolism of *E. coli* – linking metabolite and regulatory networks BT - systems biology and biotechnology of *Escherichia coli*". In: *Systems Biology and Biotechnology of Escherichia coli*. Springer.
- Haringa, C., Deshmukh, A. T., Mudde, R. F. & Noorman, H. J. (2017a). "Euler-Lagrange analysis towards representative down-scaling of a 22 m<sup>3</sup> aerobic *S. cerevisiae* fermentation". In: *Chemical Engineering Science* 170, pp. 653–669.
- Haringa, C. & Mudde, R. F. (2018). "Inter-compartment interaction in multi-impeller mixing part II: Experiments, sliding mesh and Large Eddy simulations". In: *Chemical Engineering Research and Design* 136, pp. 886–899.
- Haringa, C., Noorman, H. J. & Mudde, R. F. (2017b). "Lagrangian modeling of hydrodynamic–kinetic interactions in (bio)chemical reactors: Practical implementation and setup guidelines". In: *Chemical Engineering Science* 157, pp. 159–168.
- Haringa, C., Tang, W., Deshmukh, A. T., Xia, J., Reuss, M., Heijnen, J. J., Mudde, R. F. & Noorman, H. J. (2016). "Euler-Lagrange computational fluid dynamics for (bio)reactor scale-down: an analysis of organism life-lines". In: *Engineering in Life Sciences* 16.7, pp. 1–29.
- Haringa, C., Tang, W., Wang, G., Deshmukh, A. T., Winden, W. A. van, Chu, J., Gulik, W. M. van, Heijnen, J. J., Mudde, R. F. & Noorman, H. J. (2018a). "Computational fluid dynamics simulation of an industrial *P. chrysogenum* fermentation with a coupled 9-pool metabolic model: Towards rational scale-down and design optimization". In: *Chemical Engineering Science* 175, pp. 12–24.
- Haringa, C., Vandewijer, R. & Mudde, R. F. (2018b). "Inter-compartment interaction in multi-impeller mixing part I: Experiments and multiple reference frame CFD". In: *Chemical Engineering Research and Design* 136, pp. 870–885.
- Hartmann, H., Derksen, J. J., Montavon, C., Pearson, J., Hamill, I. S. & van den Akker, H. E. (2004). "Assessment of large eddy and RANS stirred tank simulations by means of LDA". In: *Chemical Engineering Science* 59.12, pp. 2419–2432.
- Heijnen, J. J. & van't Riet, K. (1984). "Mass transfer, mixing and heat transfer phenomena in low viscosity bubble column reactors". In: *Chemical Engineering* 28.2, B21–B42.
- Heins, A. L., Lencastre Fernandes, R., Gernaey, K. V. & Lantz, A. E. (2015). "Experimental and in silico investigation of population heterogeneity in continuous *Saccharomyces cerevisiae* scale-down fermentation in a two-compartment setup". In: *Journal of Chemical Technology and Biotechnology* 90.2, pp. 324–340.
- Helmstetter, C. E. (1996). "Timing of Synthetic Activities in the Cell Cycle". In: *Escherichia coli and Salmonella. Cellular and Molecular Biology*. 2nd ed. ASM Press, pp. 1627–1639.
- Henson, M. A., Müller, D. & Reuss, M. (2002). "Cell population modelling of yeast glycolytic oscillations". In: *Biochemical Journal* 368.2, pp. 433–446.
- Hewitt, C. J. & Nienow, A. W. (2007). "The scale-up of microbial batch and fed-batch fermentation processes." In: *Advances in Applied Microbiology* 62, pp. 105–35.

- Higbie, R. (1935). “The rate of absorption of a pure gas into a still liquid during short periods of exposure”. In: *Transactions of the American Institute of Chemical Engineers* 31, pp. 364–389.
- Hjortso, A. M. & Nielsen, J. (1995). “Population balance models of autonomous microbial oscillations”. In: *Journal of Biotechnology* 42.3, pp. 255–269.
- Ishii, M. & Zuber, N. (1979). “Drag coefficient and relative velocity in bubbly, droplet or particulate flows”. In: *AIChE Journal* 25.5, pp. 843–855.
- Jahn, M., Seifert, J., von Bergen, M., Schmid, A., Bühler, B. & Müller, S. (2013). “Subpopulation-proteomics in prokaryotic populations”. In: *Current Opinion in Biotechnology* 24.1, pp. 79–87.
- Jahoda, M., Mostek, M., Kukuková, A. & Machoň, V. (2007). “CFD modelling of liquid homogenization in stirred tanks with one and two impellers using large eddy simulation”. In: *Chemical Engineering Research and Design* 85.5, pp. 616–625.
- Joshi, J. B., Nere, N. K., Rane, C. V., Murthy, B. N., Mathpati, C. S., Patwardhan, A. W. & Ranade, V. V. (2011). “CFD simulation of stirred tanks: Comparison of turbulence models. Part I: Radial flow impellers”. In: *Canadian Journal of Chemical Engineering* 89.1, pp. 23–82.
- Junker, B. H. (2004). “Scale-up methodologies for *Escherichia coli* and yeast fermentation processes”. In: *Journal of Bioscience and Bioengineering* 97.6, pp. 347–364.
- Junne, S., Klingner, A., Itzeck, D., Brand, E. & Neubauer, P. (2012). “Consistency of scale-up from bioprocess development to production”. In: *Biopharmaceutical Production Technology* 1, pp. 511–543.
- Kálal, Z., Jahoda, M. & Fort, I. (2014). “Modelling of the bubble size distribution in an aerated stirred tank: Theoretical and numerical comparison of different breakup models”. In: *Chemical and Process Engineering* 35.3, pp. 331–348.
- Karcz, J., Siciarz, R. & Bielka, I. (2004). “Gas hold-up in a reactor with dual system of impellers”. In: *Chemical Papers* 58.6, pp. 404–409.
- Käß, F., Junne, S., Neubauer, P., Wiechert, W. & Oldiges, M. (2014). “Process inhomogeneity leads to rapid side product turnover in cultivation of *Corynebacterium glutamicum*”. In: *Microbial Cell Factories* 13.1, p. 6.
- Kawase, Y. & Moo-Young, M. (1990). “Bioprocess Engineering The effect of antifoam agents on mass transfer in bioreactors”. In: *Bioprocess Engineering* 5.4, pp. 169–173.
- Kawase, Y., Halard, B. & Moo-Young, M. (1992). “Liquid-Phase mass transfer coefficients in bioreactors”. In: *Biotechnology and Bioengineering* 39.11, pp. 1133–1140.
- Keasling, J. D., Kuo, H. & Vahanian, G. (1995). “A Monte Carlo simulation of the *Escherichia coli* cell cycle.” In: *Journal of theoretical biology* 176.3, pp. 411–30.
- Khodayari, A. & Maranas, C. D. (2016). “A genome-scale *Escherichia coli* kinetic metabolic model k-ecoli457 satisfying flux data for multiple mutant strains”. In: *Nature Communications* 7.1, pp. 1–12.
- Kita, K., Konishi, K. & Anraku, Y. (1984). “Terminal oxidases of *Escherichia coli* aerobic respiratory chain”. In: *Journal of Biological Chemistry* 259.5, pp. 3368–3374.
- Koh, P., Schwarz, M., Zhu, Y., Bourke, P., Peaker, R. & Franzidis, J. (2003). “Development of CFD models of mineral flotation cells”. In: pp. 171–176.

- 
- Kolmogorov, A. (1941). "The local structure of turbulence in incompressible viscous fluid for very large reynolds' numbers". In: *Akademiia Nauk SSSR Doklady* 30, pp. 301–305.
- Koppes, L. J., Woldringh, C. L. & Nanninga, N. (1978). "Size variations and correlation of different cell cycle events in slow growing *Escherichia coli*". In: *Journal of Bacteriology* 134.2, pp. 423–433.
- Kukuková, A., Moštěk, M., Jahoda, M. & Machoň, V. (2005). "CFD prediction of flow and homogenization in a stirred vessel: Part I vessel with one and two impellers". In: *Chemical Engineering and Technology* 28.10, pp. 1125–1133.
- Kumar, S. & Ramkrishna, D. (1996). "On the solution of PBE by discretization - I. A fixed pivot technique". In: *Chemical Engineering Science* 51.8, pp. 1311–1332.
- Kuschel, M., Siebler, F. & Takors, R. (2017). "Lagrangian trajectories to predict the formation of population heterogeneity in large-scale bioreactors". In: *Bioengineering* 4.27, pp. 1–13.
- Kuschel, M. & Takors, R. (2020). "Simulated oxygen and glucose gradients as a prerequisite for predicting industrial scale performance a priori". In: *Biotechnology and Bioengineering* 117.9, pp. 2760–2770.
- Kusumoto, K., Sakiyama, M., Sakamoto, J., Noguchi, S. & Sone, N. (2000). "Menaquinol oxidase activity and primary structure of cytochrome bd from the amino-acid fermenting bacterium *Corynebacterium glutamicum*". In: *Archives of Microbiology* 173.5-6, pp. 390–397.
- Laakkonen, M., Alopaeus, V. & Aittamaa, J. (2006). "Validation of bubble breakage, coalescence and mass transfer models for gas-liquid dispersion in agitated vessel". In: *Chemical Engineering Science* 61.1, pp. 218–228.
- Laakkonen, M., Moilanen, P., Alopaeus, V. & Aittamaa, J. (2007a). "Modelling local gas-liquid mass transfer in agitated vessels". In: *Chemical Engineering Research and Design* 85.5, pp. 665–675.
- Laakkonen, M., Moilanen, P., Alopaeus, V. & Aittamaa, J. (2007b). "Modelling local bubble size distributions in agitated vessels". In: 62.3, pp. 721–740.
- Lapin, A., Müller, D. & Reuss, M. (2004). "Dynamic behavior of microbial populations in stirred bioreactors simulated with Euler-Lagrange methods: Traveling along the lifelines of single cells". In: *Industrial and Engineering Chemistry Research* 43.16, pp. 4647–4656.
- Lapin, A., Schmid, J. & Reuss, M. (2006). "Modeling the dynamics of *E. coli* populations in the three-dimensional turbulent field of a stirred-tank bioreactor - A structured - segregated approach". In: *Chemical Engineering Science* 61.14, pp. 4783–4797.
- Lara, A. R., Galindo, E., Ramírez, O. T. & Palomares, L. A. (2006). "Living with heterogeneities in bioreactors". In: *Molecular Biotechnology* 34.3, pp. 355–381.
- Larsson, G., Törnkvist, M., Ståhl Wernersson, E., Trägårdh, C., Noorman, H. & Enfors, S. O. (1996). "Substrate gradients in bioreactors: Origin and consequences". In: *Bioprocess Engineering* 14.6, pp. 281–289.
- Laurien, E. & Oertel jr., H. (2018). *Numerische Strömungsmechanik*. Springer.
- Lehr, F., Millies, M. & Mewes, D. (2002). "Bubble-size distributions and flow fields in bubble columns". In: *AIChE Journal* 48.11, pp. 2426–2443.

- Lemoine, A., Limberg, M. H., Kästner, S., Oldiges, M., Neubauer, P. & Junne, S. (2016). “Performance loss of *Corynebacterium glutamicum* cultivations under scale-down conditions using complex media”. In: *Engineering in Life Sciences* 16.7, pp. 620–632.
- Letek, M., Fiuza, M., Ordóñez, E., Villadangos, A. F., Ramos, A., Mateos, L. M. & Gil, J. A. (2008). “Cell growth and cell division in the rod-shaped actinomycete *Corynebacterium glutamicum*”. In: *Antonie van Leeuwenhoek* 94.1, pp. 99–109.
- Leuchtenberger, W., Huthmacher, K. & Drauz, K. (2005). “Biotechnological production of amino acids and derivatives: Current status and prospects”. In: *Applied Microbiology and Biotechnology* 69.1, pp. 1–8.
- Li, Z., Hu, M., Bao, Y. & Gao, Z. (2012). “Particle image velocimetry experiments and large eddy simulations of merging flow characteristics in dual Rushton turbine stirred tanks”. In: *Industrial and Engineering Chemistry Research* 51.5, pp. 2438–2450.
- Liebl, W. (2006). “Corynebacterium–Nonmedical”. In: *The Prokaryotes*. New York, NY: Springer, pp. 796–818.
- Lieder, S., Jahn, M., Koepff, J., Müller, S. & Takors, R. (2016). “Environmental stress speeds up DNA replication in *Pseudomonas putida* in chemostat cultivations”. In: *Biotechnology Journal* 11.1, pp. 155–163.
- Lindner, S. N., Seibold, G. M., Henrich, A., Krämer, R. & Wendisch, V. F. (2011). “Phosphotransferase system-independent glucose utilization in *Corynebacterium glutamicum* by inositol permeases and glucokinases”. In: *Applied and Environmental Microbiology* 77.11, pp. 3571–3581.
- Linek, V., Kordač, M., Fujasová, M. & Moucha, T. (2004). “Gas-liquid mass transfer coefficient in stirred tanks interpreted through models of idealized eddy structure of turbulence in the bubble vicinity”. In: *Chemical Engineering and Processing: Process Intensification* 43.12, pp. 1511–1517.
- Löffler, M., Simen, J. D., Jäger, G., Schäferhoff, K., Freund, A. & Takors, R. (2016). “Engineering *E. coli* for large-scale production – Strategies considering ATP expenses and transcriptional responses”. In: *Metabolic Engineering* 38, pp. 73–85.
- Luo, H. & Svendsen, H. F. (1996). “Theoretical model for drop and bubble breakup in turbulent dispersions”. In: *AIChE Journal* 42.5, pp. 1225–1233.
- Luo, J. Y. & Gosman, A. D. (1994). “Prediction of impeller induced flows in mixing vessels using multiple frames of reference”. In: *Institution of Chemical Engineers Symposium Series*, pp. 549–556.
- Machado, D., Costa, R. S., Ferreira, E. C., Rocha, I. & Tidor, B. (2012). “Exploring the gap between dynamic and constraint-based models of metabolism”. In: *Metabolic Engineering* 14.2, pp. 112–119.
- Maia, C. I., Fonseca, M. M. R., Vasconcelos, J. M. T., Alves, S. S. & Mora, A. (1999). “Effect of antifoam addition on gas-liquid mass transfer in stirred fermenters”. In: *Bioprocess Engineering* 20.2, pp. 165–172.

- 
- Markopoulos, J. & Pantouflas, E. (2001). "Power consumption in gas-liquid contactors agitated by double-stage Rushton turbines". In: *Chemical Engineering and Technology* 24.11, pp. 1147–1150.
- Mersmann, A., Einkenel, W. D. & Käppel, M. (1975). "Auslegung und Maßstabsvergrößerung von Rührapparaten". In: *Chemie Ingenieur Technik* 47.23, pp. 953–964.
- Micale, G., Brucato, A., Grisafi, F. & Ciofalo, M. (1999). "Prediction of flow fields in a dual-impeller stirred vessel". In: *AIChE Journal* 45.3, pp. 445–464.
- Monod, J. (1949). "The growth of bacterial cultures". In: *Annual Review of Microbiology* 3.1, pp. 371–394.
- Montante, G., Lee, K. C., Brucato, A. & Yianneskis, M. (2001). "Numerical simulations of the dependency of flow pattern on impeller clearance in stirred vessels". In: *Chemical Engineering Science* 56.12, pp. 3751–3770.
- Montante, G., Moštek, M., Jahoda, M. & Magelli, F. (2005). "CFD simulations and experimental validation of homogenisation curves and mixing time in stirred Newtonian and pseudoplastic liquids". In: *Chemical Engineering Science* 60.8-9, pp. 2427–2437.
- Morchain, J., Gabelle, J.-C. & Cockx, A. (2014). "A coupled population balance model and CFD approach for the simulation of mixing issues in lab-scale and industrial bioreactors". In: *American Institute of Chemical Engineers* 60.1, pp. 27–40. eprint: arXiv:1402.6991v1.
- Morrison, C. & Lähteenmäki, R. (2017). "Public biotech in 2016 - The numbers". In: *Nature Biotechnology* 35.7, pp. 623–629.
- Moštek, M., Kukuková, A., Jahoda, M. & Machoň, V. (2005). "CFD prediction of flow and homogenization in a stirred vessel: Part II vessel with three and four impellers". In: *Chemical Engineering and Technology* 28.10, pp. 1134–1143.
- Moucha, T., Linek, V. & Prokopová, E. (2003). "Gas hold-up, mixing time and gas-liquid volumetric mass transfer coefficient of various multiple-impeller configurations: Rushton turbine, pitched blade and techmix impeller and their combinations". In: *Chemical Engineering Science* 58.9, pp. 1839–1846.
- Müller, S., Harms, H. & Bley, T. (2010). "Origin and analysis of microbial population heterogeneity in bioprocesses". In: *Current Opinion in Biotechnology* 21.1, pp. 100–113.
- Murthy, B. N. & Joshi, J. B. (2008). "Assessment of standard  $k - \epsilon$ , RSM and LES turbulence models in a baffled stirred vessel agitated by various impeller designs". In: *Chemical Engineering Science* 63.22, pp. 5468–5495.
- Murthy, J., Mathur, S. & Choudhury, D. (1994). "CFD simulation of flows in stirred tank reactors using a sliding mesh technique". In: *Institution of Chemical Engineers Symposium Series*. Vol. 136, pp. 341–348.
- Naude, I., Xuereb, C. & Bertrand, J. (1998). "Direct prediction of the flows induced by a propeller in an agitated vessel using an unstructured mesh". In: *Canadian Journal of Chemical Engineering* 76.3, pp. 631–640.
- Neubauer, P., Cruz, N., Glauche, F., Junne, S., Knepper, A. & Raven, M. (2013). "Consistent development of bioprocesses from microliter cultures to the industrial scale". In: *Engineering in Life Sciences* 13.3, pp. 224–238.

- Neubauer, P. & Junne, S. (2010). “Scale-down simulators for metabolic analysis of large-scale bioprocesses”. In: *Current Opinion in Biotechnology* 21.1, pp. 114–121.
- Neumeyer, A., Hübschmann, T. & Frunzke, J. (2012). “Monitoring of population dynamics of *Corynebacterium glutamicum* by multiparameter flow cytometry”. In: *Microbial Biotechnology* 6.2, pp. 157–167.
- Newton, J. M., Schofield, D., Vlahopoulou, J. & Zhou, Y. (2016). “Detecting cell lysis using viscosity monitoring in *E. coli* fermentation to prevent product loss”. In: *Biotechnology progress* 32.4, pp. 1069–1076.
- Newton, J. M., Vlahopoulou, J. & Zhou, Y. (2017). “Investigating and modelling the effects of cell lysis on the rheological properties of fermentation broths”. In: *Biochemical Engineering Journal* 121, pp. 38–48.
- Nielsen, J., Nikolajsen, K. & Villadsen, J. (1991). “Structured modeling of a microbial system: I. A theoretical study of lactic acid fermentation”. In: *Biotechnology and Bioengineering* 38.1, pp. 1–10.
- Nienow, A. W. (1997). “On impeller circulation and mixing effectiveness in the turbulent flow regime”. In: *Chemical Engineering Science* 52.15, pp. 2557–2565.
- Nienow, A. W. (1998). “Hydrodynamics of stirred bioreactors”. In: *Applied Mechanics Reviews* 51.1, p. 3.
- Nienow, A. W. & Lilly, M. D. (1979). “Power drawn by multiple impellers in sparged agitated vessels”. In: *Biotechnology and Bioengineering* 21.12, pp. 2341–2345.
- Nieß, A., Löffler, M., Simen, J. D. & Takors, R. (2017). “Repetitive short-term stimuli imposed in poor mixing zones induce long-term adaptation of *E. coli* cultures in large-scale bioreactors: experimental evidence and mathematical model”. In: *Frontiers in Microbiology* 8, pp. 1–9.
- Nishimura, Y. & Bailey, J. E. (1981). “Bacterial population dynamics in batch and continuous-flow microbial reactors”. In: *American Institute of Chemical Engineers* 27.1, pp. 73–81.
- Nyholm, N. (1976). “A mathematical model for microbial growth under limitation by conservative substrates”. In: *Biotechnology and Bioengineering* 18.8, pp. 1043–1056.
- Oldshue, J. Y. (1966). “Fermentation mixing scale-up techniques”. In: *Biotechnology and Bioengineering* 8.1, pp. 3–24.
- Oosterhuis, N. M. & Kossen, N. W. (1981). “Power input measurements in a production scale bioreactor”. In: *Biotechnology Letters* 3.11, pp. 645–650.
- Oosterhuis, N. M. & Kossen, N. W. (1984). “Dissolved oxygen concentration profiles in a production-scale bioreactor”. In: *Biotechnology and Bioengineering* 26.5, pp. 546–550.
- Pigou, M. & Morchain, J. (2015). “Investigating the interactions between physical and biological heterogeneities in bioreactors using compartment, population balance and metabolic models”. In: *Chemical Engineering Science* 126, pp. 267–282.
- Pirt, S. J. (1965). “The maintenance energy of bacteria in growing cultures”. In: *Proceedings of the Royal Society of London. Series B. Biological Sciences* 163, pp. 224–231.
- Poorte, R. E. & Biesheuvel, A. (2002). “Experiments on the motion of gas bubbles in turbulence generated by an active grid”. In: *Journal of Fluid Mechanics* 461, pp. 127–154.

- 
- Prasher, B. D. & Wills, G. B. (1973). "Mass transfer in an agitated vessel". In: *Industrial and Engineering Chemistry Process Design and Development* 12.3, pp. 351–354.
- Prince, M. & Blanch, H. (1990). "Bubble coalescence and break-up in air-sparged bubble columns". In: *AIChE Journal* 36.10, pp. 1485–1499.
- Puthli, M. S., Rathod, V. K. & Pandit, A. B. (2005). "Gas-liquid mass transfer studies with triple impeller system on a laboratory scale bioreactor". In: *Biochemical Engineering Journal* 23.1, pp. 25–30.
- Qian, H. & Elson, E. L. (2002). "Single-molecule enzymology: Stochastic Michaelis-Menten kinetics". In: *Biophysical Chemistry* 101, pp. 565–576.
- Ranade, V. V. & Van den Akker, H. E. (1994). "A computational snapshot of gas-liquid flow in baffled stirred reactors". In: *Chemical Engineering Science* 49.24, pp. 5175–5192.
- Rodriguez, S. (2019). "LES and DNS Turbulence Modeling". In: *Applied Computational Fluid Dynamics and Turbulence Modeling*. Cham: Springer, pp. 197–223.
- Roels, J. A. & Heijnen, J. J. (1980). "Power dissipation and heat production in bubble columns: Approach based on nonequilibrium thermodynamics". In: *Biotechnology and Bioengineering* 22.11, pp. 2399–2404.
- Roels, J. (1983). *Energetics and Kinetics in Biotechnology*. Elsevier Biomedical Press.
- Rosseburg, A., Fitschen, J., Wutz, J., Wucherpennig, T. & Schlüter, M. (2018). "Hydrodynamic inhomogeneities in large scale stirred tanks – Influence on mixing time". In: *Chemical Engineering Science* 188, pp. 208–220.
- Rushton, J. H. & Bmbinet, J.-J. (1968). "Holdup and flooding in air liquid mixing". In: *The Canadian Journal of Chemical Engineering* 46.1, pp. 16–21.
- Rushton, J. & Costich, E. H. (1950). "Power characteristics of mixing impeller". In: *Chemical Engineering Progress* 46, pp. 395–404.
- Russell, D. W. & Sambrook, J. (2001). *Molecular cloning: a laboratory manual*. Vol. 1. Cold Spring Harbor Laboratory.
- Sabatino, R. D., Myers, T. W., Bambara, R. A., Kwon-shin, O., Marraccino, R. L. & Frickey, P. H. (1988). "Calf thymus DNA polymerases  $\alpha$  and  $\delta$  are capable of highly processive DNA synthesis". In: *Biochemistry* 27.8, pp. 2998–3004.
- Sagaut, P., Deck, D. & Terracol, M. (2006). *Multiscale and Multiresolution Approaches in Turbulence*. Imperial College Press.
- Sánchez Mirón, A., García Camacho, F., Contreras Gómez, A., Grima, E. M. & Chisti, Y. (2000). "Bubble-column and airlift photobioreactors for algal culture". In: *AIChE Journal* 46.9, pp. 1872–1887.
- Sander, R. (2015). "Compilation of Henry's law constants (version 4 .0) for water as solvent". In: *Atmospheric Chemistry and Physics* 15.8, pp. 4399–4981.
- Scargiali, F., D'Orazio, A., Grisafi, F. & Brucato, A. (2007). "Modelling and simulation of gas - Liquid hydrodynamics in mechanically stirred tanks". In: *Chemical Engineering Research and Design* 85.5, pp. 637–646.
- Schilling, B. M., Pfefferle, W., Bachmann, B., Leuchtenberger, W. & Deckwer, W. D. (1999). "A special reactor design for investigations of mixing time effects in a scaled-down industrial L-

- lysine fed-batch fermentation process". In: *Biotechnology and Bioengineering* 64.5, pp. 599–606.
- Schmidt, F. R. (2005). "Optimization and scale up of industrial fermentation processes". In: *Applied Microbiology and Biotechnology* 68.4, pp. 425–435.
- Schügerl, K., Lücke, J., Lehmann, J & Wagner, F (1978). "Application of tower bioreactors in cell mass production". In: *Advances in Biochemical Engineering*. Vol. 8. Springer, pp. 63–131.
- Shewale, S. D. & Pandit, A. B. (2006). "Studies in multiple impeller agitated gas – liquid contactors". In: *Chemical Engineering Science* 61.2, pp. 489–504.
- Shuler, M. L. (1999). "Single-cell models: Promise and limitations". In: *Journal of Biotechnology* 71.1-3, pp. 225–228.
- Skarstad, K., Boye, E. & Steen, H. B. (1986). "Timing of initiation of chromosome replication in individual *Escherichia coli* cells." In: *The EMBO journal* 5.7, pp. 1711–1717.
- Skarstad, K., Steen, H. B. & Boye, E. (1985). "Escherichia coli DNA Distributions Measured by Flow Cytometry and Compared with Theoretical Computer Simulations". In: *Journal of Bacteriology* 163.2, pp. 661–668.
- Skarstad, K., Stokke, C. & Fla, I. (2012). "An easy-to-use simulation program demonstrates variations in bacterial cell cycle parameters depending on medium and temperature". In: *Public Library of Science* 7.2.
- Steel, R. & Maxon, W. D. (1966). "Dissolved oxygen measurements in pilot- and production-scale novobiocin fermentations". In: *Biotechnology and Bioengineering* 8.1, pp. 97–108.
- Taghavi, M., Zadghaffari, R., Moghaddas, J. & Moghaddas, Y. (2011). "Experimental and CFD investigation of power consumption in a dual Rushton turbine stirred tank". In: *Chemical Engineering Research and Design* 89.3, pp. 280–290.
- Takeo, S., Ohnishi, J., Komatsu, T., Masaki, T., Sen, K. & Ikeda, M. (2007). "Anaerobic growth and potential for amino acid production by nitrate respiration in *Corynebacterium glutamicum*". In: *Applied Microbiology and Biotechnology* 75.5, pp. 1173–1182.
- Takors, R., Bathe, B., Rieping, M., Hans, S., Kelle, R. & Huthmacher, K. (2007). "Systems biology for industrial strains and fermentation processes - Example: Amino acids". In: *Journal of Biotechnology* 129.2, pp. 181–190.
- Tomiyama, A., Kataoka, I., Zun, I. & Sakaguchi, T. (1998). "Drag Coefficients of Single Bubbles under Normal and Micro Gravity Conditions". In: *JSME International Journal Series B Fluids and Thermal Engineering* 41.2, pp. 472–479.
- Tricot, Y.-M. (1997). "Surfactants: Static and Dynamic Surface Tension". In: *Liquid film coating*, pp. 99–136.
- Turner, T. E., Schnell, S. & Burrage, K. (2004). "Stochastic approaches for modelling in vivo reactions". In: *Computational Biology and Chemistry* 28.3, pp. 165–178.
- van't Riet, K. & Smith, J. M. (1973). "The behaviour of gas-liquid mixtures near Rushton turbine blades". In: *Chemical Engineering Science* 28.4, pp. 1031–1037.
- Van'T Riet, K. (1979). "Review of Measuring Methods and Results in Nonviscous Gas-Liquid Mass Transfer in Stirred Vessels". In: *Industrial and Engineering Chemistry Process Design and Development* 18.3, pp. 357–364.

- 
- Vasconcelos, J. M. T., Alves, S. S. & Barata, J. M. (1995). "Mixing in gas-liquid contactors agitated by multiple turbines". In: *Chemical Engineering Science* 50.14, pp. 2343–2354.
- Villadsen, J., Nielsen, J. & Lidén, G. (2011). "Scale-up of bioprocesses". In: *Bioreaction Engineering Principles*. Springer, pp. 497–546.
- von Kármán, T. (1934). "Turbulence and skin friction". In: *Journal of the Aeronautical Sciences* 1.1, pp. 1–20.
- Vrábel, P., van der Lans, R. G. J. M., Luyben, K. C. A. M., Boon, L. & Nienow, A. W. (2000). "Mixing in large-scale vessels stirred with multiple radial or radial and axial up-pumping impellers: modelling and measurements". In: *Chemical Engineering Science* 55.23, pp. 5881–5896.
- Vrábel, P., van der Lans, R. G. J. M., van der Schot, F. N., Ch, K., Luyben, A. M., Xu, B. & Enfors, S.-O. (2001). "CMA : integration of fluid dynamics and microbial kinetics in modelling of large-scale fermentations". In: *Chemical Engineering Journal* 84, pp. 463–474.
- Walsh, G. (2018). "Biopharmaceutical benchmarks 2018". In: *Nature Biotechnology* 36.12, pp. 1136–1145.
- Wang, R. S., Saadatpour, A. & Albert, R. (2012). "Boolean modeling in systems biology: An overview of methodology and applications". In: *Physical Biology* 9.5.
- Warmoeskerken, M. M. & Smith, J. M. (1985). "Flooding of disc turbines in gas-liquid dispersions: A new description of the phenomenon". In: *Chemical Engineering Science* 40.11, pp. 2063–2071.
- Warmoeskerken, M. & Smith, J. (1981). "Surface contamination effects in stirred tank reactors". In: *Proceedings of 8th conference of mixing*. Vol. 9.
- Wendisch, V. F., Spies, M., Reinscheid, D. J., Schnicke, S., Sahm, H. & Eikmanns, B. J. (1997). "Regulation of acetate metabolism in *Corynebacterium glutamicum*: Transcriptional control of the isocitrate lyase and malate synthase genes". In: *Archives of Microbiology* 168.4, pp. 262–269.
- Werner, S., Kaiser, S. C., Kraume, M. & Eibl, D. (2014). "Computational fluid dynamics as a modern tool for engineering characterization of bioreactors". In: *Pharmaceutical Bioprocessing* 2.1, pp. 85–99.
- Wiedmann, J. A. (1983). "Zum überflutungsverhalten zwei- und dreiphasig betriebener Rührreaktoren". In: *Chemie Ingenieur Technik* 55.9, pp. 689–700.
- Xueming, S., Xiaoling, L. & Yulin, L. (2008). "Experimental Study of Influence of the Impeller Spacing on Flow Behaviour of Double-Impeller Stirred Tank". In: *The Canadian Journal of Chemical Engineering* 81.6, pp. 1239–1245.
- Yagi, H. & Yoshida, F. (1974). "Oxygen absorption in fermenters - effects of surfactants, antifoaming agents, and sterilized cells". In: *Journal of Fermentation Technology* 52, pp. 905–916.
- Yawalkar, A. A., Heesink, A. B. M., Versteeg, G. F. & Pangarkar, V. G. (2008). "Gas-Liquid Mass Transfer Coefficient in Stirred Tank Reactors". In: *The Canadian Journal of Chemical Engineering* 80.5, pp. 840–848.
- Yokota, A. & Ikeda, M. (2017). *Amino Acid Fermentation*. 159th ed. Springer.

- Youngren, B., Nielsen, H. J., Jun, S. & Austin, S. (2014). “The multifork *Escherichia coli* chromosome is a self-duplicating and self-segregating thermodynamic ring polymer”. In: *Genes and Development* 28.1, pp. 71–84.
- Yukawa, H. & Inui, M. (2013). *Corynebacterium glutamicum: Biology and Biotechnology*. Springer, p. 416.
- Zadghaffari, R., Moghaddas, J. S. & Revstedt, J. (2010). “Large-eddy simulation of turbulent flow in a stirred tank driven by a Rushton turbine”. In: *Computers and Fluids* 39.7, pp. 1183–1190.
- Zlokarnik, M. (1999). *Rührtechnik*. Springer.

---

## A Tables

### A.1 List of instruments

Table A.1: Instruments

Instrument	Manufacturer
ATmega328	Arduino
Benchtop shaker AK85	Infors AG
Bioreactor KLF 2000 (3.7 L)	Bioengineering
Centrifuge 5430 R; rotor F-35-6-30	Eppendorf
Centrifuge 5430 R; rotor FA 45-30-11	Eppendorf
Conductmeter LF521	Wissenschaftlich-Technische Werkstätten
Exhaust gas analyser BCP-O <sub>2</sub> and BCP-CO <sub>2</sub>	BlueSens
Glas vials	VWR
HC-SR04 Distance Sensor Module	Arduino
Mass flowmeter, Model 3585	Analyt MTC Messtechnik
Microscope BH-2-RFCA	Olympus
Nano V3	Arduino
Oxygen exchange capOEC-PSt3-NAU-OIW	PreSens
Oxygen probe InPro 6800	Mettler-Toledo
Oxygen probe OXYBase WR-RS485-L5-OIW	PreSens
pH probe 405-DPAS-SC-K8S,	Mettler Toledo
Photometer DR 2800 (biomass)	Hach Lange
Photometer Ultrospec 2100 pro (glucose)	GE Healthcare
Pump 101U	Watson-Marlow
Rheometer MCR 501	Anton Paar
Scale Combics 3	Sartorius
Scale Kern 572	Kern& Sohn
Syringe pump LA-30	HLL Landgraf Laborsysteme
Temperature sensor PT-100	Bioengineering
Tensiometer BP100	Krüss
Tensiometer STA1A	SINTERFACE Technologies
Total carbon analyzer Multi N/C 2100s	Analytik Jena

## A.2 List of software

Table A.2: Software

Software	Manufacturer
Ansys Fluent	Ansys Inc.
LabVIEW	National Instruments, USA
(MATLAB R2019a)	The MathWorks, Inc.

## A.3 List of chemicals

Table A.3: Chemicals

Chemical	Manufacturer
4',6-diamidino-2'-phenylindole (DAPI)	Sigma Aldrich
Ammonium sulphate, $(\text{NH}_4)_2\text{SO}_4$ , $\geq 99\%$	Carl Roth GmbH&Co. KG
Biotin, D(+)-, $\geq 98.5\%$	Carl-Roth GmbH &Co. KG
Calcium chloride, $\text{CaCl}_2$	Merck Chemicals GmbH
Copper(II) sulfate pentahydrate, $\text{CuSO}_4 \cdot 5 \text{H}_2\text{O}$ , $\geq 99\%$	Sigma-Aldrich Co. LLC.
Glucose, $\alpha$ -D(+)-, monohydrate, $\geq 99.5\%$	Carl-Roth GmbH &Co. KG
Hydrochloric acid, $\text{HCl}$ , $\geq 32\%$	Sigma Aldrich Co. LLC.
Iron(II) sulfate heptahydrate, $\text{FeSO}_4 \cdot 7 \text{H}_2\text{O}$ , $\geq 99\%$	Sigma-Aldrich Co. LLC.
Magnesium sulphate heptahydrate, $\text{MgSO}_4 \cdot 7 \text{H}_2\text{O}$ , $\geq 99\%$	Carl Roth GmbH&Co. KG
Manganese(II) sulfate monohydrate, $\text{MnSO}_4 \cdot \text{H}_2\text{O}$ , $\geq 98\%$	Carl Roth GmbH&Co. KG
Nickel(II) sulphate hexahydrate, $\text{NiSO}_4 \cdot 6 \text{H}_2\text{O}$ , $\geq 98\%$	Carl-Roth GmbH &Co. KG
Potassium dihydrogen phosphate, $\text{KH}_2\text{PO}_4$ , $\geq 98\%$	Carl Roth GmbH&Co. KG
Potassium hydrogen phosphate, di-, $\text{K}_2\text{HPO}_4$ , $\geq 98\%$	Carl Roth GmbH&Co. KG
Protocatechuic acid, 3,4-dihydroxybenzoic acid, $\geq 97\%$	Carl Roth GmbH&Co. KG
Sodium chloride, $\text{NaCl}$ , $\geq 99.8\%$	Carl Roth GmbH&Co. KG
Struktol <sup>®</sup> J 647	Schill&Seilacher
TRIS PUFFERAN <sup>®</sup> $\geq 99.9\%$	Carl Roth GmbH&Co. KG
Tryptone	BD
Yeast extract	BD
Zinc sulfate heptahydrate, $\text{ZnSO}_4 \cdot 7 \text{H}_2\text{O}$ , $\geq 99\%$	Sigma-Aldrich Co. LLC.

---

## **B Authors contribution**

This chapter summarises my (Maïke Kuschel) contribution to the manuscripts which are already published or recently submitted. The content of the manuscripts are supplementary provided as well.

### **Manuscript I**

Kuschel<sup>†</sup>, M., Siebler<sup>†</sup>, F., and Takors, R. (2017). "Lagrangian Trajectories to Predict the Formation of Population Heterogeneity in Large-Scale Bioreactors". In: *Bioengineering* 4.27, pp. 1-13.

<sup>†</sup> These authors contributed equally to this work.

Both, Maïke Kuschel and Flora Siebler, equally conducted all parts of the simulations, evaluations, and preparations of the manuscript.

### **Manuscript II**

Kuschel, M., and Takors, R. (2020). "Simulated oxygen and glucose gradients as a prerequisite for predicting industrial scale performance *a priori*". In: *Biotechnology and Bioengineering* 117.9, pp. 2760–2770.

All experiments, simulations, evaluations, and the writing of the manuscript was conducted by Maïke Kuschel.

## **B.1 Manuscript I**

---

# Lagrangian Trajectories to Predict the Formation of Population Heterogeneity in Large-Scale Bioreactors

---

Reprinted from Kuschel et al. (2017) with permission of

© MDPI Bioengineering.

Article

# Lagrangian Trajectories to Predict the Formation of Population Heterogeneity in Large-Scale Bioreactors

Maike Kuschel <sup>†</sup>, Flora Siebler <sup>†</sup> and Ralf Takors <sup>\*</sup>

Institute of Biochemical Engineering, University of Stuttgart, 70569 Stuttgart, Germany; Maike.Kuschel@ibvt.uni-stuttgart.de (M.K.); Flora.Siebler@ibvt.uni-stuttgart.de (F.S.)

<sup>\*</sup> Correspondence: takors@ibvt.uni-stuttgart.de; Tel.: +49-711-685-64535

<sup>†</sup> These authors contributed equally to this work.

Academic Editor: Christoph Herwig

Received: 23 February 2017; Accepted: 24 March 2017; Published: 29 March 2017

**Abstract:** Successful scale-up of bioprocesses requires that laboratory-scale performance is equally achieved during large-scale production to meet economic constraints. In industry, heuristic approaches are often applied, making use of physical scale-up criteria that do not consider cellular needs or properties. As a consequence, large-scale productivities, conversion yields, or product purities are often deteriorated, which may prevent economic success. The occurrence of population heterogeneity in large-scale production may be the reason for underperformance. In this study, an *in silico* method to predict the formation of population heterogeneity by combining computational fluid dynamics (CFD) with a cell cycle model of *Pseudomonas putida* KT2440 was developed. The glucose gradient and flow field of a 54,000 L stirred tank reactor were generated with the Euler approach, and bacterial movement was simulated as Lagrange particles. The latter were statistically evaluated using a cell cycle model. Accordingly, 72% of all cells were found to switch between standard and multifork replication, and 10% were likely to undergo massive, transcriptional adaptations to respond to extracellular starving conditions. At the same time, 56% of all cells replicated very fast, with  $\mu \geq 0.3 \text{ h}^{-1}$  performing multifork replication. The population showed very strong heterogeneity, as indicated by the observation that 52.9% showed higher than average adenosine triphosphate (ATP) maintenance demands (12.2%, up to 1.5 fold). These results underline the potential of CFD linked to structured cell cycle models for predicting large-scale heterogeneity *in silico* and *ab initio*.

**Keywords:** computational fluid dynamics; cell cycle model; Lagrange trajectory; scale-up; stirred tank reactor; population dynamics; energy level

## 1. Introduction

The physiological state of bacterial cells is strongly dependent on the surrounding conditions. As outlined in Müller et al. [1], external stress is a key factor inducing the formation of population heterogeneity, which differs according to growth phenotypes and cell cycle patterns. Moreover, concentration fluctuations occurring under large-scale mixing conditions have a measurable influence on growth and production yield [2–4]. Accordingly, homogeneity of the bacterial population may be affected, yielding subpopulations that co-exist next to each other [1]. Makinoshima et al. [5] observed five and ten cell populations of *Escherichia coli* during exponential growth and the subsequent stationary phase, respectively. For *Pseudomonas putida*, steady-state chemostat cultivation revealed that industry-like stress conditions induced changes in the cell cycle process. Under stress, deoxyribonucleic acid (DNA) replication was accelerated in a dose-dependent manner, yielding subpopulations with different DNA contents [6].

To investigate whether nutrient gradients of large-scale conditions foster the occurrence of population heterogeneity, the following concept was formulated. First, large-scale substrate gradients of a bioreactor should be simulated. Next, the path of bacterial cells through the gradients need to be tracked, and the resulting growth phenotypes monitored. Then, a cell cycle model can be used to translate changing growth conditions into cell cycle patterns. Apparently, this approach requires (i) a sound simulation of large-scale substrate gradients that trigger ‘stress’ in the cells and (ii) the translation of nutrient availability in growth patterns as a basis of cell cycle modelling. For the latter, the findings of Cooper and Helmstetter [7] were applied. They specified a relationship between chromosome content and cell cycle phase duration for *E. coli B/r* and showed that the amount of DNA varies continuously with the growth rate and substrate availability. Consequently, the durations of the cell cycle phases are strongly dependent on the environmental conditions.

The cell cycle of bacteria using binary fission can be divided into three parts: the time for initiation of replication (B-period), the time required for replication (C-period), and the time between replication and completed cell division (D-period). C-periods are the longest for slow-growing cells but decrease to constant values under elevated growth conditions [8]. In order to grow faster, replication and segregation are separated in time. Most bacteria initiate replication during a previous generation, leading to multifork replication.

Single-cell analysis by fluorescence-activated cell scanning has proven to be a valuable method to measure the DNA content from thousands of bacteria and to generate DNA content histograms for the population [9]. Also, latest lab on a chip techniques are a feasible method for measuring population heterogeneity [10,11]. Subpopulations with one, two, or more chromosomes can be detected. Skarstad [12] extended the model of Cooper and Helmstetter to calculate the number of individuals of *E. coli B/r* comprising a subpopulation with a specific DNA content from flow cytometry data. Furthermore, Skarstad determined the duration of the cell cycle periods for various growth rates. This was proven to be applicable for *P. putida* KT2440 as well [6].

It is still challenging to capture the magnitude and frequency of fluctuations in large scale bioprocesses and to predict the extent of the intracellular response. Several authors have suggested computational fluid dynamics (CFD) as a tool to provide detailed information of environmental conditions inside a fermenter. The gas, liquid, and bio phases are often modeled as a continuum by the Euler-Euler approach [13–15]. Typically, microorganisms react individually to different environmental conditions; therefore, a continuum description may not be advantageous. An extension of the Euler-Euler approach for the liquid phase is the use of population balance equations to model the heterogeneity of a population [16,17]. The incorporation of a detailed intracellular reaction network, however, demands a high computational effort to solve the complex distribution functions [18,19].

Since the pioneering work of Lapin et al. [20], environmental fluctuations have been studied from the perspective of microorganisms. The applied Euler-Lagrange approach uses a continuous representation of the fluid phase (Euler), combined with a segregated description of the cell population (Lagrange). The bacteria are simulated as particles, which are tracked on their way through the reactor. Statistical evaluation of these trajectories, denoted as bacterial lifelines, provide valuable information about substrate fluctuation frequencies experienced by microorganisms [21].

The influence of these fluctuations on cell cycle dynamics and energy levels has not been demonstrated yet. Thus, in this study, based on the work of Haringa et al. [21], an extensive statistical evaluation of bacterial lifelines was performed. Rather conservative operating conditions for the industrially relevant strain *P. putida* KT2440 were assumed to investigate the occurrence of and impact on population homogeneity. The Euler-Lagrange approach was combined with a cell cycle model of Lieder et al. [6] to gain deeper insights into the behaviors of cell cycle dynamics and individual distributions during large-scale fermentation.

These findings present a method to better analyze and understand the heterogeneity caused by scale up-induced stress stimuli.

## 2. Materials and Methods

### 2.1. Cell Cycle Model

Flow cytometry data ranging from  $\mu = 0.1 \text{ h}^{-1}$  to  $0.6 \text{ h}^{-1}$  for *P. putida* KT2440 were obtained by Lieder et al. [6] and processed as shown in Figure 1. The data were channeled and displayed as the frequency distribution of DNA content. The durations of cell cycle phases C (DNA replication) and D (period between replication and completed cell division) were determined iteratively by minimizing the deviation between experimental and theoretical DNA histograms. The theoretical DNA content of an asynchronous, ideal culture in which all cells have equal growth parameters was derived from the age distribution according to Cooper and Helmstetter [7]. Using this probability density function for cells of a specific cell age, Cooper and Helmstetter further calculated the theoretical chromosome content per cell at a specific cell age. This model was extended by Skarstad et al. [12] to calculate the frequency of the occurrence of a specific DNA content in an interval of ongoing DNA synthesis. The durations of phases C and D are decisive for the distribution of DNA content. Different values for C were obtained to fit the experimental histograms for various growth rates. Based on the work of Lieder [22], a function for C-phase duration, dependent on the growth rate of *P. putida* KT2440, was derived. A correlation for C proposed by Keasling et al. [23] was used.

$$C = C_{\min} \left( 1 + a e^{b\mu} \right) \quad (1)$$

where C is the length of the C period,  $C_{\min}$  is the minimal length of the C period,  $\mu$  represents the growth rate and a and b are parameters that fit the experimental data. Based on the experimental data of Lieder et al. [6], the parameter estimation resulted in  $C_{\min} = 0.77 \text{ h}$ ,  $a = 1.83$ , and  $b = 4.88$ .

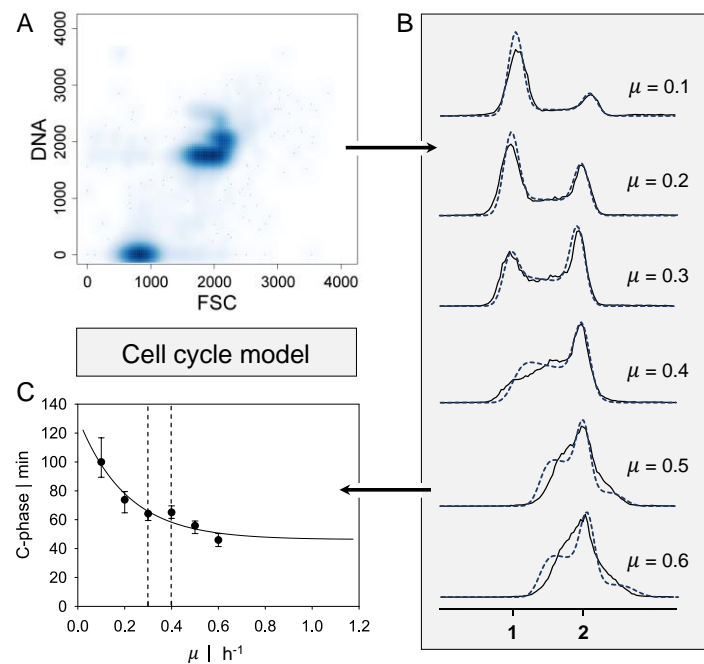


**Figure 1.** Approach for the cell cycle dynamics model. (A) Representative flow cytometry scatter plot for deoxyribonucleic acid (DNA) content of the growth rate  $\mu = 0.3 \text{ h}^{-1}$ . (B) DNA content over counts for growth rates ranging from  $\mu = 0.1 \text{ h}^{-1}$  up to  $\mu = 0.6 \text{ h}^{-1}$ . A single genome is indicated by 1, and double chromosomes by 2. Black lines present experimental data, and blue dashed lines present the calculation of the cell cycle model. (C) Approximated C-phase duration over growth rate estimated by the cell cycle model (1% parameter covariance). Black dashed lines indicate the transition regime from single-forked to multiforked replication. Flow cytometry data obtained by Lieder et al. [6].

## 2.2. Numerical Simulation

### 2.2.1. Geometry and Reactor Setup

In order to generate a pseudostationary glucose gradient of an industrial fed batch fermentation, a large-scale stirred tank bioreactor was chosen. Precise dimensions and information about the inner geometry can be found in Appendix A (Figure A1 and Table A1). The main geometry was derived from Haringa et al. [21] and only slightly modified for the purpose of this study. With an H/D ratio of 2.57, the total volume was about 54,000 L. The reactor setup included four baffles and a stirrer with two Rushton agitators. The lower stirring unit was equipped with eight blades, and the middle unit with six blades. With a stirring rate of 100 rpm, a tip speed of 5–8 m s<sup>-1</sup> was reached. The impeller Reynolds number was 1.8 × 10<sup>6</sup>, the power number 13.15, and the needed power was 226 kW.

The feeding rate was set as half of the maximum uptake rate  $q_{s,max}$  of *P. putida* with 0.738 kg<sub>glc</sub>·kg<sub>CDW</sub><sup>-1</sup>·h<sup>-1</sup>. Aeration, gas transfer, and oxygen uptake were neglected in this study. Therefore, no gassing system was installed. A cell concentration of 10 kg<sub>CDW</sub>·m<sup>-3</sup> was assumed, and a simple Monod-like kinetic was used to simulate the substrate uptake  $q_s$ :

$$q_s = q_{s,max} \cdot \frac{c_s}{K_s + c_s} \quad (2)$$

where  $q_{s,max}$  is the maximum uptake rate,  $c_s$  is the glucose concentration, and the approximated substrate specific uptake constant  $K_s$  with 10 mg·L<sup>-1</sup>. The maximum uptake rate was calculated with the biomass substrate yield  $Y_{XS} = 0.40$  g<sub>s</sub>·g<sub>CDW</sub><sup>-1</sup> and the maximum growth rate  $\mu = 0.59$  h<sup>-1</sup> [22,24].

### 2.2.2. Simulation Setup

For the numerical simulation, the commercial calculation tool ANSYS Fluent version 17.0 was used. Using this finite volume-based fluid dynamic analysis program, the virtual geometry was built, and spatial discretization was performed. A total of 445,000 numerical cells yielded the same circulation time as achieved by Haringa et al. [21]. The flow field was approximated by solving the Reynolds-averaged Navier-Stokes (RANS) equations in combination with the standard k- $\epsilon$  model for turbulence. All surfaces were set as slip boundaries, except for the frictionless top area, which implied the reactor filling height. Both impeller units were set to sliding mesh motion to generate a more realistic flow field.

For glucose feed, a separate volume at the top of the reactor was defined, and a constant mass flow was set. The feed was inserted as mass percentage, with constant pressure and volume. The hydrodynamic and kinetic was calculated every 10 ms until the overall glucose concentration was constant and a pseudostationary gradient was reached. Finally, an average flow field and glucose gradient were obtained over 150 s. In further simulations, the hydrodynamic and glucose gradient were set as frozen.

Bacteria lifelines were simulated as massless Lagrangian particles with a discrete random walk (DRW) model passing through the flow field. Every 30 ms, the position and glucose concentration for each bacterium were recorded. In total, 120,000 bacterial cells were tracked over 260 s. According to the ergodic theorem, the same average values are obtained by tracking 1,560,000 bacteria for 20 s (the approximate circulation time). The simulation would yield even more precise statistical evaluations by increasing the number of lifelines.

## 2.3. Statistical Evaluation

All bacterial lifelines were evaluated statistically and grouped according to the regime borders. The growth rate was calculated for each bacterial cell and each time interval. The regimes were classified as follows: standard forked replication S for  $\mu \leq 0.3$  h<sup>-1</sup>, the transition area T ( $0.3 < \mu < 0.4$  h<sup>-1</sup>), and multifork replication M for  $\mu \geq 0.4$  h<sup>-1</sup> derived by the cell cycle model (see Section 2.1.). By evaluating

the cell history, further classifications were made. Six regime transitions follow when two transitions and one retention time were considered:

- **STM**: transition from standard forked to multiforked with a retention time in the transition area.
- **STS**: standard forked, retention in the transition area, and back to standard forked
- **TST**: starting from the transition area with retention in a single forked area and back to transition
- **MTS**: multiforked replication regime to single forked replication with a retention time in the transition area
- **MTM**: beginning in the multifork regime with retention in the transition area and back to the multifork regime
- **TMT**: circulation from transition back to transition area with retention time in the multifork replication regime

The second capital letter always indicates the area in which the retention time  $\tau$  was measured. Before the bacterial lifelines were grouped in regimes, a moving-average filter was applied to filter unrealistic, turbulent fluctuations caused by the standard DRW model (see Appendix B). A second one-dimensional (1D) filter was conducted to erase rapid sequential regime transitions smaller than 0.09 s. Both filtering steps caused deviations from the raw data of less than 5%.

The distribution of the growth rates was derived by calculating the mean growth rate for the whole reactor and the mean growth rate for 20 s for each bacterium. This distribution combined with the cell cycle approach resulted in a distribution of different C-phase durations using Equation (1). Additionally, the energy level distribution was obtained based on Pirt's law [25]:

$$q_{\text{ATP}} = \frac{\mu}{Y_{x/\text{ATP}}} + m_{\text{ATP}} \quad (3)$$

with the *Pseudomonas putida* properties of nongrowth-associated maintenance  $m_{\text{ATP}} = 3.96 \text{ mmol}_{\text{ATP}} \cdot \text{g}_{\text{CDW}}^{-1} \cdot \text{h}^{-1}$  and the growth-associated maintenance  $Y_{x/\text{ATP}} = \frac{1}{85} \text{ g}_{\text{CDW}} \cdot \text{mmol}_{\text{ATP}}^{-1}$  [24].

### 3. Results and Discussion

In order to investigate heterogeneity in large-scale bioreactors, a pseudostationary glucose gradient occurring during fed batch fermentation of *P. putida* was simulated. Therefore, a biomass of  $10 \text{ kg} \cdot \text{m}^{-3}$  was assumed, which remained constant within the time observed. For higher biomass concentrations, stronger gradients can be expected.

#### 3.1. Gradient and Flow Field

In a 54,000 L stirred tank reactor, a pseudostationary glucose gradient was obtained with CFD simulations. The average glucose concentration was monitored until no further changes could be observed. The residual steady state glucose concentration was  $20.7 \text{ mg} \cdot \text{L}^{-1}$ . The theoretical growth rate for every numerical cell was computed (Eulerian approach), resulting in an average growth rate of  $\mu = 0.294 \text{ h}^{-1}$ . Ideal mixing was assured by comparing the average growth rate in the reactor (Eulerian approach) and the expected growth rate for the set feed rate  $\mu = 0.295 \text{ h}^{-1}$ . In the fed batch fermentation, the feeding rate amounted to half the maximum uptake rate of *P. putida*. The objective of the simulation was to generate a realistic glucose gradient with concentrations for which theoretical growth rates ranging from  $0.0 \text{ h}^{-1}$  to  $0.59 \text{ h}^{-1}$  could be approximated. Moreover, the distribution of bacteria that were introduced from different vertical positions in the reactor at the start of the simulation is displayed.

In Figure 2, three reactor cross sections are depicted to describe (A) the growth rate regimes (see also Section 2.3), (B) the flow field, and (C) the bacterial distribution. Due to asymmetric reactor geometry (see Section 2.2.1), the mean flow field and mean glucose gradient showed periodic changes. Accordingly, the averages of the flow field and gradients over 150 s were computed to track the bacteria (Figure 2C) as lifelines. Bacteria moved faster when approaching the stirrer. This clearly indicated

zones with different residence times. However, tracking the bacterial paths showed that they evenly crossed every part in the reactor.

The underlying gradient was not expected to perfectly reflect the real experiment. Several assumptions had to be made. For simplicity, bubbling flow and oxygen transfer were neglected. The kinetic reaction of substrate consumption following a Monod-like kinetic was assumed to take place in every numerical cell. This implied that the bacterial cells were distributed homogeneously at each time step, which is only a simplified scenario (Figure 2C). However, to examine the effects of cell history or lag phases of the bacteria on the gradient itself, an existing gradient had to be installed with the stated simplifications. In the following sections, a detailed statistical analysis is provided to study the influence of the gradient on the bacteria and reverse in a realistic manner.

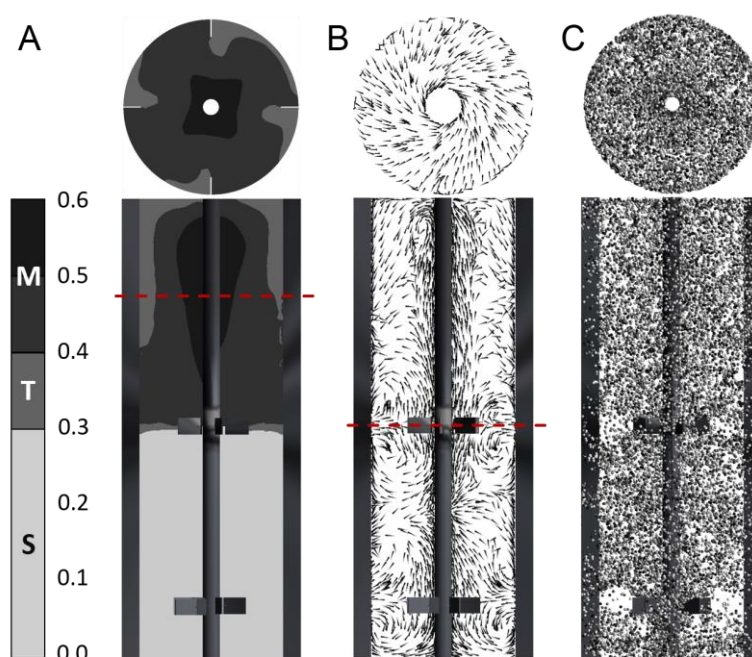


**Figure 2.** Simulation of gradients and bacterial lifelines. (A) Averaged substrate gradient calculated for 150 s, colored by regime classification: standard replication S ( $\mu < 0.3$ ) in light gray, transition regime T ( $0.3 \leq \mu \leq 0.4$ ) in gray, and multifork replication M ( $\mu > 0.4$ ) in dark gray. (B) Average flow field estimated for 150 s. (C) Representative magnified bacteria particles (around 2000) at a certain time step (colored by particle ID; low numbers in dark gray represent a starting point close to the reactor bottom, high numbers in light gray represent a starting point close to the reactor top). Horizontal section planes are indicated by dashed red lines; otherwise, the top view is shown.

### 3.2. Lagrangian Trajectory

For 260 s, 120,000 bacteria were tracked on their paths crossing different substrate concentrations. Figure 3 depicts growth rate profiles of two organisms for 20 s, referred to as lifelines L1 and L2. Figure 3C shows the related paths.

According to the regime thresholds (see Section 2.3 and Figure 3A, dashed lines), the growth rate trajectories could be transferred to replication modus curves, as described in Figure 3B). The lifeline L1 revealed high variations in glucose concentrations that were likely to induce strong metabolic changes. In contrast, environmental shifts along L2 were moderate, and there were no effects on metabolism or the cell cycle. The first lifeline L1 gave information regarding five regime transition strategies (STS, TST, STM, TMT, and MTS) and the individual residence times. Lifelines L1 and L2 started from different positions in the reactor and were unequal in length because they moved according to the

predominant velocity field. Within 20 s, L2 did not approach the feed zone, remaining in an area of reduced substrate concentration and increased shear stress, owing to the higher velocity of L2.

As shown in Figure 3B,C, within a defined timescale, bacteria completely sensed different environmental conditions. Whereas L2 seemed to remain in the same environment, L1 passed different glucose concentrations and performed several replication strategies. Each metabolic adjustment will cost energy and could have an impact on the production yield.

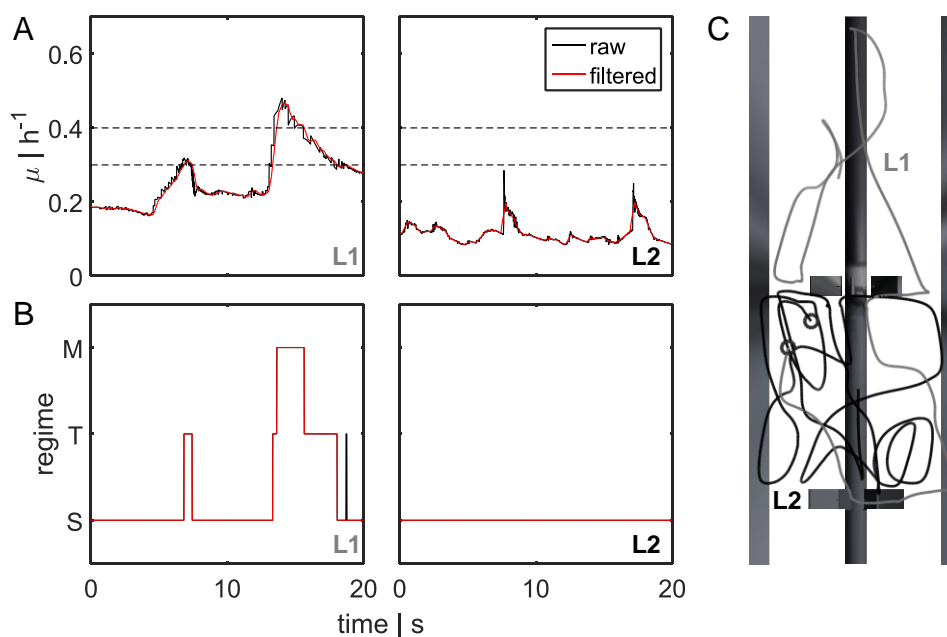


**Figure 3.** Bacterial lifeline and regime transition classification. (A) Two-dimensional (2D) bacterial lifeline for different growth rates  $\mu$  over time. The black line represents raw data, and the red line represents filtered data (moving average filter to correct discrete random walk (DRW) fluctuations). Black dashed lines indicate the transition regime from single-forked to multiforked replication. (B) Translation of filtered (one-dimensional (1D) filter) growth rate curves for the three regimes: multifork replication regime M, transition between standard forked and multiforked T, and standard replication S. Examples for two bacterial lifelines L1 and L2 are depicted. For L1, five regime transitions (STS, TST, STM, TMT, and MTS; see Section 2.3) were analyzed. (C) Bacterial movement patterns for two bacterial lifelines (L1 in gray and L2 in black). Starting positions are indicated by black circles.

### 3.3. Statistical Evaluation

#### 3.3.1. Regime Transition Frequency

All bacterial lifelines were scanned for regime transitions and retention times in order to obtain the frequency distributions as a function of  $\tau$ . Thus, six transition strategies were evaluated in a statistical manner to gain insights into cell histories and possible cell behaviors (see also Section 2.3).

Figure 4 shows the counts for each regime transition at a certain retention time. All regime transition statistics, except the TST transition, exhibited a decay after at least 10 s. Bacteria starting from the transition regime T could remain in an area of low concentration for up to 73.5 s (data not shown), where they could grow regularly (standard forked S), before changing back to the T regime. This could be explained by the flow field and gradient pictured in Figure 2A,B. The critical concentrations representing possible growth rates for the regime transition ( $\mu \geq 0.3 \text{ h}^{-1}$  and  $\mu > 0.4 \text{ h}^{-1}$ ) were located in the upper half of the reactor. Rushton turbines usually cause flow patterns moving away from the blades to the wall, where they circulate up or down, thereby forming large eddies for each stirrer set (Figure 2B). Consequently, cells will often circulate in this segment and do not pass other areas of the

reactor. The lower part of the reactor, which does not provoke a regime transition and, therefore, badly supplies the organisms with substrate, consisted of three segments. As a result, the average retention time in the TST transition was the longest ( $\bar{\tau}_{TST} = 8.54$  s). All other average and maximum retention times are listed in Table 1. The shapes of the distributions follow a Poisson distribution. The maximal retention time was defined as the limit, within which 99% of the values were located.

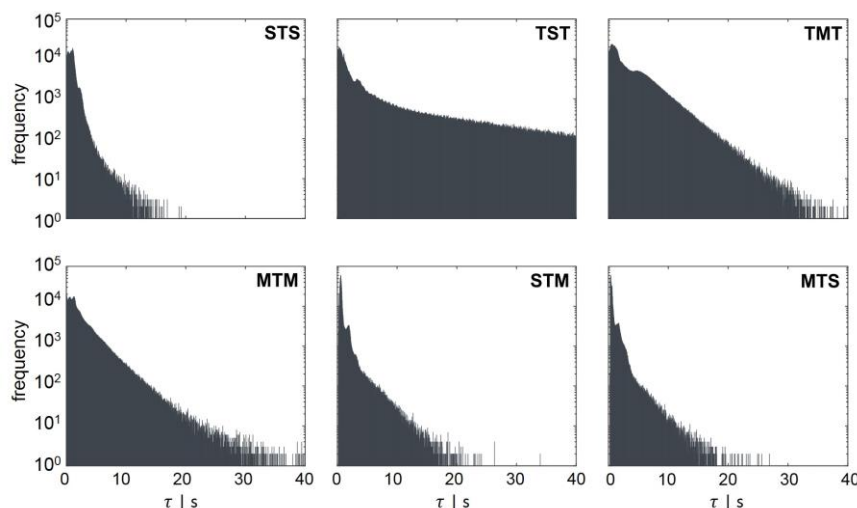


**Figure 4.** Regime transition frequency as a function of the retention time  $\tau$ . Regime transition classifications are indicated in the left corner of each panel. The second capital letter always indicates the area, in which the retention time  $\tau$  was measured. The regime transition count for each retention time was scaled logarithmically.

**Table 1.** Average and maximal retention time in a specific regime. For the six regimes (STS, TST, TMT, MTM, STM, and MTS), the average ( $\bar{\tau}$ ) and maximal retention times ( $\tau_{max}$ ) are displayed in seconds. The maximum  $\tau$  was defined as the limit, within which 99% of the values were located.

Regime Transition	$\bar{\tau}$ [s]	$\tau_{max}$ [s]
STS	0.99	3.7
TST	8.54	73.5
TMT	3.53	16.25
MTM	2.45	13
STM	0.95	6.6
MTS	0.88	5.5

Lifeline statistics provide insights into the frequency of regime transitions and residence times. Depending on the cell history, i.e., the concentrations of bacteria encountered before the bacteria passed the actual concentration, the cells will adapt accordingly. Although metabolic adaptation is known to be very rapid, the initiation of regulatory programs involving transcriptional changes is slower. Investigating the impact of large-scale conditions for *E. coli*, Löffler et al. [26] showed that fundamental transcriptional programs were initiated after 70 s of glucose shortage. After 30 s, metabolic consequences were measured, and the first transcriptional changes were detected. In total, about 600 genes were found to be up- or downregulated repeatedly, indicating a strong adaptation.

Considering this finding during the regime analysis, it is assumed that all cells travelling from high (M) to low (S) substrate availability should be influenced. Being prepared for multifork replication in M, the cells must adapt to standard replication (S). By analogy, this also includes travelers from T to S. Such cells can have a growth rate of about  $0.4 \text{ h}^{-1}$  before they adapt to growth rates of less than  $0.3 \text{ h}^{-1}$ . During the observation window of 260 s, 72.6% of all cells were expected to carry out this move at least once and to linger more than 30 s in regime S. About 14.7% of all cells were expected

to stay more than 70 s in regime S after experiencing higher glucose concentrations in regime T. Furthermore, if a regime transition from maximal to moderate growth conditions (MTS) with the retention time in regime T and S is assumed, 55.5% of all cells performed this move for more than 30 s. A retention time of 70 s was calculated for 10.4% of all cells. The time scales of 30 s and 70 s were shown to significantly influence the transcriptional response of *E. coli* [26], leading to the assumption that changes in adenosine triphosphate (ATP) and guanosine triphosphate (GTP) levels of *P. putida* KT2440 could also be expected.

### 3.3.2. Energy and C-Phase Duration Distribution

For the observation window of 260 s, the growth rate profiles of 120,000 bacteria were calculated. Given the set feed rate, the average  $\mu$  of  $0.295 \text{ h}^{-1}$  was expected. Using the Lagrangian approach, an average growth rate of  $\mu = 0.269 \text{ h}^{-1}$  was computed, indicating an adequate deviation of 8.5% compared to the Eulerian approach with  $\mu = 0.294 \text{ h}^{-1}$  (see Section 3.1).

The distribution of the ATP consumption rate  $q_{\text{ATP}}$  is presented in Figure 5A. The growth rate  $\mu$  and  $q_{\text{ATP}}$  were not evenly distributed compared to the mean value, but exhibited individual distributions according to the gradient. The ATP consumption rate was calculated applying Pirt's law (see Equation (3)). While only 6.3% of all cells had a mean ATP consumption rate of  $q_{\text{ATP,mean}} = 29.31 \pm 2 \text{ mmol}_{\text{ATP}} \cdot \text{g}_{\text{CDW}}^{-1} \cdot \text{h}^{-1}$ , 40.8% showed a reduced consumption rate of less than  $27.31 \text{ mmol}_{\text{ATP}} \cdot \text{g}_{\text{CDW}}^{-1} \cdot \text{h}^{-1}$ , and 52.9% showed an increased energy demand of  $31.31 \text{ mmol}_{\text{ATP}} \cdot \text{g}_{\text{CDW}}^{-1} \cdot \text{h}^{-1}$  in comparison to the average consumption rate. Moreover, 12.2% show an energy demand that was more than 1.5 times that of the mean value in the reactor.

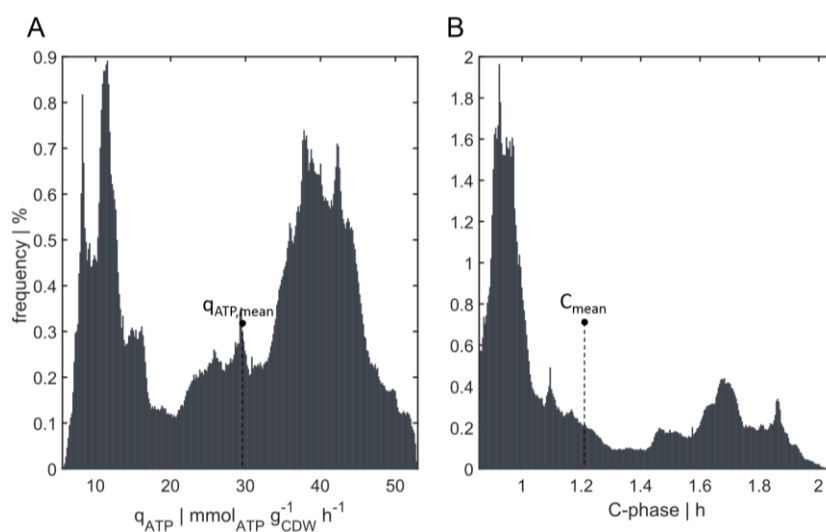


**Figure 5.** Distribution of C-phase duration and energy level. (A) Frequencies of cells with a specific adenosine triphosphate (ATP) consumption rate ( $q_{\text{ATP}}$ ) tracked for 20 s. Average value of  $q_{\text{ATP,mean}} = 29.31 \text{ mmol}_{\text{ATP}} \cdot \text{g}_{\text{CDW}}^{-1} \cdot \text{h}^{-1}$ . Range of the x-axis from  $q_{\text{ATP,min}} = 5.57 \text{ mmol}_{\text{ATP}} \cdot \text{g}_{\text{CDW}}^{-1} \cdot \text{h}^{-1}$  to  $q_{\text{ATP,max}} = 52.98 \text{ mmol}_{\text{ATP}} \cdot \text{g}_{\text{CDW}}^{-1} \cdot \text{h}^{-1}$ . (B) Frequency of cells having a specific duration of replication (C-phase). Average C-phase duration of  $C_{\text{mean}} = 1.21 \text{ h}$ . Range of the x-axis from  $C_{\text{min}} = 0.86 \text{ h}$  to  $C_{\text{max}} = 2.05 \text{ h}$ . Counts were divided into 300 bins.

The distribution will differ if increased nongrowth-associated maintenance  $m_{\text{ATP}}$  is considered. As outlined by Löffler et al. [26],  $m_{\text{ATP}}$  increases by 40–50% when cells are exposed to large-scale substrate gradients.

The individual growth profiles of the cells are the basis for deducing cell cycle patterns using the cell cycle model (see Section 2.3). Distributions of the C-length (encoding DNA replication) could be derived for the population of 120,000 bacteria. Figure 5B shows the average duration of

replication of 1.21 h and the frequency of cells with a C-phase duration ranging from  $C_{\min} = 0.86$  h to  $C_{\max} = 2.05$  h. Clearly, the bacteria were not evenly distributed according to the mean value, and there was a large heterogeneity in the reactor. Although only 22.3% of all cells had a replication phase of  $1.21 \pm 0.2$  h, about 30% possessed a C-period of more than 1.41 h. In contrast, 47.7% displayed a shorter replication phase than the average time for replication (less than 1.01 h). Moreover, approximately 56.1% of the cells were rapidly replicating cells with a growth rate higher than  $\mu = 0.3 \text{ h}^{-1}$ . For these cells, it can be assumed that they already started to completely adjust their metabolism to achieve multifork replication. As shown in Figure 5B, the bioreactor population was strongly heterogeneous, characterized by a nonequal distribution of bacteria in different cell cycle states. Three different growth phenotypes are shown: C-phase durations of (i)  $0.94 \pm 0.08$  h, (ii)  $1.68 \pm 0.1$  h, and (iii) a transition state of C-phases ranging from 1.1 to 1.5 h. Previously, subpopulations resulting from chemostat experiments have been categorized in populations containing one, two, or more than two chromosomes [27]. With this simulation setup, a model-based superposition of subpopulations containing different growth rates to mimic the scenario in a (fed)batch fermentation was shown. For the underlying gradient, new categories of subpopulations according to the C-phase durations mentioned above can be formulated.

#### 4. Conclusions

The existence of population heterogeneity in industrial fermenters has been demonstrated, but it still not completely understood. Improvements in fermenter operation, reactor design, and strain engineering can be achieved as more information of cell behaviors during large-scale production becomes available. In this study, the formation of heterogeneity by combining CFD with a cell cycle model of *P. putida* was investigated. With this method, heterogeneity can be interpreted from the bacterial point of view, particularly with respect to the growth phase durations and energy demands of the cell.

Average and maximum residence times for each transition strategy have been approximated and can be linked to scale-down experiments using STR-PFR setups. Moreover, distributions of growth rates, ATP consumptions, and C-phase durations could be generated. Such findings provide important insights into the intracellular mechanisms that determine growth phenotypes. These mechanisms may become a crucial part of strain and process engineering to predict *ab initio* and *in silico* whether and how large-scale performance will meet expectations. Realistic large-scale cultivation can be simulated by investigating the “subpopulations” individually. Specifically, it may be possible to elucidate whether the total drop in production performance during large-scale production is caused by all cells or by individual “subpopulations” that underperform.

To further investigate such problems, heterogeneity studies need to be coupled with single-cell product kinetics. Moreover, research will need to focus on the quantitative measurement of the impact of stress intensity on the  $m_{\text{ATP}}$  level. This will enable prediction of the total energy demand for a given setup.

**Acknowledgments:** The research could not have been conducted without the previous work on the cell cycle model of Sarah Lieder and the flow cytometry analysis of Susann Müller. We also thank Alexei Lapin and Alexander Nieß for their advice and support during this study. This work was supported by the German Research Foundation (DFG; GZ: TA241/5-2) and the Federal Ministry of Education and Research (BMBF; FKZ031A468B).

**Author Contributions:** Ralf Takors initiated the study and provided important advice during the entire investigation. Maike Kuschel and Flora Siebler equally conducted all parts of the simulation, evaluation, and writing of the manuscript as a team.

**Conflicts of Interest:** The authors declare no conflicts of interest.

#### Appendix A

More precise information of the reactor setup and geometry can be found in Table A1 and Figure A1.

**Table A1.** Dimensions of the reactor setup pictured in Figure A1.

Description	Symbol	Relation
Reactor diameter	$D_R$	3.00 m
Impeller diameter	$D_I$	$0.43 D_R$
Impeller height	$H_I$	$0.21 D_I$
Bottom clearance	$C_1$	$0.30 D_R$
Impeller spacing	$\Delta C$	$1.00 D_R$
Upper clearance	$C_2$	$1.27 D_R$
Baffle width	$B$	$0.10 D_R$
Liquid height	$H_L$	$C_1 + \Delta C + C_2$

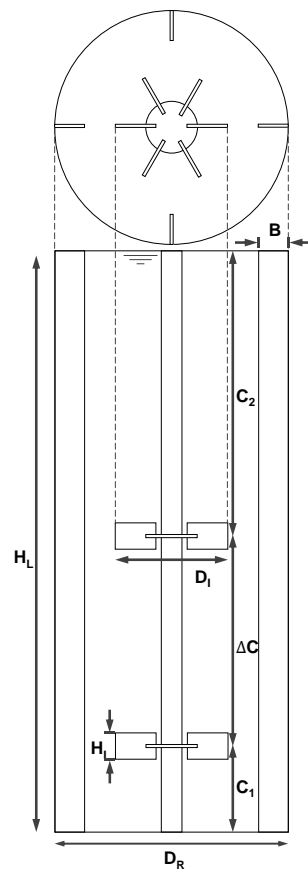


**Figure A1.** Schematic diagram of reactor geometry derived from Haringa et al. [21]. The stirred tank reactor contains four baffles and two Rushton turbines with eight blades (**bottom**) and six blades (**top**). Dimensions indicated by capital letters are explained in Table A1.

### Appendix B

The standard moving average filter of MATLAB is a linear filter (low pass filter), which removes high frequency components such as fluctuations caused by the DRW model. It is formulated as:

$$m(t) = \sum_{j=-q}^q y_{t+j} \quad q < t < N - q \tag{A1}$$

with:

$$q = \frac{\bar{\tau} - 1}{2} \tag{A2}$$

where  $N$  is the total number of measured time points and  $\bar{\tau}$  the filter timescale.

## References

1. Müller, S.; Harms, H.; Bley, T. Origin and analysis of microbial population heterogeneity in bioprocesses. *Curr. Opin. Biotechnol.* **2010**, *21*, 100–113. [[CrossRef](#)] [[PubMed](#)]
2. Bylund, F.; Collet, E.; Enfors, S.; Larsson, G. Substrate gradient formation in the large-scale bioreactor lowers cell yield and increases by-product formation. *Bioprocess Eng.* **1998**, *18*, 171–180. [[CrossRef](#)]
3. Enfors, S.; Jahic, M.; Rozkov, A.; Xu, B.; Hecker, M.; Ju, B. Physiological responses to mixing in large scale bioreactors. *J. Biotechnol.* **2001**, *85*, 175–185. [[CrossRef](#)]
4. Takors, R. Scale-up of microbial processes: Impacts, tools and open questions. *J. Biotechnol.* **2012**, *160*, 3–9. [[CrossRef](#)] [[PubMed](#)]
5. Makinoshima, H.; Nishimura, A.; Ishihama, A. Fractionation of *Escherichia coli* cell populations at different stages during growth transition to stationary phase. *Mol. Microbiol.* **2002**, *43*, 269–279. [[CrossRef](#)] [[PubMed](#)]
6. Lieder, S.; Jahn, M.; Koepff, J.; Müller, S.; Takors, R. Environmental stress speeds up DNA replication in *Pseudomonas putida* in chemostat cultivations. *Biotechnol. J.* **2016**, *11*, 155–163. [[CrossRef](#)] [[PubMed](#)]
7. Cooper, S.; Helmstetter, C.E. Chromosome replication and the division cycle of *Escherichia coli*. *J. Mol. Biol.* **1968**, *31*, 519–540. [[CrossRef](#)]
8. Girault, M.; Kim, H.; Arakawa, H.; Matsuura, K.; Odaka, M.; Hattori, A.; Terazono, H.; Yasuda, K. An on-chip imaging droplet-sorting system: A real-time shape recognition method to screen target cells in droplets with single cell resolution. *Sci. Rep.* **2017**, *7*, 1–10. [[CrossRef](#)] [[PubMed](#)]
9. Cheng, Y.H.; Chen, Y.C.; Brien, R.; Yoon, E. Scaling and automation of a high-throughput single-cell-derived tumor sphere assay chip. *Lab Chip* **2016**, *16*, 3708–3717. [[CrossRef](#)] [[PubMed](#)]
10. Helmstetter, C.E. Timing of Synthetic Activities in the Cell Cycle. In *Escherichia coli and Salmonella. Cellular and Molecular Biology*; Neidhardt, F.C., Ed.; American Society for Microbiology (ASM) Press: Washington, DC, USA, 1996; pp. 1627–1639.
11. Müller, S. Modes of cytometric bacterial DNA pattern: A tool for pursuing growth. *Cell Prolif.* **2007**, *40*, 621–639. [[CrossRef](#)] [[PubMed](#)]
12. Skarstad, K.; Steen, H.B.; Boye, E. *Escherichia coli* DNA distributions measured by flow cytometry and compared with theoretical computer simulations. *J. Bacteriol.* **1985**, *163*, 661–668. [[PubMed](#)]
13. Larsson, G.; Törnkvist, M.; Ståhl Wernersson, E.; Trägårdh, C.; Noorman, H.; Enfors, S.O. Substrate gradients in bioreactors: Origin and consequences. *Bioprocess Eng.* **1996**, *14*, 281–289. [[CrossRef](#)]
14. Noorman, H.; Morud, K.; Hjertager, B.H.; Traegaardh, C.; Larsson, G.; Enfors, S.O. CFD modeling and verification of flow and conversion in a 1 m<sup>3</sup> bioreactor. *BHR Gr. Conf. Ser. Publ.* **1993**, *5*, 241–258.
15. Schmalzriedt, S.; Jenne, M.; Mauch, K.; Reuss, M. Integration of physiology and fluid dynamics. *Adv. Biochem. Eng.* **2003**, *80*, 19–68.
16. Morchain, J.; Gabelle, J.-C.; Cockx, A. A coupled population balance model and CFD approach for the simulation of mixing issues in lab-scale and industrial bioreactors. *Am. Inst. Chem. Eng.* **2014**, *60*, 27–40. [[CrossRef](#)]
17. Bezzo, F.; Macchietto, S.; Pantelides, C.C. General hybrid multizonal/CFD approach for bioreactor modeling. *AIChE J.* **2003**, *49*, 2133–2148. [[CrossRef](#)]
18. Mantzaris, N.V.; Liou, J.; Daoutidis, P.; Sreenc, F. Numerical solution of a mass structured cell population balance model in an environment of changing substrate concentration. *J. Biotechnol.* **1999**, *71*, 157–174.
19. Henson, M.A. Dynamic modeling of microbial cell populations. *Curr. Opin. Biotechnol.* **2003**, *14*, 460–467. [[CrossRef](#)]
20. Lapin, A.; Müller, D.; Reuss, M. Dynamic behavior of microbial populations in stirred bioreactors simulated with Euler-Lagrange methods: Traveling along the lifelines of single cells. *Ind. Eng. Chem. Res.* **2004**, *43*, 4647–4656. [[CrossRef](#)]
21. Haringa, C.; Tang, W.; Deshmukh, A.T.; Xia, J.; Reuss, M.; Heijnen, J.J.; Mudde, R.F.; Noorman, H.J. Euler-Lagrange computational fluid dynamics for (bio)reactor scale-down: An analysis of organism life-lines. *Eng. Life Sci.* **2016**, *16*, 652–663. [[CrossRef](#)] [[PubMed](#)]
22. Lieder, S. *Deciphering Population Dynamics as a Key for Process Optimization*; University of Stuttgart: Stuttgart, Germany, 2014.
23. Keasling, J.D.; Kuo, H.; Vahanian, G. A Monte Carlo simulation of the *Escherichia coli* cell cycle. *J. Theor. Biol.* **1995**, *176*, 411–30. [[CrossRef](#)] [[PubMed](#)]

24. Van Duuren, J.B.J.H.; Puchalka, J.; Mars, A.E.; Bückner, R.; Eggink, G.; Wittmann, C.; Dos Santos, V.A.P.M. Reconciling in vivo and *in silico* key biological parameters of *Pseudomonas putida* KT2440 during growth on glucose under carbon-limited condition. *BMC Biotechnol.* **2013**, *13*, 93. [[CrossRef](#)] [[PubMed](#)]
25. Pirt, S.J. The maintenance energy of bacteria in growing cultures. *Proc. R. Soc. Lond. Ser. B. Biol. Sci.* **1965**, *163*, 224–231. [[CrossRef](#)]
26. Löffler, M.; Simen, J.D.; Jäger, G.; Schäferhoff, K.; Freund, A.; Takors, R. Engineering *E. coli* for large-scale production—Strategies considering ATP expenses and transcriptional responses. *Metab. Eng.* **2016**, *38*, 73–85. [[CrossRef](#)] [[PubMed](#)]
27. Lieder, S.; Jahn, M.; Seifert, J.; von Bergen, M.; Müller, S.; Takors, R. Subpopulation-proteomics reveal growth rate, but not cell cycling, as a major impact on protein composition in *Pseudomonas putida* KT2440. *AMB Express* **2014**, *4*, 71. [[CrossRef](#)] [[PubMed](#)]



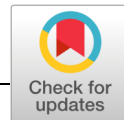
© 2017 by the authors. Licensee MDPI, Basel, Switzerland. This article is an open access article distributed under the terms and conditions of the Creative Commons Attribution (CC BY) license (<http://creativecommons.org/licenses/by/4.0/>).

## **B.2 Manuscript II**

---

Simulated oxygen and glucose gradients  
as a prerequisite for predicting  
industrial scale performance *a priori*

---



## ARTICLE

# Simulated oxygen and glucose gradients as a prerequisite for predicting industrial scale performance a priori

Maike Kuschel | Ralf Takors

Institute of Biochemical Engineering,  
University of Stuttgart, Stuttgart, Germany**Correspondence**Ralf Takors, Institute of Biochemical  
Engineering, University of Stuttgart,  
Allmandring 31, 70569 Stuttgart, Germany.  
Email: takors@ibvt.uni-stuttgart.de**Funding information**Deutsche Forschungsgemeinschaft,  
Grant/Award Number: TA 241/5-2**Abstract**

Transferring bioprocesses from lab to industrial scale without loss of performance is key for the successful implementation of novel production approaches. Because mixing and mass transfer is usually hampered in large scale, cells experience heterogeneities eventually causing deteriorated yields, that is, reduced titers, productivities, and sugar-to-product conversions. Accordingly, reliable and easy-to-implement tools for a priori prediction of large-scale performance based on dry and wet-lab tests are heavily needed. This study makes use of computational fluid dynamic simulations of a multiphase multi-impeller stirred tank in pilot scale. So-called *lifelines*, records of 120,000 *Corynebacterium glutamicum* cells experiencing fluctuating environmental conditions, were identified and used to properly design wet-lab scale-down (SD) devices. Physical parameters such as power input, gas hold up,  $k_L a$ , and mixing time showed good agreement with experimental measurements. Analyzing the late fed-batch cultivation revealed that the complex double gradient of glucose and oxygen can be translated into a wet-lab SD setup with only few compartments. Most remarkably, the comparison of different mesh sizes outlined that even the coarsest approach with a mesh density of  $1.12 \times 10^5 \text{ \#/m}^3$  was sufficient to properly predict physical and biological readouts. Accordingly, the approach offers the potential for the thorough analysis of realistic industrial case scenarios.

**KEYWORDS**

cellular lifelines, CFD, double gradient, stirred tank

## 1 | INTRODUCTION

The transformation of current chemical industry into a sustainable, circular economy demands the successful implementation of large-scale production processes accessing the low-value, high-volume products of tomorrow. Emerging fields are the production of amino acids and organic acids (Becker & Wittmann, 2012; Morrison & L  htenm  ki, 2017). Typically, microbial hosts are the most important production platforms with *Corynebacterium glutamicum* being one of the established producers (Leuchtenberger, Huthmacher, &

Drauz, 2005; Takors et al., 2007). Stirred tank reactors, still the preferred choice of large-scale production, show reduced power-per-volume ratios with increasing reactor size (Junker, 2004). Consequently, scale-up from smaller laboratory scales is usually hampered due to limited mixing and mass transfer, leading to the formation of substrate and gas gradients. The repeated exposure of cells to these fluctuating microenvironmental conditions cause unwanted reduction of productivities, conversion yields, and rising by-product formations (Bylund, Collet, Enfors, & Larsson, 1998; Enfors et al., 2001; Garcia-Ochoa & Gomez, 2009; Hewitt & Nienow, 2007;

This is an open access article under the terms of the Creative Commons Attribution License, which permits use, distribution and reproduction in any medium, provided the original work is properly cited.

   2020 The Authors. *Biotechnology and Bioengineering* published by Wiley Periodicals LLC

Junne, Klingner, Itzeck, Brand, & Neubauer, 2012; Neubauer et al., 2013; Schmidt, 2005; Vrabel et al., 2001). Accordingly, tools are needed to reliably predict large-scale impacts while studying the microbial system in lab-scale. Different wet-lab scale-down (SD) devices have been developed (Kab, Junne, Neubauer, Wiechert, & Oldiges, 2014; Loffler et al., 2016). Commonly, their design is motivated by mixing time studies of large tanks that tend to overestimate the residence time of microbes in stressful zones of the bioreactor.

On the other hand, computational fluid dynamics (CFD) gain momentum to provide detailed information on environmental conditions inside a fermenter (Morchain, Gabelle, & Cockx, 2014; Pigou & Morchain, 2015) since the pioneering studies of Lapin, Schmid, and Reuss (2006). In the recent years, substrate gradients in industrial scale fed-batch production were successfully simulated outlining the impact of concentration fluctuations on microorganisms by comprehensive statistical analysis (Haringa, Deshmukh, Mudde, & Noorman, 2017; Haringa et al., 2016; Kuschel, Siebler, & Takors, 2017). Thereof, principles of SD design may be derived. Yet, the influence of oxygen as substrate in CFD simulations is often left aside. Instead, single-phase studies are performed assuming saturated dissolved oxygen levels in the entire bioreactor.

Properly considering the additional oxygen impact in stirred tank reactors (STRs) via a gaseous phase is a challenging task. Fundamental problems need to be tackled that can be grouped in (a) momentum balancing mimicked by proper drag force modeling (Bakker & Van den Akker, 1994; Brucato, Grisafi, & Montante, 1998; Buffo, Vanni, Renze, & Marchisio, 2016; Ishii & Zuber, 1979; Scargiali, D'Orazio, Grisafi, & Brucato, 2007; Tomiyama, Kataoka, Zun, & Sakaguchi, 1998), (b) bubble size distribution modeling (Hagesaether, Jakobsen, & Svendsen, 2002; Haringa et al., 2017; Kumar & Ramkrishna, 1996; Laakkonen, Moilanen, Alopaeus, & Aittamaa, 2007b), (c) modeling of bubble breakage and coalescence (Alopaeus, Koskinen, & Keskinen, 1999; Laakkonen, Alopaeus, & Aittamaa, 2006; Luo & Svendsen, 1996; Kalal, Jahoda, & Fort, 2014), and (d) mesh size impacts.

Regarding (d), all models have a strong dependency on the turbulent dissipation rate in common. The Reynolds average Navier–Stokes (RANS)  $k$ - $\epsilon$  model was found to underestimate the local turbulent quantities both, in single and in multiphase conditions. In contrast, large eddy simulations are known to allow best prediction quality but are too computationally demanding for large-scale multiphase applications (Buffo et al., 2016). As a trade-off, satisfactory results of total dissipated energy simulation via RANS  $k$ - $\epsilon$  models can be achieved (Kysela, Konfrst, Chara, Sulc, & Jasikova, 2017). However, the prediction of turbulent variables turned out to be sensitive on the discretization schemes and grid size (Coroneo, Montante, Paglianti, & Magelli, 2011). Interesting enough, velocity field or power number  $N_p$  prediction by torque was less influenced by either discretisation scheme or grid size. The observation was further exploited by Laakkonen, Moilanen, Alopaeus, and Aittamaa (2007a) who predicted turbulent dissipation rates  $\epsilon$  to be independent on grid size but depending on experimental torque measurements. Accordingly, a novel scaling factor was introduced.

This study takes a typical late stage fed-batch scenario with *C. glutamicum* as a model case to investigate (a) the suitability of the Laakkonen approach for multiphase modeling, (b) the minimum computational efforts needed to get proper physical and biological readouts, (c) the expected microbial responses on fluctuating environmental conditions, and (d) the lessons learned for properly designing wet-lab SD devices. Model predictions are validated by experimental data measured in a 300-L stirred tank bioreactor.

## 2 | MATERIALS AND METHODS

Measurements were carried out in a 300-L multi-impeller stirred bioreactor, equipped with four baffles and three Rushton turbines. Details of measurements, geometry, and parameter validation are given in Supporting Information Material A. The agitation rate was set to  $N = 5/s$ . Air was introduced through a ring sparger with a gas feed of 0.25 vvm. Experiments were performed in water ( $\rho_L = 995.7 \text{ kg/m}^3$ ,  $\eta_L = 0.0008 \text{ Pa}\cdot\text{s}$ ,  $\sigma_L = 0.0712 \text{ N/m}$ ) at 30°C and ambient pressure.

### 2.1 | Numerical simulations

#### 2.1.1 | Simulation setup

Three different grid sizes of the full  $2\pi$  domain were adopted. Details of the meshes and simulation time intervals are given in Supporting Information Material B. Numerical simulations were conducted with the commercial software ANSYS Fluent 18.1 using the realizable  $k$ - $\epsilon$  RANS turbulence model and the Eulerian multiphase model including mixture model for dispersed phase turbulence. The turbulent Schmidt number was set to 0.2. Bubble size ranged from 0.1 to 16 mm, divided in 23 classes according to Hagesaether et al. (2002). The scaling factor  $f_{sc}$  was introduced based on the assumption, that mixing energy (power calculated from impeller torque  $P_{torque}$  and gassed power input  $P_{pneum}$ ) converts to turbulent energy and dissipates to heat in the liquid phase ( $P_\epsilon$ ). Hence local energy dissipation  $\epsilon_{local}$  was converted according to

$$f_{sc} = \frac{P_{pneum} + P_{torque}}{P_\epsilon}, \quad (1)$$

$$\epsilon_{sc} = f_{sc} \epsilon_{local}. \quad (2)$$

With  $P_{pneum}$  and  $P_\epsilon$

$$P_{pneum} = \phi_G RT \ln\left(\frac{p_0}{p}\right), \quad (3)$$

$$P_\epsilon = \int \alpha_L \rho_L \epsilon dV, \quad (4)$$

and with  $\phi_G$  as molar flow,  $\alpha_L$  as liquid volume fraction,  $R$  as universal gas constant,  $T$  as temperature,  $p_0$  and  $p$  as standard and actual

pressure. For  $P_{\text{torque}}$ , see Supporting Information Material A. Phase interaction models were mainly based on the recommendations by Laakkonen et al. (2007a) and implemented via user-defined function (UDF). To account for the bubble drag coefficient, the correlation of Tomiyama for isolated bubbles in slightly contaminated systems (Tomiyama et al., 1998) was used. As Tomiyama drag closure  $C_{D,0}$  was obtained for bubbles in quiescent fluids, effective viscosity  $\mu_{\text{eff}}$  and swarm effects were included to consider drag modification under turbulent conditions (Bakker & Van den Akker, 1994; Brucato et al., 1998; Ishii & Zuber, 1979)

$$Re_{\text{eff}} = \frac{\rho_L d |u_L - u_G|}{\eta_{\text{eff}}}, \quad (5)$$

$$\eta_{\text{eff}} = \eta_L + C_5 \rho_L \epsilon_{\text{sc}}^{\frac{1}{3}} d^{\frac{4}{3}}, \quad (6)$$

with  $C_5$  as 0.02 proposed by Bakker and Van den Akker (1994). Additionally, swarm effects were accounted for by

$$C_D = f(\alpha_G) C_{D,0}(Re_{\text{eff}}), \quad (7)$$

$$f(\alpha_G) = \begin{cases} (1 - \alpha_G)^{C_6} & \alpha_G \leq 0.8 \\ 1 & \alpha_G > 0.8 \end{cases} \quad (8)$$

with  $C_6$  to be -1.3 as proposed by Buffo et al. (2016). Bubble break up and coalescence were implemented as described by Laakkonen et al. (2007a) replacing the original breakup function by a simple sine function. The moving reference frame model was applied to account for agitation. All walls were set to no-slip boundary conditions for the liquid and free-slip conditions for air with one exception—to account for gas accumulation behind the blades, no-slip boundary condition was applied for air in the impeller region. The top surface of the sparger was set to velocity inlet and the initial bubble diameter was calculated with 10 mm according to the correlation of Gaddis and Vogelpohl (1986). Degassing boundary condition was applied at the liquid height of the reactor, which has been increased before simulation according to the experimental gas hold up. The second-order upwind scheme was used for spatial discretization of momentum, turbulent kinetic energy, and dissipation rate. All simulations were performed in transient mode and second-order implicit formulation until a constant gas hold up was reached. Radial velocity, turbulent dissipation rate, and mixing time were compared between the three meshes. Further details on the solution procedure and mixing time determination can be found in Supporting Information Material D and E.

## 2.1.2 | Inclusion of biological kinetics and regime assignments

Starting from a constant gas volume fraction, glucose feed, oxygen mass transfer, and bacterial reaction were included via UDFs. A source term for glucose was defined in a small region at the fermenter top close to the shaft with a feeding rate  $F = 560 \text{ g}_s/\text{hr}$ ,

assuming a cell concentration of  $c_X = 36.5 \text{ g}_{\text{CDW}}/\text{L}$ . Oxygen mass transfer was included with the volumetric mass transfer coefficient  $k_L a$  according to

$$\frac{dc_{\text{O}_2\text{L}}}{dt} = k_L a (c_{\text{O}_2}^* - c_{\text{O}_2\text{L}}) \quad (9)$$

with  $c_{\text{O}_2}^*$  as oxygen saturation concentration calculated by Henry's law and  $c_{\text{O}_2\text{L}}$  as liquid oxygen concentration. A multisubstrate kinetic suggested by Roels (1983) was used to account for substrate consumption:

$$\mu = \mu_{\text{max}} \min \left( \frac{c_S}{c_S + K_S}; \frac{c_{\text{O}_2}}{c_{\text{O}_2} + K_{\text{O}_2}} \right) \quad (10)$$

with  $\mu$  as growth rate and  $K_S$  and  $K_{\text{O}_2}$  as half saturation concentration. Specific growth parameters of *C. glutamicum* ATCC13032 were obtained from previous batch experiments (not published) resulting in a maximal growth rate of  $\mu_{\text{max}} = 0.441 \text{ hr}^{-1}$ , a biomass glucose yield of  $Y_{\text{XS}} = 0.474 \text{ g}_{\text{CDW}}/\text{g}_s$  and a biomass oxygen yield of  $Y_{\text{XO}_2} = 0.043 \text{ g}_{\text{CDW}}/\text{mmol}_{\text{O}_2}$ . The  $K_S$  value for *C. glutamicum*  $K_S = 3.6 \times 10^{-3} \text{ g}_s/\text{L}$  was taken from literature (Lindner, Seibold, Henrich, Krämer, & Wendisch, 2011). The value for  $K_{\text{O}_2}$  was taken from *Escherichia coli*  $K_{\text{O}_2} = 2 \times 10^{-3} \text{ mmol}_{\text{O}_2}/\text{L}$  because similar cytochrome *bd* activity has been reported (Kita, Konishi, & Anraku, 1984; Kusumoto, Sakiyama, Sakamoto, Noguchi, & Sone, 2000). Simulation ran in transient mode until steady-state concentrations of glucose and oxygen were reached. They mirror a so-called "pseudo steady-state" characterized by short-term stable gradients in turbulent flow fields. This concentration profile reflects a "snap-shot" of a late pilot-scale fed-batch scenario. Coupling the reaction to the continuous liquid phase was assumed, since mixing and mass transfer are an order of magnitude higher than the reaction. However, the flow field shows periodically changing behavior. To facilitate comparability between the three meshes, power input by torque as well as velocity profiles and turbulent dissipation rate were tracked at several positions and the simulation was stopped when average values of the examined parameters were reached. Then, the glucose and oxygen gradients were classified in specific regimes according to the growth rate substrate dependency of a single substrate Monod kinetic for either glucose or oxygen, respectively. If the dimensionless substrate concentration  $c_M/K_M$  was smaller or equal to 0.5 (corresponding to  $c_M/(c_M + K_M) \leq 0.33$ ) a linear correlation between  $\mu$  and  $c_M$  exists, referring to a low concentration regime ( $L_S$  for low glucose or  $L_{\text{O}_2}$  for low oxygen). If  $c_M/K_M > 9$ , the growth rate  $\mu$  reaches 90% of  $\mu_{\text{max}}$  and the function can be approximated by a function of zero order making  $\mu$  independent of a change in substrate concentration ( $H_S$  and  $H_{\text{O}_2}$ ). The range in between refers to a transient regime ( $T_S$  and  $T_{\text{O}_2}$ ).

## 2.1.3 | Particle tracking

The analysis of heterogeneities via cellular lifelines within a bioractor was previously published in various papers (Haringa

et al., 2017, 2016; Kuschel et al., 2017). The total amount of 120,000 bacteria was introduced as massless Lagrange particles ( $St \ll 1$ ) and tracked for 260 s for each mesh. Euler and Lagrange average growth rates were compared to proof for statistical relevance. The discrete random walk model was enabled. The gradient and flow field were fixed during particle tracking. The position and the encountered glucose and oxygen concentrations for each bacterium were recorded every 15 ms. Further analysis was performed in MATLAB®.

### 2.1.4 | Statistical evaluation of bacterial lifelines

The further processing of the trajectories included a smoothing step by applying a moving average filter to remove unrealistic turbulent fluctuations. The filter window was based on the Lagrangian time scale as recommended by Haringa et al. (2017). Here, a second filter step to filter out rapid consecutive low-amplitude crossings is suggested which was enabled by a median filter. Then, the filtered trajectories were analyzed according to their regime transitions including frequency and duration of residences.

## 3 | RESULTS AND DISCUSSION

### 3.1 | Validation of physical parameters for different grid sizes

Multiphase simulations were performed using three different grid sizes (Supporting Information Material B). Sufficient mesh granularity is a critical aspect in CFD simulations especially for the proper estimation of the gas-liquid mass transfer. Typically, sensitive flow variables such as radial velocity and turbulent dissipation rate are checked for mesh independency. While  $u_{rad}$  already showed decent results for Mesh 1, differences between the meshes are significant for  $\epsilon$  (Supporting Information Material D). Accordingly, the scaling factor for  $\epsilon$  was introduced into breakup, coalescence, drag and mass transfer functions as described in Section 2.1.1. A similar scaling factor has been reported to show good results in multiphase simulations (Laakkonen et al., 2007a). Noteworthy, the scaling factor was determined from simulation in our approach. Experimental data were only required for validation purposes.

Figure 2a shows the flow field, Figure 2b shows the gas volume distribution, and Figure 2c shows the bubble size distribution of the simulation with Mesh 3. Clearly, no distinct separation of flow fields from radial pumping Rushton turbines is visible, but an overlap of vortices. The merged flow field is the result of the upward moving gas phase in combination with rather proximate impeller setting. The first impeller shows a loading regime (see Figure 2b). With the Froude number  $N^2D/g = 0.52$  and the Flow number  $Q_g/ND^3 = 0.02$ , no flooding is expected according to critical flow numbers of Rosseburg, Fitschen, Wutz, Wucherpennig, and Schlüter (2018) and others (Wiedmann, 1983). Own studies outlined the need to consider the impact of effective viscosity on the estimation of drag force.

Otherwise, bubbles left the impeller discharge streams too early leading to nonrealistic bubble accumulation close to the blades. The lower impeller disrupted entering bubbles to 4–5 mm (see Figure 2c). Smallest bubbles of 2–3 mm were found in discharge streams of the middle and the upper Rushton turbine gaining size when they moved upwards to the liquid surface. Largest bubbles were observed at the impeller shaft close to the reactor top where coalescing effects are most dominant. This tendency is in good agreement with the experimental results by Laakkonen et al. (2007a).

Table 1 summarizes all experimental and simulated data of this study. The power input by torque is predicted well by the simulation. Especially, Mesh 3 shows less than 2.8% deviation from experimental measurements. The power number  $N_p = P/\rho N^3 D^5$  of 10.88 for the entire systems is rather low compared to expected  $N_p$  of 5 per Rushton turbine in distinct turbulent flows (here  $Re \approx 2.5 \times 10^5$ ) (Rushton, Costich, & Everett, 1950). However, such high  $N_p$  are only obtained for multi-impeller systems with complete parallel flow. By contrast, Figure 2 clearly depicts the nondistinct character of the flow field in agreement with Chunmei, Jian, Xinhong, and Zhengming (2008) and Xueming, Xiaoling, and Yulin (2008) which is further supported by the low velocity ratio of the middle stirrer (Supporting Information Material D). Taking an additional reduction of power number due to the gas phase into account, Armenante and Chang (1998) found similar non-gassed power numbers for a comparable reactor configuration. Experimental (3.6%) and simulated (3.2%) gas hold up are in fair comparison, considering the experimental noise. The simulated gas hold up of 2.4% from Laakkonen et al. (2007a) is smaller than the gas hold up presented here. Although the authors chose a higher agitation rate, one instead of three Rushton turbines was used. Therefore, smaller power input and gas hold up can be expected. Highly accurate prediction of  $k_{La}$  values was achieved. Even the coarse Mesh 1 still reached good prediction quality of 92.8%. We qualify the very good prediction quality of  $k_{La}$  as a mirror of the well suitability of the Laakkonen approach. Because  $f_{sc}$  scales the turbulent energy dissipation proportionally, small differences in the prediction precision between the meshes may exist due to the nonlinear character of  $k_{La}$ , breakage and drag function. Gas hold up is furthermore directly dependent on the velocity profile which is predicted slightly different by Mesh 3 (Supporting Information Material D).

Following the approach of Vasconcelos, Alves, and Barata (1995) and choosing the geometric similarity as 100, the mixing time is estimated as  $\tau_{95} = 15.9$  s fairly agreeing with the experimental findings. Alternately, the mixing time was simulated by adjusting the Schmidt number  $Sc_T$  from 0.7 to 0.2. Whereas this is a common choice for single-phase studies (Delafosse et al., 2014; Haringa et al., 2016; Montante, Mošćek, Jahoda, & Magelli, 2005), the improvement is less incisive for multiphase simulations where the upwards motion of the gas breaks the mass-exchange barrier of the inter impeller zone (Haringa et al., 2017). Considering the experimental standard deviation of mixing experiments all meshes allow satisfactory prediction quality.

Because the bubble diameter was not experimentally measured, comparison is performed with measured Sauter mean diameters of about 1.2–4.1 mm from Laakkonen et al. (2007a) testing similar settings. Accordingly, fair agreement is observed.

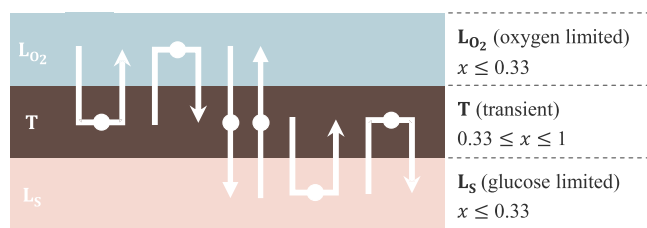


**FIGURE 1** Regime transition patterns.  $L_{O_2}TL_{O_2}$ : Particle starts and ends in low oxygen regime with a dwelling time in the transition area.  $TL_{O_2}T$ : Reverse event starting in the transition area with residence in low oxygen regime.  $L_{O_2}TL_S$ : Particle traverses all regimes from low oxygen to low glucose.  $L_S TL_{O_2}$ : Reverse movement from low glucose to low oxygen.  $TL_S T$ : Circulation from transition over low glucose back to transition area.  $L_S TL_S$ : Reverse event from low glucose to transition back to low glucose regime. The second capital letter always indicates the area in which the residence time  $\tau$  was measured [Color figure can be viewed at [wileyonlinelibrary.com](http://wileyonlinelibrary.com)]

Summarizing, simulated values fit the experimental data very well. Even for Mesh 1, deviations are acceptable.

### 3.2 | Pseudo-stationary double gradients

Pseudo-stationary double gradients of the late fed-batch scenario were obtained by embedding reactions into the continuous phase containing the media. Estimating the time needed to shift a culture to substrate depletion ( $\tau_{dep} = K_S / (q_{S,max} c_X) = 0.38$  s) reveals that  $\tau_{dep}$  is more than an order of magnitude smaller than mixing ( $\tau_{95} = 15.2 \pm 4$  s) and circulation time ( $\tau_{circ} = 2.9 \pm 0.75$  s). Accordingly, the formation of substrate gradients is likely to occur. Figure 3 shows that spatial distributions of growth are fairly similar for each simulation (average  $\mu = 0.0335$  hr<sup>-1</sup>) irrespective of the mesh quality used. Highest growth rates were reached proximate to the top impeller whereas cell growth was strongly limited in the rest of the reactor. Figure 4a,b elucidates the reasons for the growth distribution highlighting glucose and oxygen gradients exemplarily of Mesh 3.

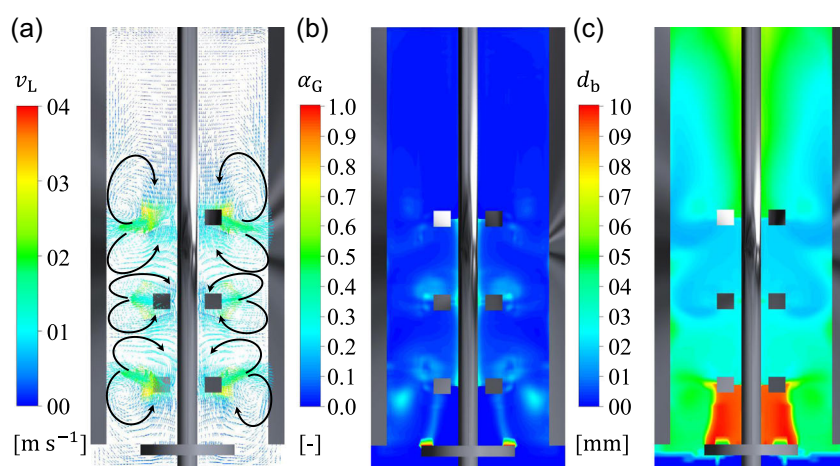


**FIGURE 2** (a) Flow field, (b) gas volume distribution, and (c) bubble size distribution of the simulation with Mesh 3 [Color figure can be viewed at [wileyonlinelibrary.com](http://wileyonlinelibrary.com)]

**TABLE 1** Comparison of simulated parameters and experimental validation

Setup	$N_p$	$\alpha_G$ (%)	$k_L a$ (hr <sup>-1</sup> )	$\tau_{95}$ (s <sup>-1</sup> )	$d_b$ (mm)
Mesh 1	9.50	2.7	116	17	3
Mesh 2	11.82	2.6	115	13.9	3
Mesh 3	11.18	3.2	122	13.1	3.4
Exp	$10.88 \pm 0.11$	$3.6 \pm 0.3$	$125 \pm 4$	$15.2 \pm 4$	1.2–4.1

Note: Experimental bubble diameter was taken from Laakkonen et al. (2007a).

Small differences between the meshes in the overall physical parameters like  $k_L a$  or  $\tau_{95}$  contributed to slight differences in the gradient formation. High glucose ( $H_S$ ) concentrations only occur next to the feed port, surrounded by a transition zone ( $T_S$ ), whereas the flow fields of the three Rushton turbines is glucose-limited ( $L_S$ ). Interestingly, the opposite scenario attunes for oxygen showing high oxygen concentrations ( $H_{O_2}$ ) in the bulk ranging from the reactor bottom to the top impeller (see Figure 4b). The overlay of glucose and oxygen gradients leads to a scenario as shown in Figure 4c, the assignment of low oxygen levels at the top ( $L_{O_2}$ ), low glucose levels in the Rushton mixing zone ( $L_S$ ) and a lean section of mid-level concentrations (T) located between  $L_{O_2}$  and  $L_S$ . It is exactly in T where highest growth rates occur. Interesting enough, T only accounts for <5% of the of the total volume according to Mesh 3. Notably, Meshes 1 and 2 provide similar prediction with 3.7% and 3.3%, respectively.

#### 3.2.1 | Statistical lifeline analysis

Applying the approach of Haringa et al. (2016) so-called *lifelines* were studied, that is, the fluctuating paths of 120,000 *C. glutamicum* massless cells were recorded and analyzed with respect to the regime changes according to Figure 1. Concentration profiles of glucose and oxygen encountered by individual cells were used to

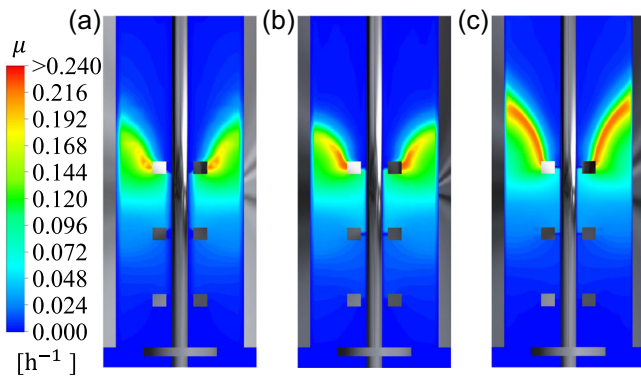


**FIGURE 3** Local distribution of simulated growth rates for (a) Mesh 1, (b) Mesh 2, and (c) Mesh 3 [Color figure can be viewed at [wileyonlinelibrary.com](http://wileyonlinelibrary.com)]

estimate growth rates applying the Roels multisubstrate kinetic. The average growth rate ( $\mu = 0.0291 \text{ hr}^{-1}$ ) was comparable for all meshes and is in good agreement with the Eulerian approach ( $\mu = 0.0335 \text{ hr}^{-1}$ ). Thereof, the conclusion was drawn that a sufficient number of particles was used. Figure 5d shows an exemplary lifeline for 25 s. The normalized glucose and oxygen concentrations are displayed in Figure 5a for 200 s. The profiles are consistent with the gradient depicted in the previous section. High glucose concentrations are coupled to low oxygen concentrations and vice versa. Only if both substrates are present in moderate concentrations higher growth rates can be obtained as demonstrated in Figure 5b. The profiles were translated into regime transitions for further analysis as illustrated in Figure 5c. Characteristic patterns are marked in red.  $TL_S T$  may serve as an example for interpretation: After 18 s, the bacterial fluctuating path  $TL_S T$  starts from moderate glucose and oxygen levels (T), traverses quickly to low glucose

**FIGURE 4** Concentration profiles derived from Mesh 3 of glucose (a) fed from the top and oxygen (b) introduced by a ring sparger close to the reactor bottom. Coloration from dark to light colors indicates high, transient, or low concentrations. Overlapping both gradients results in the regimes (c) with low glucose  $L_S$ , transient T, and low oxygen  $L_{O_2}$  concentrations [Color figure can be viewed at [wileyonlinelibrary.com](http://wileyonlinelibrary.com)]

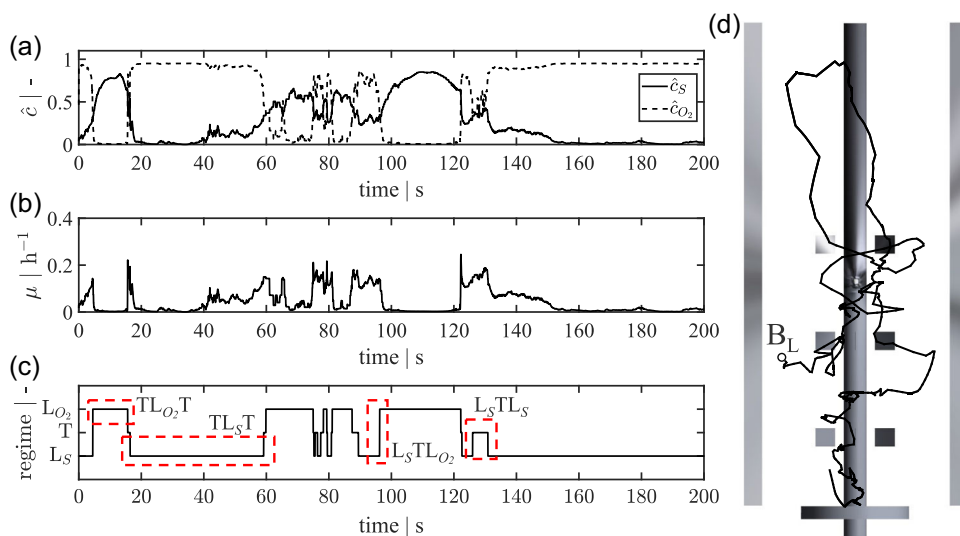
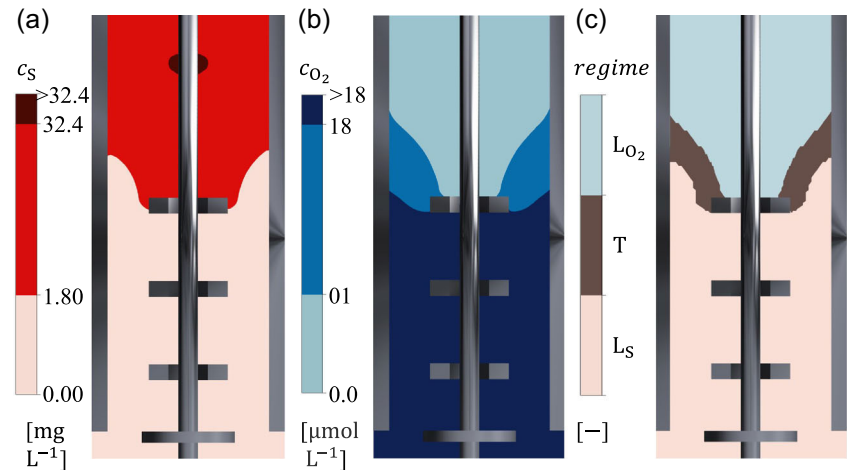


**FIGURE 5** (a) Profiles of normalized ( $\hat{c} = c_M/c_{MK_M}$ ) glucose and oxygen concentration and (b) the resulting growth rate of a bacterial lifeline recorded for 200 s. (c) The profiles were translated to low glucose  $L_S$ , low oxygen  $L_{O_2}$ , and a transient regime T. (d) Bacterial lifeline in the bioreactor for 25 s [Color figure can be viewed at [wileyonlinelibrary.com](http://wileyonlinelibrary.com)]

**TABLE 2** Regime transition statistics

Regime transition	Frequency (%)	$\bar{\tau}$ (s)	$\tau_{\max}$ (s)
L <sub>S</sub> TL <sub>S</sub>	10.06	0.36	1.05
TL <sub>S</sub> T	31.36	5.50	75.66
TL <sub>O<sub>2</sub></sub> T	26.47	2.99	13.47
L <sub>O<sub>2</sub></sub> TL <sub>O<sub>2</sub></sub>	4.62	0.38	1.23
L <sub>S</sub> TL <sub>O<sub>2</sub></sub>	15.99	0.20	0.81
L <sub>O<sub>2</sub></sub> TL <sub>S</sub>	11.50	0.33	1.20

Note: Total frequency, average ( $\bar{\tau}$ ), and maximal ( $\tau_{\max}$ ) residence time are listed for each regime transition pattern.

concentrations (L<sub>S</sub>) where the cells stays for 40 s before cycling back to moderate glucose and oxygen levels encoded as T. Notably, time  $\tau$  code for residence periods of the middle zone (mid-capital letter) because transition times are quite short.

Bacterial lifeline patterns were statistically evaluated to obtain frequency distributions as a function of  $\tau$ . Finally, six transition strategies were evaluated and compared for the three meshes. Statistical readouts comprised the total frequency of the events, average and maximal residence times (see Table 2). Maximal residence times correspond to the limit, within which 99% of the values were located. For example, Figure 6 depicts the regime transition distributions of Mesh 3. Remarkably long residence times are assessed for the regime transition TL<sub>S</sub>T. Some bacteria may linger up to 76 s in the glucose-limited zone before moving back to the transition area. However, the average residence time in L<sub>S</sub> is about 5.5 s. With ~31% TL<sub>S</sub>T is the most frequent regime transition. The following reason may be deduced from Figure 3: cells are trapped in the trailing vortices of the three impellers causing circulation within the low glucose regime. The second most frequent regime transition is TL<sub>O<sub>2</sub></sub>T with 26.5%. Maximum (13.5 s) and average (3 s) residence times are clearly shorter than in regime TL<sub>S</sub>T. Notably, all distribution patterns comprising T as key residence zone show rapid decays after <1.5 s.

Those regimes host cells less than 0.4 s in T which is in the magnitude of  $\tau_{\text{dep}}$ . In essence, the fast crossings of zone T reflect its small dimension and the high fluid velocities at the top impeller.

Using Mesh 3 as reference, Figure 7 depicts deviations of average regime residence times regarding Meshes 1 and 2. For instance, results of L<sub>S</sub>TL<sub>S</sub> and L<sub>S</sub>TL<sub>O<sub>2</sub></sub> differ only about 1% and 7% for Meshes 2 and 1, respectively. Most important, the dominating transitions TL<sub>S</sub>T and TL<sub>O<sub>2</sub></sub>T only differ by max 31% (Mesh 2), with Mesh 1 showing fairly good agreement of -9.6% and +16% only. This finding is highly remarkable as it means that biologically meaningful readouts (i.e., exposure to limiting regimes) can be predicted well with moderate computational efforts. Mesh 1 only possesses 1/10 grid size of Mesh 3. In other words, less computation is needed to qualify cellular performance in large-scale industrial bioreactors.

### 3.2.2 | Simplified design of scale-down devices

For the given model case scenario, the volumetric fraction of moderate substrate supply (T) is less than 5% only. Transitions through this zone take 1.2 s maximum. Hence, instantaneous metabolic responses may occur, but the initiation of transcriptional effects appears rather unlikely. For *E. coli*, Löffler et al. (2016) observed massive transcriptional responses after stress exposure periods >35 s. Still, the initiation of transcriptional response may have happened causing the propagation of the transcriptional response into well-mixed zones of the bioreactor (Nieß, Löffler, Simen, & Takors, 2017). However, *C. glutamicum* has already proven its strong robustness regarding the exposure to large-scale stress conditions. Accordingly, the transition zone may be excluded for SD design leading to a simplified two-compartment SD device similar to Käß et al. (2014). As such, the Euler-Lagrangian analysis may be simplified by lumping related regime changes finally yielding the two-compartment readouts L<sub>S</sub>L<sub>O<sub>2</sub></sub>L<sub>S</sub> and L<sub>O<sub>2</sub></sub>L<sub>S</sub>L<sub>O<sub>2</sub></sub>. With 3.4 s for the first and 5.7 s for the latter, longer residence times in glucose-limited regimes were found that may expand to maximum residence times of 15 and 80.5 s, respectively.

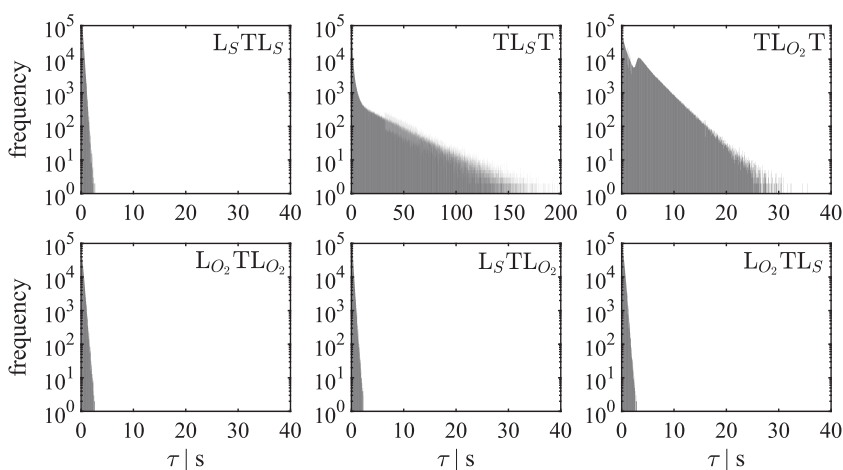


**FIGURE 6** Regime transition pattern as function of the residence time  $\tau$ . The six possible patterns are shown as semi-log plot

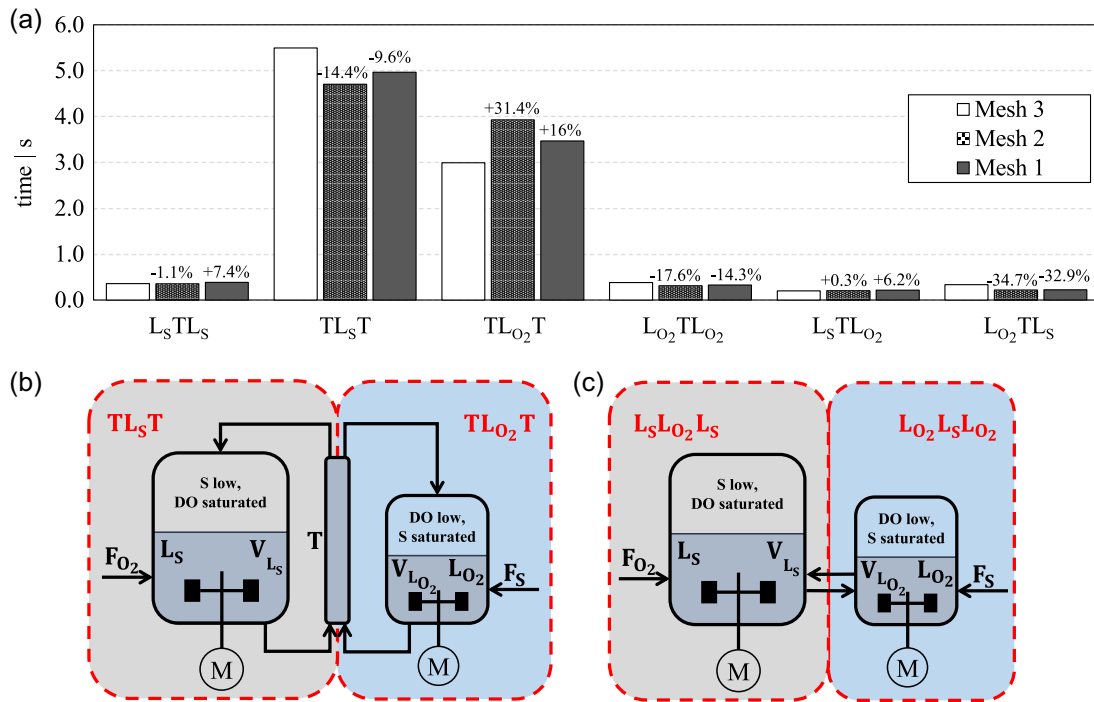


**FIGURE 7** (a) Comparison of average residence time prediction  $\bar{\tau}$  for the three simulated meshes. Deviations of Meshes 1 and 2 compared to Mesh 3 are displayed. (b and c) Examples of simplified scale-down devices [Color figure can be viewed at [wileyonlinelibrary.com](http://wileyonlinelibrary.com)]

In general, the findings of residence time distributions may be well used to design wet-lab scale-up simulators. Figure 7b illustrates that the regimes are translated in a multicompartiment setup comprising two STRs connected by a plug flow reactor (PFR). The PFR may serve as the realization of the T zone. Key limitations are installed in the STR as indicated. Each STR requires additional supply of substrate or oxygen to raise limiting levels. Pumping between PFR and both STRs follows the mindset of  $L_S TL_{O_2}$ ,  $L_S TL_S$ ,  $L_{O_2} TL_S$ , and  $L_{O_2} TL_{O_2}$  traveling paths. Regime assignments and changes may be controlled by the volume ratios of the different tanks with average dwelling times set by pumping rates. By deciding on a particular scale-up design, experimentalists basically choose the percentage of frequency changes covered by the experimental setup. For instance, the showcase of Figure 7c neglects the impact of T for the sake of simplicity. Noteworthy, the examples of Figure 7b,c mirror the 300-L pilot-scale scenario. Mimicking large-scale industrial bioreactors likely requires longer dwelling times and different volume ratios.

### 3.2.3 | Sensitivity of regime size depending on biological parameters

Given that kinetic parameters and process conditions differ from organism to organism their impact on regime size and transitions may be an important criterion for qualifying the suitability of scale-up simulators (such as Figure 7b,c) for studying the impact of liquid nutrients and oxygen. Results of a sensitivity analysis varying kinetic and operational parameters are summed in Table 3 and depicted in

Supporting Information Material F exemplarily for one scenario. Doubling the biomass concentrations  $c_X$  leads to smaller transient regime T, but to bigger regimes of limited oxygen  $L_{O_2}$  and glucose concentrations  $L_S$ . For organisms possessing higher specific maximal substrate consumption rate, the size of  $L_S$  increased, due to reduced transient regime, whereas  $L_{O_2}$  remains. The opposite scenario occurs for organisms with higher specific maximal oxygen consumption rate  $q_{O_2}$ , leaving  $L_S$  unaffected but leading to decreased T and increased  $L_{O_2}$ . Rising  $K_S$  adapts regime classification leading to bigger substrate limitation zone, smaller transient and oxygen limited zones. Higher  $K_{O_2}$  shows no effects on regime size. By doubling the feed the transient regime spreads toward the second impeller, reducing  $L_S$  but leaving  $L_{O_2}$  unaffected. Reverse behavior of the regime size was observed by lowering the respective parameter.

**TABLE 3** Sensitivity of regime size

Parameter	Influence on regime size		
	$L_S$	T	$L_{O_2}$
$c_X \uparrow$	↑	↓	↑
$q_{S,max} \uparrow$	↑	↓	→
$q_{O_2,max} \uparrow$	→	↓	↑
$K_S \uparrow$	↑	↓	↓
$K_{O_2} \uparrow$	→	→	→
$F \uparrow$	↓	↑	→

Note: Variation of organism-specific parameter or operating conditions.

Summarizing, sensitivity analysis shows that ratios of  $L_5:T:LO_2$  depend on biological kinetics and process conditions while structural settings of two-phase scale-up simulators remain. Indeed, the setup well resembles conventional settings. However, the two-phase CFD simulations give a quantitative estimate about the degree of similarity with the eyes of the microbes, now.

## 4 | CONCLUSION

The scaling factor approach (Laakkonen et al., 2007a, 2007b) was successfully applied for a two-phase flow Euler–Euler multi-impeller pilot-scale bioreactor simulation. Although, the factor was simply simulated and not derived from experimental measurements, physical properties such as power input, gas hold up,  $k_La$  value and mixing time were estimated fairly good compared to experimental tests. Interesting enough, statistical analysis of lifelines further revealed that biologically relevant readouts such as regime changes can be based well on relatively coarse mesh granularity, still giving accurate residence time distribution of <15% deviation (mostly) compared to 10-fold finer structured meshes. Consequently, a mesh density of  $1.12 \times 10^5 \# / m^3$  is suggested to be sufficient to reflect the actual situation within the bioreactor. Likewise, similar grid sizes have been used in multiphase simulations (Bach et al., 2017; Haringa et al., 2017). This finding opens the door for large-scale applications with least computational effort. Using the scaling factor not only proper estimations of physical criteria but also biological readouts such as regime changes are well predictable.

The study showcased the application for *C. glutamicum*. But sensitivity analysis showed that design and structure of wet-lab scale-up simulators should be well transferrable to other microbial kinetics and process conditions. Notably, the approach intrinsically offers an a priori quantitative assessment predicting how close lab scale conditions will mimic large-scale scenarios.

## ACKNOWLEDGMENTS

The authors gratefully acknowledge the funding by Deutsche Forschungsgemeinschaft DFG (Grant No. DFG241/5-1). The authors also thank Salaheddine Laghrami for his support with the experimental measurements. Computational resources have been provided by the High Performance Computing Center Stuttgart of the University of Stuttgart.

## CONFLICT OF INTERESTS

The authors declare that there are no conflict of interests.

## NOMENCLATURE

$C_D$	drag coefficient
$CO_2$	oxygen concentration (mmol <sub>2</sub> /L)
$c_s$	glucose concentration (g <sub>s</sub> /L)
$c_x$	biomass concentration (g <sub>CDW</sub> /L)
$F$	feeding rate (g <sub>s</sub> /hr)
$f_{sc}$	scaling factor

$k_La$	volumetric mass transfer rate (hr <sup>-1</sup> )
$KO_2$	affinity constant for oxygen (mmol <sub>2</sub> /L)
$K_s$	affinity constant for glucose (g <sub>s</sub> /L)
$N$	agitation rate (s <sup>-1</sup> )
$N_p$	power number
$P$	power (W)
$p$	pressure (Pa)
$R$	universal gas constant (J·mol <sup>-1</sup> ·K <sup>-1</sup> )
$Re$	Reynolds number
$Sc_T$	turbulent Schmidt number
$St$	Stokes number
$T$	temperature (K)
$Y_{XO_2}$	biomass oxygen yield (g <sub>CDW</sub> /mmol <sub>2</sub> )
$Y_{XS}$	biomass substrate yield (g <sub>CDW</sub> /g <sub>s</sub> )

## ABBREVIATIONS

BSD	bubble size distribution
LES	large eddy simulation
PBE	population balance model
RANS	Reynolds average Navier–Stokes
SD	scale down
UDF	user defined function

## GREEK SYMBOLS

$\alpha$	volume fraction
$\varepsilon$	turbulent dissipation rate (m <sup>2</sup> /s <sup>3</sup> )
$\eta_L$	media viscosity (Pa·s)
$\mu$	growth rate (hr <sup>-1</sup> )
$\rho_L$	media density (kg/m <sup>3</sup> )
$\sigma_L$	media surface tension (N/m)
$\tau_{95}$	mixing time (s)
$\phi_G$	molar flow (mol/s)

## SUBSCRIPTS

*	equilibrium concentration
dep	depletion
eff	effective
G	gas
L	liquid
max	maximal
sc	scaled variable

## ORCID

Ralf Takors  <http://orcid.org/0000-0001-5837-6906>

## REFERENCES

- Alpöaeus, V., Koskinen, J., & Keskinen, K. I. (1999). Simulation of the population balances for liquid-liquid systems in a nonideal stirred tank. Part 1 Description and qualitative validation of the model. *Chemical Engineering Science*, 54(24), 5887–5899.

- Armenante, P. M., & Chang, G. M. (1998). Power consumption in agitated vessels provided with multiple-disk turbines. *Industrial and Engineering Chemistry Research*, 37(1), 284–291.
- Bach, C., Yang, J., Larsson, H., Stocks, S. M., Gernaey, K. V., Albaek, M. O., & Krühne, U. (2017). Evaluation of mixing and mass transfer in a stirred pilot scale bioreactor utilizing CFD. *Chemical Engineering Science*, 171, 19–26.
- Bakker, A., & Van den Akker, H. E. A. (1994). A computational model for the gas-liquid flow in stirred reactors. *Chemical Engineering Research and Design*, 72(A4), 594–606.
- Becker, J., & Wittmann, C. (2012). Bio-based production of chemicals, materials and fuels – *Corynebacterium glutamicum* as versatile cell factory. *Current Opinion in Biotechnology*, 23(4), 631–640.
- Brucato, A., Grisafi, F., & Montante, G. (1998). Particle drag coefficients in turbulent fluids. *Chemical Engineering Science*, 53(18), 3295–3314.
- Buffo, A., Vanni, M., Renze, P., & Marchisio, D. L. (2016). Empirical drag closure for polydisperse gas-liquid systems in bubbly flow regime: Bubble swarm and micro-scale turbulence. *Chemical Engineering Research and Design*, 113, 284–303.
- Bylund, F., Collet, E., Enfors, S., & Larsson, G. (1998). Substrate gradient formation in the large-scale bioreactor lowers cell yield and increases by-product formation. *Bioprocess Engineering*, 18, 171–180.
- Chunmei, P., Jian, M., Xinhong, L., & Zhengming, G. A. O. (2008). Investigation of fluid flow in a dual Rushton impeller stirred tank using particle image velocimetry. *Chinese Journal of Chemical Engineering*, 16(5), 693–699.
- Coroneo, M., Montante, G., Paglianti, A., & Magelli, F. (2011). CFD prediction of fluid flow and mixing in stirred tanks: Numerical issues about the RANS simulations. *Computers and Chemical Engineering*, 35(10), 1959–1968.
- Delafosse, A., Collignon, M. L., Calvo, S., Delvigne, F., Crine, M., Thonart, P., & Toye, D. (2014). CFD-based compartment model for description of mixing in bioreactors. *Chemical Engineering Science*, 106, 76–85.
- Enfors, S., Jahic, M., Rozkov, A., Xu, B., Hecker, M., & Ju, B. (2001). Physiological responses to mixing in large scale bioreactors. *Journal of Biotechnology*, 85, 175–185.
- Gaddis, E. S., & Vogelwohl, A. (1986). Bubble formation in quiescent liquids under constant flow conditions. *Chemical Engineering Science*, 41(1), 97–105.
- Garcia-Ochoa, F., & Gomez, E. (2009). Bioreactor scale-up and oxygen transfer rate in microbial processes: An overview. *Biotechnology Advances*, 27, 153–176.
- Hagesaether, L., Jakobsen, H. A., & Svendsen, H. F. (2002). A model for turbulent binary breakup of dispersed fluid particles. *Chemical Engineering Science*, 57(16), 3251–3267.
- Haringa, C., Deshmukh, A. T., Mudde, R. F., & Noorman, H. J. (2017). Euler-Lagrange analysis towards representative down-scaling of a 22 m<sup>3</sup> aerobic *S. cerevisiae* fermentation. *Chemical Engineering Science*, 16, 652–663.
- Haringa, C., Tang, W., Deshmukh, A. T., Xia, J., Reuss, M., Heijnen, J. J., ... Noorman, H. J. (2016). Euler-Lagrange computational fluid dynamics for (bio)reactor scale-down: An analysis of organism life-lines. *Engineering in Life Sciences*, 16, 1–29.
- Hewitt, C. J., & Nienow, A. W. (2007). The scale-up of microbial batch and fed-batch fermentation processes. *Advances in Applied Microbiology*, 62, 105–135.
- Ishii, M., & Zuber, N. (1979). Drag coefficient and relative velocity in bubbly, droplet or particulate flows. *AIChE Journal*, 25(5), 843–855.
- Junker, B. H. (2004). Scale-up methodologies for *Escherichia coli* and yeast fermentation processes. *Journal of Bioscience and Bioengineering*, 97(6), 347–364.
- Junne, S., Klingner, A., Itzeck, D., Brand, E., & Neubauer, P. (2012). Consistency of Scale-Up from Bioprocess Development to Production. In *Biopharmaceutical Production Technology* (pp. 511–543). Weinheim, Germany: Wiley-VCH Verlag GmbH & Co. KGaA.
- Käß, F., Junne, S., Neubauer, P., Wiechert, W., & Oldiges, M. (2014). Process inhomogeneity leads to rapid side product turnover in cultivation of *Corynebacterium glutamicum*. *Microbial Cell Factories*, 13(1), 6.
- Kálal, Z., Jahoda, M., & Fort, I. (2014). Modelling of the bubble size distribution in an aerated stirred tank: Theoretical and numerical comparison of different breakup models. *Chemical and Process Engineering*, 35(3), 331–348.
- Kita, K., Konishi, K., & Anraku, Y. (1984). Terminal oxidases of *Escherichia coli* aerobic respiratory chain. *Journal of Biological Chemistry*, 259(5), 3368–3374.
- Kumar, S., & Ramkrishna, D. (1996). On the solution of PBE by discretization-I. A fixed pivot technique. *Chemical Engineering Science*, 51(8), 1311–1332.
- Kuschel, M., Siebler, F., & Takors, R. (2017). Lagrangian trajectories to predict the formation of population heterogeneity in large-scale bioreactors. *Bioengineering*, 4(2), 27.
- Kusumoto, K., Sakiyama, M., Sakamoto, J., Noguchi, S., & Sone, N. (2000). Menaquinol oxidase activity and primary structure of cytochrome bd from the amino-acid fermenting bacterium *Corynebacterium glutamicum*. *Archives of Microbiology*, 173(5–6), 390–397.
- Kysela, B., Konfrst, J., Chara, Z., Sulc, R., & Jasikova, D. (2017). Evaluation of the turbulent kinetic dissipation rate in an agitated vessel. *European Physical Journal Conferences*, 02062, 1–4.
- Laakkonen, M., Alopaeus, V., & Aittamaa, J. (2006). Validation of bubble breakage, coalescence and mass transfer models for gas-liquid dispersion in agitated vessel. *Chemical Engineering Science*, 61(1), 218–228.
- Laakkonen, M., Moilanen, P., Alopaeus, V., & Aittamaa, J. (2007a). Modelling local bubble size distributions in agitated vessels. *Chemical Engineering Science*, 62(3), 721–740.
- Laakkonen, M., Moilanen, P., Alopaeus, V., & Aittamaa, J. (2007b). Modelling local gas-liquid mass transfer in agitated vessels. *Chemical Engineering Research and Design*, 85(5), 665–675.
- Lapin, A., Schmid, J., & Reuss, M. (2006). Modeling the dynamics of *E. coli* populations in the three-dimensional turbulent field of a stirred-tank bioreactor—a structured-segregated approach. *Chemical Engineering Science*, 61, 4783–4797.
- Leuchtenberger, W., Huthmacher, K., & Drauz, K. (2005). Biotechnological production of amino acids and derivatives: Current status and prospects. *Applied Microbiology and Biotechnology*, 69(1), 1–8.
- Lindner, S. N., Seibold, G. M., Henrich, A., Krämer, R., & Wendisch, V. F. (2011). Phosphotransferase system-independent glucose utilization in *Corynebacterium glutamicum* by inositol permeases and glucokinases. *Applied and Environmental Microbiology*, 77(11), 3571–3581.
- Löffler, M., Simen, J. D., Jäger, G., Schäferhoff, K., Freund, A., & Takors, R. (2016). Engineering *E. coli* for large-scale production—strategies considering ATP expenses and transcriptional responses. *Metabolic Engineering*, 38, 73–85.
- Luo, H., & Svendsen, H. F. (1996). Theoretical model for drop and bubble breakup in turbulent dispersions. *AIChE Journal*, 42(5), 1225–1233.
- Montante, G., Moštek, M., Jahoda, M., & Magelli, F. (2005). CFD simulations and experimental validation of homogenisation curves and mixing time in stirred Newtonian and pseudoplastic liquids. *Chemical Engineering Science*, 60(8–9), 2427–2437.
- Morchain, J., Gabelle, J. C., & Cockx, A. (2014). A coupled population balance model and CFD approach for the simulation of mixing issues in lab-scale and industrial bioreactors. *American Institute of Chemical Engineers*, 60, 27–40.
- Morrison, C., & Lähteenmäki, R. (2017). Public biotech in 2016—the numbers. *Nature Biotechnology*, 35(7), 623–629.
- Neubauer, P., Cruz, N., Glauche, F., Junne, S., Knepper, A., & Raven, M. (2013). Consistent development of bioprocesses from microliter cultures to the industrial scale. *Engineering in Life Sciences*, 13, 224–238.

- Nieß, A., Löffler, M., Simen, J. D., & Takors, R. (2017). Repetitive short-term stimuli imposed in poor mixing zones induce long-term adaptation of *E. coli* cultures in large-scale bioreactors: Experimental evidence and mathematical model. *Frontiers in Microbiology*, 8(June), 1–9.
- Pigou, M., & Morchain, J. (2015). Investigating the interactions between physical and biological heterogeneities in bioreactors using compartment, population balance and metabolic models. *Chemical Engineering Science*, 126, 267–282.
- Roels, J. A. (1983). *Energetics and Kinetics in Biotechnology*. Amsterdam: Elsevier Biomedical Press.
- Rosseburg, A., Fitschen, J., Wutz, J., Wucherpfennig, T., & Schlüter, M. (2018). Hydrodynamic inhomogeneities in large scale stirred tanks – influence on mixing time. *Chemical Engineering Science*, 188, 208–220.
- Rushton, J. H., Costich, E. W., & Everett, H. J. (1950). Power characteristics of mixing impeller. *Chemical Engineering Progress*, 46, 395–404.
- Scargiali, F., D'Orazio, A., Grisafi, F., & Brucato, A. (2007). Modelling and simulation of gas–liquid hydrodynamics in mechanically stirred tanks. *Chemical Engineering Research and Design*, 85(5 A), 637–646.
- Schmidt, F. R. (2005). Optimization and scale up of industrial fermentation processes. *Applied Microbiology and Biotechnology*, 68, 425–435.
- Takors, R., Bathe, B., Rieping, M., Hans, S., Kelle, R., & Huthmacher, K. (2007). Systems biology for industrial strains and fermentation processes—Example: Amino acids. *Journal of Biotechnology*, 129(2), 181–190.
- Tomiyama, A., Kataoka, I., Zun, I., & Sakaguchi, T. (1998). Drag coefficients of single bubbles under normal and micro gravity conditions. *JSME International Journal Series B*, 41(2), 472–479.
- Vasconcelos, J. M. T., Alves, S. S., & Barata, J. M. (1995). Mixing in gas-liquid contactors agitated by multiple turbines. *Chemical Engineering Science*, 50(14), 2343–2354.
- Vrábel, P., Van Der Lans, R. G. J. M., Van Der Schot, F. N., Ch, K., Luyben, A. M., Xu, B., & Enfors, S. (2001). CMA: Integration of fluid dynamics and microbial kinetics in modelling of large-scale fermentations. *Chemical Engineering Journal*, 84, 463–474.
- Wiedmann, J. A. (1983). Zum überflutungsverhalten zwei- und dreiphasig betriebener Rührreaktoren. *Chemie Ingenieur Technik*, 55(9), 689–700.
- Xueming, S., Xiaoling, L., & Yulin, L. (2008). Experimental study of influence of the impeller spacing on flow behaviour of double-impeller stirred tank. *The Canadian Journal of Chemical Engineering*, 81(6), 1239–1245.

## SUPPORTING INFORMATION

Additional supporting information may be found online in the Supporting Information section.

**How to cite this article:** Kuschel M, Takors R. Simulated oxygen and glucose gradients as a prerequisite for predicting industrial scale performance a priori. *Biotechnology and Bioengineering*. 2020;117:2760–2770. <https://doi.org/10.1002/bit.27457>